

Hristo D. Hristov

Fresnel Zones

in wireless links, zone plate
lenses and antennas



Fresnel Zones in Wireless Links, Zone Plate Lenses and Antennas

For a listing of recent titles in the *Artech House Antennas and Propagation Library*,
turn to the back of this book.

Fresnel Zones in Wireless Links, Zone Plate Lenses and Antennas

Hristo D. Hristov



Artech House
Boston • London

Library of Congress Cataloging-in-Publication Data

Hristov, Hristo D.

Fresnel zones in wireless links, zone plate lenses and antennas / Hristo D. Hristov
p. cm. — (Artech House antennas and propagation library)

Includes bibliographical references and index.

ISBN 0-89006-849-6 (alk. paper)

1. Lens antennas. 2. Wireless communication systems. 3. Fresnel lenses. I. Series.

TK7871.67.L45 H56 2000

621.382'4—dc21

99-052314

CIP

British Library Cataloguing in Publication Data

Hristov, Hristo D.

Fresnel zones in wireless links, zone plate lenses and
antennas. — (Artech House antennas and propagation library)

1. Fresnel lenses 2. Light, Wave theory of

1. Title

535.3'24

ISBN 0-89006-849-6

Cover design by Igor Valdman

© 2000 ARTECH HOUSE, INC.

685 Canton Street

Norwood, MA 02062

All rights reserved. Printed and bound in the United States of America. No part of this book may be reproduced or utilized in any form or by any means, electronic or mechanical, including photocopying, recording, or by any information storage and retrieval system, without permission in writing from the publisher.

All terms mentioned in this book that are known to be trademarks or service marks have been appropriately capitalized. Artech House cannot attest to the accuracy of this information. Use of a term in this book should not be regarded as affecting the validity of any trademark or service mark.

International Standard Book Number: 0-89006-849-6

Library of Congress Catalog Card Number: 99-052314

10 9 8 7 6 5 4 3 2 1

To the sacred memory of my mother and father

This page intentionally left blank

Contents

	Foreword	xiii
	Preface	xv
1	Basic Electromagnetic Wave Equations	1
1.1	Wave Equations for Time-Harmonic Fields	1
1.1.1	Wave Equation for Magnetic Vector Potential	1
1.1.2	Far-Field Solution to Wave Equation	3
1.2	Wave Polarization	5
1.3	Amplitude and Phase Properties of Waves in Boundless Space	6
1.3.1	Equations for Amplitude and Phase Constants	7
1.3.2	Some Data for Ground Media	8
1.3.3	Basic Radio Link Equations	8
1.4	Boundary Field Conditions: Reflection and Transmission	12
1.4.1	Boundary Field Conditions	13
1.4.2	Reflection and Transmission of Plane Electromagnetic Waves	13

1.4.3	Some Special Cases of Reflection and Transmission	17
1.5	Interference of Electromagnetic Waves	19
1.5.1	Linear Superposition of Electromagnetic Fields	19
1.5.2	Interference Methods	21
1.6	Matrix Analysis of Plane Wave Transmission Through Dielectric Plates	25
1.6.1	Analogy Between Dielectric Media and Transmission Lines	25
1.6.2	Transmission Through Multilayer Dielectric Plates	27
	References	31
	Appendix 1A: Antenna Polarization Parameters	32
2	Fresnel-Kirchhoff Diffraction Theory	35
2.1	Huygens' Principle	35
2.2	Fresnel Zones	37
2.2.1	Fresnel Formulation of Huygens' Principle	38
2.2.2	Fresnel Zone Construction	40
2.2.3	Field Determination by Means of Fresnel Zone Construction	45
2.2.4	Particular Cases of Fresnel Zone Obstruction	48
2.2.5	Focusing Properties of Simple Fresnel Zone Lens-like Diffractors: Multizone Lenses of Soret and Wood	50
2.3	Scalar Kirchhoff's Diffraction Theory	54
2.3.1	Scalar Form of the Kirchhoff Diffraction Integral	54
2.3.2	Diffraction by Aperture in Infinite Plane Screen	58
2.3.3	Fraunhofer Diffraction by Circular Aperture	62

2.4	Fresnel Diffraction	64
2.4.1	Dimensionless Variables	65
2.4.2	Diffraction by Rectangular Aperture	66
2.4.3	Fresnel Cosine and Sine Integrals	67
2.4.4	Particular Cases of Diffraction by Rectangular Aperture	69
2.4.5	Fresnel Diffraction by Apertures of Circular Symmetry	72
2.4.6	Fresnel Diffraction by Obstacles	78
2.5	Vectorial Kirchhoff Diffraction Theory	80
	References	82
	Selected Bibliography	83
	Appendix 2A: Elementary Surface or Huygens' Source	83
3	Fresnel Zones Applied to Radio Communication Links	87
3.1	Fresnel Zones and Radio Wave Propagation	87
3.1.1	Ground-Wave Propagation Paths	88
3.1.2	Fresnel Zone Regions Important to Free-Space Propagation	89
3.1.3	Fresnel Zones in Case of Reflection	90
3.1.4	Line-of-Sight Interference Schemes for Radio Wave Propagation Over Smooth Earth	97
3.1.5	Radio Wave Propagation Over Hilly Terrain	104
3.2	Fresnel Zone Diffractors in Radio Relay Links	118
3.2.1	Metal Ring as Antenna Director	119
3.2.2	Dielectric Ring as Antenna Director	126
3.2.3	Ring Segment Diffractor as Passive Radio Wave Repeater	129
	References	136

4	Fresnel Zone Plates	139
4.1	Introduction	139
4.2	Classification of Fresnel Zone Plates	140
4.2.1	Classification According to Shape of Zonal Surface	141
4.2.2	Classification According to Cross-Sectional Structure	146
4.3	Planar Fresnel Zone Plates	153
4.3.1	Soret Zone Plate	153
4.3.2	Phase-Corrected Zone Plates	179
4.4	Curved Fresnel Zone Plates	201
4.4.1	Introduction	201
4.4.2	Dimensions of Curved Fresnel Zone Plates	203
4.4.3	Focusing Properties of Curved Zone Plates	213
	References	221
	Selected Bibliography	225
	Appendix 4A: Transmission Through Dielectric Plate With Metal Grid	226
5	Fresnel Zone Plate Antennas	231
5.1	Introduction	231
5.2	Planar Zone Plate Antennas: Transmission Versions	232
5.2.1	Soret Zone Plate Antenna	232
5.2.2	Phase-Corrected (Wood-Type) Zone Plate Antennas	253
5.3	Planar Zone Plate Antennas: Reflection Versions	268
5.3.1	Folded Phase-Reversal Zone Plate Antenna	270
5.3.2	Printed Reflector Zone Plate Antennas	274
5.4	Off-Axis Scanning in Planar Antenna With Circular Zone Plate	282
5.4.1	Some Experimental Studies	283

5.4.2	Scanning Feed Trajectory	284
5.4.3	Far-Field Gain Patterns	285
5.4.4	Numerical Results	286
5.5	Planar Offset Antenna With Elliptical Zone Plate	288
5.5.1	Geometry Formulation and Design of Elliptical Zones	288
5.5.2	Far-Field Analysis of Offset Elliptic Zone Plate Antenna: Transmission Case	289
5.5.3	Offset Antenna Designs: Numerical and Experimental Characteristics	290
5.6	Curved Zone Plate Antennas	296
5.6.1	Paraboloidal Zone Plate Antenna	297
5.6.2	Cylindrical Zone Plate Antenna	298
5.6.3	Millimeter-Wave Antennas With Curved Single-Dielectric Zone Plate	302
	References	303
	Selected Bibliography	308
	About the Author	311
	Index	313

This page intentionally left blank

Foreword

This book brings together several different areas, which are related by the concept of Fresnel zones, an idea that originated in the nineteenth century. The concept impacts the design of radio communication links and electronic countermeasures equipment (terrain bounce consideration), as well as radar propagation and ground reflection as they affect targeting accuracy, and, finally, methods of improving the characteristics of zoned lenses and antennas. The book is unique in treating these subjects from a common basis and in bringing together all of the recent research on zoned lenses and antennas.

The first two chapters provide a foundation of the electromagnetic wave description and the Fresnel-Kirchhoff diffraction theory, for use in the later chapters. Starting from the wave equation, the far-field solution is developed and consideration is given to wave polarization, amplitude and phase properties, radio link equations, field conditions, reflection and transmission, Snell's law, the Brewster angle, interference and linear superposition of electromagnetic fields, and multiple reflection and transmission by a dielectric slab. Matrix analysis of plane wave transmission through dielectric plates is also included. The second chapter treats Huygens' principle, Fresnel zones, scalar diffraction theory, diffraction by an aperture in an infinite plane, Fraunhofer diffraction by a circular aperture, Fresnel cosine and sine integrals, Fresnel diffraction by apertures or obstacles, and vectorial Kirchhoff diffraction theory. Throughout these and later chapters historical facts and information about early researchers are woven into the text. The first two chapters are a highly condensed summary of the area of electromagnetics, almost a short book on the subject.

The third chapter then applies this background information to radio communication links; line of sight propagation over various types of terrain including smooth, rough, knife-edge and other hill models; and refraction

effects. The material applies to various systems from 30 MHz to microwaves. This is a detailed and lengthy treatment, much too complex to summarize in a few sentences. In fact, this is a hallmark of the book as a whole: it is very comprehensive and diversified, containing a huge amount of detail and exhaustive analytical treatments of the subject areas. These first three chapters would make an excellent student textbook in wireless communication engineering, which is currently a very popular technical subject.

The final two chapters treat Fresnel zone plates as lenses, reflectors, and antenna systems. While there have been other treatments of Fresnel zone plates, most of them have dealt with the subject only from the "optical" point of view. This has to do with the configurations that are normally employed in set-ups at optical wavelengths. Such set-ups typically utilize focal lengths that are very large in terms of wavelength and in terms of the diameter of the zone plate lens aperture (e.g., several hundred times the diameter). These characteristics permit approximations in the analyses of focal region properties or far-field patterns that are quite different than those that are possible for the microwave/millimeter-wave case, where the focal length and diameter are often comparable in size. While the microwave/millimeter-wave zone plate may have 5 to 30 zones, the optical case may have 200 to 300 zones. Thus, there are orders of magnitude differences between the two cases. In addition, the optical case often deals with the Soret (half-opaque) zone plate rather than the Wood phase-correcting zone plate, while for reasons of better efficiency (and higher gain) the microwave/millimeter-wave case usually employs phase correction, often higher than half-wave (e.g., quarter-wave correction). Thus one cannot simply use the optical approximations in the microwave case, because certain general conclusions do not apply.

Dr. Hristov has done an excellent job of pulling together so much important material, with such careful attention to collection of references and historical material. He is, himself, a contributing researcher who has published numerous outstanding papers in the Fresnel zone plate field. The book is a significant contribution to the field, as well as a first of its kind, and Dr. Hristov is to be complimented for his work. The subject material is in very active technical areas, and the results will be applicable in many current problems in wireless communications, radar, guidance, and related fields.

*James C. Wiltse
December 1999*

Preface

About 200 years ago, the French engineer Augustin Jean Fresnel proposed a simple zone construction that helped him to explain and study various light-wave problems, from free space propagation to diffraction by a circular disk. Over time, Fresnel zones and zone plate devices found many different applications in optics, acoustics, radio wave engineering, geophysics, and so on, for ray tracing, focusing and object imaging, spatial processing and filtering, sensing, and many other uses.

This book presents in a single volume the classic electromagnetic theory of Fresnel zones and their applications to Kirchhoff's diffraction theory (physical optics), microwave propagation in wireless links, and Fresnel zone plate lenses and antennas. It is based on numerous publications, both classic and up-to-date, and is organized in five chapters. The first two chapters are mainly theoretical while the rest balance theory, designs, and applications, so both readers who are new to the field and those who are experienced in radio wave electromagnetics can benefit from the book.

Chapter 1 is an introduction and provides an overview of the basic electromagnetic equations for time harmonic fields. It begins with the wave equation for the vector potential and its far-field solution. Then follows description of the wave polarization, the amplitude and phase properties of waves in boundless space, and the boundary field conditions at a planar interface. The chapter continues with the interference wave phenomena and concludes with a matrix analysis of plane wave transmission through multilayer dielectric plates.

Chapter 2 contains an extensive treatment of the Kirchhoff diffraction theory. It starts with the original Huygens' diffraction principle and its more precise formulation made by Fresnel. Considered are Fresnel zone constructions with spherical and planar Fresnel zones, as well as their application for finding

the diffraction field in many particular cases of zone obstruction. The focusing effect of simple Fresnel zone lens-like diffractors and of Soret's and Wood's multizone lenses or zone plates are computed.

First, the Fresnel-Kirchhoff diffraction field is presented in a scalar form, and the diffraction integral is applied for two cases—(a) aperture cut in a screen surface enclosing the primary sources, and (b) aperture in an infinite plane screen placed between the source and the observation point. In the latter case, two radiation field regions are defined: the far or Fraunhofer region and the near or Fresnel region. The field in the Fraunhofer region is considered only for the specific case of plane wave diffraction by a circular aperture, while the Fresnel diffraction is discussed in detail for many particular cases of apertures and obstacles. At the end of the chapter, the far-field vectorial Kirchhoff integral for an aperture in an infinite plane is derived.

Chapter 3 is devoted to applications of Fresnel zones to microwave wireless communication links. The typical paths of wave propagation over the earth are described, and radio wave tracing by means of Fresnel zone ellipsoids is considered. The significant zones for transmission and reflection are defined, and the equations for finding their basic dimensions are derived. The reader is then briefly introduced to the standard interference lines-of-sight schemes for radio wave propagation over smooth ground, taking into account the earth curvature and the troposphere refraction.

Only the traditional, quasi-optical ray tracing by use of geometrical and physical optics is within this book's scope. That is why only some basic examples of knife-edge diffraction models are considered in the chapter, namely, straight hill, sharp hill, and wide wedge-shaped hill. The influence of troposphere refraction on link clearance and the method for drawing so-called equivalent zero-level and terrain profile curves are also briefly explained.

Fixed and mobile microwave radio communication links over hilly terrain can make use of constructive mountain diffraction and man-made passive repeaters in the form of Fresnel zone diffractors. Several designs of ring and ring-segment metal/dielectric antenna directors and passive repeaters are described as examples.

Chapter 4 presents detailed treatment of the Fresnel zone plates. The discoveries of Soret, Lord Rayleigh, and Wood in the field of optical zone plates are recalled. A comprehensive classification by zone plate shape and cross-sectional structure is made. Then extensive description and analysis of planar Fresnel zone plates are presented. Examined are the characteristics of half-opened or Soret zone plates—multiple focusing action, resolution, off-axis and frequency aberration and frequency bandwidth, and transmission function for two- and one-dimensional zone plate. A tabular comparison between Soret zone plate and ordinary refraction lens is given. Derived are equations for calculations of zone plate dimensions and focusing characteristics.

Proper attention is paid to the phase-corrected zone plates, and the phase-correction mechanism, focusing efficiency, and design and technology considerations for dielectric phase-reversal and quarter-wave zone plates are examined. The chapter ends with curved Fresnel zone plates. Derived are equations for dimensioning and axial focusing of spherical, parabolic, and conical zone plates.

Chapter 5 contains a concise presentation of theory, radiation properties, and typical applications of on/off-axis-fed, transmission/reflection, and planar/curved zone plate antennas.

First, planar transmission-mode zone plate antennas are described. Far-field equations and radiation parameters of Soret- and Wood-type antennas are studied in detail and many numerical examples are illustrated by graphs.

The chapter continues with examination of the planar reflection-mode zone plate antennas: the usual and the printed version folded phase-reversal antenna. The latter has the following nomenclature: single-layer, multilayer, and integrated circuit antennas.

There follows a theoretical and numerical representation of off-axis scanning properties of the planar antenna with a circular zone plate, which agrees well with experiments. The far-field equations for the transmission-mode offset antenna with elliptical zone plates are given. Different practical designs for DBS signal reception are also described.

The final section of this chapter deals with curved zone plate antennas. They have a priority over the planar zone plate configurations because of their better focusing, resolving, and scanning properties, as well as the possibility of creating radiation patterns that are different in shape. Moreover, the curved Fresnel zone plate antenna is not limited to a specific surface as in the case of parabolic antenna, and can be made conformal to an arbitrary curvilinear natural or man-made formation.

Several examples of curved zoned antenna configurations are considered—folded elliptical zone plate with parabolic reflector for multisatellite DBS reception, transmission-mode cylindrical zone-plate antenna for X-band LAN systems, and single-dielectric phase-corrected zone plates for millimeter waves with spherical, parabolic, conical, and other curvilinear surfaces.

It is my pleasure to acknowledge the many people who contributed to the creation of this book.

Let me first recall with gratitude the men who motivated and guided me in my younger years to the fascinating territories of wireless electromagnetics: Professor H. D. Shinev of the Technical University of Sofia, Bulgaria; the late Professor D. Taylor of the Strathclyde University, Glasgow; and Professor P. J. B. Clarricoats of Queen Mary College, London University.

Without my visit to the Eindhoven University of Technology in the Netherlands six years ago, I may have never begun this book. I am much

indebted to Dr. M. H. A. J. Herben and his former students L. Leyten, L. C. Baggen, J. M. van Houten, and C. J. Jeronimus, who at that time had already made the most extensive theoretical and design study on transmission-type Fresnel zone plate antennas. Dr. Herben kindly invited me to join his research efforts in this field and provoked my interest in applications of Fresnel zones in wave propagation and the development of more efficient zone plate antenna systems.

I would like to express my sincere appreciation to the manuscript reviewer, Professor Klaus Solbach of Gerhard-Mercator University, Duisburg, Germany, whose numerous precise comments, productive suggestions, and constructive criticisms were invaluable in the book preparation.

I am especially grateful to Dr. J. C. Wiltse of Georgia Institute of Technology, Atlanta, the world-renowned expert in millimeter-wave propagation and radar and wireless communication systems, and the most respected researcher today of Fresnel zone plates and antennas, for his interest in my work, constant advice, and help in tracing many reference sources. My sincere thanks also go to him for kindly agreeing to prepare a foreword to the book.

The text much benefited from the discussions with and computational help of Dr. J. R. Urumov, Dr. G. S. Kirov, and L. P. Kamburov, and from the many illustrations made by Nick Grudev, K. Gatzova, and I. P. Gatzov of Technical University of Varna, Bulgaria.

Thanks also are due to the Bulgarian National Research Fund for the financial support to the author and his research group in studying Fresnel zone plate antennas for mobile and satellite communications.

Grateful acknowledgment is expressed to numerous researchers in the field of the book for providing me with copies of their publications: Professor S. K. Barton from University of Manchester, U.K.; Professors Igor and Oleg Minin of Institute of Applied Physical Problems, Novosibirsk, Professor D. M. Sazonov of Moscow Power Technical University, Professor V. G. Yampolsk'i of Moscow Telecommunications Institute, and Professor A. V. Popov of IZMIRAN, Academy of Sciences, Russia; Professor W. X. Zhang of Southeast University, People's Republic of China; Professor J. Yamuchi of Hosei University and Professor T. Onodera of Kumamoto Institute of Technology, Japan; Professor S. P. Ojha and Professor K. K. Dey of Banaras Hindu University, India; Dr. D. N. Black, Electromagnetic Sciences, Inc., Atlanta, U.S.; Professor V. Cervený, Charles University, Czech Republic; and many others.

I wish to thank the colleagues from Department of Electromagnetic Systems, Denmark Technical University, Lyngby, who helped me much in search of references and useful discussions on zone plate antennas during my stay there.

I express my sincere thanks to the Institute of Electrical and Electronics Engineers, New Jersey; the Institution of Electrical Engineers, London; the

Institute of Electronics and Communication Engineers of Japan, Tokyo; Optical Society of America, Washington, D.C.; Hayden Publishing, Co., New Jersey; Horizon House Publications, Norwood, MA; Artech House, Norwood, MA; John Wiley & Sons, Inc., New York; SPIE Optical Engineering Press, Bellingham, WA; Cambridge University Press, Cambridge; Macmillan Publishers, Ltd., London; Taylor and Francis Ltd., London; Mc Graw-Hill, New York; Pergamon Press Ltd., Oxford; Prentice Hall, Inc., Englewood Cliffs, NJ; Holt, Rinehart and Winston, Inc. New York; Wiley Interscience, New York; Dover Publications, Inc., New York; Kluwer Academic/Plenum Publishers, New York; Flat Antennas, Ltd. (Formerly Mawzones Ltd.), U.K.; Norden Systems, U.S.; Claredon Press, Oxford; Pergamon Press, Oxford; Dunod, Paris; Academic Press, New York; Radio Science Press, Gent, Belgium; Mir Publishing House, Moscow; Radio I Svyaz, Moscow; Nauka Publishing House, Moscow; Eindhoven University of Technology, The Netherlands; and ESTEC (European Space Agency) for their kind permission to use figures and/or text materials from their various publications listed in the references of this book.

It would not have been possible to prepare the book without the dedicated and friendly assistance of the editorial and production staff of Artech House, and in particular, Dr. Julie Lancashire, Susanna Taggart, and Mike Webb of the London office, and Tina Kolb, Igor Valdman, and Stephen Cartisano of the Norwood office.

Finally, I express my gratitude to my family, and especially to my wife Tanya, for her patience, encouragement, and assistance.

Hristo D. Hristov
December 1999

This page intentionally left blank

1

Basic Electromagnetic Wave Equations

1.1 Wave Equations for Time-Harmonic Fields

We commence this section with a couple of basic differential Maxwell's equations to obtain the field radiated by a given antenna current. This is performed with a magnetic vector potential that satisfies the inhomogeneous wave equation. Our main concern is with the far antenna field, so after solving the wave equation for the vector potential at a very distant region we may easily derive the electric and magnetic field components.

1.1.1 Wave Equation for Magnetic Vector Potential

The basic Maxwell's equations [James Clark Maxwell (1831–1858)] for time-harmonic electromagnetic fields are normally written as follows

$$\nabla \times \mathbf{E} = -j\omega\mu\mathbf{H} \quad (1.1)$$

$$\nabla \times \mathbf{H} = j\omega\epsilon\mathbf{E} + \mathbf{J} \quad (1.2)$$

where \mathbf{E} is the electric field strength vector, V/m; \mathbf{H} is the magnetic field strength vector, A/m; \mathbf{J} is the current source vector, A/m²; $\omega = 2\pi f$ is the angular frequency, rad/s; f is the circular frequency (or frequency), Hz; μ is the medium permeability, H/m; and ϵ is the medium permittivity, F/m. In (1.1) and (1.2) the time-harmonic factor $\exp(j\omega t)$ is omitted, and \mathbf{E} , \mathbf{H} , and \mathbf{J} are complex vectors or phasors that are functions to space coordinates only. In general notation any arbitrary time-harmonic electromagnetic vector ($\vec{\mathbf{L}} \rightarrow \vec{\mathbf{E}}, \vec{\mathbf{H}}, \vec{\mathbf{J}}$, etc.) can be given in the form $\vec{\mathbf{L}}(x, y, z, t) = \mathbf{L}\exp(j\omega t)$, with

$\mathbf{L} \equiv \mathbf{L}(x, y, z)$. Also, for simplicity, the medium parameters μ and ϵ are chosen here as real quantities.

Equations (1.1) and (1.2) have to be solved for the whole space except for the source (antenna) volume where $\mathbf{J} \neq 0$. For given \mathbf{J} we shall seek a solution of (1.1) and (1.2) for \mathbf{E} and \mathbf{H} . Often, however, to make the solution simpler, auxiliary vector potentials are used [1]. One of them, the magnetic vector potential \mathbf{A} is related to \mathbf{H} as follows

$$\mathbf{H} = \frac{1}{\mu} \nabla \times \mathbf{A} \quad (1.3)$$

The electric field is also expressed by the vector potential

$$\mathbf{E} = \frac{1}{j\omega\mu\epsilon} \nabla(\nabla \cdot \mathbf{A}) - j\omega\mathbf{A} \quad (1.4)$$

The vector potential \mathbf{A} , as well as field vectors \mathbf{E} and \mathbf{H} , satisfies the inhomogeneous wave or Helmholtz equation [Herman Helmholtz (1821–1894)]

$$\nabla^2 \mathbf{A} + \beta^2 \mathbf{A} = -\mu \mathbf{J} \quad (1.5)$$

where $\beta = \omega^2 \mu \epsilon$ is the wave number or phase constant, rad/m.

Thus, if the vector potential \mathbf{A} is found as a solution of (1.5), it is easy then to obtain the electric field \mathbf{E} from (1.4) and the magnetic field \mathbf{H} from (1.3).

If the current density \mathbf{J} is defined everywhere in the antenna volume V (Figure 1.1), a possible solution of (1.5) for \mathbf{A} at the observation point P is given as

$$\mathbf{A}(P) = \frac{\mu}{4\pi} \iiint_V \mathbf{J}(P') \frac{e^{-j\beta r}}{r} dV' \quad (1.6)$$

where $r = \overline{P'P} = \sqrt{r_o^2 + r'^2 - 2r_o r' \cos \alpha}$ is the distance between an arbitrary source point P' and the observation point P ; r_o and r' are the distances from the coordinate system origin O to the observation point P and arbitrary source point P' , respectively; and α is the angle between r' and r_o directions.

The above solution of the wave equation for the magnetic vector potential gives the radial dependence of the amplitude, phase, and polarization of the outwardly traveling spherical wave in a lossless unbounded medium. The wave

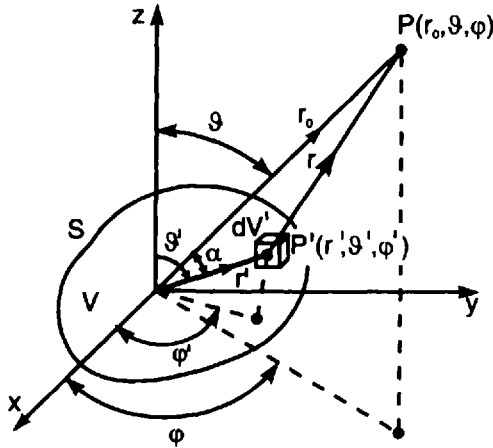


Figure 1.1 Geometry illustrating wave equation solution.

front is defined as an equiphase surface, normal to the wave-traveling direction. Each point source or elementary source volume $dV' = dx' dy' dz'$ creates a wave with a spherical phase front (spherical wave).

A great distance away from the source the spherical surface is observed as a plane; that is, the spherical wave becomes transformed into a plane wave, or a wave with an equiphase plane front. If along with the phase, the field amplitude remains constant over the planar front, the wave is regarded as a uniform plane wave [transverse electromagnetic wave (TEM or T wave)].

1.1.2 Far-Field Solution to Wave Equation

In wireless communications one is normally interested in the far or Fraunhofer region of electromagnetic waves, that is, the waves at observation points located far from the radiating antenna [Joseff Fraunhofer (1787–1826)]. As shown in Figure 1.2, in this case we may assume parallel-ray propagation, so that the distance r in (1.6) may be approximated as follows: $1/r \approx 1/r_0$ for the spherical wave amplitude decay, and $r \approx r_0 - r' \cos \alpha$ in the phase factor.

Thus, for the far-field vector potential \mathbf{A} we get [2, 3]

$$\mathbf{A}(P) = \frac{\mu}{4\pi} \frac{e^{-j\beta r_0}}{r_0} \iiint \mathbf{J}(P') e^{j\beta r' \cos \alpha} dV' \quad (1.7)$$

It is convenient to express $r' \cos \alpha$ by the source rectangular coordinates (x', y', z') and observation point angle coordinates (φ, ϑ)

where

$$A_{\vartheta} = A_x \cos \vartheta \cos \varphi + A_y \sin \vartheta \cos \varphi - A_z \sin \vartheta \quad (1.13)$$

$$A_{\varphi} = A_x \sin \varphi + A_y \cos \varphi \quad (1.14)$$

and η is the intrinsic or wave impedance of the propagation medium, Ω , which in general can be a complex quantity.

1.2 Wave Polarization

As it was shown in Section 1.1, the antenna far field has approximately a character of a uniform plane electromagnetic wave (or TEM wave), with only TEM vectors. Since the electric and magnetic field vectors \mathbf{E} and \mathbf{H} are related by the medium intrinsic impedance η it is usually a convention to operate with the former one only.

The total electric vector \mathbf{E} is a vector sum of the ϑ and φ components

$$\mathbf{E} = E_{\vartheta} \hat{\boldsymbol{\vartheta}} + E_{\varphi} \hat{\boldsymbol{\varphi}} = |E_{\vartheta_0}| e^{j(\psi_{\vartheta_0} - \beta r)} \hat{\boldsymbol{\vartheta}} + |E_{\varphi_0}| e^{j(\psi_{\varphi_0} - \beta r)} \hat{\boldsymbol{\varphi}} \quad (1.15)$$

where $|E_{\vartheta_0}|$ and $|E_{\varphi_0}|$ are the magnitudes, and ψ_{ϑ_0} and ψ_{φ_0} are the initial phases of the corresponding electric field components. The far-field vector summation is illustrated in Figure 1.2.

The vectorial nature of the antenna far field is characterized by a unique property, called a wave polarization. Generally, electromagnetic waves can be completely polarized (or polarized), partially polarized, or unpolarized [4, 5–7]. The man-made monochromatic or quasi-monochromatic radio waves subject to study in this book are polarized waves. Their transverse orthogonal components vary in time and space in the same manner.

Electromagnetic waves that contain randomly polarized components are partially polarized. The scattered radar waves from randomly moving targets are examples of partially polarized waves. Natural sources of radio waves, the “radio stars,” also produce partially polarized waves. For much higher frequencies, in the light region, the natural sources radiate unpolarized waves.

The wave polarization is normally determined by the orientation of the electric field vector as a function of the space coordinates and time. More precisely, the wave polarization is defined as a locus of the tip of the instantaneous vector

$$\begin{aligned} \text{Re}\{\bar{\mathbf{E}}(r, t)\} &= \text{Re}\{\hat{\boldsymbol{\vartheta}} E_{\vartheta_0} e^{j(\omega t - \beta r)} + \hat{\boldsymbol{\varphi}} E_{\varphi_0} e^{j(\omega t - \beta r)}\} \\ &= \hat{\boldsymbol{\vartheta}} |E_{\vartheta_0}| \cos(\omega t - \beta r + \psi_{\vartheta_0}) + \hat{\boldsymbol{\varphi}} |E_{\varphi_0}| \cos(\omega t - \beta r + \psi_{\varphi_0}) \end{aligned} \quad (1.16)$$

Here $E_{\vartheta_0} = |E_{\vartheta_0}|e^{j\psi_{\vartheta_0}}$ and $E_{\varphi_0} = |E_{\varphi_0}|e^{j\psi_{\varphi_0}}$ are the initial complex amplitudes of two field components. The total field polarization depends on the magnitude and phase relationships between the electric field components. The polarized waves are of linear, circular, or elliptical polarization [1, 4–6], described as follows.

1. Linear polarization (LP): This takes place for $\Delta\psi_0 = \psi_{\varphi_0} - \psi_{\vartheta_0} = 0$, or $\pm\pi$ (i.e., when the two wave components have unspecified amplitudes and are in phase or out of phase). In this case the locus of the total electric vector tip is a straight line.
2. Circular polarization (CP): This occurs for equal field amplitudes, or $|E_{\vartheta_0}| = |E_{\varphi_0}|$, and for a phase difference $\Delta\psi_0 = \psi_{\varphi_0} - \psi_{\vartheta_0} = \pm\pi/2$. The polarization is called circular since the electric vector is rotating and for a time period T , at a point $r = \text{const.}$, the vector's tip draws a circle. Depending on the phase difference sign the circular polarization is subdivided into two kinds:
 - Right-hand polarization (RCP)—for $\Delta\psi_0 = \psi_{\varphi_0} - \psi_{\vartheta_0} = -\pi/2$: When this phase condition applies the electric vector rotates to a clockwise or right-hand direction if the wave is viewed receding.
 - Left-hand polarization (LCP)—for $\Delta\psi_0 = \psi_{\varphi_0} - \psi_{\vartheta_0} = +\pi/2$: In this case, the vector \mathbf{E} rotates in a counterclockwise or left-hand direction. It is worth mentioning here that in the classical physics and optics the direction of vector rotation is termed in an opposite manner (i.e., the direction of rotation is such as viewed by an observer at a far point looking to the coming plane wave).
3. Elliptical polarization: When the two orthogonal waves have optional amplitudes and the phase condition is $-\pi/2 < \Delta\psi_0 < +\pi/2$, the locus of the vector's tip is an ellipse.

From a pragmatic point of view there is not much interest in waves with elliptical polarization. It is easily proven, however, that the linear and circular polarizations are specific practical cases of the elliptical polarization. The basic polarization definitions and parameters for a transmitting antenna are discussed in Appendix 1A.

1.3 Amplitude and Phase Properties of Waves in Boundless Space

Since in a region far enough from the radiating antenna the spherical wave behaves as a local plane wave we can treat it there as a uniform plane wave.

It is supposed also that the wave is linearly polarized and is propagating in a regular (homogeneous, linear, and isotropic) medium with electric-type losses only [1]. The interaction of the wave with a lossy matter gives rise to wave attenuation and phase shifting calculated by the corresponding amplitude and phase constants. The data for the relative permittivity, conductivity, and loss tangent factor of some common media, as water and ground, given in this section, helps such understanding in their electric properties (Table 1.1).

Among the basics of wireless communications are the radio link equations, including the famous Friis free-space equation. In this text we need them to describe radio links with passive repeaters and reflection/diffraction above hilly earth (Chapter 3) or to find the Fresnel zone plate antenna far field (Chapter 5).

1.3.1 Equations for Amplitude and Phase Constants

For a complex permittivity $\epsilon = \epsilon - j(\sigma/\omega)$ and a real permeability μ the real phase constant β in the wave equation is replaced by the propagation constant γ , a complex number given by [2]

$$\gamma = \alpha + j\beta = j\omega\sqrt{\mu\epsilon(1 - j\tan\delta_e)} \quad (1.17)$$

Here α is the attenuation constant, Np/m; β is the phase constant, rad/m; $\tan\delta_e = \sigma/\omega\epsilon = \sigma/2\pi f\epsilon$ is the electric loss tangent; and σ is the medium conductivity, S/m. The wave constants α and β can be calculated by

$$\alpha = \omega\sqrt{\mu\epsilon}\sqrt{\frac{1}{2}\left(-1 + \sqrt{1 + \tan^2\delta_e}\right)} \quad (1.18)$$

and

$$\beta = \omega\sqrt{\mu\epsilon}\sqrt{\frac{1}{2}\left(1 + \sqrt{1 + \tan^2\delta_e}\right)} \quad (1.19)$$

The medium intrinsic impedance η , Ω , is determined as follows

$$\eta = \sqrt{\frac{\mu}{\epsilon}} = \sqrt{\frac{\mu}{\epsilon(1 - j\tan\delta_e)}} = |\eta|e^{j\phi_\eta} \quad (1.20)$$

where $|\eta| = \sqrt{\frac{\mu}{\epsilon}}\sqrt{\cos\delta}$ and $\phi_\eta = \frac{1}{2}\arctan\left(\frac{\sigma}{\omega\epsilon}\right)$.

The phase velocity v and wavelength λ of the plane wave in a lossy medium are

$$v = \frac{\omega}{\beta} = \frac{1}{\sqrt{\mu\epsilon} \sqrt{\frac{1}{2} \left(1 + \sqrt{1 + \tan^2 \delta_e} \right)}} \quad (1.21)$$

and

$$\lambda = \frac{v}{f} = \frac{1}{f \sqrt{\mu\epsilon} \sqrt{\frac{1}{2} \left(1 + \sqrt{1 + \tan^2 \delta_e} \right)}} \quad (1.22)$$

1.3.2 Some Data for Ground Media

The common media are classified approximately as follows [7]: (1) dielectrics (insulators), for $\tan \delta_e < 0.01$; (2) quasiconductors, for $0.01 < \tan \delta_e < 100$; and (3) conductors, for $\tan \delta_e > 100$. Table 1.1 lists values of the relative permittivity and conductivity for a number of ground media. In Figure 1.3 the loss tangent factor $\tan \delta_e = \sigma/\omega\epsilon$ is plotted as a function of frequency for fresh water, urban ground, rural ground, seawater, and copper. The curves are not accurate above the microwave region since the medium constants vary with frequency.

1.3.3 Basic Radio Link Equations

Consider a far field spherical electromagnetic wave with a quasi-plane phase front that propagates in a lossy medium along the r -direction. Its complex field vectors \mathbf{E} and \mathbf{H} are

Table 1.1

Values of Permittivity and Conductivity for Some Ground Media and Copper
(After: [7], © 1984 McGraw-Hill)

Medium	Relative Permittivity (ϵ_r)	Conductivity σ (S/m)
Sea water	80	$1-6$
Fresh water	80	$10^{-3}-10^{-2}$
Moist ground	20-30	$3 \times 10^{-3}-3 \times 10^{-2}$
Dry ground	3-6	$10^{-5}-5 \times 10^{-3}$
Snow (-10°C)	1	10^{-6}
Ice (-10°C)	4-5	$10^{-2}-10^{-1}$
Copper (basis for comparison)	1	5.7×10^7

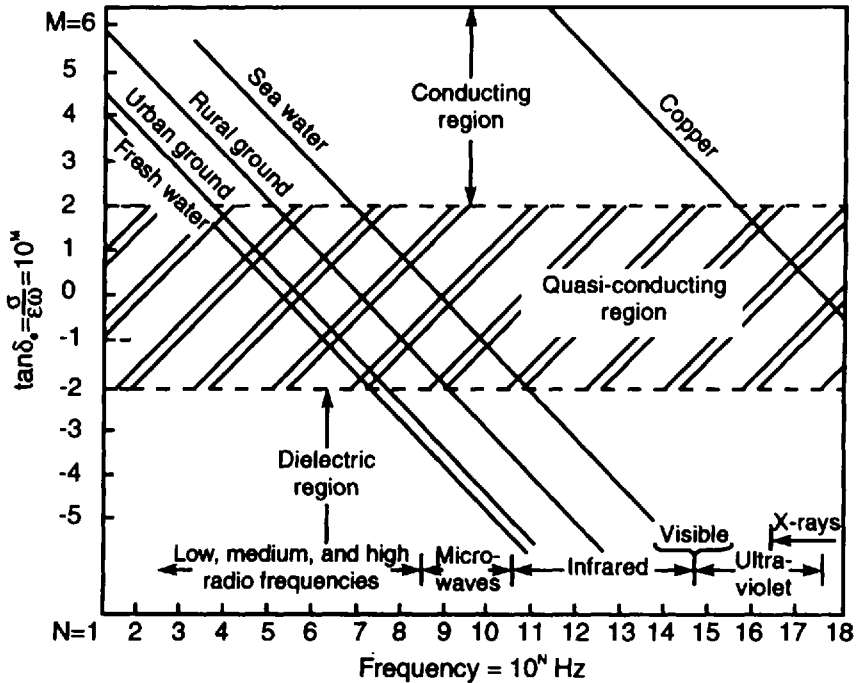


Figure 1.3 Electric loss tangent versus frequency for different media, log-log plot. (After: [7], © 1984 McGraw-Hill.)

$$\mathbf{E} = \mathbf{E}_o \frac{e^{-\alpha r}}{r} e^{-j\beta r} \tag{1.23}$$

and

$$\mathbf{H} = \frac{\mathbf{E}_o}{|\eta|} \frac{e^{-\alpha r}}{r} e^{-j(\beta r - \phi_\eta)} \tag{1.24}$$

where $\mathbf{E}_o = |\mathbf{E}_o| e^{j\psi_o}$, and $\eta = |\eta| e^{j\phi_\eta}$. Here η is the complex intrinsic impedance of the medium.

Let the power radiated by the antenna at the origin of a sphere of radius r be P_r . Over the sphere surface the average density p_{av} of the electromagnetic flux is found by [3]

$$p_{av} = \frac{P_t G_t e^{-2\alpha r}}{4\pi r^2} \quad (1.25)$$

where G_t is the directive gain of the transmitting antenna.

On the other hand, the average flux density is found as a real part of the Poynting vector $\mathbf{p} = (\mathbf{E} \times \mathbf{H}^*)/2$, or

$$p_{av} = \frac{1}{2} \text{Re}(\mathbf{p}) = \frac{1}{2} \text{Re}(\mathbf{E} \times \mathbf{H}^*) \quad (1.26)$$

Since $|\mathbf{H}|^* = |\mathbf{E}|^*/|\eta|$, (1.26) can be transformed into

$$p_{av} = \frac{1}{2} \text{Re}\left(\frac{|\mathbf{E}|^2}{|\eta|}\right) = \frac{1}{2} \frac{|\mathbf{E}|^2}{\eta} \quad (1.27)$$

where $\eta = |\eta|$.

After making p_{av} from (1.27) equal to that from (1.25) we get the electric field magnitude E_m

$$E_m = |\mathbf{E}| = \sqrt{\frac{P_t G_t \eta}{2\pi}} \frac{e^{-\alpha r}}{r} \quad (1.28)$$

and the complex electric field strength

$$E = \sqrt{\frac{P_t G_t \eta}{2\pi}} \frac{e^{-\alpha r}}{r} e^{-j\beta r} \quad (1.29)$$

at a distance r from the source.

Up to now we have assumed that the transmitting antenna radiates in a so-called boresight direction ($\vartheta = 0$, $\varphi = 0$) (i.e., a direction in which the normalized antenna radiation pattern $F(\vartheta = 0, \varphi = 0)$ is equal to unity).

For an arbitrary direction (ϑ , φ) the electric field magnitude $E_m(\vartheta, \varphi)$ is written as

$$E_m(\varphi, \vartheta) = \sqrt{\frac{P_t G_t \eta}{2\pi}} \frac{e^{-\alpha r}}{r} F(\vartheta, \varphi) \quad (1.30)$$

When the wave is propagating in a low-loss dielectric medium with $\mu = \mu_0$, (1.18) for the attenuation factor is approximated to

$\alpha \approx \frac{\omega}{2} \sqrt{\mu_o \epsilon_o \epsilon_r} \tan \delta$ and $\eta \approx \sqrt{\mu_o / \epsilon} = 120 \pi / \sqrt{\epsilon_r}$. Here $\epsilon = \epsilon_o \epsilon_r$, $\mu_o = 4 \pi \times 10^{-7}$ H/m, and $\epsilon_o = (1/36 \pi) \times 10^{-9}$ F/m. For a free-space propagation $\alpha = 0$ and $\eta = \eta_o = 120 \pi \Omega$, and thus, (1.29) becomes

$$E_m = \frac{\sqrt{60 P_t G_t}}{r} \quad (1.31)$$

or if the field vector character and angular dependence (ϑ, φ) for the free-space electric field are taken into account the field strength is

$$\mathbf{E}(\vartheta, \varphi) = E_m(\vartheta, \varphi) e^{-j\beta r} \hat{\mathbf{e}} = \frac{\sqrt{60 P_t G_t(\vartheta, \varphi)}}{r} e^{-j\beta r} \hat{\mathbf{e}} \quad (1.32)$$

where $\hat{\mathbf{e}}$ is the electric field unit vector and $G_t(\vartheta, \varphi)$ is the antenna directive gain for an arbitrary direction (ϑ, φ). For the boresight direction, where the radiation pattern has a maximum value, $G_t(\vartheta, \varphi)$ is replaced by G_t .

In (1.31) all quantities are given in SI units: P_t is in watts, W; r is in meters, m; and E_m is in volts per meter, V/m. Practically, it is more convenient to express the radiated power in kilowatts, the distance in kilometers, and the electric field in millivolts per meter, so that

$$E_m \approx \frac{245 \sqrt{P_t [\text{kW}] G_t}}{r [\text{km}]}, \text{ mV/m} \quad (1.33)$$

At the end of this paragraph, the classical radio link equation known as the Friis free-space equation will be discussed. For $\alpha = 0$, the power flux density p_{av} at the receiving point becomes

$$p_{av} = \frac{P_t G_t}{4 \pi r^2} \quad (1.34)$$

The receiving antenna is characterized by a specific parameter named effective aperture A_{eff} , m^2 proportional to its directive gain G_r and λ^2 or

$$A_{\text{eff}} = \frac{G_r \lambda^2}{4 \pi} \quad (1.35)$$

Then, the power, P_r , passed from the lossless antenna to the receiver is obtained by multiplication of p_{av} and A_{eff} , given by (1.34) and (1.35), respectively, or

$$P_r = P_t \frac{G_t G_r}{4\pi r/\lambda^2} \quad (1.36)$$

This is the Friis free-space equation.

The dominator in (1.36) describes the free-space wave diffusion losses between ideal isotropic transmitting and receiving antennas placed at the same points as the actual directive antennas—that is, this factor is independent of antennas used. It is called a spatial attenuation, L_s (or the path loss factor)

$$L_s = \left(\frac{4\pi r}{\lambda} \right)^2 \quad (1.37)$$

The losses calculated by (1.37) differ from the dissipative losses in matter. In the design of radio links, it is also convenient to use the concept of transmission losses, L_t , between the transmitting antenna and receiver input defined as

$$L_t = \frac{P_t}{P_r} = \left(\frac{4\pi r}{\lambda} \right)^2 \frac{1}{G_t G_r} \quad (1.38)$$

For isotropic antennas $G_t = G_r = 1$.

For practical needs the above equations are commonly expressed in logarithmic form in order to make use of the decibel notation. The reference units for this notation are either the appropriate SI units or some preferred arbitrary value. For instance, if we wish to express the power level in decibels with respect to 1 mW (or 0 dBm) the Friis equation can be transformed in the form

$$P_r = P_t, \text{ dBm} + G_t, \text{ dB} + G_r, \text{ dB} - 20 \log(f), \text{ MHz} \quad (1.39) \\ - 20 \log(r), \text{ km} - 32.45, \text{ dBm}$$

For example, a power level of +30 dBm corresponds to 1W, and a power level of -30 dBm to $1\mu\text{W}$.

1.4 Boundary Field Conditions: Reflection and Transmission

The differential Maxwell's equations involve space derivatives, and therefore, they are valid only for electromagnetic fields at any point within a continuous

medium. The field of interface between two different regular media can be described by the Maxwell's equations written in an integral form from which follow several particular equations known as electromagnetic boundary conditions. They account for the discontinuous change of the constitutive medium parameters ϵ and μ across the boundary surface separating region 1 ($\epsilon_1, \mu_1, \sigma_1$) on one side and region 2 ($\epsilon_2, \mu_2, \sigma_2$) on the adjacent side.

The real-world electromagnetic problems (e.g., antenna radiation, ground wave propagation, wave scattering) involve transmission, reflection, and/or diffraction at intermedia boundaries, and they are solved by means of specific initial and boundary conditions.

1.4.1 Boundary Field Conditions

If along the boundary between two media there are impressed electric sources (charges or currents) the following statements can be made regarding the electric and magnetic field components in the media, close to their interface:

1. The tangential components of \mathbf{E} are continuous ($E_{\tau 1} = E_{\tau 2}$), and the normal components of \mathbf{E} are discontinuous across the boundary, or $\epsilon_1 E_{n1} - \epsilon_2 E_{n2} = \rho_s$. Here ρ_s is the surface charge density, C/m^2 . If $\sigma_2 = \infty$, the electromagnetic field in medium 2 disappears, so $E_{\tau 2} = 0$, $E_{\tau 1} = 0$, and $E_{n1} = \rho_s / \epsilon_1$.
2. The tangential and normal components of \mathbf{H} are discontinuous across the boundary or more specifically $\mu_1 H_{n1} = \mu_2 H_{n2}$ and $H_{\tau 1} - H_{\tau 2} = J_s$. In the latter J_s , A/m , is the surface current density. For $\sigma_2 = \infty$, $H_{n2} = H_{\tau 2} = 0$; hence $H_{n1} = 0$ and $H_{\tau 1} = J_s$.
3. If there is no current flow on the boundary surface $J_s = 0$, the tangential components of \mathbf{H} are also continuous in transition between the media or $H_{\tau 1} = H_{\tau 2}$.

1.4.2 Reflection and Transmission of Plane Electromagnetic Waves

A plane electromagnetic wave falling to the planar interface between two regular semi-infinite media 1 and 2 gives rise to two plane waves: reflected and transmitted (or refracted). For simplicity, we shall consider here non-magnetic ($\mu = \mu_0$) lossless dielectric media. The wave phenomena reflection and transmission are characterized by two kinds of properties: kinematic and dynamic [8]. The kinematic properties include well-known optical laws (Figure 1.4) described as follows.

1. The law of reflection, which states that the angle of reflection ψ_r is equal to the angle of incidence ψ_i , or

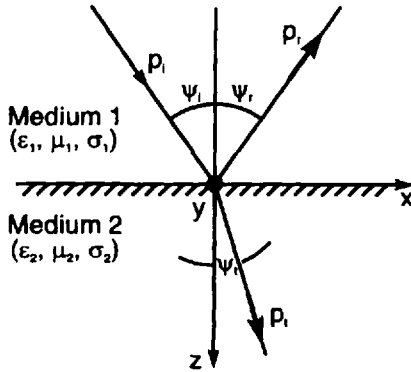


Figure 1.4 Reflection and transmission by plane interface at oblique wave incidence.

$$\psi_i = \psi_r \quad (1.40)$$

2. The law of transmission or refraction (Snell's law) according to which

$$\frac{\sin \psi_i}{\sin \psi_r} = \frac{\beta_2}{\beta_1} = \frac{n_2}{n_1} = n_{21} \quad (1.41)$$

Here ψ_i is the angle of transmission or refraction; $\beta_1 = 2\pi/\lambda_1 = \beta_0 n_1$, $\beta_2 = 2\pi/\lambda_2 = \beta_0 n_2$, and $n_1 = \sqrt{\epsilon_1/\epsilon_0}$, $n_2 = \sqrt{\epsilon_2/\epsilon_0}$ are the phase constants and indices of refraction, corresponding to the media 1 and 2; $n_{21} = n_2/n_1 = \sqrt{\frac{\epsilon_2}{\epsilon_1}}$ is called the relative index of refraction; and $\beta_0 = 2\pi/\lambda_0$ is the free-space phase constant. If the first medium is free-space, then we put $\epsilon_1 = \epsilon_0$ and $\epsilon_2 = \epsilon$, and then $n = \sqrt{\epsilon/\epsilon_0} = \sqrt{\epsilon_r}$, where ϵ_r is the relative permittivity of the second medium.

The dynamic properties are referred to as the amplitude, phase, and polarization of the waves, reflecting from and transmitting through the media interface. These properties depend on the type of the polarization, the incidence angle, and the media electromagnetic parameters. They are determined by the equations for the reflection coefficient R ($R = E_r/E_i = |R|e^{j\phi_r}$) and transmission coefficient T ($T = E_t/E_i = |T|e^{j\phi_t}$).

The plane formed by the unit vector normal to the boundary interface and the vector in the direction of incidence is called the plane of incidence (plane xz).

In the case of the perpendicular (or electric polarization) the electric field vector of the incident wave is perpendicular to the plane of incidence [i.e., $\mathbf{E}_i^\perp = E_{iy}\hat{y}$ as shown in Figure 1.5(a)]. The reflection coefficient R^\perp and transmission coefficient T^\perp for an interface between two semi-infinite lossless dielectric media are found by

$$R^\perp = \frac{E_r^\perp}{E_i^\perp} = \frac{\eta_2 \cos \psi_i - \eta_1 \cos \psi_t}{\eta_2 \cos \psi_i + \eta_1 \cos \psi_t} \tag{1.42}$$

and

$$T^\perp = \frac{E_t^\perp}{E_i^\perp} = \frac{2\eta_2 \cos \psi_i}{\eta_2 \cos \psi_i + \eta_1 \cos \psi_t} \tag{1.43}$$

where $\eta_1 = 120\pi/\sqrt{\epsilon_{r1}}$ and $\eta_2 = 120\pi/\sqrt{\epsilon_{r2}}$.

Having in mind that $\cos \psi_t = \sqrt{1 - (\sin \psi_i/n_{21})^2}$, (1.42) and (1.43) can be rewritten as functions of ψ_i and n_{21} only

$$R^\perp = \frac{\cos \psi_i - \sqrt{n_{21}^2 - \sin^2 \psi_i}}{\cos \psi_i + \sqrt{n_{21}^2 - \sin^2 \psi_i}} \tag{1.44}$$

and

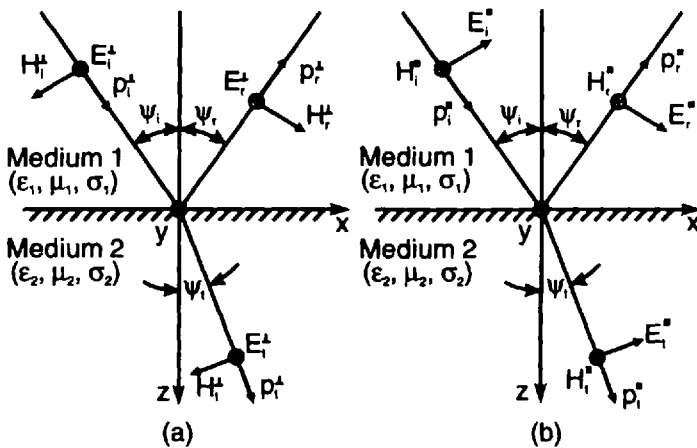


Figure 1.5 Reflection and transmission at the oblique wave incidence for (a) perpendicular (electric) polarization and (b) parallel (magnetic) polarization.

$$T^\perp = \frac{2 \cos \psi_i}{\cos \psi_i + \sqrt{n_{21}^2 - \sin^2 \psi_i}} \quad (1.45)$$

For the parallel (or magnetic) polarization the magnetic field vector of the incident wave is perpendicular to the plane of incidence (i.e., $\mathbf{H}_i^\parallel = H_{iy} \hat{\mathbf{y}}$), and the electric field vector \mathbf{E}_i^\parallel is parallel to the same plane, Figure 1.5(b). Then, the reflection and transmission coefficients R^\parallel and T^\parallel can be calculated by

$$R^\parallel = \frac{E_r^\parallel}{E_i^\parallel} = \frac{\eta_1 \cos \psi_i - \eta_2 \cos \psi_t}{\eta_1 \cos \psi_i + \eta_2 \cos \psi_t} \quad (1.46)$$

and

$$T^\parallel = \frac{E_t^\parallel}{E_i^\parallel} = \frac{2 \eta_2 \cos \psi_i}{\eta_1 \cos \psi_i + \eta_2 \cos \psi_t} \quad (1.47)$$

or as in (1.44) and (1.45) they can be expressed as follows

$$R^\parallel = \frac{n_{21}^2 \cos \psi_i - \sqrt{n_{21}^2 - \sin^2 \psi_i}}{n_{21}^2 \cos \psi_i + \sqrt{n_{21}^2 - \sin^2 \psi_i}} \quad (1.48)$$

and

$$T^\parallel = \frac{2 n_{21} \cos \psi_i}{n_{21}^2 \cos \psi_i + \sqrt{n_{21}^2 - \sin^2 \psi_i}} \quad (1.49)$$

To this point we have written formulas for the reflection and transmission coefficients, valid for plane waves with linear polarization. If the incident wave has an elliptical polarization it can be represented as a vector sum of two incident plane waves having orthogonal linear polarizations—for example, perpendicular and parallel. Then, the reflected and transmitted waves will also consist of perpendicular and parallel components E_r^\perp and E_r^\parallel found by the following reflection matrix equation

$$\begin{bmatrix} E_r^\perp \\ E_r^\parallel \end{bmatrix} = \begin{bmatrix} R^\perp & 0 \\ 0 & R^\parallel \end{bmatrix} \begin{bmatrix} E_i^\perp \\ E_i^\parallel \end{bmatrix} \quad (1.50)$$

where E_i^\perp and E_i^\parallel are the corresponding incident field strengths.

Similarly, the transmission matrix equation is written

$$\begin{bmatrix} E_t^\perp \\ E_t^\parallel \end{bmatrix} = \begin{bmatrix} T^\perp & 0 \\ 0 & T^\parallel \end{bmatrix} \begin{bmatrix} E_i^\perp \\ E_i^\parallel \end{bmatrix} \quad (1.51)$$

For complex media with conduction, dielectric, and magnetic losses the equations for the reflection and transmission coefficients can be easily transformed by replacing the real index of refraction n with a complex one, $\dot{n} = \sqrt{\dot{\epsilon}_2 \dot{\mu}_2 / \dot{\epsilon}_1 \dot{\mu}_1}$, with $\dot{\epsilon}_{1,2} = \epsilon_{1,2}(1 - j \tan \delta_{e1,2})$ and $\dot{\mu}_{1,2} = \mu_{1,2}(1 - j \tan \delta_{m1,2})$. Here $\tan \delta_e$ and $\tan \delta_m$ accounts for the electric (conduction and dielectric) losses and magnetic losses, respectively. The corresponding complex intrinsic impedances will become $\dot{\eta}_{1,2} = (\mu_o / \epsilon_{1,2})^{1/2} = |\dot{\eta}_{1,2}| \exp(j\phi_{\eta_{1,2}})$.

1.4.3 Some Special Cases of Reflection and Transmission

Let a uniform plane wave with parallel polarization be incident upon the interface between two semi-infinite lossless dielectric media. It can be proven that for each permittivity couple (ϵ_1, ϵ_2) there is an angle ψ_{iB} , called the Brewster or polarizing angle, for which the total incident wave energy is transmitted into the second medium (i.e., there is no reflected wave in the first medium). To obtain the Brewster angle we have to put $R^\parallel = 0$, or from (1.48) we have to write

$$n_{21}^2 \cos \psi_{iB} - \sqrt{(n_{21}^2 - \sin^2 \psi_{iB})} = 0 \quad (1.52)$$

Then, from (1.52) it is easily found that the total transmission occurs at

$$\psi_{iB} = \arctan(n_{21}) = \arctan \sqrt{\frac{\epsilon_2}{\epsilon_1}} \quad (1.53)$$

If a wave with an arbitrary polarization is incident at this angle upon a nonmagnetic plane boundary there will be some reflection but the reflected wave will be entirely of perpendicular polarization.

Let us consider another special case, for which $\epsilon_1 > \epsilon_2$, or $n_{21} < 1$. As shown in Figure 1.6, the incident wave travels from a more dense to a less dense medium. The Snell's refraction law in this special case requires

$$\sin \psi_t = \frac{\sin \psi_i}{n_{21}} \leq 1 \quad (1.54)$$

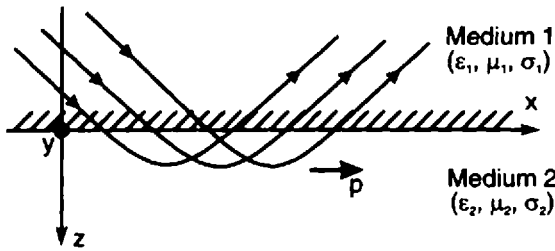


Figure 1.6 Surface wave resulting from total reflection at the interface boundary.

So, there will be an angle of incidence ψ_{ic} , named a critical angle, for which $\sin \psi_{ic}/n_{21} = 1$, or

$$\psi_{ic} = \arcsin \sqrt{\frac{\epsilon_2}{\epsilon_1}} \quad (1.55)$$

For waves incident at even higher angles $\psi_i > \psi_{ic}$, (1.54) requires $\sin \psi_t > 1$, which has no meaning for real values of ψ_t . Therefore, this inequality is valid only if the angle ψ_t is of complex value, or

$$\psi_t = \frac{\pi}{2} + j\psi_t \quad (1.56)$$

from which it is obtained that $\sin \psi_t = \cosh \psi_t$ and $\cos \psi_t = -j \sinh \psi_t$. If $\cos \psi_t$ in the equations for the reflection coefficient (1.42) and (1.46) is replaced by $\cos \psi_t = -j \sinh \psi_t$, it is found that

$$R^\perp = \frac{\eta_2 \cos \psi_i + j\eta_1 \sinh \psi_t}{\eta_2 \cos \psi_i - j\eta_1 \sinh \psi_t} \quad (1.57)$$

and

$$R^\parallel = \frac{\eta_1 \cos \psi_i + j\eta_2 \sinh \psi_t}{\eta_1 \cos \psi_i - j\eta_2 \sinh \psi_t} \quad (1.58)$$

From (1.57) and (1.58) it follows that $|R^\perp| = |R^\parallel| = 1$, which says that the incident wave is entirely transferred into a reflection wave. Curiously, despite this conclusion it is easily proved that $|T^\perp| \neq 0$ and $|T^\parallel| \neq 0$.

Physically this phenomenon is explained as follows: In the second medium a specific type of wave is formed with a plane phase front perpendicular to

the x -axis and an exponentially decreasing field amplitude in the $+z$ direction. This wave is a nonuniform plane wave, called the surface or guided wave, which travels along the boundary plane in the $+x$ direction.

The exponential field decrease is not due to medium losses. Here the process is more complicated. The average power crossing the boundary is zero. The wave penetrated in the second medium travels along a short curvilinear trajectory and gets back (or reflects) into the first medium (Figure 1.6).

The surface wave in medium 2 does not exist isolated from the field in medium 1, where it is a sum of incident and reflected waves. The resultant fields in the two media have different field structures but are inextricably tied under the boundary electromagnetic conditions. The surface wave in the second medium travels along the interface with a phase velocity $v_x = v_2 / \cosh \psi_t$, which is smaller than the velocity of the plane uniform wave $v_2 = c / \sqrt{\epsilon_{r2}}$ traveling in unbounded dielectric medium with a relative permittivity ϵ_{r2} . Remember that $c = 3 \times 10^8$ m is the wave velocity in vacuum.

The distance from the boundary at which the surface wave amplitude decreases e times is on the order of one wavelength. Therefore, it is very difficult to experimentally check the surface waves in optics, while they are easily registered at radio frequency bands.

1.5 Interference of Electromagnetic Waves

The interference is based fundamentally on the principle of linear wave superposition in space and time. Examples of electromagnetic fields in radiowave engineering resulting from the interference of uniform plane waves are the standing waves in two-wire lines, hollow waveguides, and resonators, and the surface wave propagating along the intermedia boundary, the field of microwave antenna elevated above the earth, and the field of antenna array.

1.5.1 Linear Superposition of Electromagnetic Fields

Consider a number of N electromagnetic sources situated in a regular (or uniform, linear, and isotropic) medium. The total electric field \mathbf{E} at an observation point is equal to the vector sum of the fields $\mathbf{E}_1, \mathbf{E}_2, \mathbf{E}_3 \dots$ produced by the different sources [9]

$$\mathbf{E} = \sum_{n=1}^N \mathbf{E}_n \quad (1.59)$$

A similar summation is true also for the magnetic field vectors \mathbf{H}_n .

To simplify our discussion let us first consider two plane harmonic waves of same frequency (ω) and linear polarization. Their electric field vectors can be written in a complex form as

$$\mathbf{E}_1 = \mathbf{E}_{o1} e^{j(\omega t - \beta r_1 + \phi_{o1})} = \mathbf{E}_{o1} e^{j\phi_1} \quad (1.60)$$

and

$$\mathbf{E}_2 = \mathbf{E}_{o2} e^{j(\omega t - \beta r_2 + \phi_{o2})} = \mathbf{E}_{o2} e^{j\phi_2} \quad (1.61)$$

where \mathbf{E}_{o1} , \mathbf{E}_{o2} , and ϕ_{o1} , ϕ_{o2} are the initial amplitudes and phases of the fields \mathbf{E}_1 and \mathbf{E}_2 , respectively; r_1 and r_2 are the distances from the corresponding radiators to the point of summation; $\phi_1 = \omega t - \beta r_1 + \phi_{o1}$ and $\phi_2 = \omega t - \beta r_2 + \phi_{o2}$. If the phase difference $\Delta\phi_o = \phi_{o1} - \phi_{o2}$ is constant in time, the two sources and their fields are said to be mutually coherent.

This discussion is confined to coherent radiating sources and waves. The resultant average power density p_{av} at the interference point is

$$p_{av} = \frac{1}{2} \text{Re}(\mathbf{E} \times \mathbf{H}^*) = \frac{1}{2} \text{Re}(\mathbf{E} \cdot \mathbf{E}^*) \quad (1.62)$$

As $\mathbf{E} = \mathbf{E}_1 + \mathbf{E}_2$ and $\mathbf{E}^* = \mathbf{E}_1^* + \mathbf{E}_2^*$, (1.62) becomes

$$\begin{aligned} p_{av} &= \frac{1}{2\eta} (\mathbf{E}_1 + \mathbf{E}_2) \cdot (\mathbf{E}_1^* + \mathbf{E}_2^*) \\ &= \frac{1}{2\eta} [|\mathbf{E}_1|^2 + |\mathbf{E}_2|^2 + 2\mathbf{E}_1 \cdot \mathbf{E}_2 \cos(\Delta\phi)] \end{aligned} \quad (1.63)$$

where $\Delta\phi = \phi_1 - \phi_2 = \beta\Delta r + \Delta\phi_o$ with $\Delta r = r_2 - r_1$, and η is the real intrinsic impedance. $2\mathbf{E}_{o1} \cdot \mathbf{E}_{o2} \cos(\Delta\phi)$ is the so-called interference term, which shows that p_{av} can be greater or less than the sum $p_{av1} + p_{av2}$ depending on the value of $\Delta\phi$, or

$$\frac{1}{2\eta} (|\mathbf{E}_1|^2 + |\mathbf{E}_2|^2 - 2\mathbf{E}_1 \cdot \mathbf{E}_2) \leq p_{av} \leq \frac{1}{2\eta} (|\mathbf{E}_1|^2 + |\mathbf{E}_2|^2 + 2\mathbf{E}_1 \cdot \mathbf{E}_2) \quad (1.64)$$

Since $\Delta\phi$ is a function of Δr , periodic spatial variations in the total field occur. These variations form specific "standing" type interference patterns

(e.g., the antenna array pattern and standing wave as a sum of incident and reflected traveling waves).

If the wave radiators are mutually incoherent then the phase difference, $\Delta\phi$, is a random function of time, and the mean value of $\cos(\Delta\phi)$ is zero. In this case there is no wave interference but only a simple summation, or

$$p_{av} = \frac{1}{2\eta} (|\mathbf{E}_1|^2 + |\mathbf{E}_2|^2) \quad (1.65)$$

For example, there is no interference in summation of light waves radiated by two ordinary electric filament lamps or two radio transmitters unlocked in phase.

The interference term also depends on the wave polarization. For two cross-polarized fields $\mathbf{E}_1 \cdot \mathbf{E}_2 = 0$ there is no interference.

1.5.2 Interference Methods

In this section we confine our discussion to the interference of two coherent electromagnetic waves.

1.5.2.1 Optical and Quasi-Optical Interference Methods

These interference methods are typical for the optical and quasi-optical frequency bands. They are classified broadly in two groups: interference by division of wave front and interference by division of wave amplitude [9]. Let us consider some examples of interference schemes related to these methods.

Interference by Division of Wave Front The superposition of two coherent light beams demonstrated by Thomas Young in 1802 [9, 10] was the first man-made interference experiment. The Young's experimental scheme is a classical example of interference by division of a sunlight wave front. As shown in Figure 1.7, light passes through a pinhole S and illuminates a nontransparent sheet that comprises two small holes S_1 and S_2 . The latter act as secondary Huygens' sources of spherical waves with well-defined amplitudes and a constant phase difference (i.e., they behave as mutually coherent point radiators). In other words, these radiators are fed in phase by the wave front. If a white screen is placed in the region beyond the secondary light sources, an interference pattern of bright and dark regions can be seen on it.

Two other arrangements for producing interference phenomena using the division of a single-source wave front into two mutually coherent sources are seen as modifications of Young's experiment. They are illustrated in Figure 1.8.

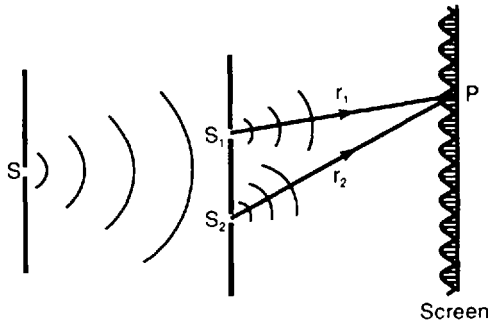


Figure 1.7 Interference by division of wave front—Young's classical experiment. (After: [9], © 1968 Holt, Rinehart & Winston.)

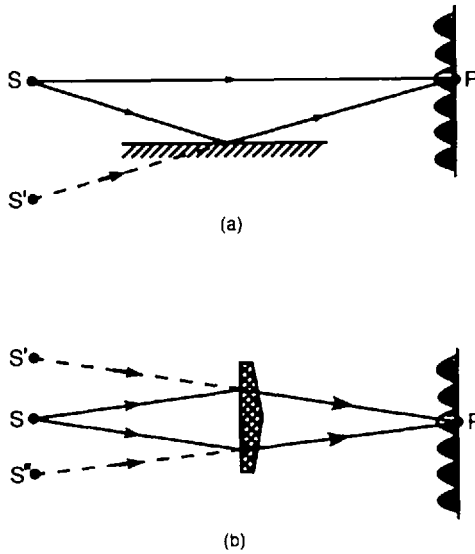


Figure 1.8 Other schemes of interference by division of wave front: (a) Lloyd's single-mirror arrangement and (b) Fresnel's biprism arrangement. (After: [9], © 1968 Holt, Rinehart & Winston.)

In Lloyd's single-mirror experiment [Figure 1.8(a)], the total field at P is due to the interference of direct and reflected wave rays. The reflected ray also appears to come from a virtual source S' . Thus, the field in the region of the screen is equivalent to that in Young's experiment. Fresnel's biprism arrangement [Figure 1.8(b)] produces two refracted coherent rays originating from a single source S . These two rays also appear to come from two virtual coherent sources S' and S'' .

Interference by Division of Wave Amplitude Let us first consider case 1 with a standing wave as the sum of incident and reflected waves. The simplest form of interference by amplitude division occurs when a plane electromagnetic wave is incident normally, or at an incidence angle $\psi_i = 0^\circ$, on the boundary between two semi-infinite media (Figure 1.4). The incident wave gives rise to two new plane waves: reflected and refracted (transmitted).

In the first medium two coherent waves with unequal amplitudes interfere: the incident wave and reflected wave traveling along the z -axis in opposite directions. The resultant (or interference) field behaves as a standing wave, which can be presented in a scalar form as

$$E = E_i + E_r = E_{oi}e^{-j\beta z} + E_{or}e^{j\beta z} \quad (1.66)$$

where E_{oi} and E_{or} are the amplitudes of the incident and reflected waves, respectively. The amplitude of this standing wave is given by

$$E_o = |E| = \sqrt{E_{oi}^2 + E_{or}^2 + 2E_{oi}E_{or}\cos(2\beta z)} \quad (1.67)$$

Here $\cos(2\beta z)$ is the standing wave interference term. For a normal incidence the reflection and transmission process does not depend on the incident wave polarization.

In case 2, with interference in multiple reflection and transmission by dielectric slab, we will consider a very popular scheme of producing an infinite number of mutually coherent waves by division of amplitude. The division occurs by multiple reflection and transmission between the two parallel boundary planes of a dielectric slab (Figure 1.9).

The total reflected and transmitted fields in this case are found as the infinite sum of the partial field contributions due to the process of multiple internal reflections.

Our final goal here is to derive the so-called infinite reflection coefficient R and transmission coefficient T that account for all partial field contributions. Let us mark the plane wave reflection and transmission coefficients at a single boundary by a subscript 1 (or R_1 and T_1) when the incident wave travels from air (medium 1) to dielectric (medium 2), and with subscript 2 (or R_2 and T_2) in case the wave travels from dielectric to air medium. The total reflected field is [11, 12]

$$\begin{aligned} E_r &= E_{r1} + E_{r2} + E_{r3} + \dots \\ &= E_i(R_1 + T_1T_2R_2p_ap_d^2 + T_1T_2R_2^3p_ap_d^4 + \dots) \end{aligned} \quad (1.68)$$

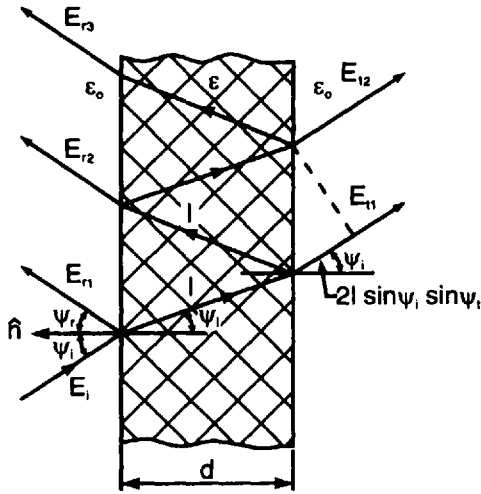


Figure 1.9 Multiple reflection and transmission by dielectric slab. (After: [11], © 1983 IEEE.)

or

$$E_r = E_i \left[R_1 - \frac{T_1 T_2}{R_1} \sum_{n=1}^{\infty} (R_1^2 p_a p_d^2)^n \right] \quad (1.69)$$

with

$$p_a = e^{j \frac{2\beta d}{\cos \psi_i} \sin \psi_i \sin \psi_t} \quad (1.70)$$

and

$$p_d = e^{-j\beta \frac{\sqrt{\epsilon/\epsilon_0}}{\cos \psi_i} d} \quad (1.71)$$

where p_a is a phase factor that takes into account the path-length difference between subsequent rays in the far-field region; and p_d is a phase factor, accounting for the phase delay due to the dielectric path $l = d/\cos \psi_i$. Further, we will make use of the following relationships: $R_2 = -R_1$, $T_1 = R_1 + 1$, $T_2 = R_2 + 1$, $\psi_r = \psi_i$, and $\sin \psi_t = \sin \psi_i / \sqrt{\epsilon/\epsilon_0}$. Then, (1.69) converges to $E_r = E_i R$, where R is given by

$$R = \frac{R_1(1 - p_a p_d^2)}{1 - R_1^2 p_a p_d^2} \quad (1.72)$$

This is the final expression of the total (or infinite) reflection coefficient. Similarly, for the total transmission coefficient T it is found that

$$T = \frac{p_i p_d (1 - R_1^2)}{1 - R_1^2 p_a p_d^2} \quad (1.73)$$

where $p_t = e^{j\beta l \cos(\vartheta_i - \vartheta_t)}$. Equations (1.72) and (1.73) are true for the two polarizations: perpendicular and parallel. Simply said, in (1.72) and (1.73) R_1 is replaced by $R_1^{\perp, \parallel}$, and then $R^{\perp, \parallel}$ and $T^{\perp, \parallel}$ are found.

1.5.2.2 Interference of Waves Radiated by Coherent Individual Sources

In the radio frequency bands the interfering waves are normally radiated by mutually coherent individual elements that form an antenna or scattering system (or array). The classical antenna array theory, which is based on the interference phenomena, is well-documented in many antenna books, so we shall not go into detail here.

1.6 Matrix Analysis of Plane Wave Transmission Through Dielectric Plates

In this section the interface region between two dielectric media is represented by a two-port network and transmission matrix equation. Similarly, the multilayer dielectric plate is considered as a number of two-port networks connected in series. A generalized matrix equation relating the incident, transmitted, and reflected waves in the multilayer plate finally results.

1.6.1 Analogy Between Dielectric Media and Transmission Lines

The propagation of a plane wave in a homogeneous medium is analogous to the wave propagation along a uniform transmission line. The electromagnetic boundary conditions at the plane interface between two mediums are similar to those at the junction between two transmission lines.

The analogy between the mediums and transmission lines is applicable to normal and oblique wave incidence at the interface plane. For the latter case, however, one must take into account the wave polarization [13, 14].

Regard a linearly polarized plane wave incident at angle ψ_1 on the boundary plane between two lossless dielectric media (Figure 1.10).

The wave impedances of the two mediums are different for the perpendicular (η_1^{\perp} and η_2^{\perp}) and parallel (η_1^{\parallel} and η_2^{\parallel}) polarization, and they are found by

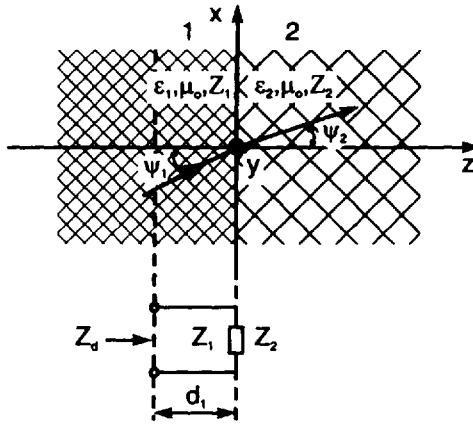


Figure 1.10 Plane wave incident on interface between two mediums. (After: [13].)

$$\begin{bmatrix} \eta_1^\perp \\ \eta_1^\parallel \end{bmatrix} = \begin{bmatrix} \eta/\sqrt{\epsilon_{r1}} \cos \psi_1 \\ \eta \cos \psi_1 / \sqrt{\epsilon_{r1}} \end{bmatrix} \quad (1.74)$$

and

$$\begin{bmatrix} \eta_2^\perp \\ \eta_2^\parallel \end{bmatrix} = \begin{bmatrix} \eta/\sqrt{\epsilon_{r2}} \cos \psi_2 \\ \eta \cos \psi_2 / \sqrt{\epsilon_{r2}} \end{bmatrix} \quad (1.75)$$

where $\eta = 120\pi$; Ω is the free space intrinsic impedance; ϵ_{r1} and ϵ_{r2} are the relative permittivities of the mediums 1 and 2, respectively; ψ_1 is the angle of incidence; and ψ_2 is the angle of refraction.

For a normal incidence $\psi_1 = \psi_2 = 0$, $\eta_1 = \eta_1^\perp = \eta_1^\parallel = \frac{\eta}{\sqrt{\epsilon_{r1}}}$. In the medium 1, at a distance $x = d_1$ from the boundary plane, the input impedance Z_d of the equivalent transmission line with characteristic impedance Z_1 , load impedance Z_2 , and a length d can be easily determined.

The voltage reflection coefficients R^\perp and R^\parallel at $x = 0$ are given by

$$\begin{bmatrix} R^\perp \\ R^\parallel \end{bmatrix} = \begin{bmatrix} (Z_2^\perp - Z_1^\perp)/(Z_2^\perp + Z_1^\perp) \\ (Z_2^\parallel - Z_1^\parallel)/(Z_2^\parallel + Z_1^\parallel) \end{bmatrix} \quad (1.76)$$

For further simplification it is appropriate to omit the common factor η , normalizing it so that for the air $\bar{\eta} = \eta/120\pi = 1$.

1.6.2 Transmission Through Multilayer Dielectric Plates

In the general case of the multilayer dielectric structure with several dielectric media and interfaces and oblique incidence of the plane wave (Figure 1.11) the normalized wave impedances for both polarizations $\bar{\eta}^\perp$ and $\bar{\eta}^\parallel$ can be expressed in a matrix form

$$\begin{aligned} \begin{bmatrix} \bar{\eta}_o^\perp \\ \bar{\eta}_o^\parallel \end{bmatrix} &= \begin{bmatrix} 1/\cos\psi \\ \cos\psi \end{bmatrix}, \quad \begin{bmatrix} \bar{\eta}_1^\perp \\ \bar{\eta}_1^\parallel \end{bmatrix} = \begin{bmatrix} 1/\sqrt{\epsilon_{r1}} \cos\psi_1 \\ \cos\psi_1/\sqrt{\epsilon_{r1}} \end{bmatrix}, \dots, \quad (1.77) \\ \begin{bmatrix} \bar{\eta}_n^\perp \\ \bar{\eta}_n^\parallel \end{bmatrix} &= \begin{bmatrix} 1/\sqrt{\epsilon_{rn}} \cos\psi_n \\ \cos\psi_n/\sqrt{\epsilon_{rn}} \end{bmatrix} \end{aligned}$$

The phase constants are the same for the two polarizations, or

$$\begin{aligned} \beta_o &= \beta_o^\perp = \beta_o^\parallel = \frac{2\pi}{\lambda} \cos\psi, \\ \beta_1 &= \beta_1^\perp = \beta_1^\parallel = \frac{2\pi}{\lambda} \sqrt{\epsilon_{r1}} \cos\psi_1, \dots, \quad (1.78) \\ \beta_n &= \beta_n^\perp = \beta_n^\parallel = \frac{2\pi}{\lambda} \sqrt{\epsilon_{rn}} \cos\psi_n \end{aligned}$$

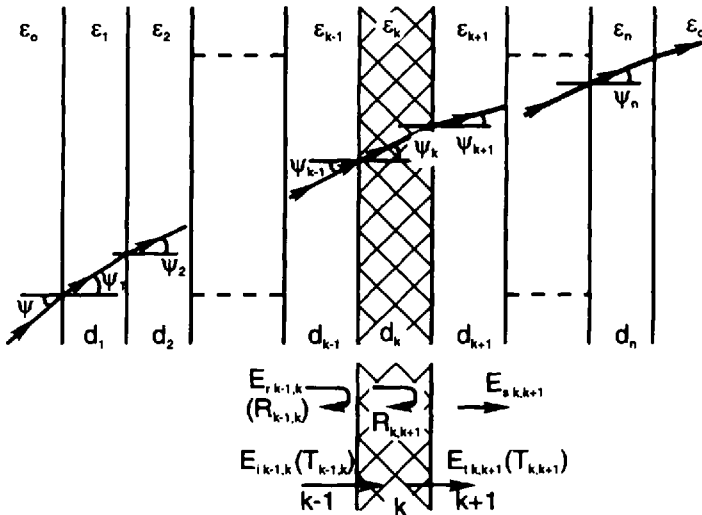


Figure 1.11 Transmission through multilayer dielectric plate. (After: [13].)

As the angle of refraction is related to the angle of incidence by the Snell's law [see (1.41)] we can write

$$\sin \psi = \sin \psi_1 \sqrt{\epsilon_{r1}} = \sin \psi_2 \sqrt{\epsilon_{r2}} = \dots = \sin \psi_n \sqrt{\epsilon_{rn}} \quad (1.79)$$

Combining (1.77) and (1.79) we find that

$$\begin{aligned} \begin{bmatrix} \frac{\eta_o^\perp}{\eta_o^\parallel} \end{bmatrix} &= \begin{bmatrix} 1/\sqrt{1 - \sin^2 \psi} \\ \sqrt{1 - \sin^2 \psi} \end{bmatrix} \cdot \begin{bmatrix} \frac{\eta_1^\perp}{\eta_1^\parallel} \end{bmatrix} = \begin{bmatrix} 1/\sqrt{\epsilon_{r1} - \sin^2 \psi} \\ \sqrt{\epsilon_{r1} - \sin^2 \psi}/\epsilon_{r1} \end{bmatrix}, \dots, \quad (1.80) \\ \begin{bmatrix} \frac{\eta_n^\perp}{\eta_n^\parallel} \end{bmatrix} &= \begin{bmatrix} 1/\sqrt{\epsilon_m - \sin^2 \psi} \\ \sqrt{\epsilon_m - \sin^2 \psi}/\epsilon_m \end{bmatrix} \end{aligned}$$

The electric thickness (or length), in radians, of the dielectric layers can be written as

$$\begin{aligned} \varphi_1 &= (2\pi/\lambda)d_1\sqrt{\epsilon_{r1} - \sin^2 \psi}, \\ \varphi_2 &= (2\pi/\lambda)d_2\sqrt{\epsilon_{r2} - \sin^2 \psi}, \dots, \quad (1.81) \\ \varphi_n &= (2\pi/\lambda)d_n\sqrt{\epsilon_m - \sin^2 \psi} \end{aligned}$$

Dielectric losses can be included via the complex dielectric constant

$$\dot{\epsilon}_r = \epsilon_r(1 - j \tan \delta) \quad (1.82)$$

where $\tan \delta$ is the dielectric loss tangent.

Thus, the layer electric thickness φ becomes a complex quantity

$$\dot{\varphi} = (2\pi/\lambda)d\sqrt{\dot{\epsilon}_r - \sin^2 \psi} \quad (1.83)$$

If $\tan \delta \ll 1$, $\dot{\varphi}$ reduces to

$$\dot{\varphi} \cong \varphi'' + j\varphi' = \frac{2\pi d}{\lambda} \frac{\epsilon_r \tan \delta}{\sqrt{\epsilon_r - \sin^2 \psi}} + j \frac{2\pi d}{\lambda} \sqrt{\epsilon_r - \sin^2 \psi} \quad (1.84)$$

Let us discuss now a matrix representation of the reflection and transmission phenomena between two dielectric media [13, 14], illustrated in Figure 1.12.

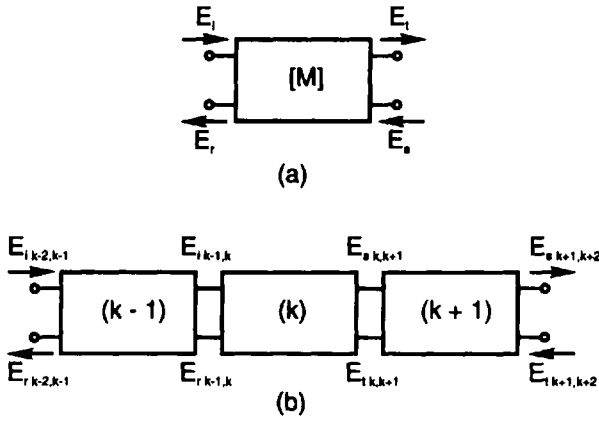


Figure 1.12 Illustration to interface (a) dielectric plate layer and (b) transmission matrix.

A two-port network equivalent to interface region is shown in Figure 1.12(a). Its transmission matrix equation is

$$\begin{bmatrix} E_i \\ E_r \end{bmatrix} = [M] = \begin{bmatrix} E_t \\ E_s \end{bmatrix} \quad (1.85)$$

where E_i , E_r , E_t , and E_s are the electric fields of the incident, reflected, transmitted, and scattered waves, and $[M]$ is a square transmission matrix equal to

$$[M] = \begin{bmatrix} M_{11} & M_{12} \\ M_{21} & M_{22} \end{bmatrix} \quad (1.86)$$

with matrix elements

$$M_{11} = \left(\frac{E_i}{E_t} \right)_{E_r=0} = \frac{1}{T_1} \quad (1.87)$$

$$M_{12} = \left(\frac{E_i}{E_s} \right)_{E_r=0} = -\frac{R_2}{T_2} \quad (1.88)$$

$$M_{21} = \left(\frac{E_r}{E_i} \right)_{E_s=0} = \frac{R_1}{T_1} \quad (1.89)$$

$$M_{22} = \left(\frac{E_r}{E_s} \right)_{E_t=0} = T_2 - \frac{R_1 - R_2}{T_1} \quad (1.90)$$

In the above matrix elements R_1 and T_1 are the input, and R_2 and T_2 are the output interface reflection and transmission coefficients, correspondingly.

If a pair of two-port networks with transmission matrices $[M_1]$ and $[M_2]$ are connected in series by a transmission line with electric length $\varphi = \varphi'' + j\varphi'$ and matrix $[M_d]$, the total transmission matrix $[M]$ is

$$[M] = [M_1][M_d][M_2] \quad (1.91)$$

where

$$[M_d] = \begin{bmatrix} e^{j\varphi} & 0 \\ 0 & e^{-j\varphi} \end{bmatrix} \quad (1.92)$$

Similarly, in the case of a dielectric plane layer, situated between two media, the waves associated with the boundary planes are linked by the following matrix equation [see Figure 1.12(b)]

$$\begin{bmatrix} E_{i,k-1,k} \\ E_{r,k-1,k} \end{bmatrix} = [M_{k-1,k}][M_{dk}][M_{k,k+1}] \begin{bmatrix} E_{t,k,k+1} \\ E_{s,k,k+1} \end{bmatrix}. \quad (1.93)$$

or

$$\begin{bmatrix} E_{i,k-1,k} \\ E_{r,k-1,k} \end{bmatrix} = [M_k] \begin{bmatrix} E_{t,k,k+1} \\ E_{s,k,k+1} \end{bmatrix} \quad (1.94)$$

where

$$[M_k] = [M_{k-1,k}][M_{dk}][M_{k,k+1}] \quad (1.95)$$

is the total transmission matrix;

$$[M_{k-1,k}] = \frac{1}{T_{k-1,k}} \begin{bmatrix} 1 & R_{k-1,k} \\ R_{k-1,k} & 1 \end{bmatrix} \quad (1.96)$$

is the input matrix (at interface $k - 1, k$);

$$[M_{dk}] = \begin{bmatrix} e^{\hat{\varphi}_{dk}} & 0 \\ 0 & e^{-\hat{\varphi}_{dk}} \end{bmatrix} \quad (1.97)$$

is the dielectric layer matrix with an electric length according to (1.84), or

$$\hat{\varphi}_{dk} \cong \frac{2\pi}{\lambda} d_k \frac{\epsilon_{rk} \tan \delta}{\sqrt{\epsilon_{rk} - \sin^2 \psi}} + j \frac{2\pi}{\lambda} d_k \sqrt{\epsilon_{rk} - \sin^2 \psi} \quad (1.98)$$

and

$$[M_{k,k+1}] = \frac{1}{T_{k,k+1}} \begin{bmatrix} 1 & R_{k,k+1} \\ R_{k,k+1} & 1 \end{bmatrix} \quad (1.99)$$

is the output matrix (at interface $k, k+1$).

After multiplying the above partial matrices, the total dielectric layer matrix becomes

$$[M_k] = \frac{1}{T_{k-1,k} T_{k,k+1}} \cdots \cdots \begin{bmatrix} e^{\hat{\varphi}_{dk}} + R_{k-1,k} R_{k,k+1} e^{-\varphi_{dk}} & R_{k,k+1} e^{\varphi_{dk}} + R_{k-1,k} \\ R_{k-1,k} e^{\varphi_{dk}} + R_{k,k+1} & R_{k-1,k} R_{k,k+1} e^{\varphi_{dk}} + R_{k-1,k} e^{-\varphi_{dk}} \end{bmatrix} \quad (1.100)$$

If the k -th dielectric layer is positioned in an unbounded air medium so that $\epsilon_{k-1} = \epsilon_0$, $\epsilon_k = \epsilon$, and $\epsilon_{k+1} = \epsilon_0$, then we may put $R_{k-1,k} = R_1$, $R_{k,k+1} = R_2$, $T_{k-1,k} = T_1$, $T_{k,k+1} = T_2$. This specific case was described in Section 1.5.2.1 [(1.68)–(1.73)]. For the n -layer dielectric plate, shown in Figure 1.11, the incident, transmitted, reflected, and scattered waves are related by the next generalized matrix equation

$$\begin{bmatrix} E_i \\ E_r \end{bmatrix} = \prod_{k=1}^{k=n+1} [M_k]_{\varphi_{n+1}=0} \begin{bmatrix} E_t \\ E_s \end{bmatrix} \quad (1.101)$$

References

- [1] Balanis, C. A., *Advanced Engineering Electromagnetics*, New York: John Wiley & Sons, 1989.
- [2] Jordan, E. C., and K. G. Balmain, *Electromagnetic Waves and Radiating Systems* (2nd edition). New Jersey: Prentice-Hall, 1968.

- [3] Stutzman, W. L., and G. A. Thile, *Antenna Theory and Design*, New York: John Wiley & Sons, 1981.
- [4] Stutzman, W. L., *Polarization in Electromagnetic Systems*, Norwood, MA: Artech House, 1993.
- [5] IEEE Standard 145, *IEEE Standard Definitions of Terms for Antennas*, 1983.
- [6] Mott, H., *Antennas for Radar and Communications: A Polarimetric Approach*, New York: Wiley-Interscience, 1992.
- [7] Kraus, J., *Electromagnetics* (3rd edition), New York: McGraw-Hill, 1984.
- [8] Jackson, J. D., *Classical Electrodynamics*, New York: John Wiley & Sons, 1975.
- [9] Fowles, G. R., *Introduction to Modern Optics*, New York: Holt Rinehart & Winston, 1968.
- [10] Klein, M. V., *Optics*, New York: John Wiley & Sons, 1970.
- [11] Burnside, W. D., and K. W. Burgener, "High Frequency Scattering by a Thin Lossless Dielectric Slab," *IEEE Trans. on Antennas and Propagat.*, Vol. AP-31, No. 1, 1983, pp. 104–110.
- [12] Cady, W. M., M. B. Karelitz, and L. A. Turner (editors), *Radar Scanners and Radomes*, MIT Radiation Lab. Series, Vol. 26, New York: McGraw-Hill, 1948.
- [13] Kaplun, V. A., *Radomes for Microwave Antennas*, Moscow: Soviet Radio Publishers, 1974 (in Russian).
- [14] Collin, R. E., *Field Theory of Guided Waves*. New York: IEEE Press, 1991.

Appendix 1A

Antenna Polarization Parameters

The antenna radiation field $E_P(\vartheta, \varphi)$ at far region observation point P can be expressed in the form¹

$$E_P(\vartheta, \varphi) = \mathbf{E}(\vartheta, \varphi)(\hat{\mathbf{e}}_\vartheta \sin \zeta + \hat{\mathbf{e}}_\varphi \cos \zeta) \quad (1A.1)$$

where $\mathbf{E}(\vartheta, \varphi)$ is the far field vector of the transmitting antenna as a function of the spherical coordinates (ϑ, φ) ; ζ is the orientation angle of the linear polarization probe antenna; and $\hat{\mathbf{e}}_\vartheta$ and $\hat{\mathbf{e}}_\varphi$ are the corresponding unit-vectors.

For a transmitted field, linearly polarized in the y -direction, or at $\vartheta = 0$, the alignment procedure leads to $\vartheta = \varphi$ for the reference (copolarized) field $E_{co}(\vartheta, \varphi)$ and $\zeta = \varphi + 90$ degrees for the cross-polarization field $E_{cr}(\vartheta, \varphi)$.

From (1A.1) it is obtained

1. Ludwig, A. C., "The Definition of Crosspolarization," *IEEE Trans. on Antennas and Propagat.*, Vol. AP-21, January 1973, pp. 116–119.

$$E_P(\vartheta, \varphi) = E_\vartheta(\vartheta, \varphi) \sin \zeta + E_\varphi(\vartheta, \varphi) \cos \zeta \quad (1A.2)$$

For the copolarization field $E_{co}(\vartheta, \varphi = \zeta)$

$$E_{co}(\vartheta, \varphi) = E_\vartheta(\vartheta, \varphi) \sin \varphi + E_\varphi(\vartheta, \varphi) \cos \varphi \quad (1A.3)$$

and for the cross-polarization field two different cases are possible:

1. $\zeta = \varphi + 90$ degrees, and then

$$E_{cr}(\vartheta, \varphi) = E_\vartheta(\vartheta, \varphi) \cos \varphi - E_\varphi(\vartheta, \varphi) \sin \varphi \quad (1A.4a)$$

2. $\zeta = \varphi + 90$ degrees, and then

$$E_{cr}(\vartheta, \varphi) = E_\vartheta(\vartheta, \varphi) \sin \varphi + E_\varphi(\vartheta, \varphi) \cos \varphi \quad (1A.4b)$$

If the transmitted field is polarized in the x -direction the angle φ is replaced by $\varphi + 90$ degrees, which results in modifications of the above equations.

With E_ϑ , E_φ , E_{co} , and E_{cr} determined, the co- and cross-polar radiation pattern, co-polar gain, cross-polar isolation, polarization ratio, and other antenna polarization parameters can be easily calculated.²

1. Normalized co-polar field pattern $F_{co}(\vartheta)|_{\varphi=\text{const.}}$, in decibels:

$$F_{co}(\vartheta) = 20 \log \left| \frac{E_{co}(\vartheta)}{E_{co}(\vartheta = 0^\circ)} \right|_{\varphi=\text{const.}} \quad (1A.5)$$

2. Cross-polar field pattern $F_{cr}(\vartheta)|_{\varphi=\text{const.}}$, in decibels:

$$F_{cr}(\vartheta) = 20 \log \left| \frac{E_{cr}(\vartheta)}{E_{cr}(\vartheta = 0^\circ)} \right|_{\varphi=\text{const.}} \quad (1A.6)$$

3. Co-polar gain pattern, in decibels:

$$G_{co}(\vartheta) = 10 \log \left(\frac{2\pi r^2}{\eta P_t} |E_{co}(\vartheta)|^2 \right)_{\varphi=\text{const.}} \quad (1A.7)$$

2. Mott, H., *Antennas for Radar and Communications: A Polarimetric Approach*, New York: Wiley-Interscience, 1992.

4. Cross-polar gain pattern, in decibels:

$$G_{cr}(\vartheta) = 10 \log \left(\frac{2\pi r^2}{\eta P_t} |E_{cr}(\vartheta)|^2 \right)_{\varphi = \text{const.}} \quad (1A.8)$$

5. Total gain pattern, in decibels:

$$G(\vartheta) = 10 \log \left(\frac{2\pi r^2}{\eta P_t} |E|^2 \right)_{\varphi = \text{const.}} \quad (1A.9)$$

6. Cross-polar isolation $I(\vartheta)$, in decibels:

$$I(\vartheta) = 20 \log \left| \frac{E_{cr}(\vartheta)}{E_{co}(\vartheta)} \right|_{\varphi = \text{const.}} \quad (1A.10)$$

7. Linear polarization ratio $P(\vartheta)$ (complex ratio of linear transverse components):

$$P(\vartheta) = \left. \frac{E_{\vartheta}(\vartheta)}{E_{\varphi}(\vartheta)} \right|_{\varphi = \text{const.}} \quad (1A.11)$$

2

Fresnel-Kirchhoff Diffraction Theory

2.1 Huygens' Principle

In his famous treatise [1] published more than 300 years ago, Christiaan Huygens (1629–1695) proposed a new mechanism for light propagation known today as Huygens' principle. In an analogy with sound, light was considered to travel as a wave motion in a certain kind of fictitious matter, called ether, that was supposed to fill the entire space including the space intervals between matter particles. Each particle of the ether set in vibration by the wave was viewed as a source of new waves. The principle of Huygens is illustrated in Figure 2.1. The initial spherical wave originating from a point source is partially obscured by an infinite screen S .

Let us observe the motion of the wave with a velocity v in the cone limited by the screen aperture S_0 . Suppose at time t the spherical wave front ν is situated inside the aperture. The wave front is considered to consist of equiphase particles (sources) a , b , and c , radiating secondary spherical wavelets so that backward the wavelets cancel while ahead they persist. At a later instant $t + \Delta t$ a new wave front ν' is formed as an envelope of outgoing spherical wavelets with radii $\rho_a = \rho_b = \rho_c = \dots = v\Delta t$, which, in turn, produces a new generation of wavelets with the envelope ν'' , and so on. In this way, the wave front is advancing in a forward direction [2–4].

According to Huygens, the wave fronts are normal to the straight optical rays, and the wave propagation in the uniform cone space (or lit region) goes along a rectilinear path. This phenomenon is known as the optical law of rectilinear propagation.

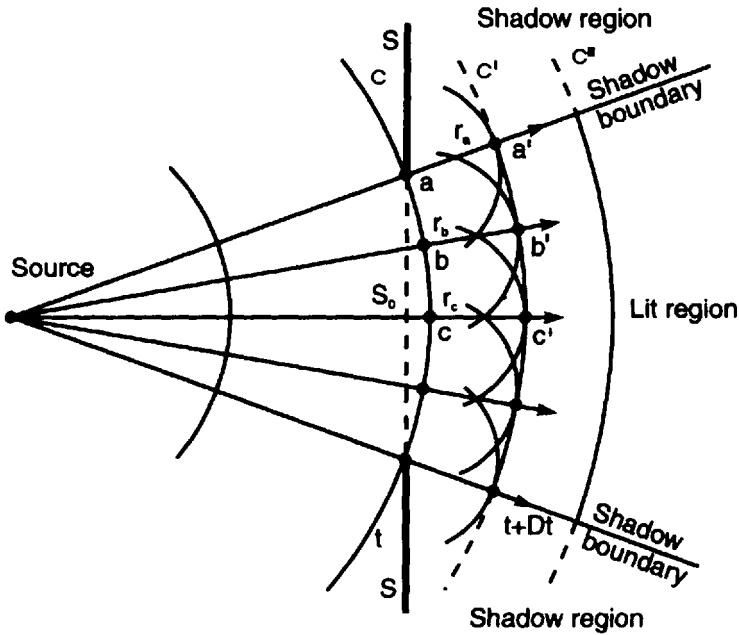


Figure 2.1 Classical construction illustrating Huygens' principle.

It is also assumed that the regions outside the cone generants (or shadow boundaries) are not lighted up by the rectilinearly propagating waves; they are called shadow or diffraction regions.

The Huygens' principle is used also for proving the laws of plane wave reflection and refraction [3–5]. For example, let us demonstrate this possibility for the refraction law (Figure 2.2). Here the incident and refraction (or transmission) angles are marked with ψ_i and ψ_t , respectively. Suppose a point A from the plane wave front AB is reaching at time $t = 0$ the refraction medium 2 (at point O). The secondary wave radiated from point O has a spherical radius $OO' = v_2\Delta t$, where v_2 is the phase velocity in the medium 2 and Δt is the time interval for which the wave travels from point O to point O' . For the same interval the wavelet from point O_3 is reaching point O_3' so that its path length is $O_3O_3' = v_1\Delta t$. Here v_1 is the phase velocity in medium 1. From the two right triangles OO_3O_3' and $OO'O_3'$, with a common hypotenuse OO_3' it is not difficult to write $O_3O_3'/OO' = \sin \psi_t/\sin \psi_i$, or

$$\frac{\sin \psi_t}{\sin \psi_i} = \frac{v_1}{v_2} \tag{2.1}$$

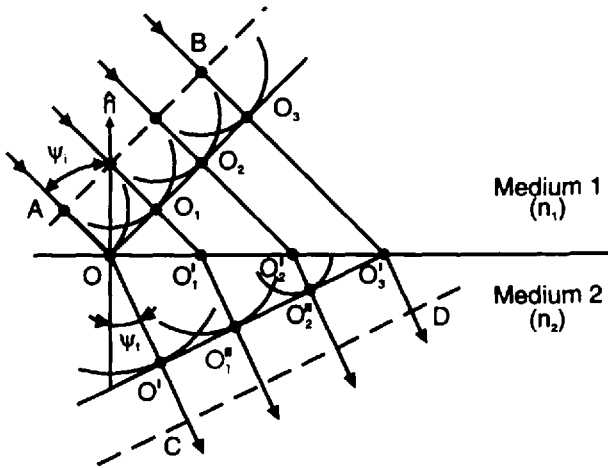


Figure 2.2 Proof of refraction law by use of Huygens' principle.

Thus, using the wave mechanism proposed by Huygens, the refraction or Snell's law is obtained.

In its initial form the principle of Huygens is relevant only to geometric optics. It is valid for extremely small wavelengths and is inadequate for explanation of all wave phenomena—for instance, the deviation (diffraction) of wave from a rectilinear ray propagation when it passes the edges of objects or through small slits.

Although Huygens created his mechanism of light motion using the ideas about secondary wavelets and their summation to form a new wave front, he was not aware of the periodic nature of light and the fact that this periodicity is tied to space and time. Most unfortunately, Huygens' wave mechanism of propagation fell into oblivion [2], and for a long time only Newton's corpuscular model of light propagation was at the root of optics [Isaac Newton (1642–1727)].

More than a century after Huygens, Thomas Young (1773–1829) discovered the principle of ray interference (see Section 1.5) and explained qualitatively what occurs when two light rays combine. He regarded the periodic properties of light as a result of combining rays with positive and negative magnitudes [4]. Later, though independently, Augustin Fresnel (1788–1827) revived Huygens' principle to establish the wave theory of light.

2.2 Fresnel Zones

Fresnel completed Huygens' deductive wave mechanism by taking into account the space and time periodicity of light waves, mutual interference, and polariza-

tion effects. Due to Fresnel, the wave front acquired a clear physical meaning as a surface on which secondary wavelets with given amplitudes and directions of radiation interfere. The modified and perfected Huygens' principle was renamed the Huygens'-Fresnel's principle. It became a fundamental method for solving wave diffraction problems.

Before applying Huygens'-Fresnel's principle to study diffraction effects we will use it to describe wave propagation in free space [3, 5-7]. Then we will examine the geometry of spherical and plane Fresnel zone constructions and apply them to approximately solve the diffraction field integral. Finally, we will describe briefly the focusing properties of single and double zone focusing elements (or lens-like diffractors) and multizone Soret and Wood zone lenses.

2.2.1 Fresnel Formulation of Huygens' Principle

Let us surround the source point P_1 by a closed surface with an arbitrary shape, and let P_2 be an observation point out of S (Figure 2.3).

Given the current density \mathbf{J}_1 in a space volume dV' (point P_1) the elementary electric field $d\mathbf{E}(P_2)$ can be found directly using, for instance, the vector potential method described in Section 1.1

$$dE(P_2) = \frac{1}{j\omega\mu\epsilon} \nabla(\nabla \cdot dA(P_2)) - j\omega dA(P_2) \quad (2.2)$$

where

$$dA(P_2) = \frac{\mu}{4\pi} J_1(P_1) \frac{e^{-j\beta(\rho_o+r_o)}}{\rho_o + r_o} dV' \quad (2.3)$$

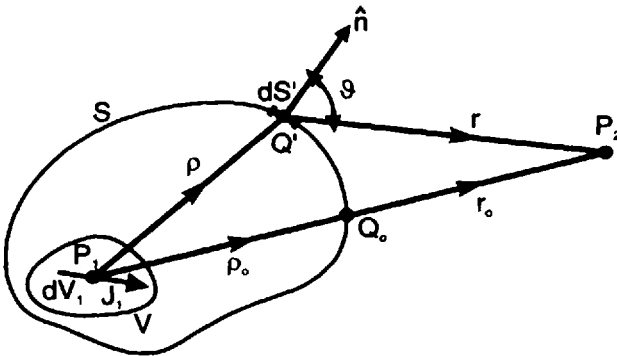


Figure 2.3 Huygens' secondary wave surface enclosing the primary current source.

Here we shall consider another, indirect method for finding the field at P_2 that resulted from the Huygens'-Fresnel's principle. It is assumed that after finding the field on the surface S we remove the wave source J_1 from P_1 . S is viewed as Huygens' source surface radiating secondary waves, and the total field at P_2 is found as a sum of all secondary waves.

Each element dS' of the imaginary radiating surface contributes elementary field with a scalar complex intensity $dE(P_2)$

$$dE(P_2) = E_S(Q') e^{j\Psi_S(Q')} \frac{e^{-j\beta r}}{r} I(\vartheta) dS' \quad (2.4)$$

where $E_S(Q')$ and $\Psi_S(Q')$ are respectively the amplitude and the phase of a scalar component of the electric field vector $E_S(Q')$ at Q' (or at dS'), and $I(\vartheta)$ is the inclination factor depending on the angle between the unit normal \hat{n} and the direction to the observation point. It corresponds to the so-called Huygens source radiation pattern (see Section 2.3.2 and Appendix 2A). According to Fresnel, it is assumed that for $\vartheta = 0$, $I(0) = I_{\max}$. With the increase of ϑ , $I(\vartheta)$ decreases monotonically and becomes zero for $\vartheta \geq \pi/2$. As will be shown in Section 2.3, Fresnel's assumption was not quite correct.

The total field at P_2 is found by integration of (2.4) over the whole closed surface S

$$E(P_2) = \iint_S E_S(Q') e^{j\Psi_S(Q')} \frac{e^{-j\beta r}}{r} I(\vartheta) dS' \quad (2.5)$$

In accordance with Fresnel, let us simplify the problem by replacing the arbitrary radiating surface with a sphere with an origin at P_1 and a radius ρ_0 [i.e., with a spherical surface that coincides with the primary source wave front (Figure 2.4)].

The complex surface field $E_S(Q') e^{j\Psi_S(Q')}$ at point $Q'(\rho' = \rho_0, \psi', \phi')$ is set equal to a far field component of the incident spherical wave $A_1 \frac{e^{-j\beta\rho_0}}{\rho_0}$, radiated by a point source or isotropic radiator located at P_1 (an isotropic radiator is defined as a hypothetical antenna having equal radiation in all directions). Here A_1 is the amplitude at a unit distance ($\rho_0 = 1$) from the source.

With the above equality in mind (2.5) becomes

$$E(P_2) = A_1 \iint_S \frac{e^{-j\beta(\rho_0+r)}}{\rho_0 r} I(\vartheta) dS' \quad (2.6)$$

$$b_n = \sqrt{n\lambda F_e} \quad (2.12)$$

Comparison of (2.12) with (2.10) shows that there is a very simple approximate ratio between the zone radii b_n and b_1

$$\frac{b_n}{b_1} = \sqrt{n} \quad (2.13)$$

If $\rho_o = r_o = F_o$, $F_e = F_o/2$ (2.12) becomes

$$b_n = \sqrt{n\lambda \frac{F_o}{2}} \quad (2.14)$$

For $r_o = \infty$ and $\rho_o = F_o = F_e/2$ the n -th Fresnel zone radius b_n is calculated by

$$b_n = \sqrt{n\lambda F_o} \quad (2.15)$$

The first (central) Fresnel zone has the shape of a spherical segment, and its area S_1 , as known from the stereometry, is given by

$$S_1 = 2\pi\rho_o(Q_1O) \cong \pi\lambda \frac{\rho_o r_o}{\rho_o + r_o} \quad (2.16)$$

The second zone is of a spherical annular shape, and its area is $S_2 = 2\pi\rho_o(Q_1Q_2)$. As a first approximation it can be found that $S_2 \approx S_1$. Moreover, for an n that is not very large, it is obtained that all Fresnel zones are almost equal in area, or

$$S_1 \cong S_2 \cong \dots \cong S_n \cong \dots \quad (2.17)$$

and each of them can also be calculated by (2.16).

2.2.2.2 Plane Fresnel Zones

We shall apply here the Fresnel zone construction to the simplest of shape surface—the infinite plane, normal to the direct propagation path P_1P_2 as illustrated in Figure 2.6. First, we will find an approximate equation for the n -th Fresnel zone radius b_n . From the right triangle P_1OQ_n we could write

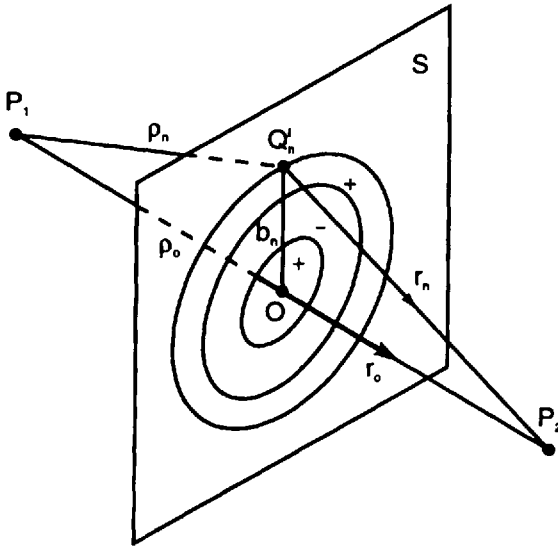


Figure 2.6 Geometry for calculation of plane Fresnel zone dimensions.

$$\rho_n = \sqrt{b_n^2 + \rho_0^2} = \rho_0 \sqrt{1 + \frac{b_n^2}{\rho_0^2}} \quad (2.18)$$

$$\text{For } b_n \ll \rho_0, \sqrt{1 + \frac{b_n^2}{\rho_0^2}} \cong 1 + \frac{1}{2} \left(\frac{b_n}{\rho_0} \right)^2$$

or

$$\rho_n \cong \rho_0 + \frac{b_n^2}{2\rho_0} \quad (2.19)$$

Similarly, from the triangle OP_2Q_n , for $b_n \ll r_0$, it is found that

$$r_n \approx r_0 + \frac{b_n^2}{2r_0} \quad (2.20)$$

The Fresnel condition for the concentric zones on S requires that $\rho_n + r_n$ differs by $\lambda/2$ from $\rho_{n-1} + r_{n-1}$, and by $n\lambda/2$ from $\rho_0 + r_0$, or

$$\rho_n + r_n \cong \rho_0 + r_0 + \frac{b_n^2}{2\rho_0} + \frac{b_n^2}{2r_0} = \rho_0 + r_0 + n \frac{\lambda}{2} \quad (2.21)$$

The radius b_n is then easily expressed by

$$b_n = \sqrt{n\lambda F_e} \quad (2.22)$$

where F_e is the equivalent focal length given by (2.11).

As in Section 2.2.2.1, if $\rho_o = r_o = F_o$ and $F_e = F_o/2$ (2.22) is transformed to

$$b_n = \sqrt{n\lambda \frac{F_o}{2}} \quad (2.23)$$

Finally, for $r_o = \infty$ and $\rho_o = F_e = F_o$ it becomes

$$b_n = \sqrt{n\lambda F_o} \quad (2.24)$$

The comparison between (2.12), (2.14), and (2.15) and (2.22), (2.23), and (2.24) shows that the Fresnel zone radius is calculated by one and the same equation, regardless of whether the surface shape is plane or spherical.

Similar considerations are true for the spherical and plane Fresnel zone areas. Suppose $\rho_o + r_o = \text{const.}$ From (2.24) it follows that the smaller the wavelength λ the bigger the number of the essential Fresnel zones.

If plane S is moved along the line of sight P_1P_2 (Figure 2.7) the Fresnel zone boundaries will outline sections of rotational surfaces as far as

$$\rho_n + r_n = \rho'_n + r'_n = \dots = \rho_o + r_o = n\lambda/2 = \text{const.} \quad (2.25)$$

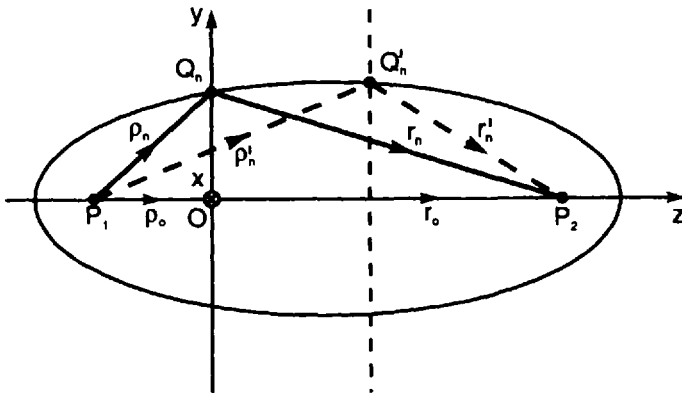


Figure 2.7 Definition of space Fresnel zone.

In fact, (2.25) determines a rotational ellipsoid around the z axis with foci in points P_1 and P_2 . The volume within the first Fresnel ellipsoid or between any two adjacent ellipsoids is called a space Fresnel zone (Fresnel zone volume or 3-D Fresnel zone).

For quasi-optical and optical wavelengths (or for $\lambda \rightarrow 0$) all ellipsoids are transformed into a narrow channel (or physical wave ray) from the source point P_1 to the receiver point P_2 . In other words, the Fresnel volumes are very thin and are highly concentrated to the mathematical ray.

Let us illustrate the above statement with the following numerical example. Find the radius and the area of the first Fresnel zone of a spherical wave with wavelength $\lambda = 1.5$ mm (millimeter-wave band) and $\rho_o = r_o = 500$ m. After placing the data in (2.10) and (2.16) we find the first zone radius $b_1 = 0.27$ m and the first zone area $S_1 \cong 0.24$ m². Thus, the propagation of millimeter waves is bounded in a very narrow channel that is said to be formed by mathematical paraxial rays.

2.2.3 Field Determination by Means of Fresnel Zone Construction

The field contributed by the n -th spherical Fresnel zone at point P_2 (Figure 2.4) is found in accordance with (2.6), or

$$E_n(P_2) = A_1 \int_0^{2\pi} \int_{r_o+(n-1)(\lambda/2)}^{r_o+n(\lambda/2)} \frac{e^{-j\beta(\rho_o+r)}}{\rho_o r} I(\vartheta) dS' \quad (2.26)$$

where $dS' = \rho_o^2 \sin \psi' d\psi' d\phi'$.

It is supposed that ρ_o and $r_o \gg \lambda$. From the triangle $P_1 P_2 Q'$ it is written

$$r^2 = \rho_o^2 + (\rho_o + r_o)^2 - 2\rho_o(\rho_o + r_o)\cos \psi' \quad (2.27)$$

The differential of (2.27) $\frac{\partial}{\partial r}(r^2)dr = \frac{\partial}{\partial \psi}[\rho_o^2 + (\rho_o + r_o)^2 - 2\rho_o(\rho_o + r_o)\cos \psi']d\psi'$ gives $rdr = \rho_o(\rho_o + r_o)\sin \psi' d\psi'$, or $\sin \psi' d\psi' = rdr/[\rho_o(\rho_o + r_o)]$. Thus, the element area dS' can be expressed in the form

$$dS' = \frac{\rho_o}{\rho_o + r_o} r dr d\phi' \quad (2.28)$$

Here ϕ' is the azimuth angle in the spherical coordinate system (ρ_o, ψ', ϕ') with a center at P_1 .

Over the n -th zone the inclination factor $I(\vartheta)$ may be replaced approximately by an average value I_n . After completing integration in (2.26) over the n -th zone its radiated field is found to be

$$E_n(P_2) = -j2\lambda(-1)^{n+1} E_o(P_2)I_n \quad (2.29)$$

where

$$E_o(P_2) = A_1 \frac{e^{-j\beta(\rho_o+r_o)}}{\rho_o + r_o} \quad (2.30)$$

is the field of free-space spherical wave at point P_2 traveling along the straight ray P_1P_2 .

The factor $(-1)^{n+1}$ in (2.29) shows that the field contributions of the successive Fresnel zones are alternately positive or negative.

The field radiated by the first zone only is

$$E_1(P_2) = -j2\lambda E_o(P_2)I_1 \quad (2.31)$$

The total field at the observation point is a sum of all zone fields

$$E(P_2) = -j2\lambda E_o(P_2) \sum_{n=1}^N (-1)^{n+1} I_n \quad (2.32)$$

where N is the total number of Fresnel zones.

The series in (2.32) can be expanded as follows

$$\sum_{n=1}^N (-1)^{n+1} I_n = I_1 - I_2 + I_3 - \dots + (-1)^{N+1} I_N \quad (2.33)$$

and presented in the form

$$\begin{aligned} \sum_{n=1}^N (-1)^{n+1} I_n &= \frac{I_1}{2} + \left(\frac{I_1}{2} - I_2 + \frac{I_3}{2} \right) + \left(\frac{I_3}{2} - I_4 + \frac{I_5}{2} \right) + \dots \\ &+ \left(\frac{I_{n-1}}{2} - I_n + \frac{I_{n+1}}{2} \right) + \dots \\ &+ \begin{cases} \frac{I_N}{2}, & N - \text{odd} \\ \frac{I_{N-1}}{2} - I_N, & N - \text{even} \end{cases} \end{aligned} \quad (2.34)$$

The inclination factor $I(\vartheta)$ decreases monotonically with increase of angle ϑ , or $I_1 > I_2 > I_3 \dots I_{n-1} > I_n > I_{n+1} \dots$ and $I_n \cong (I_{n-1} + I_{n+1})/2$. Also, for very large N , $I_N \cong 0$. Thus, in (2.33) the sums in parentheses are essentially zero, and the total sum is given by the following approximation

$$\sum_{n=1}^N (-1)^{n+1} I_n \cong \frac{I_1}{2} \quad (2.35)$$

Therefore, with the above approximation in mind, after placing (2.34) into (2.35) the total field will be found to be

$$E(P_2) = -j\lambda E_o(P_2)I_1 \quad (2.36)$$

More precise theoretical analysis gives the value of the complex coefficient $I_1 = j/\lambda = (1/\lambda)\exp(j\pi/2)$ as a product of two factors: the amplitude factor $1/\lambda$ and the phase factor $\exp(j\pi/2)$. The amplitude factor is a ratio between the secondary wave amplitude and the primary wave amplitude, and the phase factor shows that each secondary wave is $\pi/2$ in phase behind the primary wave.

After putting $I_1 = j/\lambda$ into (2.31) it is obtained that

$$E_1(P_2) = 2E_o(P_2) \quad (2.37)$$

In the same way, from (2.36), the total field will be expressed as

$$E(P_2) = E_o(P_2) = \frac{1}{2}E_1(P_2) \quad (2.38)$$

According to (2.38) the total field at point P_2 radiated by the source (or re-radiated by all Fresnel zones) is half of the field due to the first (central) Fresnel zone, or as it is produced by the first half (or first subzone) of this Fresnel zone only. Since the wave power density at some point is given by the average value of the Poynting vector, or according to (1.26) $p_{av} = \frac{1}{2\eta}\text{Re}(E \cdot E^*) = \frac{1}{2\eta}\text{Re}|E^2|$, it is seen that p_{av} is proportional to the squared field strength. Here, we assume propagation in a lossless medium, or $\eta = |\eta|$. Thus, the equation for the power (or energy) density can be written as follows

$$p_{av}(P_2) = \frac{1}{4} p_{av1}(P_2) \quad (2.39)$$

Equation (2.39) shows that the total power density at point P_2 due to all Fresnel zones is one-fourth of the power density produced by the first Fresnel zone solely. The approximate field series summation in (2.34) can also be represented in a graphical form as shown in Figure 2.8. If the size of the opening (or number of zones that fit within the opening) is increased, the total interference field at P_2 is fluctuating and converging to E_o for $n \rightarrow \infty$. As long as the series is converging with the increase of the zone number the resultant field at the observation point may be imagined as created by the secondary wave sources located within the first several zones only. The conclusions we have reached for the spherical Fresnel zone construction are also true for the field produced by the planar Fresnel zones.

2.2.4 Particular Cases of Fresnel Zone Obstruction

Suppose some of the Fresnel zones are covered by a screen (or absorber) that coincides with the zone surface S . Now, the total field at P_2 is due to the waves radiated only by zones (or subzones) not obstructed by the spherical screen (i.e., by zones that fit in the opening).

Consider several specific cases of obstruction.

- Only the inner subzone of first zone is open (not obstructed): The field at the observation point P_2 is

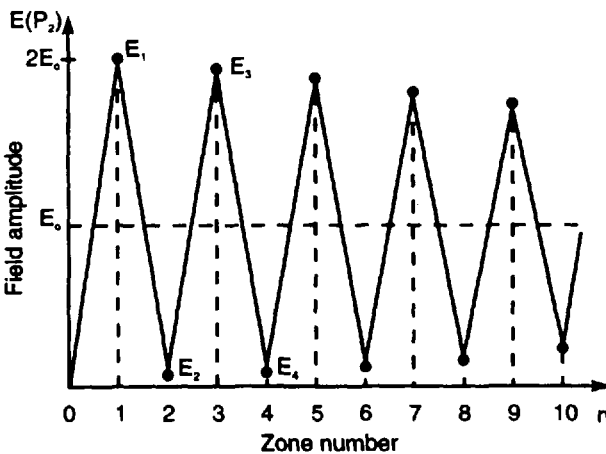


Figure 2.8 Total field calculated as sum of Fresnel zone fields versus the zone number.

$$E(P_2) = E_o(P_2) \tag{2.40}$$

This particular case was discussed in Section 2.2.3 in detail.

- The first zone is open, and the rest are screened:

$$E(P_2) = E_1(P_2) = 2E_o \tag{2.41}$$

which means that the total field at point P_2 is two times larger than if the screen was absent (point E_1 in Figure 2.8).

- Both the first and second zones are open: Now, for $N = 2$ (2.32) gives

$$E(P_2) = -j2E_o \sum_{n=1}^2 (-1)^{n+1} I_n = -j2\lambda E_o (I_1 - I_2) \cong 0 \tag{2.42}$$

since $I_1 \cong I_2$. This case corresponds to point E_2 in Figure 2.8.

- First $n - 1$ zones are obstructed: If a circular concentric screen is obstructing the first $n - 1$ zones (Figure 2.9), the resultant field at the receiving point produced by all not clear zones is found in accordance with (2.32)

$$E(P_2) = -j2\lambda E_o(P_2) \tag{2.43}$$

$$= \frac{I_n}{2} + \left(\frac{I_n}{2} - I_{n+1} + \frac{I_{n+2}}{2} \right) + \left(\frac{I_{n+2}}{2} - I_{n+3} + \frac{I_{n+4}}{2} \right) + \dots \cong \frac{I_n}{2}$$

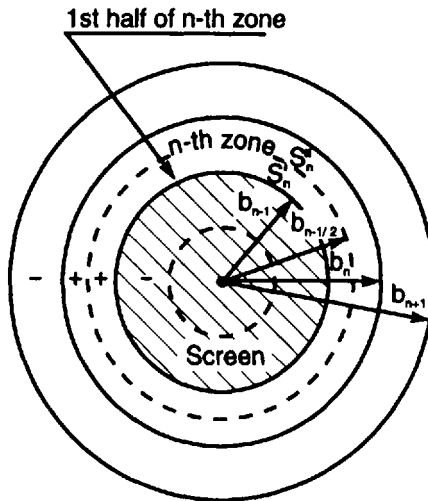


Figure 2.9 First $n - 1$ Fresnel zones obstructed by concentric disk obstacle.

All Fresnel zones (or subzones) are almost equal in area so that

$$E(P_2) = \frac{1}{2}E_n(P_2) \cong \frac{1}{2}E_1(P_2) \cong E_o(P_2) \quad (2.44)$$

From (2.44) two very curious conclusions are made:

- The total field at the receiving point is equal to the field produced by the inner n -th open subzone only.
- The field at the receiving point equals the field at the same point when there is no screen at all. In the early days of the physical optics this was a very surprising invention that confirmed the wave nature of light.

2.2.5 Focusing Properties of Simple Fresnel Zone Lens-like Diffractors: Multizone Lenses of Soret and Wood

It was proved above that the circular aperture in a screen, equal to the first Fresnel zone, can be regarded as a focusing element (lens-like diffractor). It is sketched in Figure 2.10(a). The focusing properties can be expressed by the focusing coefficient G_f (or focusing gain), defined as a squared ratio of the focused field $E(P_2)$ and free-space field $E_o(P_2)$ at the receiving point P_2 , or

$$G_f = \left(\frac{E(P_2)}{E_o(P_2)} \right)^2 \quad (2.45)$$

or in decibel notation

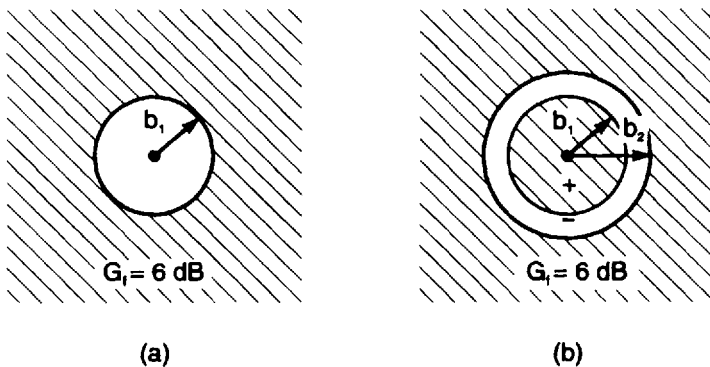


Figure 2.10 Single Fresnel zone focusing diffractor: (a) with first zone open and (b) with second zone open.

$$G_f = 20 \log \left| \frac{E(P_2)}{E_o(P_2)} \right| \quad (2.46)$$

Thus, the focusing coefficient of the first Fresnel zone according to (2.41), (2.45), and (2.46) is $G_f = 4$ (or 6 dB).

Recall that the focusing aperture is illuminated by a spherical wave from a point source at P_1 . Commonly, the points P_1 and P_2 are located on the lens axis that coincides with the z -axis, at distances ρ_o and r_o from the xy plane (or aperture plane in the case of a flat screen) and are called focal points (or foci).

The next in size single-zone lens has only the second Fresnel zone open [Figure 2.10(b)]. Assuming an equality in zone areas ($S_2 \cong S_1$) and in inclination factor values ($I_2 \cong I_1$) the field at the receiving focus is easily obtained

$$E(P_2) = \sum_n E_n(P_2) = -E_2(P_2) \cong -2E_o(P_2) \quad (2.47)$$

and the focusing coefficient is again equal to 4 (or 6 dB). Thus, the smallest in size single-zone lenses have roughly equal focusing properties. The next in focusing capability is the single-zone ring-obstructing (reflecting or absorbing) wave transmission through the second zone only [Figure 2.11(a)]. The ring is complementary to the second zone annular slot shown in Figure 2.10(b) (see more about complementary screen structures in Section 2.4.5).

For a single-ring lens-like diffractor the field focused at P_2 is found as

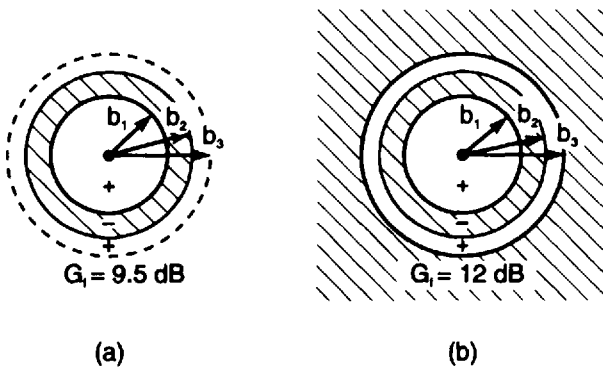


Figure 2.11 Other simple Fresnel zone focusing diffractors: (a) single-zone ring diffractor obstructing second Fresnel zone and (b) double-zone ring diffractor obstructing second and fourth Fresnel zones.

$$E(P_2) = E_1(P_2) + \frac{1}{2} E_3(P_2) \cong 3E_o(P_2) \quad (2.48)$$

and its focusing coefficient is

$$G_f \cong 9 \text{ (or 9.5 dB)} \quad (2.49)$$

Here, the following approximations also took place: $S_3 \cong S_2 \cong S_1$, $I_3 \cong I_2 \cong I_1$, and $|E_3(P_2)| \cong |E_2(P_2)| \cong |E_1(P_2)|$.

The zone lens shown in Figure 2.11(b) consists of two open zones (the first and third zones) cut in an infinite screen. The two zones are radiating in phase. If again, the above area and the inclination factor approximations are understood then the field localized at point P_2 is given by

$$E(P_2) = \sum_{n=1,3} E_n(P_2) = E_1(P_2) + E_3(P_2) \cong 4E_o(P_2) \quad (2.50)$$

and the focusing coefficient of the double annular slot lens is $G_f \cong 16$ (or 12 dB). Following the above reasonings and increasing further the number of open Fresnel zones cut in a thin screen plate (odd or even), Soret created in 1875 the optical multizone plate [9]. It is illustrated in Figure 2.12, where in (a) the zone-plate lens has odd zones open, and in (b) it has even zones open. In other words, the Soret zone plate comprises a set of plane concentric Fresnel zone rings that are alternatively open (transparent) and opaque (reflecting or absorbing).

Remember that Fresnel zone lenses in Figure 2.12 are cut in infinite plane screen or absorber. Thus, the total field at focal point P_2 is obtained as a sum of partial fields produced by N_o open zones, or for $N_o \cong N/2$.

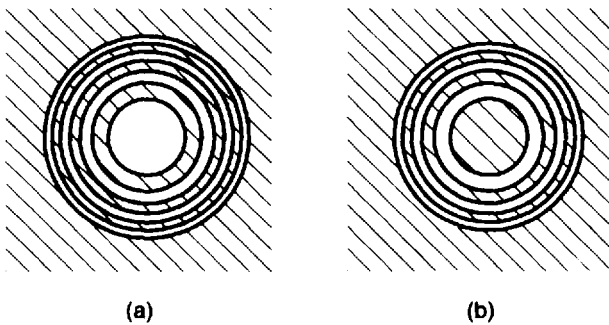


Figure 2.12 Soret's multizone plate cut in infinite planar screen with (a) odd zones open and (b) even zones open.

$$E(P_2) = \sum_{n=1}^N E_n(P_2) = E_1(P_2) + E_3(P_2) + \dots + E_n(P_2) + \dots + E_N(P_2) \quad (2.51)$$

with $n = 1, 3, 5, \dots$ for the zone plate in Figure 2.12(a), and

$$E(P_2) = \sum_{n=1}^N E_n(P_2) = E_2(P_2) + E_4(P_2) + \dots + E_n(P_2) + \dots + E_N(P_2) \quad (2.52)$$

with $n = 2, 4, 6, \dots$ for the zone plate in Figure 2.12(b). The inclination factor $I(\vartheta)$ for $N \gg 1$ decreases faster and $E_1(P_2) > E_2(P_2) > \dots > E_N(P_2)$.

Imagine that in Figure 2.12(a), for example, the screen left out of the zone area is removed. Then the field intensity at P_2 will be slightly less than $E(P_2)$ given by (2.51), or according to (2.44) it is found that

$$E(P_2) = \sum_{n=1}^N E_n(P_2) = E_1(P_2) + E_3(P_2) + \dots + E_n(P_2) + \dots \quad (2.53) \\ + \frac{1}{2} E_N(P_2)$$

for odd clear zones. N is the total number of zones (open and closed).

If for simplicity we still assume that $E_1(P_2) \cong E_3(P_2) \cong \dots \cong E_N(P_2) \cong 2E_o(P_2)$ the total field for $N \cong 2N_o$ is approximately found by

$$E(P_2) = N_o E_o(P_2) \cong \frac{N}{2} E_o(P_2) \quad (2.54)$$

for N odd, and the focusing coefficient is simply found as a squared number of all open zones, or

$$G_f \cong N_o^2 \quad (2.55)$$

or in decibels it is calculated by $20 \log N_o$.

If $N_o = 7$, for example, $G \cong 49$, (or 16.9 dB).

Since only half of the zone-plate lens area, the open one, is used in the focusing process, the Soret zone plate has a low focusing efficiency. In order to improve the zone-plate lens focusing effect Wood [10, 11] developed at

optical wavelengths a similar zone plate with opaque zones that are replaced by transmitting phase-reversing rings.

In contrast with ordinary lenses, the Fresnel zone lens does not smoothly transform the incoming spherical wave into an outgoing spherical (or plane) wave. It is a stepwise phase transformer, and the maximum phase error in the lens aperture equals π . So, the focusing efficiency of the Fresnel zone plates is inherently smaller than the efficiency of the ordinary lenses.

2.3 Scalar Kirchhoff's Diffraction Theory

On the basis of the Huygens'-Fresnel's principle Gustav Kirchhoff (1824–1887) proposed an approximate diffraction method and a corresponding theory that is essentially equivalent to Fresnel's formulation but gives in addition an accurate expression for the inclination factor [6].

Kirchhoff's diffraction theory (physical optics) is presented here in a scalar form, which means that the electromagnetic field polarization is neglected or that all contributions to the total diffraction field are assumed to be of the same polarization. In this section Kirchhoff's diffraction integrals are applied for (1) a diffraction aperture cut in a screen (absorbing) surface enclosing the primary sources and (2) a diffraction aperture in an infinite plane screen (absorber) placed between the source and the observation point.

In the antenna theory the following space regions are normally defined: the near-field region, the Fresnel region, and the far-field or Fraunhofer region. As an example, the Fraunhofer diffraction by a circular aperture is studied at the end of this section.

2.3.1 Scalar Form of the Kirchhoff Diffraction Integral

Starting from the Helmholtz wave equation (1.5) and the second Green theorem [George Green (1793–1841)] Kirchhoff derived an electromagnetic theorem for the observation point field [6–8]. In accordance with Figure 2.13 this theorem can be written in the following scalar form

$$E(P_2) = \frac{1}{4\pi} \iint_S \left[\Phi(r) \frac{\partial E(Q')}{\partial n} - E(Q') \frac{\partial \Phi(r)}{\partial n} \right] dS' \quad (2.56)$$

Here \hat{n} is the unit vector normal to the surface element dS' , $E(P_2)$ is the scalar component of the electric field at the observation point P_2 , $E(Q')$ and $\partial E(Q')/\partial n$ are respectively the electric field component and its first derivative at a surface element point Q' , and $\Phi(r) = e^{-j\beta r}/r$ is a spherical wave function.

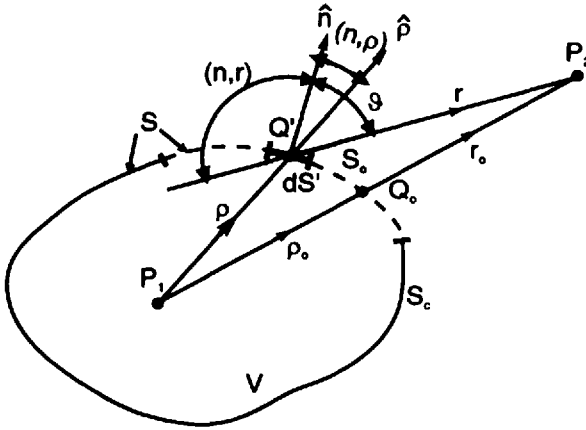


Figure 2.13 Geometry for derivation of Fresnel's-Kirchhoff's diffraction integral.

The first- and second-order derivatives of $E(Q')$ and $\Phi(r)$ are continuous in the volume V and on the surface S . Also, both $E(Q')$ and $\Phi(r)$ satisfy the following scalar Helmholtz (or wave) equations

$$\nabla^2 \begin{bmatrix} E(Q') \\ \Phi(r) \end{bmatrix} + \beta^2 \begin{bmatrix} E(Q') \\ \Phi(r) \end{bmatrix} = 0 \quad (2.57)$$

Suppose that two surface portions form the closed surface of integration S in (2.56): (1) the open portion S_o , and (2) the screened portion S_c . For solving (2.56) we need to know the functions $E(Q')$ and $\partial E(Q')/\partial n$ on $S = S_o + S_c$, but, unfortunately, it is impossible to find them exactly. The real physical aperture influences the incident wave. It is partially transmitted through and partially reflected, absorbed, and scattered (diffracted) by the aperture. The combination of all these phenomena makes the problem too complicated, and to contend with this Kirchhoff replaced the exact boundary conditions on S by the so-called approximate (or Kirchhoff's) boundary conditions

$$E(Q') = 0 \text{ and } \partial E(Q')/\partial n = 0 \text{ on } S_c \quad (2.58)$$

and

$$E(Q') = E_i(Q') \text{ and } \partial E(Q')/\partial n = \partial E_i(Q')/\partial n \text{ on } S_o \quad (2.59)$$

where

$$E_i(Q') = A_1 \frac{e^{-j\beta\rho}}{\rho} \quad (2.60)$$

represents incident spherical wave radiated by the source at P_1 . The distance $\rho = P_1 Q'$ is much bigger than the wavelength, or Q' is viewed as a point in the far-field region of the source.

The Kirchhoff's aperture boundary conditions have clear physical meaning: Incident field over the aperture is identical to field without screen, while outside field over the screen portion is zero, as if ideally absorbed inside screen. In fact, these conditions express in mathematical form the classical Huygens' principle.

Let us simplify (2.56). The gradient of $E(Q')$ is in the direction of $\hat{\rho}$ and therefore we can write

$$\begin{aligned} \frac{\partial E_i(Q')}{\partial n} &= \frac{\partial E_i(Q')}{\partial \rho} \cos(n, \rho) = -A_1 \frac{e^{-j\beta\rho}}{\rho} \left(j\beta + \frac{1}{\rho} \right) \cos(n, \rho) \quad (2.61) \\ &\cong -j\beta A_1 \frac{e^{-j\beta\rho}}{\rho} \cos(n, \rho) \end{aligned}$$

where $1/\rho$ is neglected compared to $\beta = 2\pi/\lambda$, and the angle (n, ρ) depends on the integration surface curvature.

Similarly, for the other derivative we find

$$\frac{\partial}{\partial n} \left(\frac{e^{-j\beta r}}{r} \right) \cong -j\beta \frac{e^{-j\beta r}}{r} \cos(n, r) \quad (2.62)$$

with r much larger compared to the aperture size and wavelength, or $\beta = 2\pi/\lambda \gg 1/r$.

Placing (2.61) and (2.62) into (2.56) gives

$$E(P_2) = \frac{j}{2\lambda} \iint_{S_a} E_i(Q') \frac{e^{-j\beta r}}{r} [\cos(n, \rho) - \cos(n, r)] dS' \quad (2.63)$$

or

$$E(P_2) = \frac{j}{2\lambda} A_1 \iint_{S_a} \frac{e^{-j\beta(\rho+r)}}{\rho r} [\cos(n, \rho) - \cos(n, r)] dS' \quad (2.64)$$

In Figure 2.13, ϑ' is the angle between the normal unit vector $\hat{\mathbf{n}}$ and radial unit vector $\hat{\boldsymbol{\rho}}$. The above equations are known as Kirchhoff's diffraction integrals.

If we put $\cos(n, r) = \cos(\pi - \vartheta) = -\cos \vartheta$, $\cos(n, \rho) = \cos \vartheta'$ and

$$I(\vartheta, \vartheta') = \frac{1}{2}(\cos \vartheta' + \cos \vartheta) \quad (2.65)$$

(2.63) and (2.64) can be rewritten as follows

$$E(P_2) = \frac{j}{\lambda} \iint_{S_o} E_i(Q') \frac{e^{-j\beta r}}{r} I(\vartheta, \vartheta') dS' \quad (2.66)$$

and

$$E(P_2) = \frac{j}{\lambda} A_1 \iint_{S_o} \frac{e^{-j\beta(\rho+r)}}{r\rho} I(\vartheta, \vartheta') dS' \quad (2.67)$$

If we choose the integration surface to be a sphere with a radius $\rho = \rho_o$, we come to the special case studied by Fresnel in introducing his zone-construction mechanism of wave propagation (see Section 2.2.1). In this case $\vartheta' = 0$, $\cos \vartheta' = 1$, and then (2.64) becomes

$$E(P_2) = \frac{j}{\lambda} A_1 \iint_{S_o} \frac{e^{-j\beta(\rho_o+r)}}{\rho_o r} F_h(\vartheta) dS' \quad (2.68)$$

where

$$F_h(\vartheta) = I(\vartheta, \vartheta' = 0) = \frac{1}{2}(1 + \cos \vartheta) \quad (2.69)$$

Now the inclination factor $I(\vartheta, \vartheta' = 0)$ is a cardioid function equal to the radiation pattern $f_h(\vartheta)$ of the so-called Huygens' source (2A.14). For the first Fresnel zone center $\vartheta = 0$ we get $(f_h \vartheta) = 1$, which is in agreement with the amplitude assumption of Fresnel, but for $\vartheta = \pi/2$, $f_h(\vartheta)$ is not equal to zero as Fresnel supposed.

If Q' is a far-field point of the primary source at P_1 , the incident wave $E_i(Q')$ is treated as a quasi-plane wave, at least within the aperture S_o . Thus,

in this special case the spherical surface is viewed as a quasi-plane surface with an aperture in it. Now, $\cos \vartheta'$ is again equal to 1 and thus (2.68) and (2.69) are also approximately valid for the quasi-plane aperture case. Kirchhoff's analysis can easily be extended to waves with a more general shape of wave front.

As it was supposed, the Kirchhoff diffraction solution cannot be expected to be accurate at distances from the aperture that are larger than the wavelength. The solution does not reproduce the approximate fields given by (2.58) and (2.59) or the real fields in the immediate neighborhood of screens and obstacles. In these cases, more exact analytical and numerical boundary-value methods have to be employed.

2.3.2 Diffraction by Aperture in Infinite Plane Screen

Let us apply the Fresnel-Kirchhoff diffraction integral (2.64) to the special case of the infinite plane screen with an arbitrarily shaped aperture (Figure 2.14).

When the distances d_1 and d_2 from $P_1(x_1, y_1, z = d_1)$ and $P_2(x_2, y_2, z_2 = d_2)$ to the aperture are much larger than its maximum size, the inclination factor $I(\vartheta, \vartheta' = 0^\circ)$ varies a little over the aperture, and we may take it out in front of the integral. Also, if points P_1 and P_2 are not far from the z -axis, we may treat them on an equal footing with Q' and expand ρ and r around d_1 and d_2 , accordingly.

Let us first expand ρ around d_1 . From the geometry in Figure 2.14 we write

$$\rho = \sqrt{d_1^2 + (x_1 - x')^2 + (y_1 - y')^2} = d_1 \sqrt{1 + \frac{(x_1 - x')^2}{d_1^2} + \frac{(y_1 - y')^2}{d_1^2}} \quad (2.70)$$

Here x' and y' are the coordinates of secondary source point Q' .

From the above assumptions it follows that $(x_1 - x')^2/d_1^2 \ll 1$, $(y_1 - y')^2/d_1^2 \ll 1$, and therefore, applying the binomial approximation $\sqrt{1 + x} \cong 1 + 0.5x$ when $x \ll 1$ to (2.70) we find that

$$\rho \cong d_1 + \frac{(x_1 - x')^2}{2d_1} + \frac{(y_1 - y')^2}{2d_1} \quad (2.71)$$

In a like manner we expand r around d_2

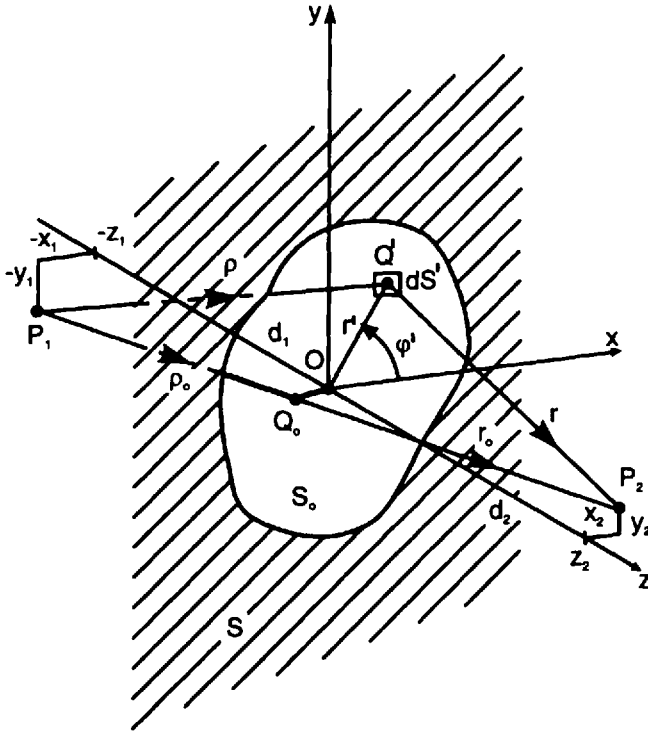


Figure 2.14 Fresnel diffraction by aperture in plane infinite screen.

$$r \cong d_2 + \frac{(x_2 - x')^2}{2d_2} + \frac{(y_2 - y')^2}{2d_2} \quad (2.72)$$

Then we find the wave path from P_1 through Q' to P_2 as

$$\rho + r \cong d_1 + d_2 + \frac{(x_1 - x')^2}{2d_1} + \frac{(x_1 - x')^2}{2d_2} + \frac{(y_1 - y')^2}{2d_1} + \frac{(y_2 - y')^2}{2d_2} \quad (2.73)$$

After some algebraic manipulations (2.73) is transformed to

$$\rho + r \cong P_1 P_2 + \frac{(x' - x_o)^2 + (y' - y_o)^2}{2F_e} \quad (2.74)$$

where

$$P_1 P_2 = d_1 + d_2 + \frac{(x_2 - x_1)^2 + (y_2 - y_1)^2}{2(d_1 + d_2)} \quad (2.75)$$

is an approximate expression for the distance between points P_1 and P_2 ,

$$F_e = \frac{1}{d_1} + \frac{1}{d_2} = \frac{d_1 d_2}{d_1 + d_2} \quad (2.76)$$

is the equivalent focal length and [2]

$$\begin{bmatrix} x_o \\ y_o \\ z_o \end{bmatrix} = \frac{1}{d_1 + d_2} \begin{bmatrix} d_1 x_2 + d_2 x_1 \\ d_1 y_2 + d_2 y_1 \\ 0 \end{bmatrix} \quad (2.77)$$

determines in matrix form the coordinates x_o and y_o of the aperture point $Q_o(x_o, y_o, 0)$. Note, that the points P_1 , Q_o , and P_2 are collinear.

Let us transform the Kirchhoff diffraction integral (2.67) into a form appropriate for solving real-world diffraction problems. For the conditions that are assumed in this section the inclination factor $I(\vartheta, \vartheta') = 0^\circ = F_h(\vartheta)$ is almost constant and (2.67) becomes

$$E(P_2) = \frac{j}{\lambda} A_1 F_h(\vartheta) \iint_{S_o} \frac{e^{-j\beta(r+\rho)}}{r\rho} dS' \quad (2.78)$$

The slowly varying amplitude factor $1/\rho r$ in (2.78) is replaced by $1/d_1 d_2$ and approximated as follows

$$\frac{1}{d_1 d_2} = \frac{1}{F_e(d_1 + d_2)} \cong \frac{1}{F_e(P_1 P_2)} \quad (2.79)$$

where

$$P_1 P_2 \cong d_1 + d_2 \quad (2.80)$$

The phase exponential in (2.78) is rapidly oscillating, and we shall replace $\rho + r$ by the approximation (2.81). Thus, the diffraction integral takes the form

$$E(P_2) = \frac{j}{\lambda F_e} E_o(P_2) F_h(\vartheta) \iint_{S_o} e^{-j\beta f(x', y')} dx' dy' \quad (2.81)$$

where [2, 8]

$$\begin{aligned} f(x', y') &= \frac{1}{2F_e} [(x' - x_o)^2 + (y' - y_o)^2] \\ &= -\frac{x_o}{F_e} x' - \frac{y_o}{F_e} y' + \frac{1}{2F_e} (x'^2 + y'^2) + \frac{1}{2F_e} (x_o^2 + y_o^2) \end{aligned} \quad (2.82)$$

is the exponential phase function, and

$$E_o(P_2) \cong A_1 \frac{e^{-j\beta(d_1+d_2)}}{d_1 + d_2} \quad (2.83)$$

is the field at P_2 of a free-space spherical wave radiated at P_1 and propagating along the straight path P_1P_2 .

In the phase equation (2.82) there are two types of terms: linear and quadratic. The quadratic terms characterize the spherical wave-front curvature. If we neglect them, (2.82) becomes

$$f(x', y') = px' + qy' \quad (2.84)$$

where $p = -x_o/F_e$ and $q = -y_o/F_e$.

In this special case, it is customary to speak of Fraunhofer or far-field diffraction. It occurs in practice when both the incident and diffracted waves are effectively plane (i.e., when the source point P_1 and the receiver point P_2 are both far enough from the diffraction aperture). If this condition is not valid, the quadratic terms predominate in (2.82) and we may speak of Fresnel diffraction.

When the points P_1 and P_2 lie on the z -axis $x_o = y_o = 0$, and then (2.82) becomes a pure quadratic equation, or

$$f(x', y') = \frac{1}{2F_e} (x'^2 + y'^2) \quad (2.85)$$

We may call this particular case of Fresnel diffraction a pure Fresnel diffraction. There is no sharp line of distinction between Fraunhofer and Fresnel regions. The division of space into two wave areas is only typical for the light diffraction theory. In radio antenna theory, the space surrounding the antenna is normally subdivided into three regions [12]:

1. Near or inductive field region: In this case, the distance d_2 from the diffraction (or antenna) aperture to a receiver point P_2 within the

region is commonly assumed to be less than $0.6\sqrt{L_{\max}^3/\lambda}$, where L_{\max} is the largest dimension of the aperture and λ is the wavelength. The most important feature of this space is that here the reactive electromagnetic energy predominates.

2. Radiation near-field (or Fresnel) region: The size of this space region is determined by the inequality $0.6\sqrt{L_{\max}^3/\lambda} \leq d_2 \leq 2L_{\max}^2/\lambda$. Here we find complex electromagnetic energy consisting of active and reactive components.
3. Far-field (or Fraunhofer) region: This is the so-called antenna far-field or radiation region for which each observation point is at a distance d_2 much larger than the wavelength and the aperture size, or $d_2 > 2L_{\max}^2/\lambda$.

2.3.3 Fraunhofer Diffraction by Circular Aperture

As mentioned in the former section, the Fraunhofer diffraction is the foundation of the approximate theory of the aperture antennas, and therefore, it is examined in detail in antenna textbooks. Here we will describe briefly only one specific case—the Fraunhofer diffraction by a circular aperture.

Placing $f(x', y')$ from (2.84) into the diffraction integral (2.81), we obtain

$$E(P_2) = \frac{j}{\lambda F_e} E_o(P_2) F_b(\vartheta) \iint_{S_o} e^{-j\beta(px' + qy')} dS' \quad (2.86)$$

Without loss of generality we suppose here that the aperture plane is normal to the line P_1Q , or $x_1 = y_1 = 0$. In accordance with Figure 2.15 the rectangular coordinates (x', y') of Q' can be replaced by aperture polar coordinates (r', φ') , and the exponent in the integrand of (2.86) becomes $j\beta r' \sin \vartheta \cos(\varphi - \varphi')$. Also, $dS' = dx' dy' = r' dr' d\varphi'$.

Now, the integral equation (2.86) for the far diffraction field can be presented in the form

$$\begin{aligned} E(P_2) &= \frac{j}{\lambda} F_b(\vartheta) E_o(P_2) \int_0^{a_o} r' dr' \int_0^{2\pi} e^{j\beta r' \sin \vartheta \cos(\varphi - \varphi')} d\varphi' \quad (2.87) \\ &= \frac{j}{\lambda} F_b(\vartheta) E_o(P_2) 2\pi \int_0^{a_o} J_o(\beta r' \sin \vartheta) r' dr' \end{aligned}$$

where a_o is the aperture radius.

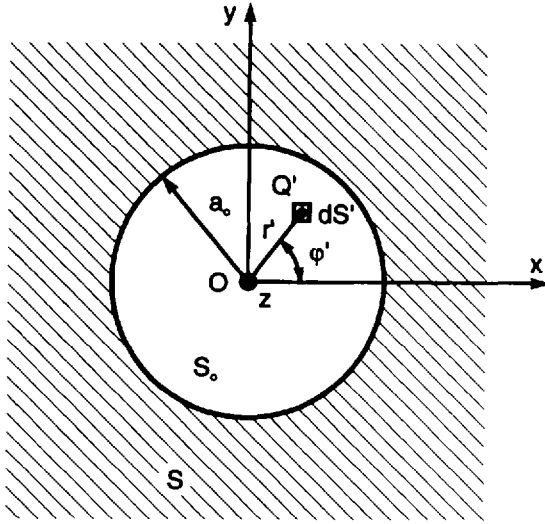


Figure 2.15 Circular aperture in infinite plane screen.

After integration with respect to r' and doing some replacements, it is found that

$$E(P_2) = \frac{j}{\lambda} E_i(\rho_o) \frac{e^{-j\beta r_o}}{r_o} S_o F(\vartheta) \quad (2.88)$$

where $f(\vartheta)$ denotes the total diffraction (or radiation) pattern of the circular aperture with a geometrical area $S_o = \pi a_o^2$, given by

$$F(\vartheta) = \frac{1 + \cos \vartheta}{2} \frac{2J_1(ba_o \sin \vartheta)}{ba_o \sin \vartheta} = F_h(\vartheta) F_a(\vartheta) \quad (2.89)$$

$E_i(\rho_o) = A_1 \frac{e^{-j\beta \rho_o}}{\rho_o} \approx \text{Const.} e^{-j\beta \rho_o}$ is an effective plane wave incident normally to the aperture.

$$F_h(\vartheta) = \frac{1}{2} (1 + \cos \vartheta) \quad (2.90)$$

is the elementary surface (or Huygens' source) radiation pattern, and

$$F_a(\vartheta) = \frac{2J_1(\beta a_o \sin \vartheta)}{\beta a_o \sin \vartheta} \quad (2.91)$$

is the aperture point array radiation pattern, which does not take into account the directive properties of the element dS' .

The integration in (2.87) was performed using the following equations

for the Bessel functions: $J_0(z) = \frac{1}{2\pi} \int_0^{2\pi} e^{jz\cos\varphi} d\varphi$ and $2J_1(z) = \int_0^z J_0(z) dz$. Here

$J_0(z)$ and $J_1(z)$ are the Bessel functions of zero and first order, respectively.

The diffraction case considered here corresponds to the far-field study of a circular aperture antenna with a constant amplitude-phase distribution. The far-field diffraction (or radiation) patterns $|F_h(\vartheta)|$, $|F_a(\vartheta)|$ and $|F(\vartheta)|$ are plotted for $2a_0/\lambda = 3$ in Figure 2.16, with dashed, thick solid, and thin solid lines, respectively.

2.4 Fresnel Diffraction

At this point, we introduce dimensionless variables in the diffraction integrals, which depend on the wavelength and positions of the source point P_1 , observation point P_2 , and aperture point Q' . Then, expressions of the Fresnel diffraction factors for different rectangular and circular apertures are worked out.

The Fresnel diffraction field of a screen structure and its complementary aperture diffraction field are related by the Babinet's principle. This relation is demonstrated by comparative calculations and plots for diffraction factors of particular apertures with circular symmetry and their complementary screens.

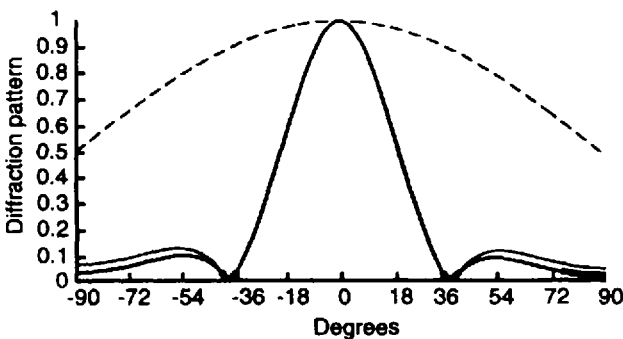


Figure 2.16 Far-field diffraction (radiation) patterns versus observation angle for $2a_0/\lambda = 3.0$: (a) elementary (Huygens') source pattern (dashed line), (b) aperture point array pattern (thin solid line), and (c) total pattern (thick solid line).

2.4.1 Dimensionless Variables

The coordinates x' and y' can be expressed in the scale of the first Fresnel zone radius $b_1 = \sqrt{\lambda F_e}$ as follows

$$x' = \sqrt{n_x \frac{\lambda d_1 d_2}{d_1 + d_2}} = \sqrt{n_x} b_1 \quad (2.92)$$

$$y' = \sqrt{n_y \frac{\lambda d_1 d_2}{d_1 + d_2}} = \sqrt{n_y} b_1 \quad (2.93)$$

where n_x and n_y are the Fresnel zone numbers fit along x' and y' , respectively. Next, we introduce dimensionless variables u and v defined as [2]

$$\begin{bmatrix} u \\ v \end{bmatrix} = \sqrt{\frac{2}{\lambda F_e}} \begin{bmatrix} x' - x_o \\ y' - y_o \end{bmatrix} = \begin{bmatrix} \sqrt{2n_x} - \frac{b_1 d_1 x_2 + d_2 x_1}{d_1 d_2} \\ \sqrt{2n_y} - \frac{b_1 d_1 y_2 + d_2 y_1}{d_1 d_2} \end{bmatrix} \quad (2.94)$$

If the source and observation points are on the aperture axis z , or if $x_1 = x_2 = 0$ and $y_1 = y_2 = 0$, then $x_o = y_o = 0$, and (2.94) is simplified to

$$\begin{bmatrix} u \\ v \end{bmatrix} = \sqrt{\frac{2}{\lambda f_e}} \begin{bmatrix} x' \\ y' \end{bmatrix} = \begin{bmatrix} \sqrt{2n_x} \\ \sqrt{2n_y} \end{bmatrix} \quad (2.95)$$

With these new variables the aperture $S_o(x', y')$ is transformed into a domain $A_o(u, v)$, and (2.81) becomes [2]

$$E(P_2) = \frac{j}{2} E_o(P_2) \iint_{A_o} e^{-j\frac{\pi}{2}(u^2 + v^2)} dudv \quad (2.96)$$

where for the time being $F_b(\vartheta)$ is neglected.

Equation (2.96) can be written also in the form

$$E(P_2) = E_o(P_2) F_d(u, v) \quad (2.97)$$

where

$$F_d(u, v) = \frac{j}{2} \iint_{A_o} e^{-j\frac{\pi}{2}(u^2 + v^2)} dudv \quad (2.98)$$

is called the Fresnel diffraction factor. It determines the change in free-space wave intensity, $E_o(P_2)$, due to the diffraction phenomenon.

2.4.2 Diffraction by Rectangular Aperture

Figure 2.17 shows a rectangular aperture in the xy -plane, which is cut in an infinite screen S . The aperture limits are determined as follows

$$w_1 \leq x' \leq w_2 \text{ and } h_1 \leq y' \leq h_2 \quad (2.99)$$

The corresponding dimensionless limits are found from (2.94)

$$\begin{bmatrix} u_1 \\ v_1 \end{bmatrix} = \sqrt{\frac{2}{\lambda F_e}} \begin{bmatrix} w_1 - x_o \\ h_1 - x_o \end{bmatrix} \text{ and } \begin{bmatrix} u_2 \\ v_2 \end{bmatrix} = \sqrt{\frac{2}{\lambda F_e}} \begin{bmatrix} w_2 - x_o \\ h_2 - x_o \end{bmatrix} \quad (2.100)$$

Here u and v integrations are mutually independent and the surface integral (2.98) becomes a product of two separate linear integrals [2, 8]

$$F_d(u, v) = \frac{j}{2} \int_{u_1}^{u_2} e^{-j\frac{\pi}{2}u^2} du \int_{v_1}^{v_2} e^{-j\frac{\pi}{2}v^2} dv = F_d(u)F_d(v) \quad (2.101)$$

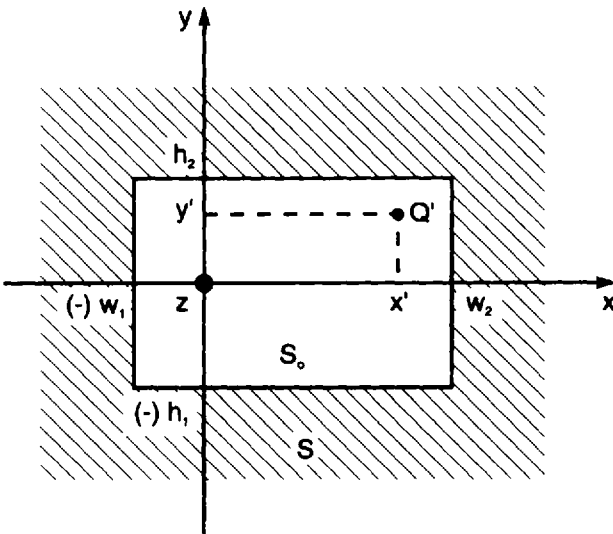


Figure 2.17 Rectangular diffraction aperture in infinite plane screen.

where $F_d(u, v)$ is the total Fresnel diffraction factor that is a product of the partial diffraction factors $F_d(u)$ and $F_d(v)$

$$F_d(u) = \sqrt{\frac{j}{2}} \int_{u_1}^{u_2} e^{-j\frac{\pi}{2}u^2} du \quad (2.102)$$

$$F_d(v) = \sqrt{\frac{j}{2}} \int_{v_1}^{v_2} e^{-j\frac{\pi}{2}v^2} dv \quad (2.103)$$

With (2.102) and (2.103) in mind, (2.97) for the diffracted field at point P_2 becomes

$$E(P_2) = E_o(P_2)F_d(u)F_d(v) \quad (2.104)$$

2.4.3 Fresnel Cosine and Sine Integrals

The Fresnel diffraction factors can be more easily analyzed and calculated by introducing the Fresnel cosine and sine integrals. The integrals in (2.102) and (2.103) can be expressed in the form

$$\begin{aligned} \int_{u_1}^{u_2} e^{-j\frac{\pi}{2}u^2} du &= \int_0^{u_2} e^{-j\frac{\pi}{2}u^2} du - \int_0^{u_1} e^{-j\frac{\pi}{2}u^2} du \\ &= \left[\int_0^{u_2} \cos\left(\frac{\pi}{2}u^2\right) du - j \int_0^{u_2} \sin\left(\frac{\pi}{2}u^2\right) du \right] \\ &\quad - \left[\int_0^{u_1} \cos\left(\frac{\pi}{2}u^2\right) du - j \int_0^{u_1} \sin\left(\frac{\pi}{2}u^2\right) du \right] \\ &= [C(u_2) - jS(u_2)] - [C(u_1) - jS(u_1)] \end{aligned} \quad (2.105)$$

and

$$\begin{aligned}
\int_{v_1}^{v_2} e^{-j\frac{\pi}{2}v^2} dv &= \int_0^{v_2} e^{-j\frac{\pi}{2}v^2} dv - \int_0^{v_1} e^{-j\frac{\pi}{2}v^2} dv \\
&= \left[\int_0^{v_2} \cos\left(\frac{\pi}{2}v^2\right) dv - j \int_0^{v_2} \sin\left(\frac{\pi}{2}v^2\right) dv \right] \\
&\quad - \left[\int_0^{v_1} \cos\left(\frac{\pi}{2}v^2\right) dv - j \int_0^{v_1} \sin\left(\frac{\pi}{2}v^2\right) dv \right] \\
&= [C(v_2) - jS(v_2)] - [C(v_1) - jS(v_1)]
\end{aligned} \tag{2.106}$$

where, for convenience, the Fresnel cosine and sine integrals [13], $C(\tau)$ and $S(\tau)$, correspondingly, are used as follows

$$C(\tau_i) = \int_0^{\tau_i} \cos\left(\frac{\pi}{2}\tau^2\right) d\tau \tag{2.107}$$

$$S(\tau_i) = \int_0^{\tau_i} \sin\left(\frac{\pi}{2}\tau^2\right) d\tau \tag{2.108}$$

with $\tau = \begin{bmatrix} u \\ v \end{bmatrix}$ and $\tau_i = \begin{bmatrix} u_i \\ v_i \end{bmatrix}$, for $i = 1$ or 2 .

Let us list some important relations for the Fresnel integrals: $C(\tau) = -C(\tau)$, $S(\tau) = -S(\tau)$, $C(j\tau) = -jC(\tau)$, $S(j\tau) = -jS(\tau)$, $C(+\infty) = S(+\infty) = 0.5$, $C(-\infty) = S(-\infty) = -0.5$, $C(0) = S(0) = 0$.

The Fresnel integrals $C(\tau)$ and $S(\tau)$ are plotted in Figure 2.18, and their behavior can be illustrated also by means of the so-called Cornu spiral (Figure 2.19) where $S(\tau)$ is drawn versus $C(\tau)$ in a complex coordinate plane. The variable τ is equal to the spiral length and is marked over the curve. The spiral coils from point $-0.5 - j0.5$ (for $\tau = -\infty$) to point $0.5 + j0.5$ (for $\tau = +\infty$).

By use of the Fresnel cosine and sine integrals the diffraction factors for the rectangular aperture (2.102) and (2.103) become

$$F_d(u) = \sqrt{\frac{j}{2}} \{ [C(u_2) - C(u_1)] - j[S(u_2) - S(u_1)] \} \tag{2.109}$$

and

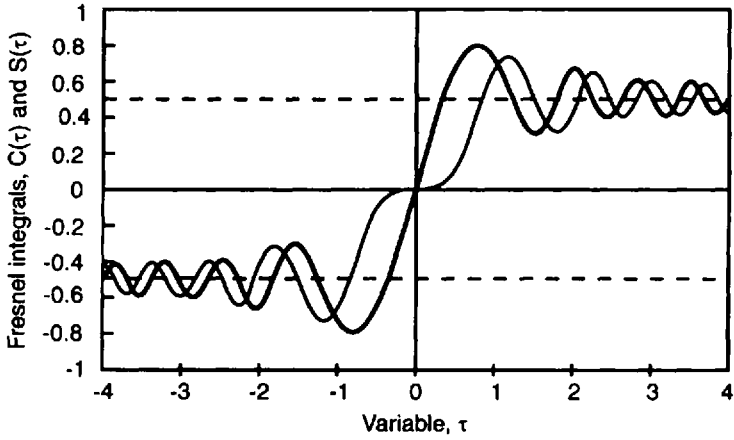


Figure 2.18 Plots of Fresnel integrals: $C(\tau)$ represents the cosine Fresnel integral (thick solid line) and $S(\tau)$ represents the sine Fresnel integral (thick solid line).

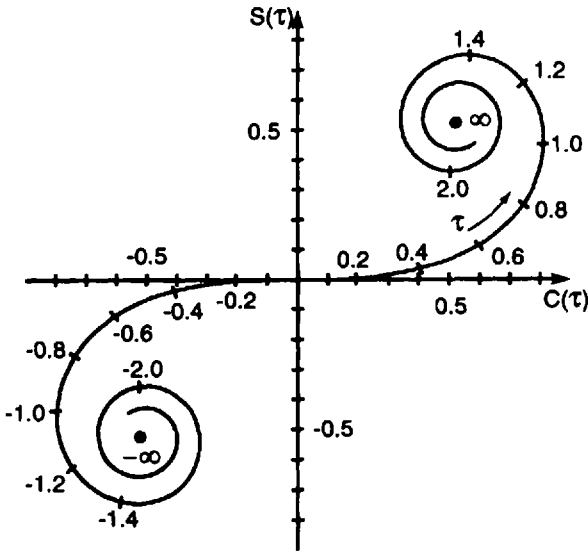


Figure 2.19 Plot of $S(\tau)$ versus $C(\tau)$, or Cornu spiral.

$$F_d(v) = \sqrt{\frac{j}{2}} \{ [C(v_2) - C(v_1)] - j[S(v_2) - S(v_1)] \} \quad (2.110)$$

2.4.4 Particular Cases of Diffraction by Rectangular Aperture

Here the diffraction theory of rectangular aperture, worked out in Section 2.4.2, is utilized for studying Fresnel diffraction by some particular aperture

configurations: rectangular aperture of infinite size, semi-infinite screen, and infinite slit.

2.4.4.1 Diffraction by Rectangular Aperture With Infinite Dimensions

Using Fresnel cosine and sine integrals the field strength in case of Fresnel diffraction by a rectangular aperture can be obtained by

$$E(P_2) = \frac{j}{2} E_o(P_2) \{ [C(u_2) - C(u_1)] - j[S(u_2) - S(u_1)] \} \quad (2.111)$$

$$\{ [C(v_2) - C(v_1)] - j[S(v_2) - S(v_1)] \}$$

Consider a rectangular aperture with infinite dimensions, or $w_1 = b_1 = -\infty$ and $w_2 = b_2 = +\infty$. In this specific case, there is no obstruction to the incident wave, or this is a free-space propagation. The limits of the aperture in the uv domain are $u_1 = v_1 = -\infty$ and $u_2 = v_2 = +\infty$. Therefore, in case of an infinite-in-size rectangular aperture the field at the observation point P_2 is easily calculated from (2.111)

$$E(P_2) = \frac{j}{2} E_o(P_2) \{ [C(+\infty) - C(-\infty)] - j[S(+\infty) - S(-\infty)] \}^2 = E_o(P_2) \quad (2.112)$$

This result confirms the free-space propagation effect for an infinite rectangular aperture and proves the right choice of the constant j/λ .

2.4.4.2 Diffraction by Straight Edge of Semi-infinite Screen

Using Figure 2.17, the semi-infinite screen can be defined: (1) along the x -axis the screen is infinite in size, so $-\infty \leq x' \leq +\infty$, and (2) along the y -axis the illuminated region runs from $y' = b_1$ to $y' = \infty$, or the inequality $b_1 \leq y' \leq +\infty$ is taking place.

Thus, for the corresponding dimensionless variables it is written: $-\infty \leq u \leq +\infty$ and $v_1 \leq v \leq +\infty$, where $v_1 = \sqrt{2/\lambda} F_c(b_1 - y_o)$, and in the present case the field at the observation point P_2 is found

$$E(P_2) = \frac{j}{2} E_o(P_2) \int_{-\infty}^{+\infty} e^{-j\frac{\pi}{2}u^2} du \int_{v_1}^{+\infty} e^{-j\frac{\pi}{2}v^2} dv \quad (2.113)$$

$$= \frac{j}{2} (1 - j) E_o(P_2) \left(\int_0^{+\infty} e^{-j\frac{\pi}{2}v^2} dv - \int_0^{v_1} e^{-j\frac{\pi}{2}v^2} dv \right)$$

or

$$\begin{aligned}
 E(P_2) &= \frac{j}{2}(1-j)\{[C(+\infty) - jS(+\infty)] - [C(v_1) - jS(v_1)]\}E_o(P_2) \quad (2.114) \\
 &= \frac{1}{2}(1+j)\left\{\left[\frac{1}{2} - C(v_1)\right] - j\left[\frac{1}{2} - S(v_1)\right]\right\}E_o(P_2)
 \end{aligned}$$

The Fresnel diffraction by a straight infinite edge based on Kirchhoff's scalar approximation is illustrated in Figure 2.20 where the Fresnel diffraction factor $F(v) \equiv |F_d(v)| = |E(P_2)/E_o(P_2)|$ versus v is plotted for $y_o = 0$ in the equation $v = \sqrt{2/\lambda F_e}(b_1 - y_o)$. Two different regions can be specified in this chart: (1) shadow region ($v > 0$) and (2) illuminated region ($v < 0$).

In the shadow region, the diffraction factor $F(v)$ decreases monotonously from a value of 0.5 at the edge ($v = 0$) toward zero when $v \rightarrow +\infty$. In the illuminated region, however, it oscillates and tends to one when $v \rightarrow -\infty$.

It is seen also that the maximum value of $F(v)$ is not at the edge of the geometrical shadow but in the illuminated region, slightly away from the edge. For some heights of the screen edge the diffracted field $E(P_2)$ was found to be bigger or lesser than the free-space field $E_o(P_2)$. This means that depending

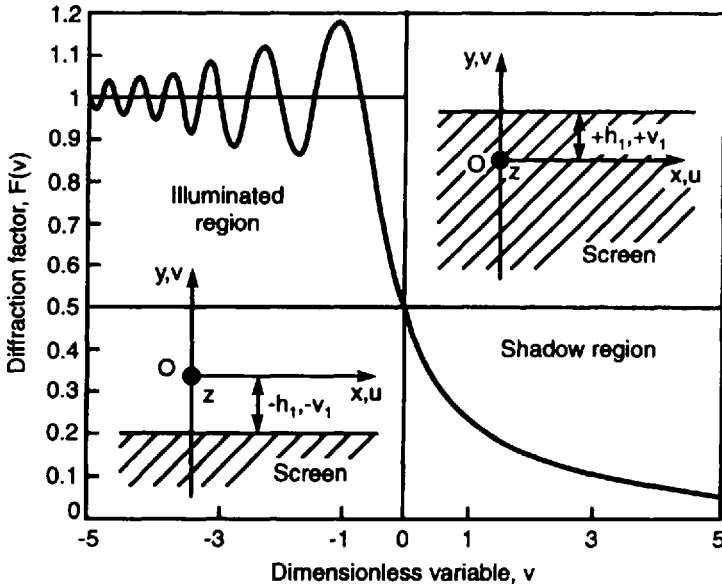


Figure 2.20 Diffraction factor of semi-infinite screen.

on the edge height the semi-infinite screen is acting as a passive field “amplifier” or “attenuator.”

2.4.4.3 Diffraction by Slit

Using Figure 2.17, an infinite slit cut along the x -axis, for instance, can be intersecting, with $-\infty \leq x' \leq +\infty$ (or $-\infty \leq u \leq +\infty$) and $h_1 \leq y' \leq h_2$ (or $v_1 \leq v \leq v_2$), where $v_1 = \sqrt{2/\lambda F_e}(h_1 - y_o)$ and $v_2 = \sqrt{2/\lambda F_e}(h_2 - y_o)$.

In this limiting case the Fresnel diffraction factor becomes

$$F_d(u, v) = \frac{j}{2} \int_{-\infty}^{+\infty} e^{-j\frac{\pi}{2}u^2} du \int_{v_1}^{v_2} e^{-j\frac{\pi}{2}v^2} dv \quad (2.115)$$

$$= \frac{j}{2}(1 - j) \left(\int_0^{v_2} e^{-j\frac{\pi}{2}v^2} dv - \int_0^{v_1} e^{-j\frac{\pi}{2}v^2} dv \right)$$

or

$$F_d(u, v) = \frac{j}{2}(1 - j) \{ [C(v_2) - jS(v_2)] - [C(v_1) - jS(v_1)] \} \quad (2.116)$$

$$= \frac{1}{2}(1 + j) \{ [C(v_2) - C(v_1)] - j[S(v_2) - S(v_1)] \}$$

Depending on the dimensionless slit width $\delta v = v_2 - v_1$ the following two particular types of slits are commonly examined: (1) the narrow slit, when $\delta v \cong 1$ and (2) the wide slit, when $\delta v \gg 1$. These two cases are illustrated in Figure 2.21 wherein the Fresnel diffraction pattern $|F_d(v)|$ for $\delta v = 1$ (thick line) and $\delta v = 10$ (thin line), respectively, is plotted. As it is seen, the appearance of the diffraction pattern is quite sensitive to the slit width. The limiting case $\delta v \rightarrow 0$ corresponds to the Fraunhofer (far-field) diffraction.

2.4.5 Fresnel Diffraction by Apertures of Circular Symmetry

In Figure 2.14 let the source point P_1 lie on the z -axis, or $x_1 = y_1 = 0$ and the diffraction aperture S_o is of circular shape (Figure 2.22). The Fresnel diffraction field equation (2.81) at point P_2 may be written now in the form

$$E(P_2) = \frac{j}{\lambda F_e} E_o(P_2) \iint_{S_o} e^{-j\beta f(r', \varphi')} r' dr' d\varphi' \quad (2.117)$$

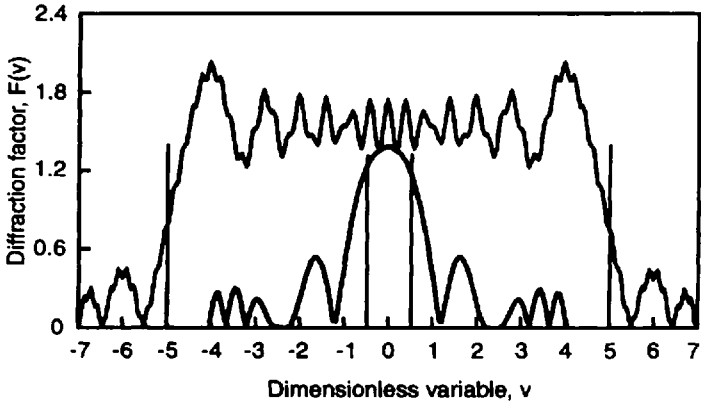


Figure 2.21 Fresnel diffraction patterns of infinite slits: (a) narrow slit with $\delta v = 1$ (thick line) and (b) wide slit with $\delta v = 10$ (thin line).

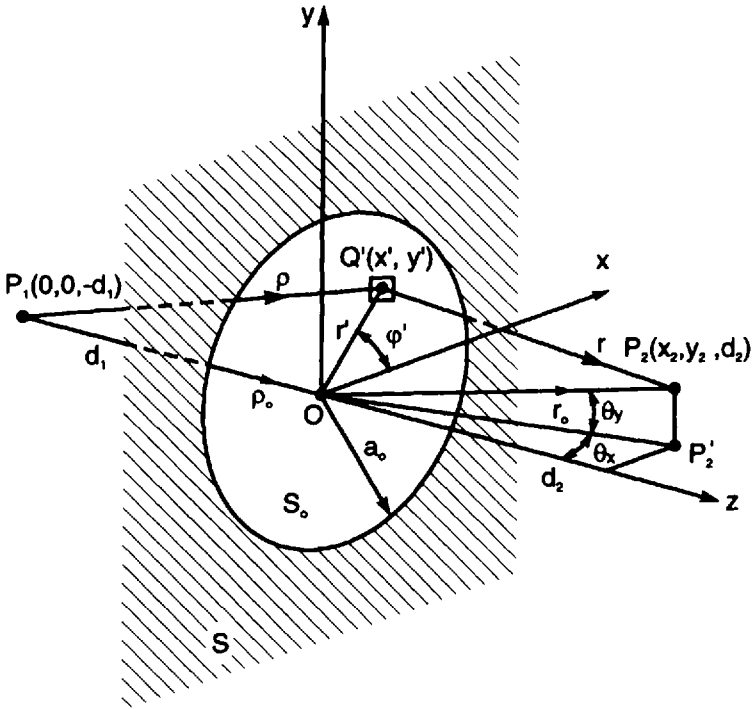


Figure 2.22 Geometry for Fresnel diffraction by circular aperture in infinite screen (or absorber), with the source point located on the z -axis and the observation point in the $z = d_2$ plane.

where the rectangular coordinates (x', y') are replaced by polar coordinates (r', φ') using the relationships: $x' = r' \cos \varphi'$ and $y' = r' \sin \varphi'$. Also, it is assumed that the observation point P_2 is not far from the z -axis and that $F_h(\vartheta) \cong 1$.

The phase function $f(r', \varphi')$ may be found starting from (2.82) wherein the second order x_0 and y_0 terms are neglected

$$f(r', \varphi') \cong \frac{r'^2}{2F_c} - \frac{x_2}{d_2} r' \cos \varphi' - \frac{y_2}{d_2} r' \sin \varphi' \quad (2.118)$$

Introduce a dimensionless radius χ related to r' by

$$r' = \sqrt{\frac{\lambda F_c}{2}} \chi \quad (2.119)$$

Then $r' dr' d\varphi'$ becomes $0.5 b_1^2 \chi d\chi d\varphi'$ and $\beta f(r', \varphi')$ is transformed to

$$\beta f(\chi, \varphi') \cong \frac{\pi}{2} \chi^2 - k_x \chi \cos \varphi' - k_y \chi \sin \varphi' \quad (2.120)$$

where

$$k_x = \frac{2\pi}{\lambda} \frac{b_1}{\sqrt{2}} \frac{x_2}{d_2} = \frac{2\pi}{\lambda} \frac{b_1}{\sqrt{2}} \tan \vartheta_x \quad (2.121)$$

and

$$k_y = \frac{2\pi}{\lambda} \frac{b_1}{\sqrt{2}} \frac{y_2}{\sqrt{d_2^2 + x_2^2}} = \frac{2\pi}{\lambda} \frac{b_1}{\sqrt{2}} \tan \vartheta_y \quad (2.122)$$

In the above equations we set $\vartheta_x = \arctan(x_2/d_2)$ and $\vartheta_y = \arctan(x_2/d_2)$, as shown in Figure 2.22. Now, the diffraction equation (2.117) takes the form

$$E(P_2) = \frac{j}{2} E_0(P_2) \int_0^{2\pi} \int_0^{\chi_0} e^{-j\left(\frac{\pi}{2}\chi^2 - k_x \chi \cos \varphi' - k_y \chi \sin \varphi'\right)} \chi d\chi d\varphi' \quad (2.123)$$

where

$$\chi_o = \sqrt{2} \frac{a_o}{b_1} = \sqrt{\frac{2}{\lambda F_e}} a_o \quad (2.124)$$

Suppose that point P_2 lies in the xz plane (or $y_2 = 0$), put $k_x = k$ and complete the φ' integration

$$\int_0^{2\pi} e^{jk_x \chi \cos \varphi'} d\varphi' = 2\pi J_o(k_x \chi) \quad (2.125)$$

and (2.123) takes the form

$$E(P_2) = E_o(P_2) F_d(k, \chi_o) \quad (2.126)$$

where

$$F_d(k, \chi_o) = j\pi \int_0^{\chi_o} e^{-j\frac{\pi}{2}\chi^2} J_o(k\chi) \chi d\chi = \frac{j}{2} [C(k, \chi_o) - jS(k, \chi_o)] \quad (2.127)$$

with

$$C(k, \chi_o) = 2\pi \int_0^{\chi_o} \cos\left(\frac{\pi}{2}\chi^2\right) J_o(k\chi) \chi d\chi \quad (2.128)$$

and

$$S(k, \chi_o) = 2\pi \int_0^{\chi_o} \sin\left(\frac{\pi}{2}\chi^2\right) J_o(k\chi) \chi d\chi \quad (2.129)$$

Here $C(k, \chi_o)$ and $S(k, \chi_o)$ may be considered as more general cosine and sine Fresnel integrals.

For the particular case of $x_2 = y_2 = 0$ the observation point P_2 is placed on the z -axis, and because $k = 0$, $J_o(k\chi) = 1$, and (2.127) becomes

$$F_d(\chi_o) = j\pi \int_0^{\chi_o} e^{-j\frac{\pi}{2}\chi^2} \chi d\chi \quad (2.130)$$

or [2]

$$F_d(\Phi) = j \int_0^{\Phi_0} e^{-j\Phi} d\Phi \quad (2.131)$$

where $\Phi = (\pi/2)\chi^2$, $d\Phi = \pi\chi d\chi$, $\Phi_0 = (\pi/2)\chi_0^2 = a_0^2(\pi/\lambda)F_e$.

In the limiting case of diffraction by infinite circular aperture $a_0 = \infty$ and $\Phi_0 = \infty$, and as expected, $F_d(\Phi) = j \int_0^{\infty} e^{-j\Phi} d\Phi = 1$ and $E(P_2) = E_0(P_2)$.

Figure 2.23 illustrates the Fresnel diffraction pattern $|F_d(\vartheta)|$ of a circular aperture calculated according to (2.127) at the xz plane. It is drawn versus the observation angle, $\vartheta = \vartheta_x = \arctan(x_2/d_2)$, in degrees, for an aperture radius a_0 equal to: (1) the first Fresnel zone radius $b_1 = 7.07\lambda$ (solid line), (2) the second Fresnel zone radius b_2 (dashed line), and (3) the third Fresnel zone radius b_3 (dotted line). For $\vartheta = 0$, the diffraction graph confirms the results obtained by the Fresnel zone construction (see Section 2.2.2). Here the focal distances d_1 and d_2 are chosen equal to 100λ .

Figure 2.24 helps us to compare the Fresnel zone diffraction pattern $|F_d(\vartheta)|$ of a circular aperture calculated from (2.127) (dashed line), for

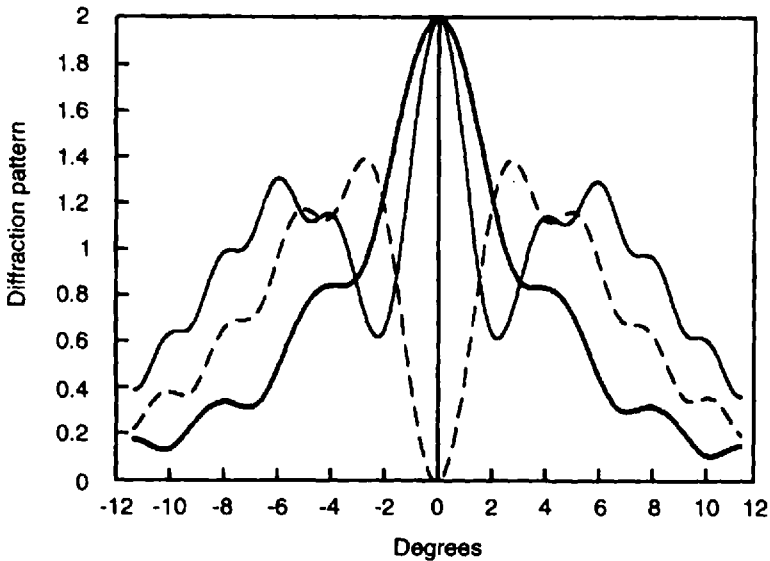


Figure 2.23 Fresnel diffraction pattern by circular aperture versus observation angle for $a_0 = b_1$ (solid line), $a_0 = b_2$ (dashed line), and $a_0 = b_3$ (dotted line).

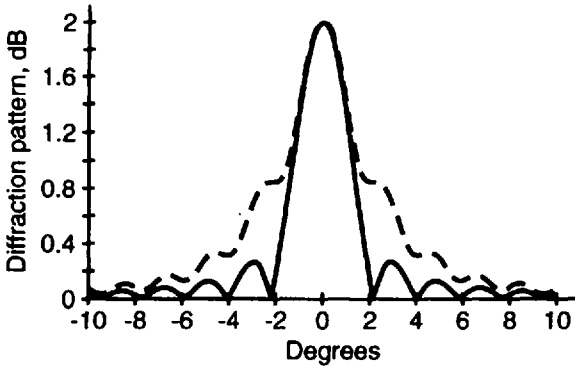


Figure 2.24 Comparison of radiation patterns of circular aperture for the Fresnel diffraction ($a_o = b_1 = 15.8\lambda$ and $d_1 = d_2 = 500\lambda$, dashed line) and the Fraunhofer diffraction ($a_o = b_1 = 15.8\lambda$ and $d_1 = d_2 \rightarrow \infty$, solid line).

$a_o = b_1 = 15.8\lambda$, $d_1 = d_2 = 500\lambda$, and the far-field (or Fraunhofer) diffraction pattern (solid line). The latter is calculated from (2.91) for the same size aperture and scaled to reach a maximum of 2 as in the Fresnel diffraction pattern. Note that the aperture dimensionless radius χ_o is equal to $\sqrt{2}$ and $k_y = 2\pi b_1 \tan \vartheta / \sqrt{2}\lambda$.

From Figure 2.24 it is easily concluded that the far-field diffraction pattern has clearly outlined main lobe and side lobes while the Fresnel region diffraction pattern is a continuous function, without distinctly defined pattern lobes.

Using the above analysis for circular aperture it is not difficult to find the diffraction field produced by an annular slot of inner radius a_1 and outer radius a_2 , Figure 2.10(b). Equation (2.127) for the Fresnel diffraction factor can be applied here in the form

$$\begin{aligned}
 F_d &= j\pi \int_{\chi_1}^{\chi_2} e^{-j\frac{\pi}{2}\chi^2} J_0(k\chi) \chi d\chi & (2.132) \\
 &= \frac{j}{2} \{ [C(k, \chi_2) - C(k, \chi_1)] - j[S(k, \chi_2) - S(k, \chi_1)] \}
 \end{aligned}$$

where $\chi_1 = \sqrt{2} \frac{a_1}{b_1}$ and $\chi_2 = \sqrt{2} \frac{a_2}{b_1}$.

2.4.6 Fresnel Diffraction by Obstacles

A complementary diffraction screen is obtained by replacing the aperture S_o by an obstacle replica S'_o and vice versa. Simple examples of complementary screens are the circular aperture in infinite screen and the same size opaque disk in free space.

According to Babinet's principle [14], formulated for scalar optical fields, the sum of the fields diffracted by the complementary screens is equal to the incident wave field in the absence of screens.

Using our notations let us express the Babinet's principle for scalar electromagnetic components at the observation point P_2 as follows

$$E_o^{(a)}(P_2) F_d^{(a)}(P_2) + E_o^{(o)}(P_2) F_d^{(o)}(P_2) = E_o(P_2) \quad (2.133)$$

where $E_o^{(a)}(P_2) F_d^{(a)}(P_2)$ is the field diffracted by the aperture S_o , $E_o^{(o)}(P_2)$ is the field diffracted by the obstacle S'_o complementary to the aperture, and $E_o(P_2)$ is the incident wave field. Here the superscripts (a) and (o) stand for aperture and obstacle, correspondingly.

After eliminating $E_o(P_2)$ in (2.133) the diffraction factor $F_d^{(o)}(P_2)$ of the complementary obstacle is found by

$$F_d^{(o)}(P_2) = 1 - F_d^{(a)}(P_2) \quad (2.134)$$

where $F_d^{(a)}(P_2)$ is the diffraction factor of the aperture.

Let us illustrate the behavior of the fields diffracted by a circular aperture and its complementary disk. In Figure 2.25 the diffraction pattern $|F_d^{(a)}(\chi)|$ of a circular aperture (curve 1) is compared to the diffraction pattern $|F_d^{(o)}(\chi)| = |1 - F_d^{(a)}(\chi)|$ of a disk, complementary to the aperture (curve 2). They are drawn versus the dimensionless quantity $\chi = \sqrt{2}(a_o/b_1)$. Curve 1 oscillates in a typical Fresnel zone-type manner with maxima at $a_o = b_1, b_3, b_5, \dots$ around unity, or normalized free-space amplitude (for odd Fresnel zone radii), and with minima at $a_o = b_2, b_4, b_6, \dots$ (for even Fresnel zone radii). Curve 2 illustrates the shadowing effect of the disk obstacle with increase of its radius, for $\lambda = \text{const.}$ and $F_e = \text{const.}$

Figure 2.26 shows the diffraction patterns of a circular aperture (thick line) and its complementary disk (thin line) at the focal plane $z_2 = d_2$ as a function of x_2 , or the corresponding angle $\vartheta = \arctan(x_2/d_2)$, in degrees, calculated for $a_o = b_1 = 15.8\lambda$ and $d_1 = d_2 = 100\lambda$. As was expected, for $\vartheta = 0$ degrees the diffraction pattern of circular aperture has a value of two, and the disk pattern is equal to the free-space value of one. The latter value

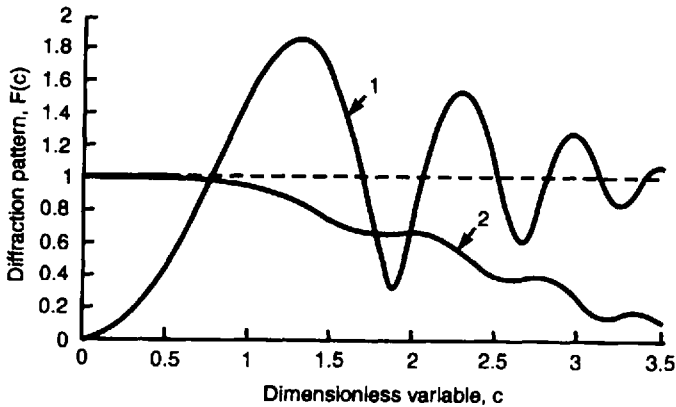


Figure 2.25 Diffraction patterns of circular aperture (curve 1) and complementary disk (curve 2) drawn versus dimensionless quantity χ .

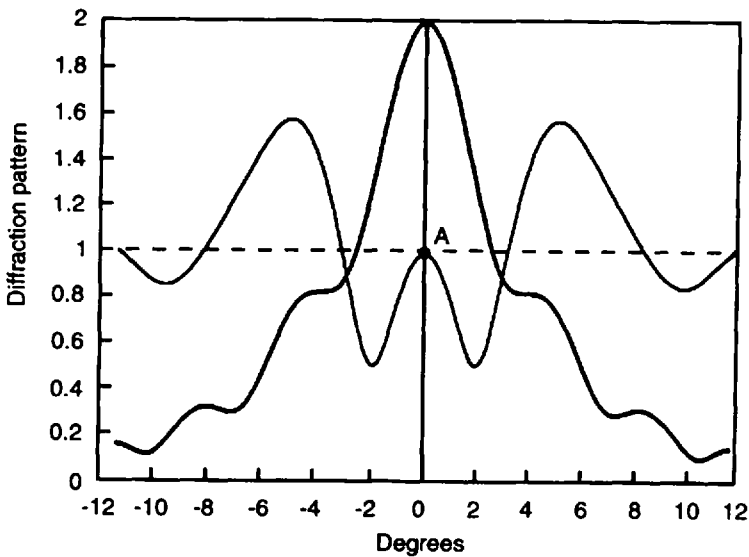


Figure 2.26 Diffraction patterns of circular aperture (thick line) and its complementary disk (thin line) in focal plane $z_2 = d_2$ as a function of ϑ , in degrees, calculated for $a_0 = b_1 = 15.8\lambda$ and $d_1 = d_2 = 100\lambda$.

corresponds to the so-called Poisson's bright spot predicted by Fresnel in his study of light diffraction by disk obstacle. This means that the field amplitude at the center of the diffraction pattern of a circular obstacle equals the field amplitude when there is no obstacle.

2.5 Vectorial Kirchhoff Diffraction Theory

The Kirchhoff diffraction theory is normally applied to scalar electromagnetic fields. Scalar wave problems are typical in acoustics and for many practical examples in optics. At radio wave frequencies, however, when one also accounts for the polarization of the diffracted fields, appropriate vectorial modifications of the Kirchhoff diffraction theory have to be accomplished.

Let us rewrite the scalar Kirchhoff's theorem (2.56) in a similar but vectorial form

$$\mathbf{E}(P_2) = \frac{1}{4\pi} \iint_S \Phi(r) \left[\frac{\partial \mathbf{E}(P')}{\partial n} - \mathbf{E}(P') \frac{\partial \Phi(r)}{\partial n} \right] dS' \quad (2.135)$$

Each of the components of vectors $\mathbf{E}(P_2)$ and $\mathbf{E}(Q')$, $E_{x,y,z}(P_2)$ and $E_{x,y,z}(Q')$, satisfies the scalar wave equation (2.57). Note that the only coordinate system for which this is true is the rectangular Cartesian system.

Vectorial equation (2.135) is applicable for a space without sources bounded by a surface of integration S , which is arbitrary in shape and totally closed. When the surface is open, or has an aperture S_o , as in Figure 2.13, for instance, a more complicated vectorial equation derived by Kottler is used [14]

$$\begin{aligned} \mathbf{E}(P_2) = & \frac{1}{4\pi} \iint_S \left[\Phi(r) \frac{\partial \mathbf{E}(P')}{\partial n} - \mathbf{E}(P') \frac{\partial \Phi(r)}{\partial n} \right] dS' \quad (2.136) \\ & + \frac{j}{4\pi\epsilon_o} \oint_L \nabla \Phi(r) \mathbf{H} dl' - \frac{1}{4\pi} \oint_L \Phi(r) \mathbf{E} dl' \end{aligned}$$

In Kottler's equation two line integrals around the aperture edge L are added to the Kirchhoff's diffraction theorem. With these field corrections the diffraction solution satisfies Maxwell's equations, which the approximate scalar solutions in Section 2.3 and Section 2.4 do not.

Another very important special case of vectorial Kirchhoff's diffraction is the circumstance in which the surface S is an infinite plane screen with apertures. Following [14] we will give here a brief derivation of a vectorial diffraction equation similar to the scalar Kirchhoff diffraction integral.

Consider an incident wave traveling to the screen in the $+z$ direction, with a tangential electric component $E_i(Q')$ at the aperture point Q' (Figure 2.27). On basis of the surface-equivalence principle [12] the vector aperture field $\mathbf{E}_i(Q')$ can be replaced by a surface magnetic current given by

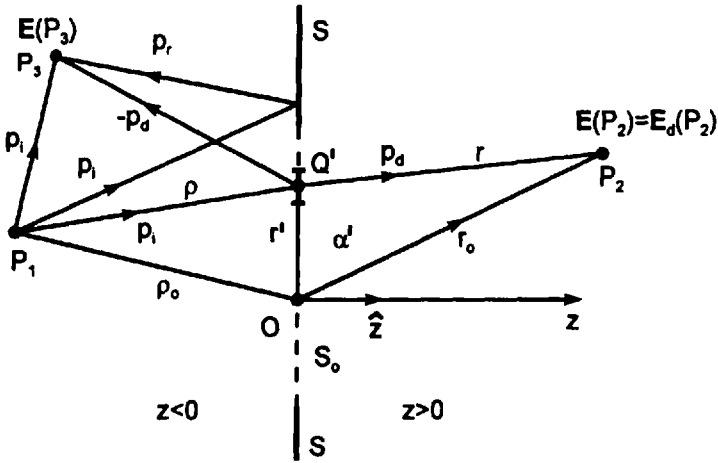


Figure 2.27 Geometry for derivation of the vectorial Kirchhoff diffraction integral.

$$\mathbf{J}_S^{(m)}(Q') = -2\hat{\mathbf{z}} \times \mathbf{E}_i(Q') \quad (2.137)$$

On the screen out of the aperture this equivalent current is set to be zero.

The electric vector potential \mathbf{A}' (see Appendix 2A) in the region $z > 0$ is written as follows

$$\mathbf{A}' = \frac{\epsilon}{4\pi} \iint_{S_o} \mathbf{J}_S^{(m)} \frac{e^{-j\beta r}}{r} dS' \quad (2.138)$$

where $\mathbf{J}_S^{(m)}$ is a magnetic current density over the aperture S_o .

In our case $\mathbf{J}_S^{(m)}$ is replaced by $\mathbf{J}_S^{(m)}(Q')$ so it is found

$$\mathbf{A}'(P_2) = -\frac{\epsilon}{2\pi} \iint_{S_o} \hat{\mathbf{z}} \times \mathbf{E}_i(Q') \frac{e^{-j\beta r}}{r} dS' \quad (2.139)$$

By definition, the electric field $\mathbf{E}(P_2)$ at P_2 is expressed by $\mathbf{A}'(P_2)$ in the form [12]

$$\mathbf{E}(P_2) = -\frac{1}{\epsilon} \nabla \times \mathbf{F}(P_2) \quad (2.140)$$

or after putting (2.139) into (2.140) a vectorial equation for the diffracted field $\mathbf{E}_d \equiv \mathbf{E}(P_2)$ in the front half-space (or for $z > 0$) is obtained

$$\mathbf{E}(P_2) = \frac{1}{2\pi} \nabla \times \iint_{S_o} \hat{\mathbf{z}} \times \mathbf{E}_i(Q') \frac{e^{-j\beta r}}{r} dS' \quad (2.141)$$

In the region $z < 0$ the field $\mathbf{E}(P_3)$ at a point P_3 is found as a sum of three components: incident $\mathbf{E}_i(P_3)$, reflected $\mathbf{E}_r(P_3)$, and diffracted $\mathbf{E}_d(P_3)$, or

$$\mathbf{E}(P_3) = \mathbf{E}_i(P_3) + \mathbf{E}_r(P_3) - \mathbf{E}_d(P_3) \quad (2.142)$$

The diffracted field at far region observation points is found by the far-field approximation, or $r \cong r_o - \cos \alpha'$ for the field phase, and $1/r_o \cong 1/r$ for the field amplitude.

For a smooth integration surface and with the above far-field approximation in mind (2.141) becomes

$$\mathbf{E}(P_2) = \frac{j}{\lambda} \frac{e^{-j\beta r_o}}{r_o} \hat{\mathbf{r}} \times \iint_{S_o} \hat{\mathbf{z}} \times \mathbf{E}_i(Q') e^{j\beta \cos \alpha'} dS' \quad (2.143)$$

where $\hat{\mathbf{r}}$ is the unit vector pointing in r direction and $\hat{\mathbf{z}} \equiv \hat{\mathbf{n}}$ is the unit vector normal to the plane aperture.

References

- [1] Huygens, C., *Traite de la lumiere*, Leiden: Van der Aa, 1690. (Reprint, Paris: Dunod, 1992.)
- [2] Klein, M. V., *Optics*, New York: John Wiley & Sons, 1970.
- [3] Kubbinga, H., "Christiaan Huygens and the Foundations of Optics," *Pure Appl. Optics*, Apr. 1995, pp. 723–739.
- [4] Landsberg, G. S., *Optika*, Moscow: Nauka, 1978 (in Russian).
- [5] Fresnel, *Euvres Completes*, Vol. 1, Note 1, Paris, 1866, pp. 365–372.
- [6] Kirchhoff, G., *Berl. Ber.*, 1882, 641, *Ann. d. Physik*, Vol. 18, 2, 1883, 663.
- [7] Baker, B. B., and E. T. Compson, *The Mathematical Theory of Huygens Principle* (2d ed), Oxford: Clarendon Press, 1950.
- [8] Born, M., and E. Wolf, *Principles of Optics*, Second Edition, Oxford: Pergamon Press, 1964.
- [9] Soret, J. L., "Uber die durch Kreisgitter erzeugten Diffraktionsphanomene, Leipzig: *Pogg. Annalen der Physik und Chemie*, Vol. 156, 1875, pp. 99–113.
- [10] Wood, R. W., "Phase-Reversal Zone Plates, and Diffraction Telescopes," *Philosophical Magazine*, Series 5, Vol. 45, No. 277, pp. 511–523, June 1898.

- [11] Wood, R. W., *Physical Optics* (3rd ed), New York: The MacMillan Co., 1934, pp. 37–39.
- [12] Balanis, C. A., *Advanced Engineering Electromagnetics*, New York: John Wiley & Sons, 1989.
- [13] Abramovitz, M., and I. Stegun (editors), *Handbook of Mathematical Functions*. New York: Dover, 1968.
- [14] Jackson, J. D., *Classical Electrodynamics* (2d ed), New York: John Wiley & Sons, 1975.

Selected Bibliography

- Kottler, F., “Electromagnetische Theorie der Beugung an schwarzen Schirmen,” *Ann. Phys.*, 71, 1923, s. 457–508.
- Mach, E., *The Principles of Physical Optics: Historical and Philosophical Treatment*, Dover, 1926. (First edition in German, Munich, 1913.)

Appendix 2A Elementary Surface or Huygens’ Source

Each point on the wave front can be represented as an infinite small radiating element of area $dS' = dx' dy'$ called in the antenna theory a surface radiating element or Huygens’ source.¹

Figure 2A.1 shows a surface element $dx' dy'$ of a uniform plane wavefront, which is incident in the $+z$ direction, normally to xy plane. At $z = 0$, the wave has an electric vector \mathbf{E}_o and a magnetic field vector \mathbf{H}_o .

From the equivalence theorem it follows

$$\mathbf{J}_s^{(e)} = \hat{\mathbf{z}} \times \mathbf{H}_o \quad (2A.1)$$

and

$$\mathbf{J}_s^{(m)} = -\hat{\mathbf{z}} \times \mathbf{E}_o \quad (2A.2)$$

where $\hat{\mathbf{z}}$ is the unit vector in the z direction, and $\mathbf{J}_s^{(e)}$ and $\mathbf{J}_s^{(m)}$ are the equivalent surface electric and magnetic current densities, respectively.

From (2A.1) and (2A.2) the scalar components of the currents are written

$$J_x^{(e)} = -H_{oy} \text{ and } J_y^{(m)} = -E_{ox} \quad (2A.3)$$

1. Jordan, E. C., and K. G. Balmain, *Electromagnetic Waves and Radiating Systems* (2d ed), New Jersey: Prentice-Hall, 1968.

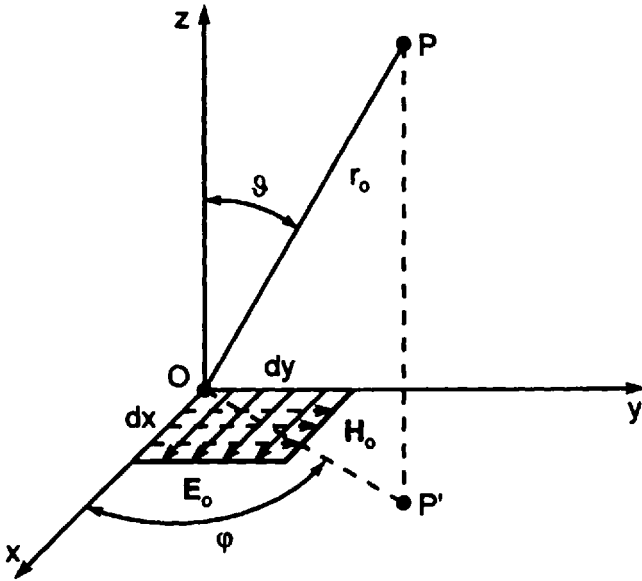


Figure 2A.1 Huygens' source.

Here the medium intrinsic impedance can be determined as a ratio of the transverse electric and magnetic components, or $\eta = E_{ox}/H_{oy}$.

The Huygens' element dS' is replaced by a couple of electric and magnetic current sheets. The electric current sheet is $(J_x^{(e)} dy') dx'$ and the magnetic current sheet is $(J_y^{(m)} dx') dy'$. With these current sources computed, it is not difficult to determine their radiated field using, for instance, the far-field vector potential expressions (1.9)–(1.14). On the basis of (1.9) the vector potential corresponding to the elementary electric-current sheet can be written

$$dA_x = \frac{\mu}{4\pi} (J_x^{(e)} dy') dx' \frac{e^{-j\beta r}}{r} = -\frac{\mu}{4\pi} \frac{E_{ox}}{\eta} \frac{e^{-j\beta r_0}}{r_0} e^{j\beta \sin \vartheta (x' \cos \varphi + y' \sin \varphi)} dS' \quad (2A.4)$$

Then, the elementary components of the electric far field are easily found

$$dE_{\vartheta}^{(e)} = -j\omega dA_{\vartheta} \quad (2A.5)$$

and

$$dE_{\varphi}^{(e)} = -j\omega dA_{\varphi} \quad (2A.6)$$

with $dA_{\vartheta} = dA_x \cos \vartheta \cos \varphi$ and $dA_{\varphi} = -dA_x \sin \varphi$.

In an analogy to the elementary magnetic vector potential $d\mathbf{A}$, a so-called electric vector potential $d\mathbf{A}'$ corresponding to the elementary magnetic-current sheet is defined, with the y -component given by

$$dA'_y = \frac{\epsilon}{4\pi} (J_y^{(m)} dx') dy' \frac{e^{-j\beta r}}{r} = -\frac{\epsilon}{4\pi} E_{ox} \frac{e^{-j\beta r_o}}{r_o} e^{j\beta \sin \vartheta (x' \cos \varphi + y' \sin \varphi)} dS' \quad (2A.7)$$

Then, the corresponding elementary far-field components are given by

$$dE_{\vartheta}^{(m)} = -j\omega\eta dA'_{\varphi} \quad (2A.8)$$

$$dE_{\varphi}^{(m)} = j\omega\eta dA'_{\vartheta} \quad (2A.9)$$

with $dA'_{\varphi} = dA'_y \cos \varphi$ and $dA'_{\vartheta} = -dA'_y \sin \varphi \cos \vartheta$.

Usually we are interested in the electric field only. The total elementary electric fields are due to both electric-current and magnetic-current sources, or

$$dE_{\vartheta} = dE_{\vartheta}^{(e)} + dE_{\vartheta}^{(m)} = \frac{jE_{ox}}{\lambda} \frac{e^{-j\beta r_o}}{r_o} e^{j\beta \sin \vartheta (x' \cos \varphi + y' \sin \varphi)} F_{\vartheta}(\varphi, \vartheta) dS' \quad (2A.10)$$

where

$$F_{\vartheta}(\varphi, \vartheta) = \frac{1}{2} \cos \varphi (1 + \cos \vartheta) \quad (2A.11)$$

and

$$dE_{\varphi} = dE_{\varphi}^{(e)} + dE_{\varphi}^{(m)} = -\frac{jE_{ox}}{\lambda} \frac{e^{-j\beta r_o}}{r_o} e^{j\beta \sin \vartheta (x' \cos \varphi + y' \sin \varphi)} F_{\varphi}(\varphi, \vartheta) dS' \quad (2A.12)$$

with

$$F_{\varphi}(\varphi, \vartheta) = \frac{1}{2} \sin \varphi (1 + \cos \vartheta) \quad (2A.13)$$

$F_{\vartheta}(\varphi, \vartheta)$ and $F_{\varphi}(\varphi, \vartheta)$ are the so-called ϑ and φ partial radiation patterns of the Huygens' source.

The total radiation pattern $F(\varphi, \vartheta)$ is calculated as follows

$$F(\varphi, \vartheta) = F(\vartheta) = \sqrt{F_{\vartheta}^2(\varphi, \vartheta) + F_{\varphi}^2(\varphi, \vartheta)} = \frac{1}{2}(1 + \cos \vartheta) \quad (2A.14)$$

which has the shape of rotational cardioid, Figure 2A.2(b). The planar pattern is a cardioidal line as shown in Figure 2A.2(a). It is called a unidirectional-type of pattern, because for $\vartheta = 0$ degrees, $F(\vartheta) = 1$ and for $\vartheta = 180$ degrees, $F(\vartheta) = 0$.

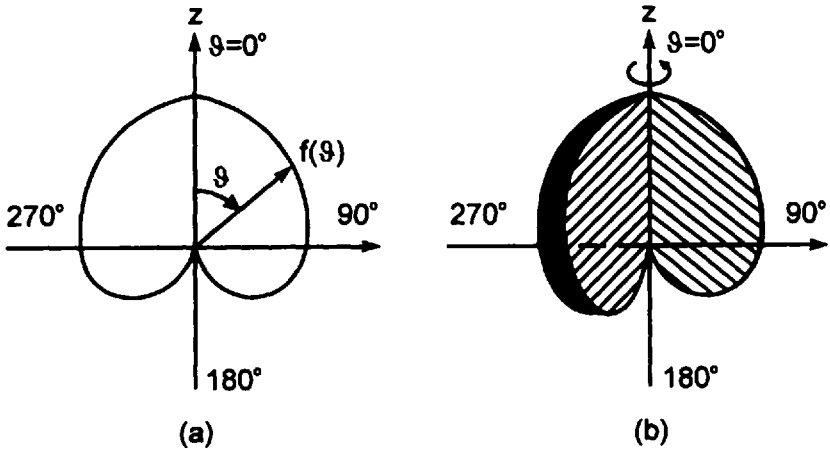


Figure 2A.2 Polar radiation pattern of Huygens' source: (a) planar or 2D pattern and (b) space or 3D pattern.

3

Fresnel Zones Applied to Radio Communication Links

3.1 Fresnel Zones and Radio Wave Propagation

Fresnel zone regions have found various practical applications to radio wave propagation, particularly for estimating hilly terrain obstruction, reflection by a rough earth or ionosphere, and transmission through layered ground or atmosphere environment. This section briefly describes the typical paths of wave propagation over the earth and considers radio wave tracing by means of Fresnel zone ellipsoids. The significant zones for transmission and reflection are defined, and the equations for finding their basic dimensions are derived. The reader is then briefly introduced to the standard interference line-of-sight schemes for radio wave propagation over smooth ground, taking into account also the earth curvature and troposphere refraction. One and the same terrain with hills may be considered as a smooth earth surface for long and medium waves, while for short waves and microwaves the hills must be regarded as sizable obstacles to ground-wave propagation.

Radio wave propagation over hilly terrain is a very complicated matter and may be treated with a combination of different rigorous and approximate methods of reflection, transmission, and diffraction. Within the scope of this book we shall confine ourselves to the classical, quasi-optical ray tracing over hills using geometrical optics (GO) and physical optics (PO) models, based on the approximate knife-edge Fresnel diffraction theory considered in Section 2.4.5.2.

Supplemented by the other high-frequency diffraction methods, such as the geometrical theory of diffraction (GTD), the physical theory of diffraction

(PTD), and the parabolic equation (PE) method, PO has been successfully applied for finding the field attenuation at VHF and UHF over terrain profiles of arbitrary shapes and in solving one- and two-dimensional rural and urban propagation problems [1–10].

Some basic examples of knife-edge diffraction models are considered, namely, straight hill, sharp hill, and wide wedge-shaped hill. Also, we examine a four-ray model of a sharp hill, where in addition to the direct incident and diffracted rays, reflected rays from earth areas in front of and in back of the hill are included. The troposphere refraction influence on link clearance and the method for drawing so-called equivalent zero-level and terrain profile curves are briefly explained.

3.1.1 Ground-Wave Propagation Paths

The radio waves may propagate in different ways and reach the receiving point over various wave paths. In this text we shall consider only propagation paths in the low-Earth atmosphere or so-called ground-wave paths.

The most typical propagation paths in the earth's atmosphere are illustrated in Figure 3.1. They correspond to the following propagation modes [11]:

1. A surface wave guided along the earth's surface (path 1);
2. Ground-space waves that include the direct wave (path 2), ground-reflected wave (path 3), and wave diffracted by an earth obstacle (path 4);

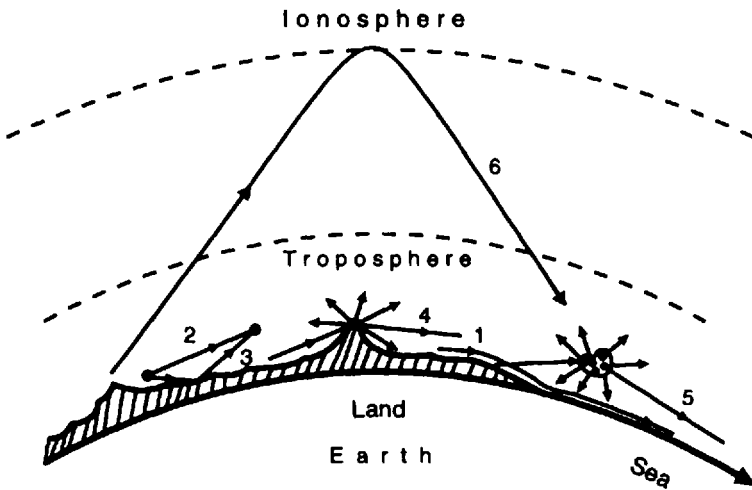


Figure 3.1 Ground-wave propagation paths. (After: [11], © 1968 Prentice-Hall.)

3. Tropospheric waves produced by scattering from space irregularities (path 5) or by refraction in the troposphere;
4. Sky waves reflected (scattered) from the ionosphere (path 6).

Since the atmosphere refractivity is neglected, all wave paths are drawn as rectilinear rays. As we shall see, for some of the ground-wave propagation modes the field at the receiving point can be easily evaluated by use of the Fresnel zone mechanism.

3.1.2 Fresnel Zone Regions Important to Free-Space Propagation

In a homogeneous infinite space the various Fresnel zones have different influences on the propagation process; mainly, the first several Fresnel zones produce the field at the receiving point.

In accordance with the definition given in Section 2.2.2 and Figure 3.2 the n -th space Fresnel zone is the volume between the n -th and $(n-1)$ -th ellipsoids with $P_1 P_2$ being a free-space (or direct) ray over the earth's surface.

In practice, a free-space propagation or clear direct path means that there is no obstruction or reflection in the space bounded by the first several zones, the most important of which is the first one.

The radius b_n of the n -th Fresnel zone is approximately calculated by

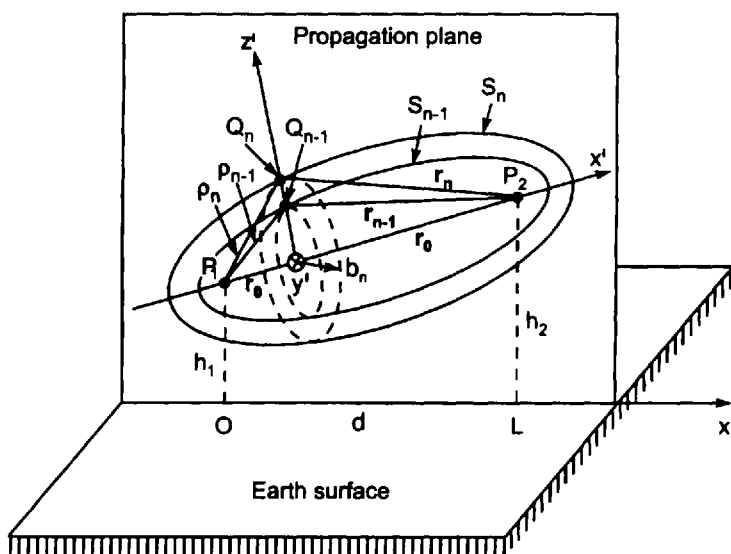


Figure 3.2 Fresnel zones in direct wave propagation.

$$b_n = \sqrt{n\lambda F_e} \quad (3.1)$$

where $F_e = \rho_o r_o / (\rho_o + r_o)$ is the equivalent focal length.

In the radio link design procedures there are different criteria for the size of the zone space securing nearly free-space propagation. This size is measured by the Fresnel zone radius, which for constant λ and F_e depends only on the zone number n . Usually, the direct path is regarded as reasonably clear inside the first Fresnel zone ($n = 1$), with a zone radius b_1

$$b_1 = \sqrt{\lambda F_e} \quad (3.2)$$

More generally, the so-called significant propagation region is defined in practice as much larger than the first Fresnel zone. If we mark with b_s the radius of such a region, it is normally calculated by choosing $n = 8 \div 12$ [12, 13]. If $n = 8$, for instance, b_s is given by

$$b_s \cong 2.8\sqrt{\lambda F_e} \quad (3.3)$$

In this case, the error in calculation of the field at the receiving point using the Fresnel zone construction does not surpass 16%.

Sometimes, the so-called minimum Fresnel propagation region is introduced [12, 14]. It is obtained for $n = 1/3$, or when $(\rho_n + r_n) - (\rho_o + r_o) = \lambda/6$, and the corresponding minimum zone radius b_{\min} is given by

$$b_{\min} \cong 0.6\sqrt{\lambda F_e} \quad (3.4)$$

Naturally, in the last case there is no good clearance along the propagation path, and the received signal may not be adequate.

Up to this point and in Section 3.1.3, all reasonings are based on the assumption that the antenna acts as a point source and that the antenna directivity is neglected.

3.1.3 Fresnel Zones in Case of Reflection

Fresnel zones in case of reflection from plane earth serve to estimate the shape and size of ground region that is most significant for the reflected radio waves. These are elliptical zones with dimensions that for a given wavelength depend on the distance between the transmitter and receiver and the heights of their antennas.

3.1.3.1 Fresnel Zones and Significant Earth Region in Reflection

In case of radio wave reflection from a plane earth surface it is a common practice to introduce auxiliary image antennas. This is illustrated in Figure 3.3 where $P_1'(0, 0, -h_1)$ is an image of the actual antenna point $P_1(0, 0, +h_1)$. Thus, the ground-reflected field at the receiving point P_2 can be found as radiated by the virtual image antenna at P_1' with a distance $P_1'Q_o$ to the reflection point $Q_o(x_o, y_o, 0)$ equal to P_1Q_o .

The wave path $P_1'Q_o$ is related to a set of confocal ellipsoids of revolution. The intersection curves of these ellipsoids with the earth plane are ellipses with an origin at point $Q_{on}(x_{on}, 0, 0)$ known as Fresnel zones for reflection.

Let us derive the Fresnel zone equations. Each point $Q_n(x_n, y_n, 0)$ of the n -th ellipse is a point of reflection with a phase equal to $n\pi$. The Fresnel zone condition for reflection may be written as

$$(\rho_n + r_n) - (\rho_o + r_o) = n \frac{\lambda}{2} \tag{3.5}$$

where

$$\rho_n = \sqrt{x_n^2 + y_n^2 + h_1^2} \tag{3.6}$$

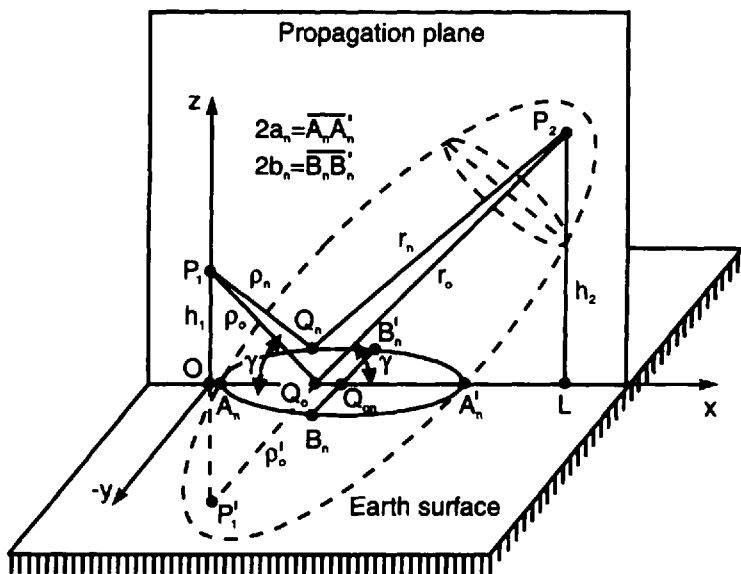


Figure 3.3 Geometry for studying Fresnel zones for reflection. (After: [15].)

and

$$r_n = \sqrt{(OL^2 - x_n^2) + y_n^2 + h_2^2} \quad (3.7)$$

with $y_n \ll x_n$.

Denote the distance between the transmitter and receiver by d or $d = OL$ and assume that $h_1, h_2 \ll d$. Equation (3.5) can be transformed into [15, 16]

$$Ax_n^2 + By_n^2 + Cx_n + D = 0 \quad (3.8)$$

where

$$A = 4 \left[(h_1^2 + h_2^2) + n\lambda \left(d_o + n\frac{\lambda}{4} \right) \right] \quad (3.9)$$

$$C = -4d \left[2h_1(h_1 + h_2) + n\lambda \left(d_o + n\frac{\lambda}{4} \right) \right] \quad (3.10)$$

$$D = 4 \left(d_o + n\frac{\lambda}{2} \right) h_1^2 - \frac{C^2}{16d^2} \quad (3.11)$$

with $d_o = \rho_o + r_o$.

The center point Q_{on} has a coordinate x_{on} given by

$$x_{on} = x_o \left[1 + \frac{h_2 - h_1}{2h_1} \frac{1}{1 + \frac{(h_1 + h_2)^2}{n\lambda \left(d_o + n\frac{\lambda}{4} \right)}} \right] \quad (3.12)$$

with $x_o = h_1 \cot \gamma$, where γ is the grazing angle measured by the earth plane. The major semi-axis a_n and the minor semi-axis b_n of the n -th ellipse are calculated by the following equations [15]

$$a_n = A_n Q_{on} = \frac{d_o + n \frac{\lambda}{2}}{2 \left[n\lambda \left(d_o + n \frac{\lambda}{4} \right) + (h_1 + h_2)^2 \right]} \quad (3.13)$$

$$\times \sqrt{n\lambda \left(d_o + n \frac{\lambda}{4} \right) \left[\left(n\lambda d_o + n \frac{\lambda}{4} \right) + 4h_1 h_2 \right]}$$

$$b_n = B_n Q_{on} = \frac{a_n}{d_o + n \frac{\lambda}{2}} \sqrt{n\lambda \left(d_o + n \frac{\lambda}{4} \right) + (h_1 + h_2)^2} \quad (3.14)$$

Assume that the first several elliptical zones (say $n = 8 - 12$) form the so-called significant Fresnel region for reflection, and depending on antenna heights over the ground plane consider the following particular cases.

- Case 1 ($h_1 \ll h_2$): In this specific case (3.12)–(3.14) can be approximated, and the center coordinate x_{on} of the n -th ellipse measured from the coordinate origin O and its semi-axes a_n and b_n can be calculated by

$$x_{on} \cong h_1 \cot \gamma \left(1 + \frac{n}{2h_1 \sin \gamma} \right) \quad (3.15)$$

$$a_n \cong \frac{1}{\sin \gamma} \sqrt{\frac{n\lambda h_1}{\sin \gamma} \left(1 + \frac{n\lambda}{4h_1 \sin \gamma} \right)} \quad (3.16)$$

$$b_n \cong a_n \sin \gamma \quad (3.17)$$

From (3.15) and (3.16) it can be proved that for $h_1 \ll h_2$, $x_{on} \cong a_n$, and therefore, the n -th reflection significant Fresnel region is located near to the transmitting antenna base, stretched toward the receiving point.

- Case 2 ($h_1 \gg h_2$): Now the coordinate x_{on} and the semi-axes a_n and b_n are given by equations similar to (3.15)–(3.17), with only h_1 replaced by h_2 , or

$$x_{on} \cong h_2 \cot \gamma \left(1 + \frac{n\lambda}{2h_2 \sin \gamma} \right) \quad (3.18)$$

$$a_n \cong \frac{1}{\sin \gamma} \sqrt{\frac{n\lambda h_2}{\sin \gamma} \left(1 + \frac{n\lambda}{4h_2 \sin \gamma} \right)} \quad (3.19)$$

$$b_n \cong a_n \sin \gamma \quad (3.20)$$

Now the significant Fresnel region is located close to the receiving antenna and is drawn out toward the transmitter.

- Case 3 ($h_1 \cong h_2 \cong h$): In this occasion (3.12)–(3.14) become

$$x_{on} \cong h \cot \gamma \quad (3.21)$$

$$a_n \cong \frac{1}{\sin \gamma} \sqrt{\frac{n\lambda h}{2 \sin \gamma}} \quad (3.22)$$

$$b_n \cong a_n \sin \gamma \quad (3.23)$$

From the equations for a_n and b_n it is clearly seen that the ellipses become longer (or more eccentric) with decrease of the grazing angle γ . Normally $h_1 + h_2 \ll d$, and in the general case $h_1 \neq h_2$. Thus, the grazing angle is approximately found from

$$\tan \gamma \cong \sin \gamma \cong \frac{h_1 + h_2}{d} \quad (3.24)$$

3.1.3.2 Special Features of Radio Wave Reflection From Flat Earth

For VLF, LF, and MF bands (or for radio frequencies from 3 KHz to 3 MHz) it is common to assume that $h_1 = 0$ and $h_2 = 0$, and under these circumstances the whole wave path on the earth plane becomes equal to the significant Fresnel region length. In such a situation there is an immediate influence of the ground on the field strength because of the surface wave phenomenon, and the ground reflection waves are not possible. However, the idea of a significant Fresnel zone region may be applied again in evaluating the surface wave propagation [16].

For UHF and SHF bands (or for frequencies from 30 MHz to 30 Hz) the size of the significant Fresnel region is tens of kilometers in length and tens of meters only in width. In case of wave reflection from the earth most important are its reflective properties within the first Fresnel zone. Even for a smooth earth surface the reflection coefficient R may vary considerably within the limits of this zone depending on the electric homogeneity of reflecting ground and/or the change in grazing angle γ .

To find out the limits of the assumption of homogeneous reflection across the Fresnel zone, consider a wave reflected from a homogeneous ground plane. Let the coordinate x_0 of reflection point Q_0 (Figure 3.3) vary within the first Fresnel zone ($n = 1$), from point $A_n = A_1$ to point $A'_n = A'_1$. So we can write $\Delta x \ll A_1 A'_1 = 2a_1$. Examine the change of the reflection coefficient R along the x -axis within zone length $2a_1$ [15]

$$\frac{\Delta R}{\Delta x} = \frac{\partial R}{\partial \gamma} \frac{\partial \gamma}{\partial x} \quad (3.25)$$

Consider a small change ΔR of the reflection coefficient R within the first Fresnel zone, or to be more specific

$$|\Delta R| = \left| \frac{\Delta R}{\Delta x} \Delta x = \frac{\partial R}{\partial \gamma} \frac{\partial \gamma}{\partial x} \Delta x \right| \ll |R(\gamma)| \quad (3.26)$$

Δx is not a small quantity compared to the distance between the transmitter and receiver, which is true for small grazing angles.

The reflection coefficient for parallel (or vertical) polarization changes faster than the corresponding coefficient for perpendicular (or horizontal) polarization, or

$$\left| \frac{\partial R^{\parallel}(\gamma)}{\partial \gamma} \right| > \left| \frac{\partial R^{\perp}(\gamma)}{\partial \gamma} \right| \quad (3.27)$$

and therefore, it is adequate to examine only the former of the two wave polarizations. In accordance with (1.48), for $\psi_i = \pi/2 - \gamma$ and $n_{21} = \sqrt{\epsilon_r}$, $R^{\parallel}(\gamma)$ is given by

$$R^{\parallel}(\gamma) = \frac{\epsilon_r \sin \gamma - \sqrt{\epsilon_r - \cos^2 \gamma}}{\epsilon_r \sin \gamma + \sqrt{\epsilon_r - \cos^2 \gamma}} \quad (3.28)$$

Here $\epsilon_r = \epsilon/\epsilon_0 = [\epsilon - j(\sigma/\omega)]/\epsilon_0$ is the complex relative permittivity.

For small grazing angles (say $\gamma \ll \pi/2$ or $\cos^2 \gamma \approx 1$), (3.28) becomes

$$R^{\parallel}(\gamma) \cong \frac{\epsilon_r \sin \gamma - \sqrt{\epsilon_r - 1}}{\epsilon_r \sin \gamma + \sqrt{\epsilon_r - 1}} \quad (3.29)$$

and then

$$\left| \frac{\partial R^{\parallel}(\gamma)}{\partial \gamma} \right| \cong \frac{2\epsilon_r \sqrt{\epsilon_r - 1}}{(\epsilon_r \sin \gamma + \sqrt{\epsilon_r - 1})^2} \quad (3.30)$$

Assume that $h_1 \ll h_2$ and $h_2 \gg \lambda$. According to (3.19), the length of the first Fresnel zone on the ground plane is

$$2a_1 \cong \frac{\lambda}{\sin^2 \gamma} \quad (3.31)$$

Then calculate $\partial \gamma / \partial x$, for $x = x_0$. From Figure 3.3 it is found that

$$x_0 = \frac{h_2}{\tan \gamma} \cong \frac{h_2}{\sin \gamma} \quad (3.32)$$

Thus,

$$\left. \frac{\partial \gamma}{\partial x} \right|_{x=x_0} = -\frac{h_2}{x_0^2} = -\frac{\sin^2 \gamma}{h_2} \quad (3.33)$$

Placing (3.29), (3.30), and (3.33) into (3.26) gives

$$|\Delta R^{\parallel}| = \left| \frac{2\epsilon_r \sqrt{\epsilon_r - 1}}{(\epsilon_r \sin \gamma + \sqrt{\epsilon_r - 1})^2} \frac{\lambda}{h_2} \right| \quad (3.34)$$

As $|R^{\parallel}| \cong 1$ and $|\Delta R^{\parallel}| \ll 1$ it follows that

$$\frac{h_2}{\lambda} \gg \left| \frac{2\epsilon_r \sqrt{\epsilon_r - 1}}{(\epsilon_r \sin \gamma + \sqrt{\epsilon_r - 1})^2} \right| \quad (3.35)$$

This inequality is the condition under which $\Delta R \ll 1$ so that the earth reflection is constant across the Fresnel zone. Thus, the concept of earth reflection wave, and therefore, the corresponding two-wave interference scheme is valid.

If $|\epsilon_r| \rightarrow \infty$, or if the ground surface behaves as an ideal screen, the expression $|(2\epsilon_r \sqrt{\epsilon_r - 1}) / (\epsilon_r \sin \psi + \sqrt{\epsilon_r - 1})^2|$ tends to zero, and the interference scheme becomes true for all antenna heights.

3.1.4 Line-of-Sight Interference Schemes for Radio Wave Propagation Over Smooth Earth

If the transmitting and receiving antennas are elevated over a flat earth the field at the receiving point is obtained by use of a simple two-ray interference scheme. The field analysis in this case is based on many practical assumptions, and results in an approximate equation for the field interference factor. This equation is then modified if the earth curvature and troposphere refraction cannot be ignored.

3.1.4.1 Interference Scheme With Antennas Elevated Over Flat Earth

The simplest interference scheme for space wave propagation over the ground is the flat-earth scheme (Figure 3.4). The transmitting and receiving antennas are at such a distance apart that the earth curvature and tropospheric refraction may be ignored. It is supposed that the antennas are elevated over a flat surface, so that $h_1, h_2 \gg \lambda$. The earth surface is also assumed smooth, uniform, and imperfectly conducting.

The total (or interference) field at the receiving point P_2 is

$$\mathbf{E}(P_2) = \mathbf{E}_1(P_2) + \mathbf{E}_2(P_2) \quad (3.36)$$

where

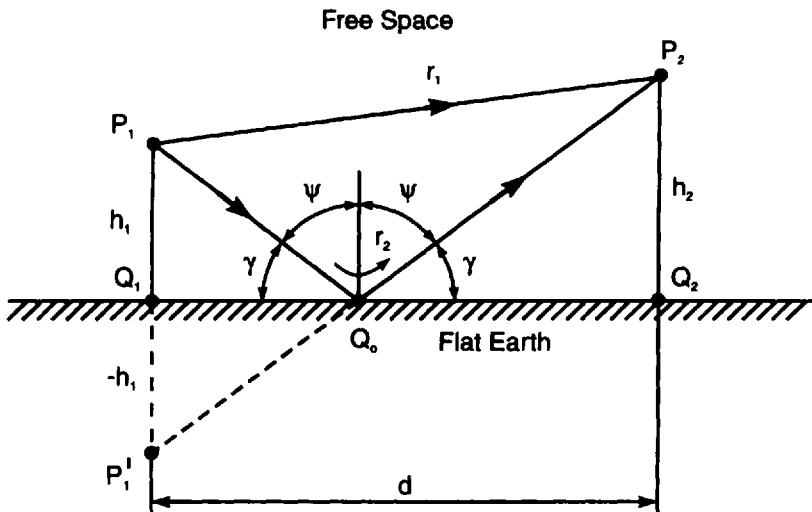


Figure 3.4 Interference arrangement for flat ground surface.

$$\mathbf{E}_1(P_2) = \frac{\sqrt{60G_{t1}P_t}}{r_1} e^{-j\beta r_1} \hat{\mathbf{e}}_1 \quad (3.37)$$

is the direct field vector, and

$$\mathbf{E}_1(P_2) = \frac{\sqrt{60G_{t2}P_t}}{r_2} |R| e^{-j(\beta r_2 + \theta_R)} \hat{\mathbf{e}}_2 \quad (3.38)$$

is the reflected field vector.

Here P_t is the power radiated by the transmitting antenna; G_1 and G_2 are the antenna gains in directions from P_1 to P_2 and Q_o , respectively; $r_1 = P_1P_2$ and $r_2 = P_1Q_o + Q_oP_2$; $|R|$ is the absolute value and θ_R is the argument of the complex reflection coefficient $R = |R|e^{j\theta_R}$; and $\hat{\mathbf{e}}_1$ and $\hat{\mathbf{e}}_2$ are unit vectors of the direct and reflected electric wave fields, respectively.

In practice, the antennas are so far apart and the grazing angle is so small that the following approximations take place: $r_1 \cong r_2 \cong d$ (for the field amplitude), $\Delta r = r_2 - r_1 \cong 2\frac{h_1h_2}{d}$ (for the field phase difference), $G_{t1} \cong G_{t2} \cong G_t$, $R^{\parallel} \cong R^{\perp} \cong R$, and $E_1^{\parallel}(P_2) \cong E_1^{\perp}(P_2)$ and $E_2^{\parallel}(P_2) \cong E_2^{\perp}(P_2)$. Also, $\hat{\mathbf{e}}_1 \cong \hat{\mathbf{e}}_2 \cong \hat{\mathbf{e}}$, or \mathbf{E}_1 and \mathbf{E}_2 are considered collinear field vectors.

With these approximations in mind the interference field becomes

$$\mathbf{E}(P_2) \cong \frac{\sqrt{60P_tG_t}}{d} e^{-j\frac{2\pi}{\lambda}r_1} (1 + |R|e^{-j\Delta\Phi}) \hat{\mathbf{e}} \quad (3.39)$$

where

$$\Delta\Phi = \frac{2\pi}{\lambda}\Delta r + \theta_R = \frac{4\pi h_1h_2}{\lambda d} + \theta_R \quad (3.40)$$

is the phase difference between the direct and reflected waves at the receiving point. The amplitude of the interference field is

$$|E(P_2)| = \frac{\sqrt{60P_tG_t}}{d} |F_i| \quad (3.41)$$

where

$$|F_i| = \left| 1 + |R| e^{-j\left(\frac{4\pi h_1 h_2}{\lambda d} + \theta_R\right)} \right| \tag{3.42}$$

or

$$|F_i| = \sqrt{1 + |R|^2 + 2|R|\cos\left(\frac{4\pi h_1 h_2}{d\lambda} + \theta_R\right)} \tag{3.43}$$

is called the field interference factor.

Interference maxima take place at distances $d_{m'}$ for which the field components $E_1(P_2)$ and $E_2(P_2)$ are summed in phase, or $\Delta\Phi = 2\pi m'$, $m' = 1, 2, 3, \dots$ (Figure 3.5). For these distances the interference factor is equal to $|F_{im'}| = (1 + |R_{m'}|) > 1$, where the reflection coefficient $R_{m'}$ is found for a grazing angle $\gamma_{m'}$ corresponding to $d_{m'}$.

By analogy, interference minima are obtained at distances $d_{m''}$ for which the field components $E_1(P_2)$ and $E_2(P_2)$ are summed out of phase, or $\Delta\Phi = (2m'' + 1)\pi$, $m'' = 1, 2, 3, \dots$, and in these cases the value of the interference factor is $|F_{im''}| = (1 - |R_{m''}|) < 1$, with reflection coefficient $R_{m''}$ calculated for a grazing angle $\gamma_{m''}$.

The last maximum corresponds to $m' = 1$ (or to a distance d_{lmax}), for which $\Delta\Phi = 2\pi$. For a fixed terrestrial line-of-sight communication link the receiver is normally located at or near to d_{lmax} .

For $d > d_{lmax}$, the interference factor is monotonically decreasing or behaving as a typical attenuation (or loss) factor.

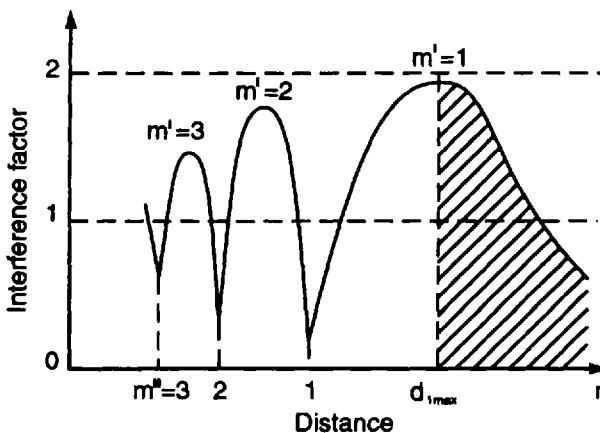


Figure 3.5 Interference attenuation factor versus distance between transmitter and receiver for antennas elevated over flat earth. (After: [17].)

3.1.4.2 Rayleigh's Criterion for Roughness of the Earth's Surface

In radio wave propagation the earth's roughness is a relative parameter that depends on the size of the ground irregularities compared to the wavelength used. At very low radio frequencies a ground terrain with hills hundreds of meters in height may be considered a smooth surface while for the higher microwave frequencies even field with grass may be viewed as a rough surface.

The roughness of a reflecting ground can be determined by the Rayleigh's criterion, which is well-known in optics. To simplify the problem let us assume that all earth irregularities are of the same average height H_{av} . The earth's surface may be assumed to be a smooth plane if [13]

$$H_{av} < \frac{\lambda}{16 \sin \gamma} \quad (3.44)$$

where γ is the grazing angle. It is derived from the condition that the phase delay between two reflections be less than $\pi/4$.

Equation (3.44) is called Rayleigh's criterion for mirror reflection. Though this criterion does not account for wave polarization, ground electrical parameters, earth curvature, or the shape of the surface irregularities, it is normally used for estimation of the initial earth roughness. If the condition (3.44) is not fulfilled, a scattering instead of reflection occurs and then one speaks about scattered or diffused radio waves.

3.1.4.3 Application of Fresnel Zones to Reflection and Diffraction of Radio Waves Near Seaside

Figure 3.6 illustrates a coastal radar site near a shoreline [18]. To calculate reflection from the sea and diffraction at a shoreline, a system of elliptical Fresnel zones for each antenna pattern lobe is projected onto the sea surface.

The main lobe 1 forms Fresnel zones on the sea surface, far out from the shore, and is essentially reflected by the corresponding significant zone area surrounding point A . Close to the shore, a higher angle lobe (or first sidelobe, marked by 2) is pointing down to the sea (point B). The effect of the reflecting surface may be represented by an image antenna located in the earth under the radar antenna at a depth h_1 below the surface SS' . The shoreline may then be considered as a diffracting knife-edge (point C) for rays coming from the image antenna.

Assume that BC is equal to the semi-axis a_2 of the second elliptical Fresnel zone [see (3.13)]. In this special case, the reflected wave is mainly due to reflections by the first two Fresnel zones that are out of phase, and thus, it will be too weak. If the first Fresnel zone is only uncut by the shoreline (or $BC = a_1$) the reflected wave may become undesirably strong.

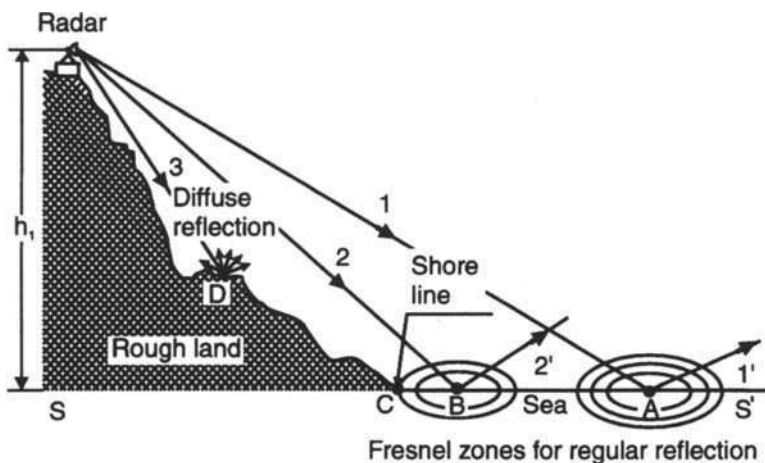


Figure 3.6 Fresnel zones on sea surface important for reflection and diffraction of coast radar signals. (After: [18], © 1968 Academic Press.)

The second sidelobe (marked by 3) pointing to the rough land is diffused rather than reflected from the point D area. The diffused field in a particular direction is relatively small and may be neglected in the interference pattern.

3.1.4.4 Accounting for Earth Curvature and Tropospheric Refractivity

For a large distance between the transmitter and receiver point the wave refraction in the low troposphere and the earth curvature must be also taken into account. The tropospheric wave rays are rather bent because of laterally varying low atmosphere refractivity, and the space Fresnel zones are no longer represented by ellipsoids of revolution. In such propagation conditions, the Fresnel zone volume is bounded by a curved-in-shape closed surface shown in Figure 3.7 [19].

The earth's curvature is taken into account by introducing new antenna heights h_1' and h_2' above the plane AB tangent at reflection point Q_0 (Figure 3.8), and a wave divergence factor D_s into (3.43) for the flat-earth interference factor. In other words, the propagation over a smooth spherical earth is transformed into a straight ray interference scheme over a fictitious flat earth AB , and the curvilinear (refracted) rays r_1 and r_2 traveling over the actual earth with a radius $a_0 = 6370$ km are replaced by rectilinear rays r_1' and r_2' over a fictitious spherical earth with an equivalent radius a_e given by [11, 13]

$$a_e = \frac{a_0}{1 - \frac{a_0}{\rho}} = a_0 k_e \quad (3.45)$$

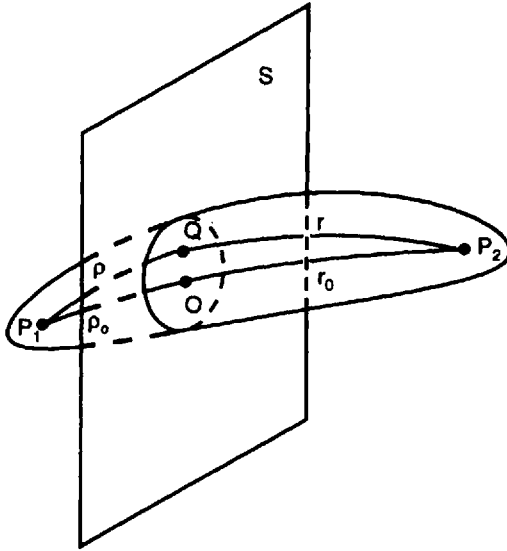


Figure 3.7 Curvilinear tropospheric ray and its corresponding Fresnel zone volume. (After: [19], © 1992 Geophysics Press.)

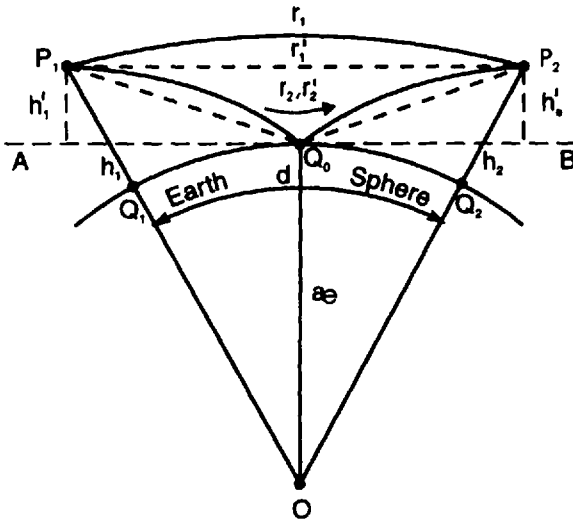


Figure 3.8 Equivalent interference ray scheme accounting for earth curvature and refraction in the troposphere.

so that

$$k_e = \frac{1}{1 - \frac{a_0}{\rho_c}} \quad (3.46)$$

Here ρ_c is the radius of the actual ray curvature given by

$$\rho_c = -\frac{2}{g_\epsilon} \quad (3.47)$$

where $g_\epsilon = d\epsilon_r/dh$ is the rate of change (or gradient) of the relative tropospheric permittivity ϵ_r with height h . The index of troposphere refraction $n = \sqrt{\epsilon_r} \cong 1 + (\epsilon_r - 1)/2$ is of value $1.00026 \div 1.00046$ at the earth's surface. For the so-called standard atmosphere $g_\epsilon = -8 \cdot 10^{-8}$ 1/m, the ray curvature radius is $\rho_c = 4a_0 = 25,000$ km, $k_e = 4/3$, and the effective radius is $a_e = 8,500$ km.

The heights h_1' and h_2' are less than the actual antenna heights h_1 and h_2 , and are calculated by the following approximate expressions [11, 17]

$$h_1' = h_1 - \frac{d^2}{2a_e} \left(\frac{h_1}{h_1 + h_2} \right)^2 \quad (3.48)$$

and

$$h_2' = h_2 - \frac{d^2}{2a_e} \left(\frac{h_2}{h_1 + h_2} \right)^2 \quad (3.49)$$

The wave reflected from a spherical earth is diverged by the convex reflection surface that means the reflected field at the receiving point will be weaker than for a flat earth. This effect may be taken into account by multiplying the plane earth reflection coefficient $|R|$ by the divergence factor D_s , given by [12]

$$D_s = \frac{1}{\sqrt{1 + \frac{2d^2 h_1'^2 h_2'^2}{a_e (h_1' + h_2')^3}}} \quad (3.50)$$

With the above quantities accounting for the earth's curvature and tropospheric refraction the interference equation (3.43) for the flat-earth scheme is transformed into

$$|F_i| = \sqrt{1 + (|R|D_s)^2 + 2|R|D_s \cos\left(\frac{4\pi h'_1 h'_2}{d} + \theta_R\right)} \quad (3.51)$$

Interference interpretation of the field in a refractive troposphere for elevated antennas over smooth spherical earth is valid only for grazing angles subject to the following inequality [12]

$$\sin \gamma \geq \frac{\sqrt{2}}{2} \sqrt{\frac{3\lambda}{a_e}} \quad (3.52)$$

To estimate reflectivity of a rough spherical earth, it is necessary to check it by means of Rayleigh's criterion within the reflection Fresnel zone area on the tangent plane AB . The position coordinate x_{on} of the n -th zone and its dimensions $2a_n$ and $2b_n$ are calculated by (3.12)–(3.14). For the so-called minimum Fresnel zone of reflection $n = 1/3$ these equations become [12]

$$x_{o\min} = d \frac{h'_2 - h'_1}{2(h'_1 + h'_2) \left[1 + \frac{(h'_1 + h'_2)^2}{\lambda d} \right]} \quad (3.53)$$

$$2a_{\min} = d \frac{\sqrt{\lambda d (\lambda d + 12h'_1 h'_2)}}{\lambda d + 3(h'_1 + h'_2)^2} \quad (3.54)$$

$$2b_{\min} = \sqrt{\frac{\lambda d (\lambda d + 12h'_1 h'_2)}{3[\lambda d + 3(h'_1 + h'_2)^2]}} \quad (3.55)$$

In the absence of troposphere refraction $g_t = 0$, $a_e = a_o$, and all above equations become valid for the interference scheme with rectilinear rays over a smooth spherical earth.

3.1.5 Radio Wave Propagation Over Hilly Terrain

In this section propagation in microwave links over hilly earth is analyzed as the basis of Fresnel-Kirchhoff (or physical optics) diffraction theory. The equations presented here were set up long ago in engineering practice for designing

fixed wireless links (e.g., radio broadcasting, radio relay, and radar) and also for modeling of urban and rural mobile communication channels.

3.1.5.1 Terrain Profile and Link Clearance

The terrain profile in the plane of propagation is normally drawn using a parabolic scale. In Cartesian coordinates the profile is built in regard to ground zero (or sea) level (Figure 3.9) by means of the following parabolic equation for the equivalent height y of the ground level contour

$$y = \frac{zd}{2a_0} \left(1 - \frac{z}{d} \right) \quad (3.56)$$

where a_0 is the earth radius in absence of refraction in the troposphere (or for $g_t = d\epsilon_r/dh = 0$).

According to (3.56) the distance z is laid off on the horizontal axis instead of along the earth's curvature, and the heights are laid off on the vertical axis instead of to the earth's surface, as would be customary.

Considering radio wave propagation over hilly terrain, the link designer has to choose the antenna sites and heights in such a way that the significant Fresnel region will pass clear of the hilltops [12, 13, 18, 20]. As shown in Figure 3.9 for zero refraction the direct rectilinear ray between antennas at P_1

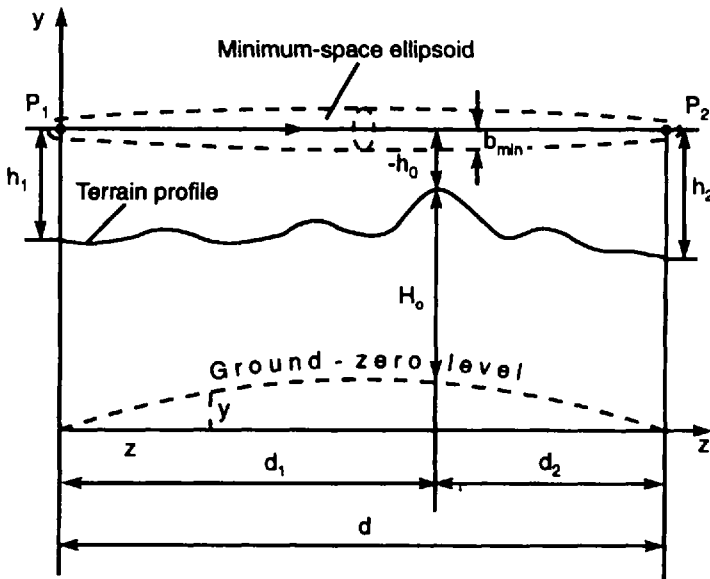


Figure 3.9 Terrain profile built in reference to ground zero level.

and P_2 is passing at height h_o above the highest hill (or $-h_o$), measured from the line P_1P_2 . This height determines the link clearance for securing an open link, and it has to be chosen so that it is not less the radius b_{min} of the minimum Fresnel zone (or $|h_o| \geq b_{min}$) calculated by (3.4). If $h_o = 0$, the direct ray is tangential to the hill's top. Finally, when $h_o > 0$ (subject to level P_1P_2), the hill cuts across the direct ray, and one may speak of a closed link.

3.1.5.2 Radio Wave Diffraction by a Straight Sharp Hill Modeled as Single Knife-Edge Screen

A terrain diffraction problem arises when UHF/microwave radio waves propagate over narrow hills, steep mountains, or high buildings. A hill with a narrow profile in the propagation plane and a straight ridge (Figure 3.10 [14]) may be modeled as a single knife-edge screen [14], if

$$\sqrt{\frac{w_1}{\lambda}}, \sqrt{\frac{w_2}{\lambda}} < 8.10^{-2} \frac{d_1 d_2}{(d_1 + d_2) H_o} \tag{3.57}$$

where $w_1 + w_2$ is the total width of the hill.

In Figure 3.11 two schemes of wave propagation across a knife-edge hill are presented. H_o is the height of the knife-edge hill, and h_o is the link clearance defined as a distance between the top point Q and intersection point Q' of the line of sight P_1P_2 with y -axis. In Figure 3.11(a) the hill cuts the line P_1P_2 , the point P_2 is in the shadow region, and the clearance h_o is given a plus sign.

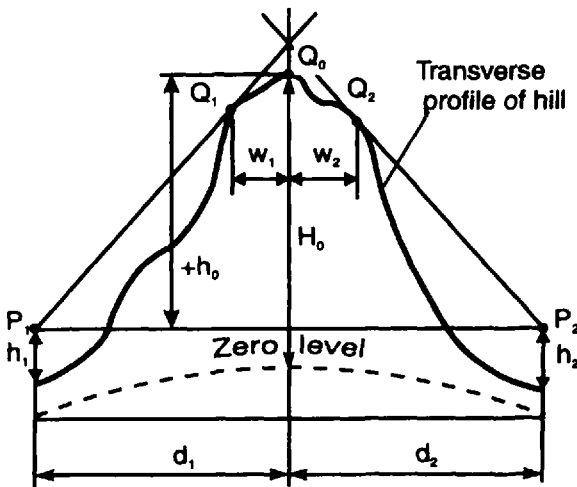


Figure 3.10 Geometry for defining shape of hill. (After: [14].)

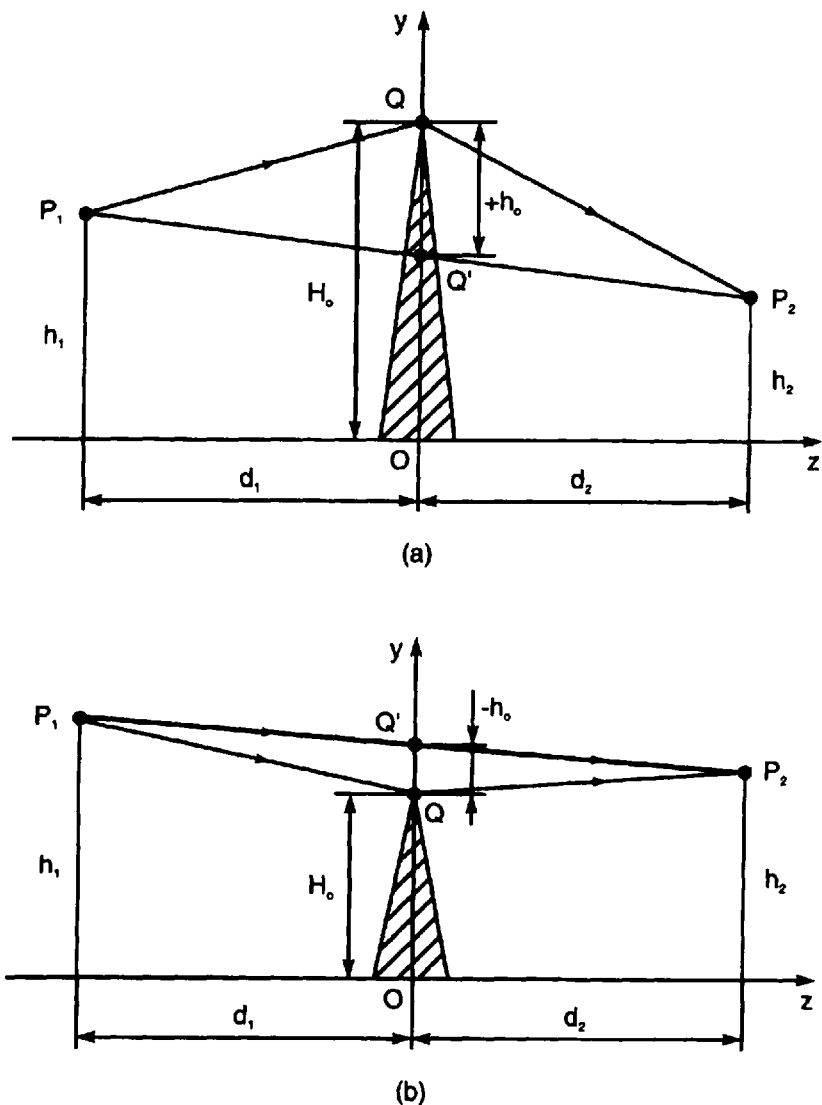


Figure 3.11 Wave propagation in presence of a knife-edge hill.

(Note that the choice of the sign for the closed link condition might appear misleading to the reader, but it is made in correspondence with the designation made in Section 2.4 [Figures 2.17 and 2.20].) The field at the receiving point will be produced as a result of wave diffraction by the knife-edge hill. Figure 3.11(b) illustrates the line-of-sight (or open-link) situation. Now the hill does not obstruct the line P_1P_2 . The clearance h_o has a minus sign; the receiving

point is positioned in the illuminated region; and the field is a result of two interfering wave rays: direct $P_1 Q' P_2$ and diffracted $P_1 Q P_2$. In the actual radio wave links it is customary that $d_1, d_2 \gg h_1, h_2, H_o$ and that $h_1, h_2, H_o \gg \lambda$.

As it was pointed out, the knife-edge hill diffraction may be studied quite successfully by means of Fresnel-Kirchhoff diffraction theory for a straight edge of semi-infinite screen (Section 2.4.5.2). From (2.114) the absolute value of the diffraction factor $F_d(v_o)$ is written as

$$F_d = |F_d(v_o)| = \left| \frac{E(P_2)}{E_o(P_2)} \right| \quad (3.58)$$

where

$$F_d(v_o) = \frac{1}{2}(1 + j)\{[0.5 - C(v_o)] - j[0.5 - S(v_o)]\} \quad (3.59)$$

with

$$v_o = \frac{\sqrt{2}}{b_1}(H_o - y_o) \quad (3.60)$$

Here $b_1 = \sqrt{d_1 d_2 (d_1 + d_2)}$ is the first Fresnel zone radius, and $y_o = \frac{d_1 h_2 + d_2 h_1}{d_1 + d_2}$.

Two special cases can be considered: (1) for $h_1 = h_2 = H_o$, $y_o = H_o$, and $v_o = 0$ and (2) for $h_1 = h_2 = 0$, $y_o = 0$, and $v_o = \sqrt{2}H_o/b_1$.

The diffraction factor (or knife-edge loss) in logarithmic form is calculated by

$$F_d = 20 \log \left\{ \frac{1}{\sqrt{2}} \sqrt{[0.5 - C(v_o)]^2 + [0.5 - S(v_o)]^2} \right\} \quad (3.61)$$

3.1.5.3 Approximation of Straight Knife-Edge Problem by Means of Significant Diffraction Segment

A simple engineering solution of the Fresnel diffraction integral was proposed in [21]. A concept of significant diffraction segment was introduced and applied for working out a lot of basic diffraction problems: single and multiple knife-edge diffraction, diffraction by rectangular and circular apertures, and many others.

Let us define first the significant diffraction segment in a dimensionless coordinate plane uv (see Section 2.4), as illustrated in Figure 3.12. The wave diffraction semi-infinite (or knife-edge) screen is of edge height v_0 , calculated by (3.60). Here P_1 and P_2 lay on the z -axis and $y_0 = 0$.

The first Fresnel zone is divided into two equal-in-area subzones: inner ($n = 1/2$) and outer ($n = 1$) with radii $b_{1/2}$ and b_1 , respectively. As it was proven in Section 2.2.2 in absence of screen, the total field at point P_2 equals the field produced solely by the inner subzone. However, in Figure 3.12 only a part of this significant subzone is open—the shaded segment ABCDA, called the significant diffraction segment. It is described by the following dimensionless quantities [21]

$$\chi_{1/2} = \sqrt{v_0^2 + u_{1/2}^2} \tag{3.62}$$

$$\Delta v_{1/2} = \sqrt{v_0^2 + u_{1/2}^2} - v_0 \tag{3.63}$$

$$u_{1/2} = \frac{\sqrt{2}}{2} \tag{3.64}$$

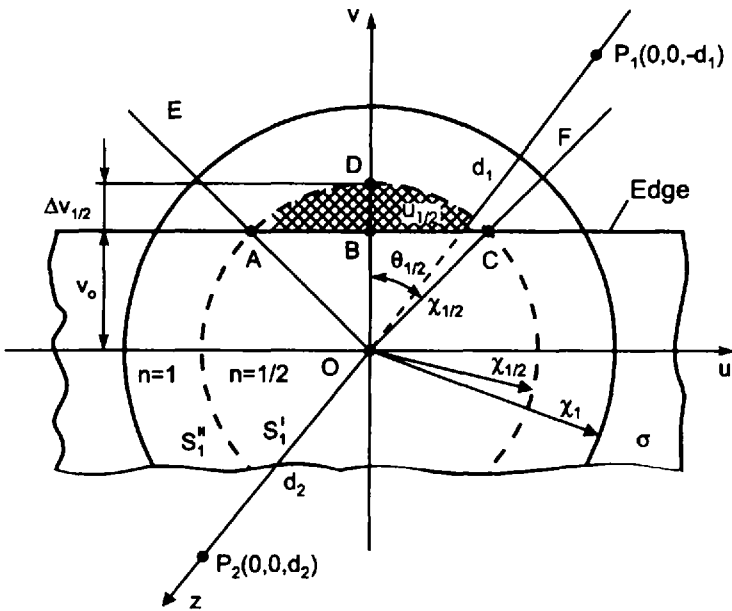


Figure 3.12 Definition of the significant diffraction segment. (After: [21].)

$$\theta_{1/2} = \arctan \frac{u_{1/2}}{v_o} \quad (3.65)$$

where $\chi_{1/2} = \sqrt{2}(b_{1/2}/b_1)$, $\Delta v_{1/2} = OD - OC$ and $u_{1/2}$ are the dimensionless radius, chord height, and chord half-length of the first subzone, respectively. $\theta_{1/2}$ is the angle opposite to the half-chord.

From (3.64) it follows that the dimensionless chord of the significant segment is equal to $\sqrt{2}$ and does not depend on the height of the edge and wavelength. On the other hand, in Section 2.4.4.2 it was shown that the diffraction integral along the infinite screen edge is of value

$$\left| \int_{-\infty}^{+\infty} e^{-j\frac{\pi}{2}u^2} du \right| = \sqrt{2} \quad (3.66)$$

or it exactly equals the segment chord length ($2u_{1/2} = \sqrt{2}$). On this basis, the solution of the Fresnel-Kirchhoff diffraction integral could be much simplified by restriction of the integration procedure within the sector EOF instead of over the whole semi-infinite aperture ($-\infty \leq u \leq +\infty$ and $v_o \leq v \leq +\infty$).

Leaving out the explicit theory derived in [21] we shall confine ourselves here to the ultimate diffraction equations. Consider the following cases:

- Case 1—Diffraction field in the shadow region: The field at the receiving point is given by

$$E(P_2) = E_o(P_2)F'_d(v_o) \quad (3.67)$$

where $E_o(P_2)$ is the field when the screen is absent, and $F'_d(v_o)$ is the field diffraction factor valid for the shadow region only. In general, $F'_d(v_o)$ is a complex expression written in the form

$$F'_d(v_o) = |F'_d(v_o)| e^{j\Phi'_d(v_o)} \quad (3.68)$$

where

$$|F'_d(v_o)| = \frac{1}{\pi} \arctan \frac{1}{\sqrt{2}v_o} \quad (3.69)$$

and

$$\Phi'_d(v_o) = \frac{\pi}{2} [(\sqrt{v_o^2 + 0.5} - v_o)^2 - v_o^2 - 0.5] \quad (3.70)$$

Here v_o is also calculated by (3.60).

- Case 2—Diffraction field in the illuminated region: Now the diffraction factor is written as

$$F''_d(v_o) = |F'_d(v_o)| e^{j\Phi''_d(v_o)} = 1 - |F'_d(v_o)| e^{j\Phi'_d(v_o)} \quad (3.71)$$

so that

$$|F''_d(v_o)| = \sqrt{1 + |F'_d(v_o)| \{|F'_d(v_o)| - 2 \cos[\Phi'_d(v_o)]\}} \quad (3.72)$$

and

$$\Phi''_d(v_o) = \arctan \frac{|F'_d(v_o)| \sin[\Phi'_d(v_o)]}{1 - |F'_d(v_o)| \cos[\Phi'_d(v_o)]} \quad (3.73)$$

Here $|F'_d(v_o)|$ and $\Phi'_d(v_o)$ are found by equations (3.69) and (3.70).

In Figure 3.13 a diffraction factor plot F_d , in decibels, versus the dimensionless edge height v_o is drawn. It was computed from the exact equation

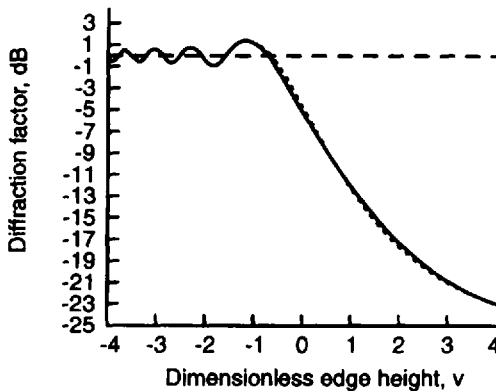


Figure 3.13 Comparison between exact and approximate equations: knife-edge diffraction factor versus dimensionless height drawn by exact equation (dashed line) and approximate equations (solid line).

(3.61), dashed line, and from the approximate, significant segment equations (3.69) and (3.70), solid line.

It is seen that the two curves for F_d run extremely close. The calculations show a maximum error in using the significant segment equations of less than 5%.

3.1.5.4 Four-Ray Diffraction by a Straight Sharp Hill

Often, the knife-edge diffraction scheme includes in addition a reflected ray from smooth earth areas in front and back of the hill of height H_o . In this case, the so-called four-ray diffraction scheme is considered (Figure 3.14) [13, 17].

The total diffraction field at the receiving point P_2 is obtained as a sum of four field components

$$\begin{aligned}
 E(P_2) = & |E_o^{(1-3)}(P_2)| F_{d3}(v_o) e^{-j\beta(r_1+r_3)} \\
 & + |E_o^{(1-4)}(P_2)| F_{d4}(v_o) R(Q'_o) e^{-j\beta(r_1+r_4)} \\
 & + |E_o^{(2-3)}(P_2)| F_{d3'}(v_o) R(Q_o) e^{-j\beta(r_2+r_3)} \\
 & + |E_o^{(2-4)}(P_2)| F_{d4'}(v_o) R(Q) R(Q'_o) e^{-j\beta(r_2+r_4)}
 \end{aligned} \tag{3.74}$$

where $|E_o^{(1-3)}(P_2)|$, $|E_o^{(1-4)}(P_2)|$, $|E_o^{(2-3)}(P_2)|$, and $|E_o^{(2-4)}(P_2)|$ would be the field amplitudes at point P_2 if 1-3, 1-4, 2-3, and 2-4 were free-space propagation paths; $F_{d3}(v_o)$, $F_{d4}(v_o)$, $F_{d3'}(v_o)$, and $F_{d4'}(v_o)$ are the corresponding diffraction factor values due to the incident direct and reflected rays 1 and 2,

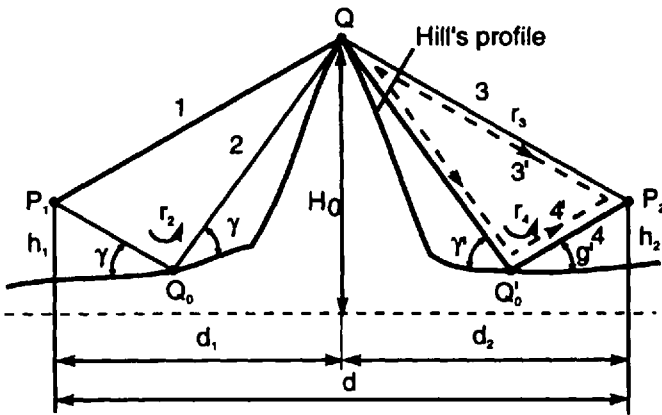


Figure 3.14 Four-ray knife-edge diffraction scheme for narrow hill. (After: [13], © 1987 Prentice-Hall.)

and $R(Q_o)$ and $R(Q'_o)$ are the reflection coefficients at earth points Q_o and Q'_o .

For certain amplitude and phase conditions in the described four-ray diffraction arrangement a so-called obstacle gain is possible. This effect may occur if diffraction losses are not very high and the reflection coefficients have values near to -1 . These assumptions are feasible for small grazing angles γ and γ' .

In case of approximately equal incident and diffraction ray paths, or if $r_1 \cong r_2$ and $r_3 \cong r_4$

$$|E_o^{(1-3)}(P_2)| \cong |E_o^{(1-4)}(P_2)| \cong |E_o^{(2-3)}(P_2)| \cong |E_o^{(2-4)}(P_2)| \cong |E_o(P_2)|$$

and $F_{d3}(v_o) \cong F_{d4}(v_o) \cong F_{d3}(v_o) \cong F_{d4}(v_o) \cong F_d(v_o)$, the total field is given by

$$E(P_2) \cong |E_o(P_2)| F_d(v_o) [e^{-j\beta(r_1+r_3)} - e^{-j\beta(r_1+r_4)} - e^{-j\beta(r_2+r_3)} + e^{-j\beta(r_2+r_4)}] \quad (3.75)$$

For certain favorable relationships between h_1 , h_2 , H_o , d_1 , and d_2 , $F_d(v_o) \rightarrow 1$, and the total field at the receiving point will be about four times the free-space field, or $E(P_2) \cong 4E_o(P_2)$.

For long radio link paths, even in the absence of diffraction obstacles, the receiving point will be in deep shadow, and the field attenuation due to diffraction around the earth will be extremely high. However, the presence of diffraction obstacles can give, in certain circumstances, considerable rise in the field at the receiving point.

3.1.5.5 Radio Wave Diffraction by Sharp Hill With a Round Ridge Section

Consider now a narrow but not straight hill, with a height H that varies along the hill's ridge (Figure 3.15). In that case it would be normal to expect a certain relationship between the field diffracted by the hill and the ridge profile function $H(x)$. The Fresnel diffraction factor by such a hill is found in the form [2]

$$F_d = \frac{1}{b_1} \int_{-\infty}^{+\infty} dx \int_0^{\infty} e^{-j\frac{\pi}{b_1^2}[x^2 + (H(x)+y)^2]} dy \quad (3.76)$$

where $b_1 = \sqrt{d_1 d_2 (d_1 + d_2)}$ is the first Fresnel zone radius.

Commonly, the ridge height change ΔH is much smaller than the ridge height. After denoting with H_{av} the average value of the ridge profile function

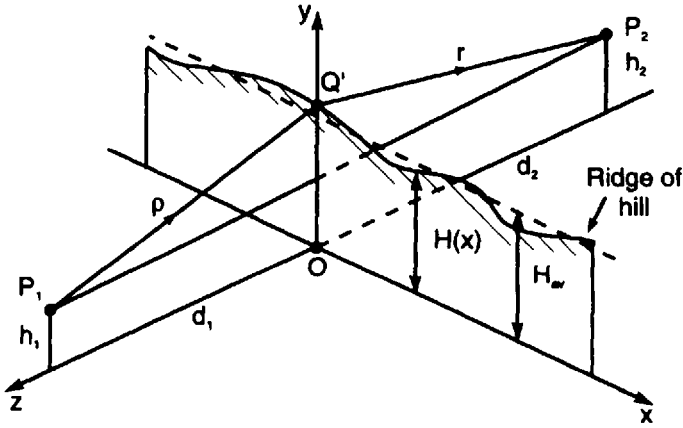


Figure 3.15 Modeling of hill with variable ridge profile by semi-infinite plane. (After: [2].)

$H(x)$ and taking into account that $\Delta H \ll H_{av} = \text{const.}$ (3.76) can be worked over in the following form

$$F_d = \frac{F_d(v_{av})}{b_1} \int_{-\infty}^{+\infty} e^{-j\frac{\pi}{b_1^2}[x^2 + H^2(x)]} dx \quad (3.77)$$

where

$$F_d(v_{av}) = \frac{1}{2}(1 + j)\{[0.5 - C(v_{av})] - j[0.5 - S(v_{av})]\} \quad (3.78)$$

with

$$v_{av} = \frac{\sqrt{2}}{b_1} \left(H_{av} - \frac{d_1 h_2 + d_2 h_1}{d_1 + d_2} \right) \quad (3.79)$$

The Fresnel diffraction integral, and thus, the diffraction factor is reaching maximum value when the exponential power expression in (3.77) becomes independent of x , or

$$x^2 + H^2(x) = \text{const.} \quad (3.80)$$

This is an equation of a circle. Denote with H_0 the value of $H(x)$ for $x = 0$ and then (3.80) becomes

$$x^2 + H^2(x) = H_o^2 \quad (3.81)$$

Thus, when the ridge profile is a round section in the shape of a circular segment ABC of radius H_o and width L (Figure 3.16 [2]), the complex diffraction factor can be found approximately by

$$F_{do} \cong \frac{1}{b_1} F_d(v_{av}) e^{-j\frac{\pi}{b_1^2} H_o^2} \left(\int_{-\infty}^{-L/2} dx + \int_{-L/2}^{+L/2} dx + \int_{+L/2}^{+\infty} dx \right) \quad (3.82)$$

We can neglect the field due to diffraction by the ridge topology outside of the first Fresnel zone segment (or $\int_{-\infty}^{-L/2} dx \cong \int_{+L/2}^{+\infty} dx \cong 0$) and then for (3.82) we find that

$$F_{do} \cong \frac{1}{b_1} F_d(v_o) e^{-j\frac{\pi}{b_1^2} H_o^2} \int_{-L/2}^{+L/2} dx = \frac{L}{b_1} F_d(v_{av}) e^{-j\frac{\pi}{b_1^2} H_o^2} \quad (3.83)$$

with an absolute value

$$|F_{do}| = |F_d(v_{av})| \frac{L}{b_1} \quad (3.84)$$

If the segment width equals the first Fresnel zone diameter (or if $L = 2b_1$) then

$$|F_{domax}| = 2|F_d(v_{av})| \quad (3.85)$$

This is the optimum-in-size round ridge for which the diffraction field at the receiving point is twice the field due to the diffraction by the straight-

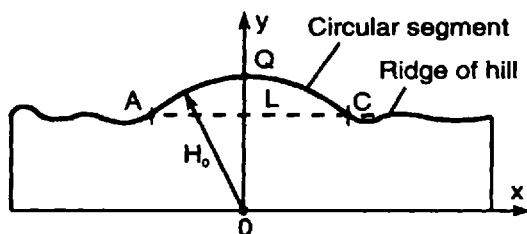


Figure 3.16 Hill with round-shaped ridge segment. (After: [2].)

ridge hill with a height H_{av} that corresponds to an increase in power at the receiving point by 6 dB.

3.1.5.6 Radio Wave Diffraction by Hill Modeled as Multiple Knife-Edge Screen Configuration

For a wide, wedge-shaped straight hill, the widths w_1 and w_2 do not satisfy (3.57), and in this situation the straight ridge may be modeled as a multiple knife-edge screen configuration. In most cases, the three-screen configuration describes very well the wedge-type wide hill (Figure 3.17 [2]).

The total attenuation (diffraction) factor F_d of the above configuration is calculated by [2, 14]

$$F_d = \prod_{i=1}^3 F_d(v_i) \tag{3.86}$$

or in decibels

$$F_d = 20 \log \left[\prod_{i=1}^3 F_d(v_i) \right] \tag{3.87}$$

where

$$F_d(v_i) = \frac{1}{2} (1 + j) \{ [0.5 - C(v_i)] - j[0.5 - S(v_i)] \} \tag{3.88}$$

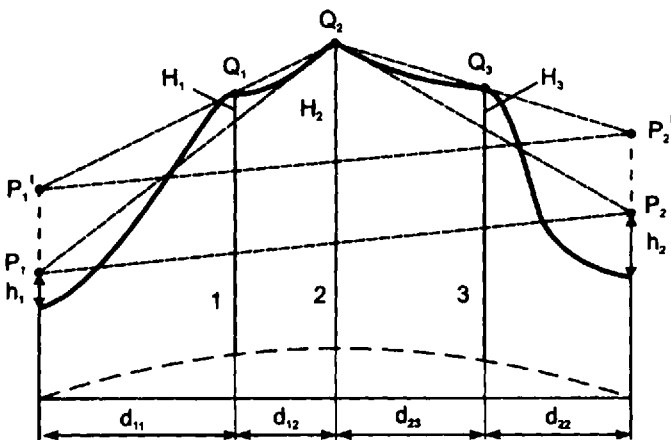


Figure 3.17 Modeling of wedge-shaped wide hill by three knife-edge configuration. (After: [14].)

are the partial (or single knife-edge) attenuation factors, corresponding to $i = 1, 2, 3$, with

$$v_1 = H_1 \sqrt{\frac{2(d_{11} + d_{12})}{\lambda d_{11} d_{12}}} \quad (3.89)$$

$$v_2 = H_2 \sqrt{\frac{2d}{\lambda(d_{11} + d_{12})(d_{23} + d_{22})}} \quad (3.90)$$

$$v_3 = H_3 \sqrt{\frac{2(d_{23} + d_{22})}{\lambda d_{23} d_{22}}} \quad (3.91)$$

Here $d = d_{11} + d_{12} + d_{23} + d_{22}$.

The partial attenuation factors $F_d(v_1)$ and $F_d(v_3)$ correspond to diffraction loss due to the side knife-edge screens 1 and 3, if the receiving antenna is situated at point Q_2 , or at the top of the middle knife-edge screen 2. $F_d(v_2)$ is the attenuation factor corresponding to a diffraction by the middle knife-edge screen in case the radiating antenna is elevated at point P_1' and the receiving antenna at point P_2' .

3.1.5.7 Influence of Refraction in Troposphere on Link Clearance

The influence of the tropospheric refraction is equivalent to a change in the terrain profile and link clearance. For drawing the zero level line when $g_t \neq 0$ the earth radius a_0 in (3.56) is replaced by the equivalent earth radius $a_e = a_0/(1 + a_0 g_t/2)$ and then (3.56) becomes

$$y = \frac{zd}{2a_e} \left(1 - \frac{z}{d}\right) \quad (3.92)$$

All heights in the terrain topology will be changed by $\Delta \bar{y} = y \mp y'$, and the link clearance will be altered by $|\Delta \bar{h}|$, or [14]

$$|\Delta \bar{h}| = -0.25 g_t d_1 d_2 d \quad (3.93)$$

$$|\bar{h}_o| = |h_o| \mp |\Delta \bar{h}| \quad (3.94)$$

Here d_1 , d_2 , and d are taken more or less the same as in the case of zero refraction ($g_t = 0$).

For a positive refraction $g_t < 0$, and the link clearance becomes higher, or $|\bar{h}_o| = |h_o| + |\Delta \bar{h}|$. This example is illustrated in Figure 3.18 where dashed

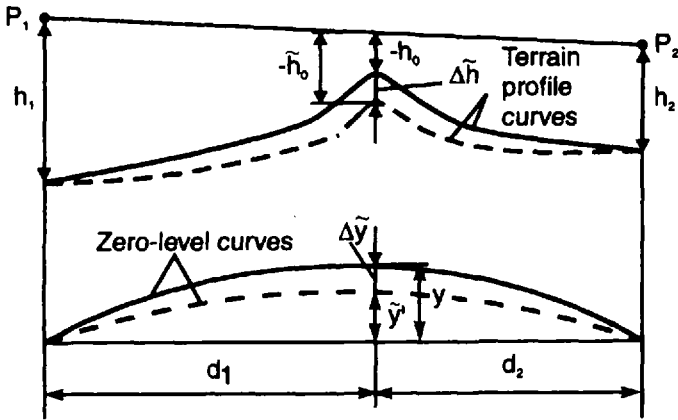


Figure 3.18 Actual zero-level curve terrain profile (solid lines) and equivalent zero-level and terrain profile curves for positive refraction (dashed lines). (After: [14].)

lines plot the equivalent zero-level and terrain profile curves while the solid lines show the actual zero-level and profile curves.

For a negative refraction $g_r > 0$, the link clearance becomes smaller, or $|\tilde{h}_0| = |h_0| - |\Delta\tilde{h}|$.

3.2 Fresnel Zone Diffractors in Radio Relay Links

Not long ago the ground line-of-sight radio relay links were the most widespread and reliable means for the long-distance transmission of microwave signals. Today they give way to satellite, optical, and mobile communication systems. Nevertheless, radio relay links are still serving as important chains of local and global communication networks.

Microwave radio relay links over hilly terrain often make use of constructive mountain diffraction and of man-made passive repeaters. The most efficient and cheaper radio repeaters are the diffractive constructions or so-called radio diffractors. They are placed in front of antennas or on the mountains that shade the line-of-sight paths between radio relay stations. In the former case, the diffractor is named an antenna director, while in the latter one it is called a passive repeater.

Figure 3.19 [22] sketches a section of radio relay link. It comprises two ring-shaped antenna directors D_1 and D_2 and a single passive repeater, PR, placed between two radio relay stations, with antennas A_1 and A_2 [22].

The application of diffractors in radio relay communication links enables a significant increase in distance between the active stations, or a more than

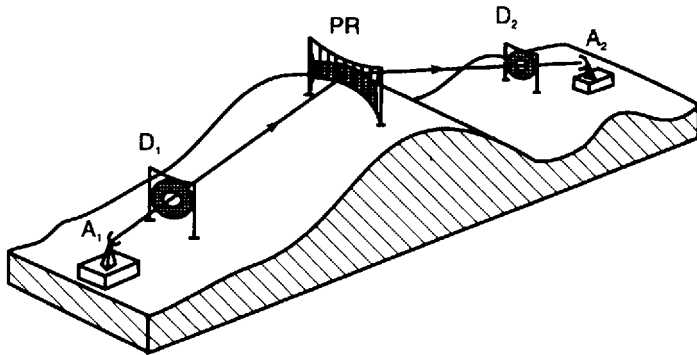


Figure 3.19 Section of radio relay link with two ring directors and a single passive repeater elevated over a mountain. (After: [22].)

25–35-dB rise in power level at the receiver point without wave path length reduction. The diffractors have a simpler structure and a larger aperture efficiency and may be constructed more economically not only compared to active microwave repeaters, but also to periscopic or double-dish passive repeaters. In the present section, we describe metal and dielectric ring-shaped antenna directors and ring segment passive repeaters elevated over mountains.

3.2.1 Metal Ring as Antenna Director

Microwave antennas with a high gain and large aperture efficiency are conventional requisites of radio communication systems. Rise in gain of aperture antennas is normally attained by enlargement of operative antenna dimensions and a suitable feed design. In addition, low material and fabrication costs are desirable goals. The price of a reflector antenna, for instance, is multiplied eight to nine times in doubling its aperture diameter.

In ground radio communication systems the gain of the antenna can be notably increased by adding in front of its radiation aperture a simple focusing diffractor in the shape of a metal ring known as an opaque antenna director [14, 20–26]. The metal ring director covers the second Fresnel zone so that its destructive (or out-of-phase) field is cut off, and the total field at the receiving point becomes much stronger. Another important advantage of the antenna director over the reflector antenna is that its efficiency does not depend substantially on the manufacturing precision.

The directive properties of the antenna system can be determined on the basis of the approximate Fresnel zone theory and more precisely by use of the Fresnel-Kirchhoff diffraction integral (Chapter 2). It was supposed there that the ring was illuminated by a point source of spherical wave. The field at the

focal point was found three times higher by virtue of the ring director only, that is equivalent to a 9.5-dB increase in gain.

The diffraction pattern of a metal ring obstacle illuminated by a uniform spherical wave source can be determined by means of the Babinet's principle [Section 2.4.7, (2.133)]. It is formally valid for ideal complementary screens. Normally, the real reflector is a metal screen that has some (though very small) wave transitivity. It depends on the wave frequency and angle of incidence, screen material, thickness, and solidity. Thus, for a real screen (2.133) is not strictly valid and can be expressed approximately as follows

$$R_{\text{scr}} E_o(P_2) F_d^{(o)}(P_2) < E_o(P_2) - E_o(P_2) E_d^{(a)}(P_2) \quad (3.95)$$

where R_{scr} is the screen reflection coefficient whose value is less but near to one, and $E_o(P_2) = \frac{\sqrt{60P_t}}{d} e^{-j\beta d}$, with $r = d = d_1 + d_2$, and $G_t = 1$.

Therefore, with this assumption in mind we can write for the diffraction factor $F_d^{(\text{m.ring})}$ of the metal ring the following

$$F_d^{(\text{m.ring})} \cong R_{\text{scr}} (1 - F_d^{\text{c.slot}}) \quad (3.96)$$

where $F_d^{\text{c.slot}}$ is the diffraction factor of the ring's complementary annular slot cut in an infinite ideal screen. For the second Fresnel zone slot $F_d^{\text{c.slot}}$ is found by (2.132) for $a_1 = b_1$ and $a_2 = b_2 = b_1\sqrt{2}$.

In case of Fresnel zone slot with radii b_{n-1} and b_n , (2.132) may be rewritten in the form

$$\begin{aligned} F_d^{(\text{c.slot})} &= j\pi \int_{\chi_{n-1}}^{\chi_n} e^{-j\frac{\pi}{2}\chi^2} J_0(k\chi) \chi d\chi \\ &= \frac{j}{2} \{ [C(k, \chi_n) - C(k, \chi_{n-1})] - j[S(k, \chi_n) - S(k, \chi_{n-1})] \} \end{aligned} \quad (3.97)$$

where $\chi_{n-1} = \sqrt{2} \frac{b_{n-1}}{b_1}$ and $\chi_n = \sqrt{2} \frac{b_n}{b_1}$.

However, if the point source is replaced by a directive antenna A , as in practice, the ring will be illuminated unevenly and will produce a smaller increase in gain.

Let d_1 and d_2 be the distances from the ring director to the transmitting antenna and to the receiving point P_2 , respectively. For a known normalized

antenna radiation pattern $F_a(\psi)$ the field taper in the ring plane will depend on distance d_1 . For $d_2 \gg d_1$, d_1 may be chosen according to the following relation [21]

$$\frac{2\lambda}{\tan^2 \psi_{0.7}} \leq d_1 \leq \frac{2\lambda}{\tan^2 \psi_{0.9}} \quad (3.98)$$

Here $\psi_{0.7}$ and $\psi_{0.9}$ are the angles satisfying the equations $F_a(\psi_{0.7}) = 0.7$ and $F_a(\psi_{0.9}) = 0.9$, respectively.

An antenna system comprising a primary antenna and a circular ring director D is sketched in Figure 3.20(a). An exemplary design of a ring director drawn after [22] is shown in Figure 3.20(b). It is made of metal mesh that greatly blocks the destructive second Fresnel zone.

Let us examine now the directive properties of this antenna system in the case of an axially symmetric idealized antenna gain pattern $G_a(\psi)$ given by the following expression [27]

$$G_a(\psi) = \begin{cases} G_{a0} \cos^m \psi, & 0 \leq \psi \leq \pi/2 \\ 0, & \psi > \pi/2 \end{cases} \quad (3.99)$$

where ψ is the illumination angle,

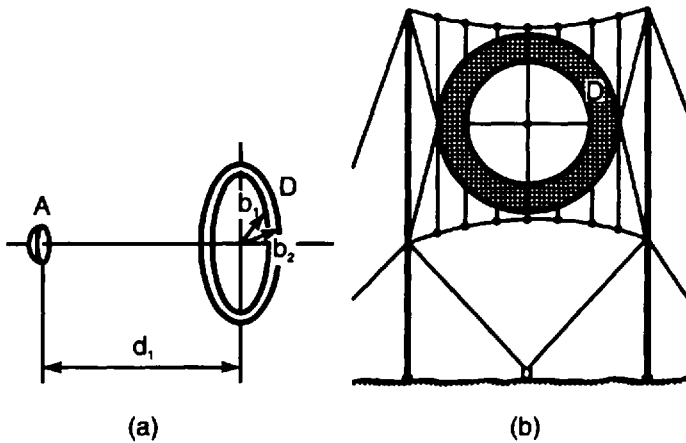


Figure 3.20 Ring-shaped antenna director: (a) sketch of antenna system consisting of primary antenna and metal ring director, and (b) design of ring director made of metal mesh. (After: [22].)

$$G_{ao} = G_a(\psi = 0) = 2(m + 1) \tag{3.100}$$

is the maximum antenna gain, and $m = 1, 2, 3, \dots$ is a positive integer.

The corresponding normalized antenna field pattern $F_a(\psi)$ is

$$F_a(\psi) = \begin{cases} \sqrt{\cos^m \psi}, & 0 \leq \psi \leq \pi/2 \\ 0, & \psi > \pi/2 \end{cases} \tag{3.101}$$

or from (3.99), (3.100), and (3.101) we find that

$$G_a(\psi) = \begin{cases} G_{ao} F_a^2(\psi), & 0 \leq \psi \leq \pi/2 \\ 0, & \psi > \pi/2 \end{cases} \tag{3.102}$$

In decibels, the gain radiation pattern $G_a(\psi)$ is calculated as

$$G_a(\psi) = 10 \log G_{ao} + 20 \log F_a(\psi) \tag{3.103}$$

A geometry comprising a primary antenna A situated at point P_1 and a second zone ring director D placed at a distance d_1 in front of the antenna is shown in Figure 3.21 [20]. Here ψ_1 and ψ_2 are the opening angles corresponding to the inner and outer ring edges.

The electric field at the receiving point $P_2(x_2, 0, d_2)$ is found in accordance with (3.96)

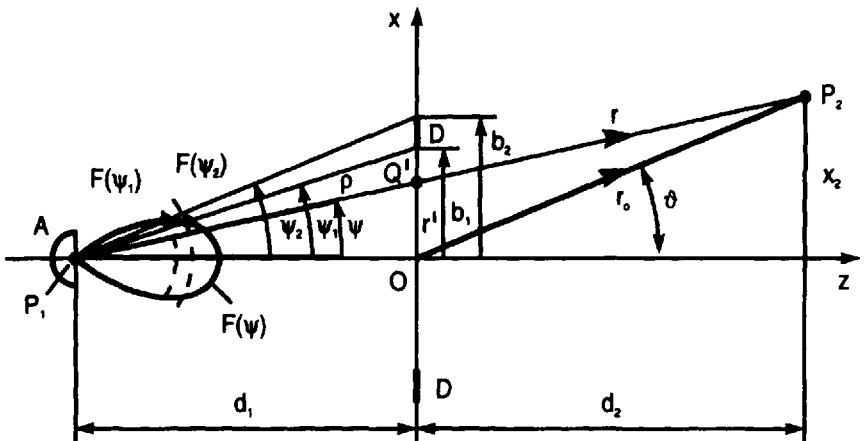


Figure 3.21 Geometry of antenna system consisting of antenna and director. (After: [20].)

$$E(P_2) \cong R_{\text{scr}} F_d^{(\text{m.ring})} E_o(P_2) = R_{\text{scr}} (1 - F_d^{(\text{c.slot})}) E_o(P_2) \quad (3.104)$$

where from (1.31), for transmitting antenna gain $G_t = G_{ao}$ it is written

$$E_o(P_2) = \frac{\sqrt{60 P_t G_{ao}}}{d} e^{-j\beta d} \quad (3.105)$$

with $d = d_1 + d_2$.

If $d_2 \gg d_1$, and $x_2 \ll d_2$, we may put $\psi \cong \vartheta = \arctan\left(\frac{x_2}{d_2}\right)$, that is particularly true for small observation angles (for example, for $\vartheta < 15$ degrees \div 20 degrees).

Here $E_o(P_2)$ is the electric field at the receiving point created by the antenna with the ring removed, and P_t is the antenna radiated power. Now, for a directive ring illumination, by means of (3.96), (3.97), and (3.98), the metal-ring diffraction factor $F_d^{(\text{m.ring})}$ versus the observation angle ϑ can be settled as follows

$$F_d^{(\text{m.ring})}(\vartheta) = R_{\text{scr}} \left\{ F_a(\vartheta) - j\pi \int_{\chi_1}^{\chi_2} F_a(\vartheta) e^{-j\frac{\pi}{2}\chi^2} J_0[k_x(\vartheta)\chi] \chi d\chi \right\} \quad (3.106)$$

Here, we shall recall that

$$\chi = \frac{\sqrt{2}}{b_1} r' \quad (3.107)$$

and therefore $\chi_1(r' = b_1) = \sqrt{2}$, $\chi_2(r' = b_2) = \sqrt{2}b_2/b_1$, with $b_1 = \sqrt{\lambda F_e}$, being the first Fresnel zone radius, and $F_e = d_1 d_2 / (d_1 + d_2)$ being the equivalent focal length.

Also

$$k_x = \frac{2\pi}{\lambda} \frac{b_1}{\sqrt{2}} \frac{x_2}{d_2} = \frac{2\pi}{\lambda} \frac{b_1}{\sqrt{2}} \tan \vartheta \quad (3.108)$$

According to Figure 3.21, the illumination angle ψ can be replaced by the dimensionless radius χ , or

$$\psi = \text{atan}\left(\frac{r'}{d_1}\right) = \text{atan}\left(\frac{b_1}{\sqrt{2}d_1}\chi\right) \quad (3.109)$$

and with $\vartheta \cong \psi$ the normalized field illumination pattern (3.101) becomes

$$F_a(\chi) = \sqrt{\cos^m\left[\text{atan}\left(\frac{b_1}{\sqrt{2}d_1}\chi\right)\right]} \quad (3.110)$$

or (3.106) can be also written in the form

$$F(\vartheta) = F_d^{(m,\text{ring})}(\vartheta) = R_{\text{scr}}\left\{F_a(\vartheta) - j\pi\int_{\chi_1}^{\chi_2} F_a(\chi)e^{-j\frac{\pi}{2}\chi^2}J_0[k_x(\vartheta)\chi]\chi d\chi\right\} \quad (3.111)$$

$F(\vartheta)$ expresses the total radiation pattern of the antenna system consisting of antenna and director.

In an analogy with (3.103) the total antenna gain pattern $G(\vartheta)$ can be also expressed in decibel form, or

$$G(\vartheta) = 10\log G_{a0} + 20\log F(\vartheta) \quad (3.112)$$

In [22] the total field radiation pattern is given in a simplified form as follows

$$F(\vartheta) \cong F_a(\vartheta) + F_a(\psi_1, \psi_2)F_{\text{dir}}(\vartheta)e^{-j\beta d_1}(1 - \cos \vartheta) \quad (3.113)$$

where $F_a(\vartheta)$ is again the normalized primary antenna pattern, and $F_{\text{dir}}(\vartheta)$ is the normalized diffraction pattern of the director, given by

$$F_{\text{dir}}(\vartheta) \cong \frac{7.59[3.47J_0(u_1) + 4.12J_0(u_2)] + ju_1[3.47J_1(u_1) + 4.12J_1(u_2)]}{7.59^2 - u_1^2} \quad (3.114)$$

Here $u_1 = \frac{2\pi}{\lambda}b_1\sin\vartheta$ and $u_2 = \frac{2\pi}{\lambda}b_2\sin\vartheta$. J_0 and J_1 are the Bessel functions of zero and first order, respectively. At first sight, for $u_1 \rightarrow 7.59$ $F_{\text{dir}}(\vartheta) \rightarrow \infty$, but it was proved that for $u_1 \rightarrow 7.59$, $F_{\text{dir}}(\vartheta)$ is equal to $0.202\exp(j121 \text{ degrees})$.

$$F_a(\psi_1, \psi_2) = F_a(\psi_1) + F_a(\psi_2) \quad (3.115)$$

The primary, axially symmetric gain pattern $G_a(\vartheta)$, calculated from (3.102) for $\psi \equiv \vartheta$, and $m = 6,000$ is drawn with a dashed line in Figure 3.22. Its maximum value is $G_{a0} = G_a(0 \text{ degrees}) = 40.8 \text{ dB}$. Figure 3.22 compares the exact system gain pattern (solid line), (3.106) for $R_{scr} = 1$, and the approximate system gain pattern (dotted line), (3.113), both calculated for a frequency of 8 GHz, $d_1 = 400\text{m}$, $d_2 = 25,000\text{m}$, $b_1 = 3.84\text{m}$, and $b_2 = 5.43\text{m}$. As it is seen, due to the metal ring director there is a sharp increase in gain close to $\vartheta = 0$ degrees, and a very narrow main lobe is formed.

From Figure 3.22 it is concluded that the approximated radiation pattern agrees well with the exact one, especially for small observation angles. The maximum gain of the antenna system is $G(0 \text{ degrees}) \equiv 49.3 \text{ dB}$, or the gain enhancement due to the metal director is 8.4 dB. So, this value is 1.1 dB less than the gain increase given by the uniformly illuminated metal director [or 9.5 dB, according to (2.48) and (3.112) for $R_{scr} = 1$ and $F_a(\vartheta) = 1$].

The experimental radiation pattern of the above antenna system, for the same frequency and dimensions, is plotted with a solid line in Figure 3.23 [22]. It is compared to the experimental radiation pattern of a primary horn antenna (dashed line). For a small angle of observation the experimental pattern of the antenna system is similar to the calculated radiation pattern shown in Figure 3.22.

As a result of reflection from the metal director the back lobes of the radiation pattern become intolerably high (around $-10 \div -15 \text{ dB}$). Also, there is an increase of sidelobes off the main lobe over a wide angular range. The

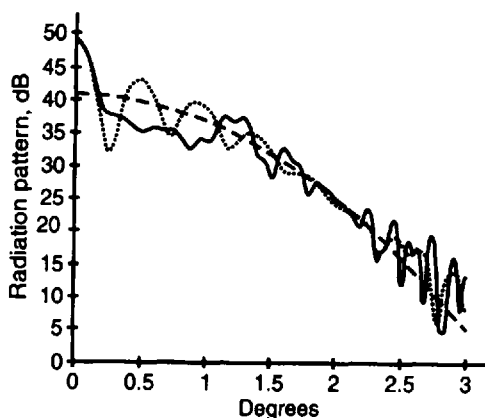


Figure 3.22 Primary antenna pattern of antenna (dashed line) and antenna system pattern: exact (solid line) and approximate (dotted line).

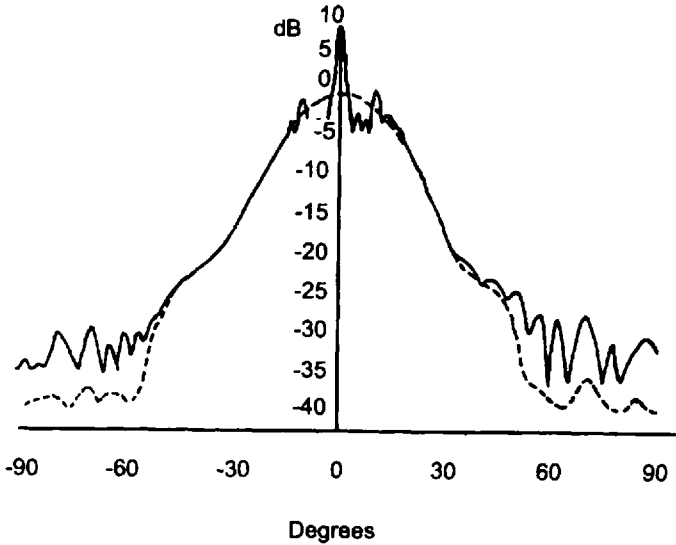


Figure 3.23 Experimental radiation pattern of horn antenna without director (dashed line) and with metal ring director (solid line).

experiments show that the back lobes could be lessened to $-25 \div -35$ dB down by a small inclination of the ring or to much lower levels using dielectric ring directors.

3.2.2 Dielectric Ring as Antenna Director

As it was said, the metal ring director cuts off the destructive field of the second Fresnel zone and acts as passive amplifying element. On the other hand, however, the director area is lost for the reradiation process, so the ring aperture radiation efficiency is decreased.

Instead, if the second zone field is not obstructed but reversed in phase by any means, this will give a bigger total field and, hence, a higher antenna system gain. Practically, such means may be any kind of π radians phase shifter in shape of transmissive ring replacing the metal ring director. The ideal π radians phase shifter is one that has a transmission coefficient $T = -1$.

In the simplest case the phase-reversing director is a ring cut out by a solid dielectric plate with thickness t_π corresponding to a phase lag of π radians compared to the wave passing through the open aperture and found by

$$t_\pi = \frac{\lambda}{2(\sqrt{\epsilon_r} - 1)} \quad (3.116)$$

where ϵ_r is the relative permittivity.

If an ideal dielectric director is illuminated by a very distant point source, or almost uniformly, its maximum possible gain is about 25 (or 14 dB). However, the actual dielectric director has a smaller gain as a result of dielectric loss and mismatch with the surrounding free space.

The transmission loss L_t in a dielectric plate of thickness t_π is

$$L_t = e^{-\frac{\pi}{\lambda} \sqrt{\epsilon_r} \tan \delta_r t_\pi} \quad (3.117)$$

where $\tan \delta_r$ is the electric loss tangent.

The transmission loss L_d causes a gain decrease ΔG calculated in decibels by [25, 26]

$$\Delta G = 20 \log \left\{ \frac{1}{2} \left[1 + e^{-\frac{\sqrt{\epsilon_r} \tan \delta_r}{2(\sqrt{\epsilon_r} - 1)}} \right] \right\} \quad (3.118)$$

The mismatch between the phase-reversing dielectric plate of thickness t_π and the free space may be characterized by its power transmission coefficient $|T|^2$ [26]

$$|T_d|^2 = 1 - \frac{1}{1 + \frac{4\epsilon_r}{(\sqrt{\epsilon_r} - 1)^2} \operatorname{cosec} \frac{\sqrt{\epsilon_r}}{(\sqrt{\epsilon_r} - 1)}} \quad (3.119)$$

Analysis of (3.119) shows that $|T_d|^2 = 1$ for a number of ϵ_r , but the most suitable is about 4.0. With this value put in (3.118) the gain decrease ΔG is less than 0.2 if $\tan \delta_r$ does not exceed 0.015.

The diffraction pattern of a dielectric ring obstacle illuminated by a uniform spherical wave source can be found starting from (3.96), rewritten here for $R_{\text{scr}} = 1$ as follows

$$F_d^{(\text{m.ring})} = 1 - F_d^{(\text{c.slot})} \quad (3.120)$$

The diffraction factor $F_d^{(\text{d.ring})}$ of dielectric ring director (same in radial size as the corresponding metal ring), may be expressed as follows

$$F_d^{(\text{d.ring})} = F_d^{(\text{m.ring})} + T_d F_d^{(\text{c.slot})} \quad (3.121)$$

where T_d is the complex transmission coefficient of the dielectric ring.

For the ideal π -phase shifting ring we put in (3.121) $T_d = 1$ and therefore

$$F_d^{(d.\text{ring})} = F_d^{(m.\text{ring})} - F_d^{(c.\text{slot})} = 1 - 2F_d^{(c.\text{slot})} \quad (3.122)$$

The total field E at the receiving point P_2 radiated by the system of antenna with an axially symmetric pattern $F_a(\vartheta)$ and a phase-reversing dielectric ring director may be expressed in the form

$$E(P_2) = E_o(P_2)F_d^{(d.\text{ring})} = \left\{ F_a(\vartheta) - j\pi \int_{\chi_1}^{\chi_2} F_a(\chi) e^{-j\frac{\pi}{2}\chi^2} J_o\{k_x(\vartheta)\chi\} \chi d\chi \right\} \quad (3.123)$$

Figure 3.24 shows the gain pattern of the antenna system with a dielectric ring director located in front of the primary antenna at a distance $d_1 = 400\text{m}$ (solid line). It is compared to the radiation pattern of the antenna with a metal ring director (dotted line) and the primary antenna pattern (dashed line). The two antenna systems, with metal and dielectric ring directors, were studied for one and the same parameters given in Section 3.2.1. Calculations show that replacing the metal ring director by phase reversing the dielectric one gives a total antenna system gain of 53.4 dB or 4.1 dB higher than the

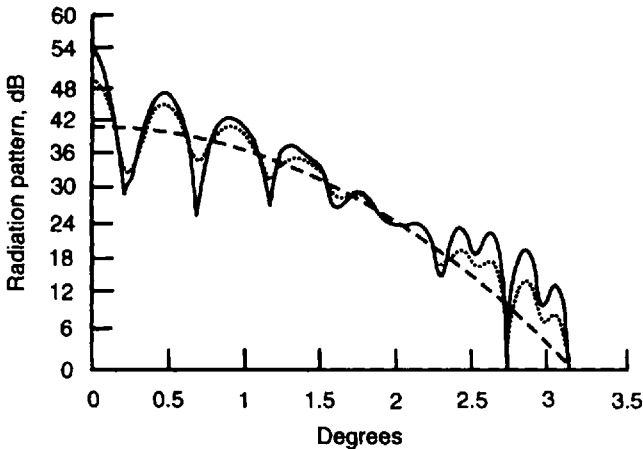


Figure 3.24 Gain diffraction pattern of an antenna system with a dielectric ring director (solid line) compared to the gain diffraction pattern of an antenna system with a metal director (dotted line) and a primary antenna radiation pattern (dashed line).

gain of the antenna system with the metal director. The gain increase over the gain of the primary antenna is 12.6 dB (remember that for a uniformly illuminated phase-reversing ring the gain increase is about 14 dB).

Up to this point, we have examined only solid dielectric ring directors. There are many other dielectric or dielectric-like plate designs that can be utilized in the manufacture of directors or passive repeaters. Examples include multilayered dielectric plates, metal grid reinforced dielectrics, or dielectric-like (or phase-delay) metal structures. Theory and specific constructions of complex dielectric and dielectric-like plate structures will be considered in Chapters 4 and 5 in connection with designing and manufacturing zone plate lenses or antennas.

3.2.3 Ring Segment Diffractor as Passive Radio Wave Repeater

A segment of Fresnel zone opaque ring S_F raised over a hill shading the receiver point P_2 (Figure 3.25 [20]) may serve as an efficient passive repeater. It screens only a part of an arbitrary Fresnel zone and forms a broad secondary radiation (diffraction) pattern in the vertical plane, and thus, the receiver point becomes illuminated. The geometry of such a segment ring diffractor is shown in Figure 3.26. Here the segment diffractor fits into a fraction of the first Fresnel zone with zone radii $b_n = \sqrt{n\lambda F_e}$ and $b_2 = \sqrt{2b_1}$.

The principal dimensions of the ring sector repeater are its length $2l$ and width δb , in addition to its curvature parameter c . They can be calculated by the following relations [20, 22]

$$\delta b_{\text{opt}} = b_2 - b_1 \cong \frac{\lambda}{2 \sin \vartheta_o} \quad (3.124)$$

$$\vartheta_o = \frac{\rho + r}{2a_o} + \frac{H - h_1}{\rho} + \frac{H - h_2}{r} \quad (3.125)$$

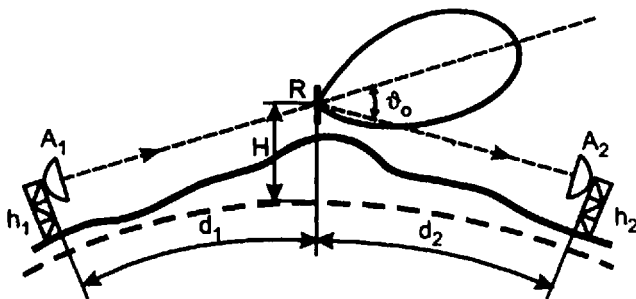


Figure 3.25 Passive repeater over hill between two radio stations. (After: [22].)

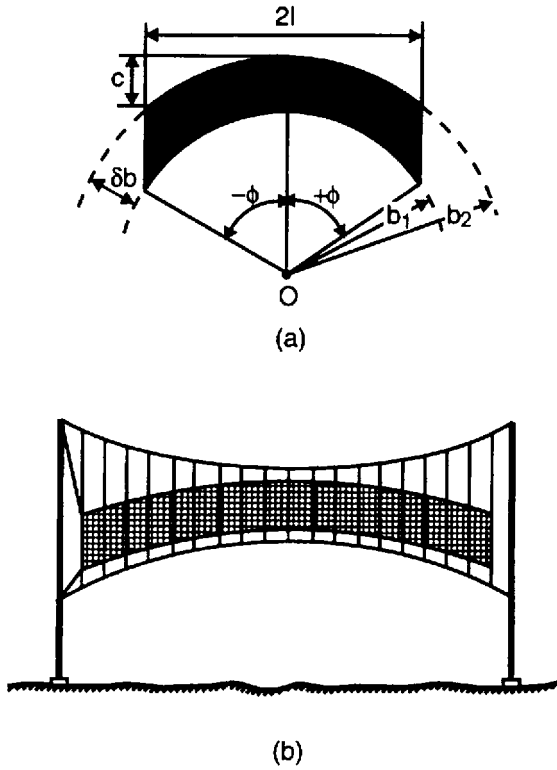


Figure 3.26 Ring segment diffractor as passive repeater: (a) geometry of diffractor and (b) design of passive repeater. (After: [20].)

$$c = 0.5 \delta b_{\text{opt}} \left(\frac{2l}{\sqrt{2\lambda F_e}} \right)^2 = 0.5 \delta b_{\text{opt}} \bar{L}^2 \tag{3.126}$$

where a_o is the earth's radius, and ϑ_o is the angle between the directions of the incident ray A_1Q and diffracted ray QA_2 pointing to the receiving point (see Figure 3.25 [22]). Depending on the link length and terrain profile, this angle may reach 15 degrees + 25 degrees.

In (3.126) \bar{L} is a normalized diffractor length, expressed as

$$\bar{L} = \frac{2l}{\sqrt{2\lambda F_e}} \tag{3.127}$$

For long-haul links, $\vartheta_o \ll 1$ and the next approximations become true: $\sin \vartheta_o \cong \vartheta_o$, $\rho \cong d_1$, and $\rho \cong d_1$. Also

$$\delta b \equiv \frac{\lambda}{2\vartheta_0} \quad (3.128)$$

$$\vartheta_0 = \frac{\rho + r}{2a_0} + \frac{H - h_1}{\rho} + \frac{H - h_2}{r} \quad (3.129)$$

To make radio diffractors lighter, cheaper, and wind-resistant, they are made in practice as nonsolid structures. As an example we shall describe briefly a parallel wire grid.

This structure is polarization-anisotropic, and it is a good reflector only for the incident wave with an electric field vector parallel to the wires. If we mark with d_w the interwire distance, with ρ the wire radius and with ψ the wave incidence angle measured from the grid normal, the complex reflection coefficient R_{scr} for a dense parallel wire grid is found by the following approximate equation [22]

$$R_{\text{scr}} = -\frac{1}{1 + j \frac{2d_w}{\lambda} \ln \frac{d_w}{2\pi\rho}} \quad (3.130)$$

which is used for $d/\lambda < 0.15 \div 0.25$.

In an analogy with the dielectric ring director the efficiency of the ring segment repeater can be increased by 6 dB (in theory) if it acts as a π -radians phase shifter made of dielectric plate. While the screen-type diffractor cuts off the wave component out of phase to the received field, the dielectric-type diffractor will transform this component into an in-phase one, and thus, it will strengthen the signal at the receiver point.

Other advantages of the dielectric-type passive repeater over the equal in size screen-type one are [25, 26]: (1) a twice-reduced aperture for the same gain, (2) broader frequency characteristics, and (3) much smaller back lobes in the diffraction pattern.

The dielectric-type passive repeaters also have some constructive and manufacturing disadvantages, such as bigger thickness and weight and higher cost. All other explanations and equations presented above for the ring-shape dielectric director are also entirely valid for the dielectric passive repeater.

Now we shall provide some additional data on the dielectric materials suitable for manufacturing of passive diffractors. Except to make proper phase shifting, the diffractor plate has to satisfy a lot of structural, electrical, and environmental requirements. In the foregoing discussion, it was pointed out that for the solid phase-reversing dielectric plate, the most appropriate value

of its permittivity ϵ_r , is about 4.0. Along with this, it has to be made by high-frequency (or low-loss) dielectric, with a loss tangent less than 0.01.

In [25] it was reported that the first dielectric-type diffractors were fabricated by polyester or silicone resin reinforced with glass fiber. At a carrier frequency of 11 GHz a permittivity of 3.9–4.1 was obtained for a resin plate with a thickness between 13.25–14.20 mm.

Today, a great selection of rubberized fabrics and other high-quality dielectric-type materials much better for the manufacture of dielectric diffractors are available.

A further increase in efficiency can be achieved by making a repeater in the form of a vertical grating consisting of several ring segment elements [Figure 3.27(a)] [20]. In principle, the grating is acting as a Soret's type Fresnel plate lens, consisting not of whole zone rings, but only of zone ring segments [Figure 3.27(b)]. Therefore, the widths and spacings of ring segments are easily found

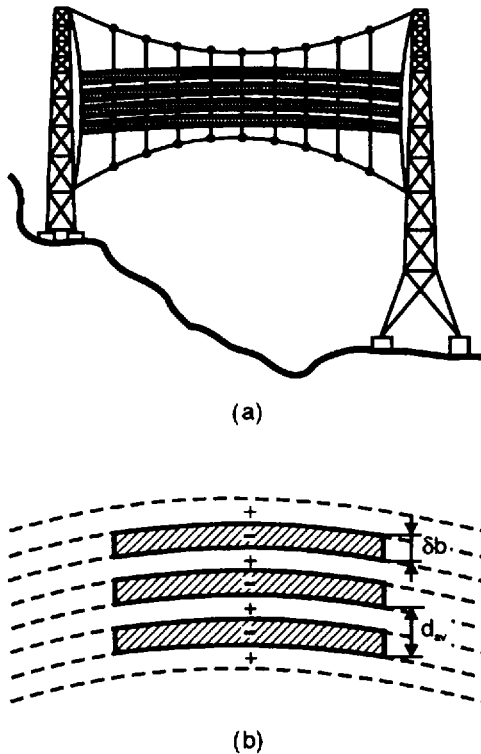


Figure 3.27 Design of passive grating repeater of ring segment elements: (a) construction of passive repeater comprising four ring segment diffractors (After: [20]), and (b) geometry of Fresnel zone segment array.

by the Fresnel zone size equations and the equations (3.124)–(3.129) for a passive repeater in the form of a single ring segment.

The Fresnel diffraction pattern of the ring segment repeater can be calculated by analogy with (3.112), with integration over φ' within the angular sector 2Φ [Figure 3.25(a)]. Thus, the segment diffraction factor $F_d^{(m,seg)}$ may be expressed as

$$F_d^{(m,seg)} = R_{scr} \left\{ F(\vartheta) - \frac{j}{2} \int_{-\Phi}^{+\Phi} \int_{\chi_1}^{\chi_2} F(\chi) e^{-j \left[\frac{\pi}{2} \chi^2 - k_x(\vartheta_x) \chi \cos \varphi' - k_y(\vartheta_y) \chi \sin \varphi' \right]} \chi d\chi d\varphi' \right\} \quad (3.131)$$

However, instead of dealing with the complicated (3.131), which comprises a double integral in calculating the segment diffraction pattern, we can use the next simplified diffraction expressions, taken from [20].

The overall diffraction pattern of the ring-segment repeater is found in the following approximate form

$$F_d(u, v) = \frac{\sin\left(\frac{\pi}{2} v\right)}{\frac{\pi}{2} v} \frac{|F(\xi_1) + F(\xi_2)|}{2k_v |F(\bar{L})|} \quad (3.132)$$

where

$$F(\xi_{1,2}) = \int_0^{\xi_{1,2}} e^{-j \frac{\pi}{2} t^2} dt \quad (3.133)$$

and

$$F(\bar{L}) = \int_0^{\bar{L}} e^{-j \frac{\pi}{2} t^2} dt \quad (3.134)$$

are complex integrals with $\xi_{1,2} = \bar{L} q_v \mp \frac{u}{q_v}$, $q_v = \sqrt{|1-v|}$, $v = \vartheta/\vartheta_0$, $u = \sqrt{2F_c/\lambda} \sin \varphi$. Here φ and ϑ are the observation angles to point P_2 in the horizontal plane and vertical plane, respectively. The ray QP_2 has angular coordinates $\varphi = 0$ degrees and $\vartheta = \vartheta_0$, as shown in Figure 3.25.

The vertical diffraction pattern is calculated from (3.132) for $\varphi = 0$ degrees, and the horizontal diffraction pattern is also calculated from (3.132) for $\nu = 1$ (or $\vartheta = \vartheta_0$). In the latter case (3.132) may be simplified further to become

$$F_d(\vartheta) = \frac{\sin\left(\frac{2\pi}{\lambda} l \sin \vartheta\right)}{\frac{2\pi}{\lambda} l \sin \vartheta} \quad (3.135)$$

This is the well-known expression for the radiation pattern of an antenna with uniform aperture field.

The vertical diffraction pattern of the passive repeater grating consisting of N ring segment elements can be calculated approximately using the well-known antenna pattern multiplication equation valid for equidistant arrays

$$F_N(\vartheta, \varphi) = F_d[\nu(\vartheta), u(\varphi)] \frac{\sin(0.5N\beta d_{av} \sin \vartheta \sin \varphi)}{\sin(0.5\beta d_{av} \sin \vartheta \sin \varphi)} \quad (3.136)$$

where N is the number of grating elements, $\beta = 2\pi/\lambda$ is the free-space phase constant, $d_{av} \cong 2\delta b_{av}$ is the average array distance found by the mean value formula

$$d_{av} \cong 2 \frac{\sum_{i=1}^N \delta b_i}{N} \quad (3.137)$$

and $F_d[\nu(\vartheta), u(\varphi)]$ is the element diffraction pattern as given by (3.131).

Let us now illustrate the directive properties of the ring segment repeaters with the following numerical example. The ring segment repeater is mounted over a hill at a height $H = 350\text{m}$ above the ground-zero level. The radio-relay station antennas are lifted at heights $h_1 = 150\text{m}$ and $h_2 = 120\text{m}$, and their distances to the passive repeater footing are $d_1 = 35,000\text{m}$ and $d_2 = 50,000\text{m}$, respectively (Figure 3.25). The signal carrier frequency is 10 GHz. For these link dimensions and this frequency the following segment dimensions were computed: $2l = 21.1\text{m}$, $\delta b = 0.88\text{m}$, and $\delta H = 0.16\text{m}$. The angle ϑ_0 for this long-haul radio link was found equal to 0.97 degrees.

In Figure 3.28 the normalized vertical diffraction pattern of the ring segment passive repeater (solid line) is compared to the corresponding patterns

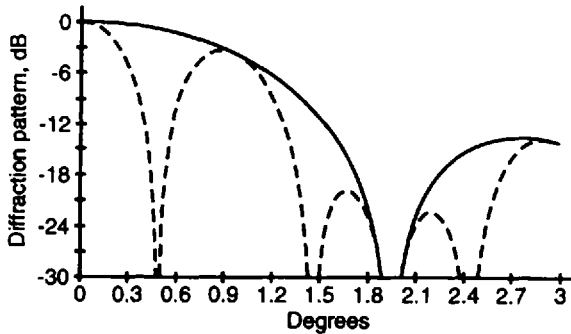


Figure 3.28 Vertical diffraction pattern of (a) a one-segment repeater (solid line) and (b) a two-segment repeater grating (dashed line).

of the two-element grating (dashed line) and three-element grating (dotted line). It is seen that the field amplitude of the wave ray pointing toward the receiver is only 3–4 dB less than the maximum level in the zero direction.

Though the absolute field value at the receiving point produced by the three-element grating is much bigger than the field in the case of the single element repeater, we should remember that it is created by a very narrow sidelobe. This makes the radio communication between the two stations very unstable in case of a big change in troposphere refraction conditions with time. As the horizontal segment size is much larger than the vertical, it is natural to expect a very narrow diffraction pattern in the horizontal plane. For the link and segment parameters given above, the horizontal diffraction pattern has a 3-dB beamwidth equal to 0.08 degrees and a first sidelobe level of -13 dB (Figure 3.29).

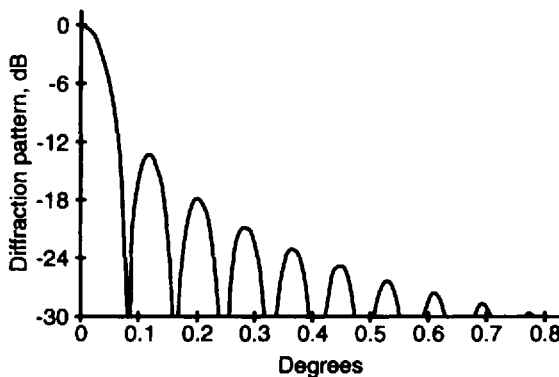


Figure 3.29 Horizontal diffraction pattern of a one-segment passive repeater.

References

- [1] Millington, G., R. Hewitt, and F. S. Immirzi, "Double Knife-Edge Diffraction in Field-Strength Predictions," *IEE Proceedings*, Vol. 109, Pt. C, 1962, pp. 419–429.
- [2] Troitski, V. N., "Some Topics on UHF Diffraction by Mountain Ridges," *Electrosvyaz*, No. 12, 1964, pp. 9–15 (in Russian).
- [3] Degout, J., "Multiple Knife-Edge Diffraction of Microwaves," *IEEE Trans. Antennas and Propagat.*, Vol. 14, No. 4, 1966, pp. 480–489.
- [4] Whitteker, J. H., "Fresnel-Kirchhoff Theory Applied to Terrain Diffraction Problems," *Radio Science*, Vol. 25, No. 5, Sept.–Oct. 1990, pp. 837–851.
- [5] Whitteker, J. H., "A Series Solution for Diffraction Over Terrain as Multiple Bridged Knife Edges," *Radio Science*, Vol. 28, No. 4, July–Aug. 1993, pp. 487–500.
- [6] Whitteker, J. H., "Physical Optics and Terrain Diffraction," *The Radio Scientist*, URSL, Vol. 5, Sept. 1994, pp. 111–116.
- [7] Whitteker, J. H., "Diffraction Over a Flat-topped Terrain Obstacle," *IEE Proceedings*, Vol. 137, Pt. H, 1990, pp. 113–116.
- [8] Savov, S. V., and J. B. Andersen, "Efficient Method for Calculation of Fresnel Double Integral," *Electronics Letts.*, Vol. 31, No. 6, Mar. 16, 1995, pp. 435–436.
- [9] Savov, S. V., and J. H. Whitteker, "Diffraction of Electromagnetic Waves by a Block-Shaped Obstacle," *Proc. North American Radio Science Meeting*, Montreal, Canada, July 1997, p. 430.
- [10] Savov, S. V., J. H. Whitteker, and R. Vassilev, "Attenuation of Waves Behind a Building," *Proc. of IEE*, Pt. H., (accepted).
- [11] Jordan, E. C., and K. G. Balmain, *Electromagnetic Waves and Radiating Systems* (2d ed), New Jersey: Prentice-Hall, 1968.
- [12] Kalinin, A. I., *Propagation of Radio Waves Over Ground and Space Radio Links*, Moscow: Svyaz, 1979 (in Russian).
- [13] Griffiths, J., *Radio Wave Propagation and Antennas*, London: Prentice-Hall, 1987.
- [14] Borodich, C. V. (editor), *Handbook on Radio Relay Communications*, Moscow: Radio i Svyaz, 1981 (in Russian).
- [15] Cherni, F. B., *Propagation of Radio Waves*, Moscow: Sovetskoe Radio, 1962 (in Russian).
- [16] Alpert, Ya. L., V. L. Ginzburg, and E. L. Feinberg, *Propagation of Radio Waves*, Moscow: State Publ. House for Technical and Theoretical Literature, 1953 (in Russian).
- [17] Doluhanov, M. P., *Propagation of Radio Waves*, Moscow: Mir, 1971.
- [18] Burrows, C. R., and S. S. Attwood (editors), *Radio Wave Propagation*, New York: Academic Press, 1949.
- [19] Cherveniy, V., and J. E. P. Soares, "Fresnel Volume Ray Tracing," *Geophysics*, Vol. 57, No. 7, July 1992, pp. 902–915.
- [20] Yampolski, V. G., and G. Z. Aizenberg, *Passive Repeaters for Radio Relay Links*, Moscow: Svyaz, 1972 (in Russian).
- [21] Turusbekov, M. T., *Diffraction and Passive Retranslating of Ultra Short Waves Over Mountain Terrain*, Frunze: ILIM, 1979 (in Russian).

-
- [22] Aizenberg, G. Z., V. G. Yampolski, and O. N. Tereshin, *Microwave Antennas*, Part Two, Moscow: Svyaz, 1977 (in Russian).
 - [23] Nepomnyaschi, I. L., and V. G. Yampolski, "Method for Efficiency Increase of Radio Relay Antenna," *Electrosvyaz*, Moscow, No. 1, 1973, pp. 24–30 (in Russian).
 - [24] Baibosunov, M., O. Mamaev, T. Orozbekov, and M. Turusbekov, "Development and Testing of Zone Antenna Attachment in Radio Relay Link," *Electrosvyaz*, Moscow, No. 5, May 1972 (in Russian).
 - [25] Takada, M., and M. Shinji, "An Application of the Diffractor Grating to the 11-Gc/s Microwave Systems," *IEEE Trans. Antennas Propagat.*, July 1965, pp. 532–541.
 - [26] Takada, M., and I. Ebihara, "Microwave Diffractor Grating as a New Passive Repeater," *Japan Telecom. Review*, 1967, pp. 202–209.
 - [27] Silver, S. (editor), *Microwave Antenna Theory and Design* (MIT Radiation Lab. Series, Vol. 12), New York: McGraw-Hill, 1949.

This page intentionally left blank

4

Fresnel Zone Plates

4.1 Introduction

Here we recall the story of the Fresnel zone plates following mainly [1–6]. The idea behind the zone plate consisting of alternate transparent and opaque annuli originated from the Fresnel zone principle and construction and was developed and first described by Soret [7]. Lord Rayleigh noted that the power intensity at the zone plate focus could be increased four times if the opaque zones were made transparent but constructive with a further retardation of $\lambda/2$. It was Wood, however, who proposed several ways for realizing Lord Rayleigh's idea. He further studied the Soret zone plate and created the so-called phase-reversal zone plate [1, 8]. In the Wood zone plate designs the alternate zones are retarded or advanced by π radians in such a way that all zones are productive.

Soret's invention was briefly described by Wood in the very beginning of his paper on phase-reversal zone plates and diffraction telescopes [1]: "In a paper published in Poggendorff's *Annalen* (1875) Soret showed that if we describe a number of small concentric circles on a glass plate, with radii proportional to the square roots of the natural numbers, and blacken the spaces between the alternate rings, the plate will have the property of bringing parallel rays of light to a focus, like a condensing-lens." Several lines below Wood continued: "He (Soret) showed that such a plate forms real images of luminous objects and could be used as the objective of a telescope or as the eyepiece. He also showed that in addition to acting as a condensing lens, the zone plate acted as a concave or dispersing lens. Moreover, he pointed out that the plate has multiple foci at distances a^2/λ , $a^2/3\lambda$, $a^2/5\lambda$, where a is the radius of the central circle."

After this fair recognition of Soret's remarkable achievement Wood goes on to point out Lord Rayleigh's merit and his own work for creation of the phase-reversal zone plate: "It has been pointed out by Lord Rayleigh that if it were possible to provide that the light stopped alternate zones were replaced by phase-reversal, a fourfold effect would be produced. After some experimenting I have succeeded in producing such a zone plate, perfectly transparent over its entire extent." Next Wood reports about the first ever practical application of the Fresnel zone plate: "Using one of the new plates as the objective of a telescope in connection with a low-power eyepiece, I have distinctly seen the lunar craters and have constructed telescopes in which both objective and eyepiece were zone-plates."

As the operation principle of the electromagnetic zone plate is valid at any wavelength it is applicable not only as an optical lens-like device [2–4, 9–24], but also at the RF, microwave, and millimeter-wave ranges.

Developments and applications in zoned plate lenses, similar to those in optics, have also been made in acoustics [25–28]. Curiously, the acoustical Fresnel zones are occasionally called Huygens' zones [28].

The first Fresnel zone plate used at microwaves was patented in 1936 [29]. In the next three decades extensive experimental study on several zone plate varieties was carried out at frequencies from the X to the K band [30–33, Sanyal and Singh, Selected Bibliography]. The initial millimeter-wave study of the phase-reversal zone plate lenses started during the late 1950s, and the basic results were published in 1961–62 [34, 35].

From the very beginning the main efforts in studying microwave/millimeter-wave Fresnel zone plates have been exerted toward increasing their focusing efficiency. This has been achieved with the following techniques:

- The usage of a reflector behind the zone plate [29, 32, 36, 37];
- The division of each full-wave zone into a number of subzones covered by phase-shifting ring elements [5, 38–52];
- The usage of three-dimensional plate lenses (e.g., spherical, parabolic, conical) instead of planar ones [9, 37, 53–60].

4.2 Classification of Fresnel Zone Plates

The process of face-view and cross-sectional alteration of the Fresnel zone plate to improve its lens-like properties and to expand its diverse applications begins with the classical Soret zone plate. Then it goes through all varieties of the Wood zone plate to the modulated and curvilinearly patterned zone plate structures. Today there is a great number of Fresnel zone plates differing in

their zone shapes, transmission cross structure, and technological features. Therefore, some kind of Fresnel zone plate sorting is necessary, and we shall try to proceed here mainly from the point of view of the Fresnel zone plate microwave/millimeter-wave practice.

Depending on the mode of wave propagation through the plate structure we may divide the Fresnel zone plates into two basic configurations: transmission Fresnel zone plates and reflection Fresnel zone plates, which are similar in their zonal surfaces and cross-view structures. According to their geometry, the Fresnel zone plates are shaped as planar and curved configurations.

4.2.1 Classification According to Shape of Zonal Surface

Fresnel zone plates can be manufactured on different surfaces—planar or curvilinear. Here we propose an exemplary classification of zone plate configurations depending on the shape and illumination manner.

4.2.1.1 Planar Fresnel Zone Plates

From a practical point of view the planar in form zone plates are most popular. It is not by chance that the original Fresnel, Soret, and Wood zone plates were plane constructions remarkable for their simplicity, small size, and weight.

Figure 4.1(a) illustrates a planar zone plate with circular Fresnel zones. If a plane wave is incident normally to the Fresnel zone plate surface, it is transformed into a spherical wave focused at some axial point. A spherical wave illuminating the Fresnel zone plate can be converted into a spherical

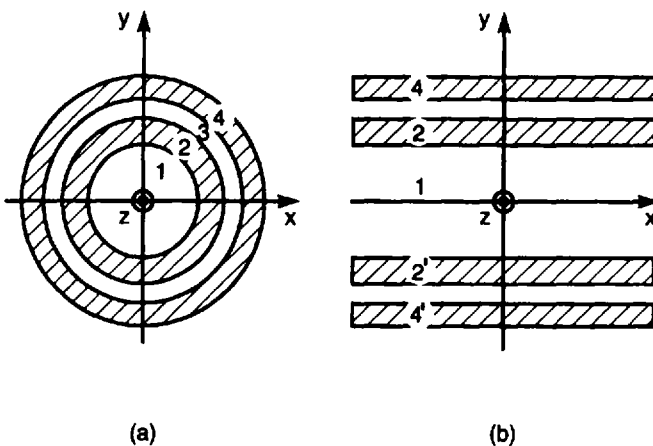


Figure 4.1 Planar Fresnel zone plates: (a) Soret or Wood zone plate and (b) symmetric linear zone plate.

wave focused at another axial point, or into a plane wave “focused” to the infinity.

If a plane or cylindrical wave is to be converged along a focal line, this can be done, for example, by a Fresnel zone plate of parallel and symmetric straight strips [Figure 4.1(b)], with widths corresponding to the Fresnel zone path-difference condition [61]. Such a Fresnel zone plate may be specified as a linear (or one-dimensional) zone plate.

Two identical linear zone plates crossed at right angles form the so-called Fresnel zone plate linear cross [Figure 4.2(a)]. More complicated Fresnel zone planar patterns have also been investigated in optics. For example, two orthogonal sets of zone patterns, designed in accord with hyperbolic transmission function, form a two-dimensional hyperbolic zone plate, sketched in Figure 4.2(b) [24]. In case of oblique wave incidence the planar Fresnel zone plate is composed of elliptical Fresnel zones, as shown in Figure 4.3(a), or of parallel but asymmetric straight zones [Figure 4.3(b)].

Normally, the Fresnel zone plate focalizes free space waves. About twenty years ago, a planar zone plate that focuses guided (or surface) optical or quasi-optical waves was manufactured [18–19]. Figure 4.4 illustrates the so-called step-index (SI) planar Fresnel zone plate, which is converging the plane-guided wave to the focal point P . The SI zone plate consists of metal or dielectric strip-type Fresnel zone elements that are fabricated via routine microelectronic technologies.

4.2.1.2 Curved Fresnel Zone Plates

To improve the focusing and resolving properties of the Fresnel zone plate it can be made as a curved thin plate or shell. In general, we may imagine a zonal plate, whose surface has no specific shape (Figure 4.5). The zones on

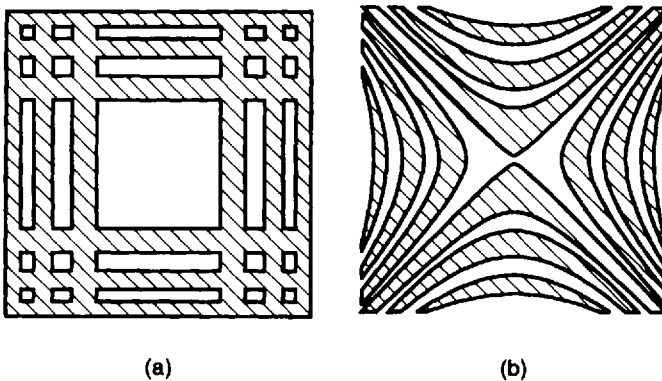


Figure 4.2 (a) Planar cross and (b) hyperbolic zone plates.

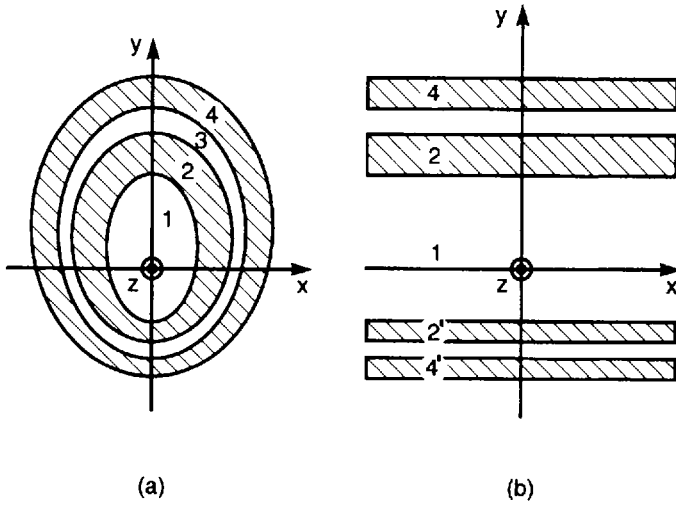


Figure 4.3 Asymmetric Fresnel zone plates: (a) Fresnel zone plate of elliptical zones and (b) Fresnel zone plate of straight linear zones.

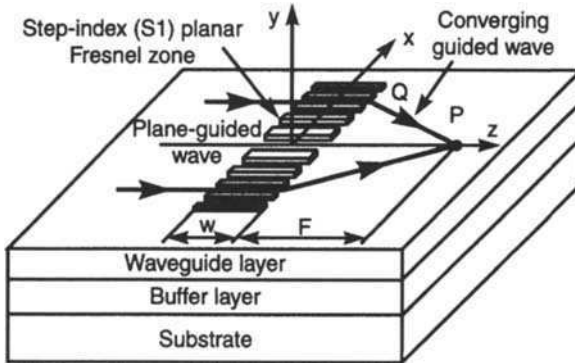


Figure 4.4 SI planar zone plate focusing guided wave.

the curved surface are drawn according to the Fresnel zone ray-difference condition. However, in practice, the most convenient are the zone plates with rotational silhouettes.

Figure 4.6 illustrates a spherical Fresnel zone plate of a radius R , with a convex face, turned to a plane-incident wave. The focal point is marked by P and the sphere center by C .

Along with the planar and spherical zone plates the next most simple in appearance are the conical and cylindrical zone plates. The conical zone plate, for

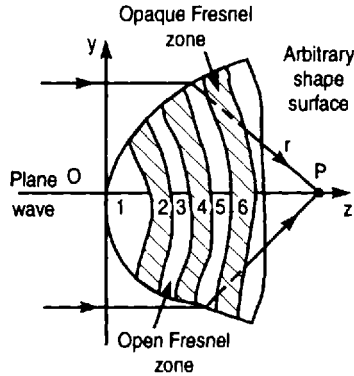


Figure 4.5 Fresnel zone plate of arbitrary shape.

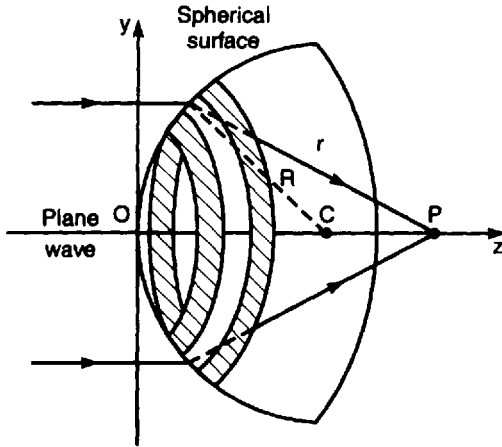


Figure 4.6 Spherical Fresnel zone plate, convex side turned to incident plane wave.

example, is particularly suitable for making collapsing, umbrella-like microwave/millimeter-wave antennas. A conical zone plate, convex side facing a normally incident plane wave, is shown in Figure 4.7(a). Fresnel circles can be approximated by their inscribed or circumscribed polygons, and thus the conical Fresnel zone plate can be changed into a pyramidal Fresnel zone plate. Figure 4.7(b) is a view of a hexagonal pyramidal zone plate.

The cylindrical Fresnel zone plates take one of the next two basic arrangements: ring-type and strip-type. The arrangement shown in Figure 4.8(a) consists of circular Fresnel zone rings. It focuses the normally incident plane wave at the primary focal point *P*.

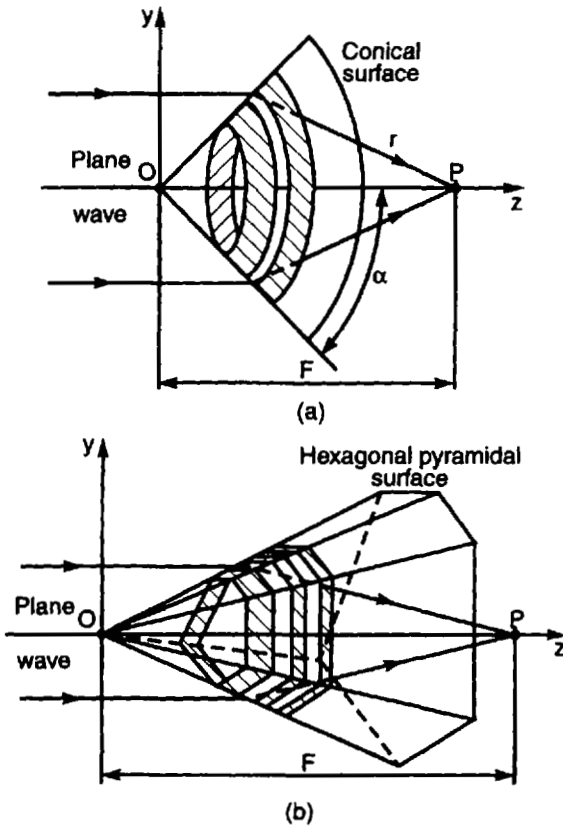


Figure 4.7 (a) Conical and (b) pyramidal zone plates, convex side facing a plane incident wave.

The second cylindrical zone plate design is made of parallel Fresnel zone strips, instead of rings, as illustrated in Figure 4.8(b). The strip-type Fresnel zone plate is a linear configuration. Unlike the previous cylindrical zone plate it focuses the plane wave not at a point but along the focal line $P'P''$. It seems that the first curved RF/microwave Fresnel zone plate and antenna were just the strip-type cylindrical ones proposed in the late 1930s by Bruce [30].

If only the upper half of the ring-type cylindrical Fresnel zone plate is taken and put on a planar screen, a nonsymmetrical Fresnel zone plate configuration is formed [Figure 4.9(a)].

Finally, if the ring- and strip-type cylindrical zone plates are laid one on top of the other, they form a particular zone configuration—a cylindrical Fresnel zone plate cross, which is shown in Figure 4.9(b).

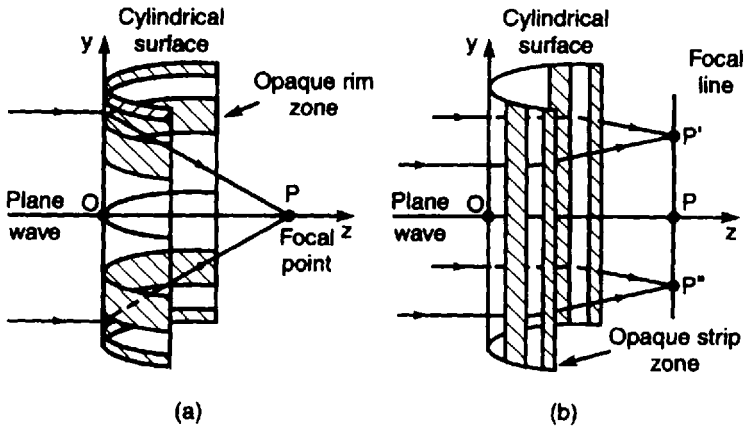


Figure 4.8 (a) Ring-type and (b) strip-type cylindrical Fresnel zone plates.

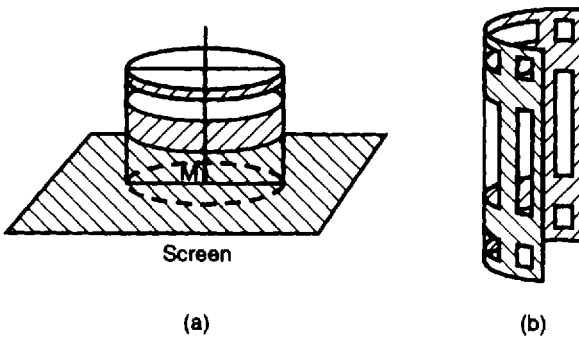


Figure 4.9 (a) Nonsymmetrical and (b) cross-type cylindrical Fresnel zone plate.

4.2.2 Classification According to Cross-Sectional Structure

4.2.2.1 Transmission (Lens-like) Fresnel Zone Plates

Subdivision of the Fresnel zone plates can be done according to their cross-sectional structure and materials used for phase corrections. In this section we summarize different varieties of the two basic types of zone plates—transmission and reflection.

Soret Zone Plates Figure 4.10 shows the transverse section of four half-open or Soret zone plate configurations consisting of open and opaque Fresnel zone annuli. In the classical microwave Soret zone plate the opaque zone elements are thin metal rings. Depending on which Fresnel zones are open, with a positive or negative phase, the Soret zone plate is sometimes named a positive

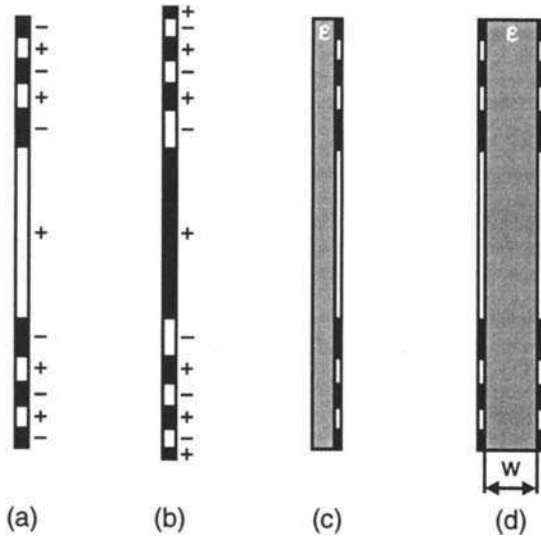


Figure 4.10 Cross-sectional view of Soret zone plates: (a) metal-ring positive Soret zone plate, (b) metal-ring negative Soret zone plate, (c) Soret zone plate with metal rings fixed on thin dielectric plate, and (d) double-element Soret zone plate array.

Soret zone plate [Figure 4.10(a)] or a negative Fresnel zone plate [Figure 4.10(b)]. The metal elements are usually fixed on a thin dielectric plate or substrate if the zone plate is made by printed microstrip technology [Figure 4.10(c)].

The focusing of the Soret zone plate is a result of two wave phenomena: diffraction by the open zone apertures and interference of diffracted waves at the focal region. Almost half of the electromagnetic energy illuminating the Soret zone plate is blocked by the opaque zones, and the phase in the open apertures is not constant. In radial direction it varies smoothly from zero to π radians. Thus, compared to the ordinary refraction lens with a constant aperture phase the Soret zone plate has very low focusing efficiency (about 10 times lower). Two successive Soret zone plate elements fixed apart at a distance w form a Soret zone plate array [62], which may have better transmission focusing properties than the single Soret zone plate element if w is properly chosen [Figure 4.10(d)].

Wood Zone Plates The original half-wave Wood zone plate is almost entirely transmissive for the incident light or microwave plane front. It is obtained by making the Soret zone plate opaque zones transmissive and phase-reversing for the waves going through them. More precisely, in each Wood zone plate

aperture the phase is also varying from zero to π radians as in the Soret zone plate.

The Wood zone plate for optical or microwave/millimeter waves originated as a single-dielectric phase-reversing transmission zone plate [Figure 4.11(a), (b)]. The phase reversing is made by means of Fresnel zone annular grooves cut in a dielectric flat plate with a permittivity ϵ transmissive for the light or microwaves. As a result, each groove is alternated by a dielectric rib.

By the elementary wave theory of the Fresnel zones the focusing efficiency of the Wood zone plate is found four times higher than the Soret zone plate efficiency but still two and a half times smaller than that of the conventional lens. In return, the Wood zone plate has much reduced thickness, weight, and dielectric losses compared to the traditional dielectric lens.

Bilaterally planar microwave varieties of Wood phase-reversal Fresnel zone plates are shown in Figure 4.11(c–e). They are made as a two-dielectric combination of Fresnel zone concentric rings of equal thickness. The aperture phase varies in radial direction as in the classical Soret zone plate and Wood zone plate. Therefore, these planar Wood zone plate varieties have the same focusing quality as the original Wood zone plate. They were proposed by Wiltse in 1976 as Fresnel zone plates suitable for microwaves/millimeter waves, but he reported them in detail about 10 years later [52].

In the special case where $\epsilon_1 = \epsilon_0$, the two-dielectric Wood-Wiltse zone plate has the simplest structure [Figure 4.11(c)], with an optimum width of

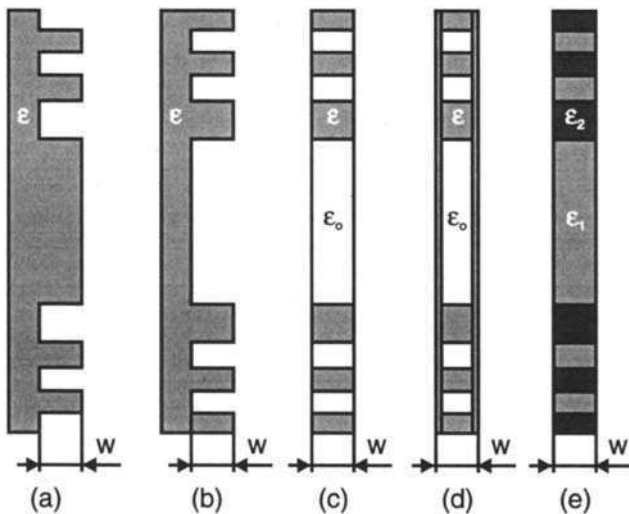


Figure 4.11 Wood zone plates with (a) negative-phase grooves, (b) positive-phase grooves, (c) solid rings alternated by air regions, (d) three-layer sandwich structure, and (e) two kinds of solid rings (ϵ_1 rings alternated by ϵ_2 rings).

$\lambda/2$ for $\epsilon_2 = 4\epsilon_0$. However, in this case some technique for steady ring fixing is necessary. This can be done, for example, by using a three-layered, sandwich-type structure as shown in Figure 4.11(d). This zone plate construction is stable, bilaterally planar, and completely encapsulated. In return, the thin dielectric slabs slightly reduce the wave transmission through the air zones [59].

Finally, if the two types of rings are made of solid dielectrics with permittivities ϵ_1 and ϵ_2 the bilaterally planar dielectric Fresnel zone plate is a self-supporting solid structure, shown in Figure 4.11(e).

Multiple Phase-Corrected Zone Plates For making the zone plate competitive in focusing efficiency to the ordinary lens, different multiple phase-correcting techniques have been employed. As will be shown later in this chapter, most frequently half-wave and quarter-wave corrections are made in practice. In the quarter-wave Fresnel zone plate each full-wave zone, which incorporates two Fresnel zones, is subdivided into four quarter-wave subzones. Different phases in the subzones were first realized by cutting stepped, annular grooves in a flat dielectric plate, as shown in Figure 4.12(a).

Instead as a four-level single-dielectric arrangement the quarter-wave zone plate can be made as a four-dielectric ring structure [Figure 4.12(b)]. Its central quarter-wave subzone is left open (or $\epsilon_1 = \epsilon_0$), and the next three subzones are covered by three concentric dielectric rings with different permittivities but equal thicknesses [49]. The next full-wave Fresnel zones have the same

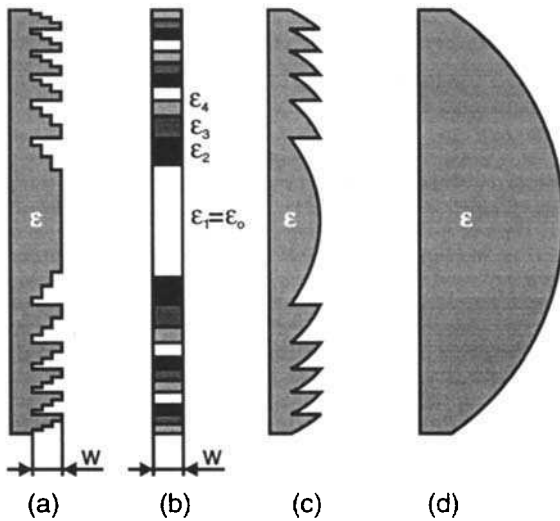


Figure 4.12 (a, b) Quarter-wave zone plates, (c) Fresnel zone lens, and (d) ordinary plane-convex lens.

arrangement. Figure 4.12(d) shows the cross section of the ordinary plane-hyperbolic lens. Compared to the zone plate lenses it is much thicker and more weighty. This disadvantage can be overcome by zone-stepping the lens thickness.

The stepped hyperbolic lens, shown in Figure 4.12(c), is done by intersection of confocal hyperbolic surfaces with a plane normal to the lens axis. The phase increment caused by two adjacent steps is 2λ radians, which corresponds to the Fresnel full wave-zone path-difference. That is why the stepped hyperbolic lens is called a Fresnel zone lens. The Fresnel zone lens can be seen as a limiting case of the multiple-step Fresnel zone plate lens. With an increase in the number of steps, the zone plate profile closely approaches that of the Fresnel zone lens.

4.2.2.2 Fresnel Zone Plate Reflectors

By placing a plane screen $\lambda/4$ behind the classic Soret zone plate the incident wave is brought back in antiphase, and the combination screen-Soret zone plate is functioning as a zone plate reflector (or folded Soret zone plate). Its cross-sectional view is sketched in Figure 4.13(a). In addition, a spacing low-permittivity material (or spacer) is necessary to support the Soret zone plate metallic rings.

An alternative Soret zone plate reflector is sketched in Figure 4.13(b), where a metal sheet is shaped in zig-zag manner to assure the required phase steps. A cross-sectional view of a metal quarter-wave-stepped plate is shown in Figure 4.13(c). These two Soret zone plate reflector structures can be encased in dielectric foam or honeycomb [63].

The first printed millimeter-wave design of a Soret zone plate reflector was developed by Huder and Menzel [36]. As shown in Figure 4.13(d), it is fabricated by use of printed technology and consists of a ground plane disk reflector and Soret zone plate rings etched on a dielectric substrate $\lambda_d/4$ in thickness.

In like fashion, a multilayer phase-correcting Fresnel zone plate reflector was constructed by Guo and Barton [43–45] and applied in variety of phase-correcting Fresnel zone plates and antennas for DBS reception. Figure 4.13(e) is a cross section of such a quarter-wave, multilayer zone plate. It consists of a metallic ground and three layers of concentric rings separated by three dielectric substrates.

A similar, reflector-like action may be achieved on the basis of the phase-reversal dielectric zone plate shown in Figure 4.11(c). For this purpose, the dielectric rings are made two times thinner (or $w/2$) and are backed by a metal disk reflector [Figure 4.13(f)]. In this way, the half-wave Fresnel zones in the Wood zone plate aperture move into phase.

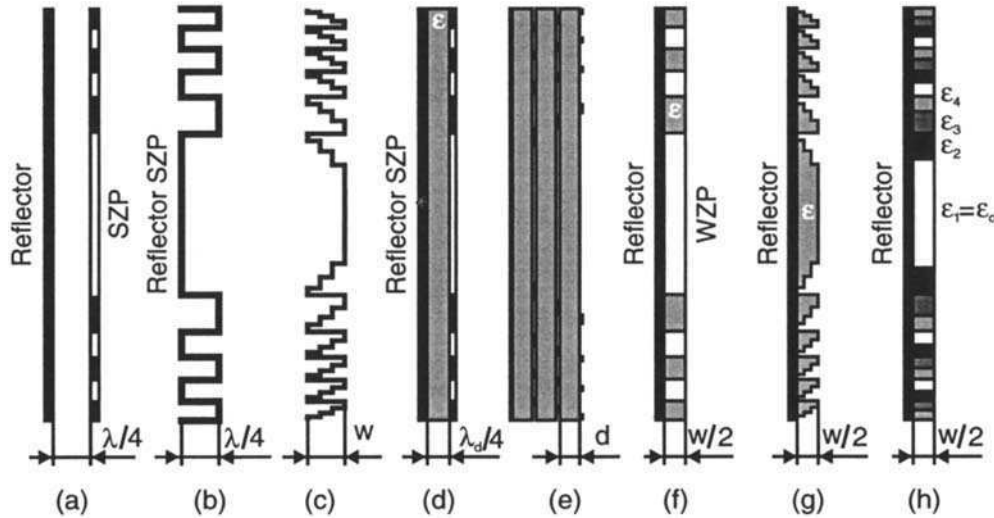


Figure 4.13 Fresnel zone plate reflectors: (a) Soret zone plate in front of reflector or folded Soret zone plate, (b) folded Soret zone plate in shape of zigzag reflector, (c) quarter-wave stepped zone plate reflector, (d) folded Soret zone plate printed on dielectric substrate, (e) multilayer zone plate reflector, (f) Wood-type zone plate reflector, (g) step-grooved dielectric zone plate with quarter-wave phase corrections, and (h) quarter wave-zone plate reflector with multi-dielectric ring configuration.

In a similar manner the transmission-type quarter-wave zone plate can be transformed into a reflection-type zone plate. Figure 4.13(g) shows such a step-grooved dielectric zone plate with a planar metal reflector. Here all grooves are twice as small in depth compared to that in the transmissive quarter-wave stepped Wood zone plate. Figure 4.13(h) illustrates another version of the quarter-wave zone plate reflector—the multidielectric one that is a modification of the zone plate construction, shown in Figure 4.12(b).

4.2.2.3 Phase-Correcting Structures of Composite Metal-Dielectrics

Compared to ordinary lenses, the dielectric Fresnel zone plates are much thinner and lighter structures. Further decrease of their thickness and weight is possible by implementing composite metal-dielectric media. They can be fabricated as one-layer or multilayer metal gratings of small metal elements imbedded in air or lightweight, low-permittivity host material [Figure 4.14(a)].

Often the metal-dielectric media are frequency-selective structures (FSS) made as grid layers of metallic obstacles or slots. Usually, the metallic elements are printed metallic dipoles, disks, rings, squares, ordinary and Jerusalem crosses, and so on, and form planar FSS grids. Figure 4.14(b) also illustrates the face view and cross-section of a phase-shifting array of double-square metal elements printed on a dielectric substrate.

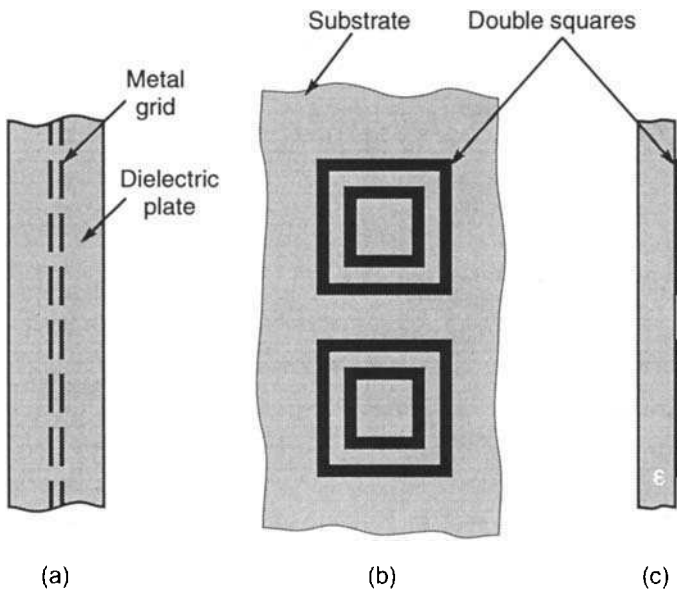


Figure 4.14 Metal-dielectric phase-correcting plate structures: (a) metal grid embedded in dielectric slab and (b, c) printed grating of double-square metal elements.

4.3 Planar Fresnel Zone Plates

In this section we consider the working mechanism, theory, and design of planar Fresnel zone plates at microwaves and millimeter waves. They come naturally from the optical Soret and Wood zone plates and have nearly the same physical and theoretical background. But together with that, they differ substantially in construction, technology, and application, requiring specific design equations and methods of analysis.

4.3.1 Soret Zone Plate

We start our more detailed study on the Soret zone plate with the intention of specifying its focusing mechanism, diffraction theory, design considerations, and equations for microwaves and millimeter waves.

4.3.1.1 Multiple Focusing Action

The classical Soret zone plate consists of concentric circular regions, alternately open and opaque. They just coincide with the Fresnel zones, whose radii are determined approximately by (2.22). To better understand the Soret zone plate focusing action let us consider the elementary diffraction theory for the case of plane wave incidence (Figure 2.6).

For this special case $\rho_o = \infty$ and $F_e = r_o = F$, and the approximate paraxial equation (2.22) for the n -th zone radius can be rewritten in the form

$$b_n = b_1 \sqrt{n}, \quad (n = 1, 2, 3, \dots) \quad (4.1)$$

where

$$b_1 = \sqrt{\lambda F} \quad (4.2)$$

Here F is the primary focal length, such that $F \gg b_n \gg \lambda$ (paraxial condition). The Soret zone plate built according to (4.1) is sometimes called the paraxial one. With regards to (2.132), the field produced by the n -th open Fresnel zone at axial point P can be found as

$$E_n(P) = j\pi E_o(P) \int_{\chi_{n-1}}^{\chi_n} e^{-j\frac{\pi}{2}\chi^2} \chi d\chi \quad (4.3)$$

where $E_o(P)$ is the field of the incident plane wave at the same point P if the zone plate is absent; $n = 1, 3, 5, \dots$ for odd (or positive phase) open zones,

and $n = 2, 4, 6, \dots$ for even (or negative phase) open zones; $\chi = r'\sqrt{F/\lambda z}$, $\chi_{n-1} = b_{n-1}\sqrt{F/\lambda z}$, and $\chi_n = b_n\sqrt{F/\lambda z}$; here z is the axial coordinate of the observation point P and $b_{n-1} \cong \sqrt{\lambda z(n-1)}$; and $b_n \cong \sqrt{\lambda zn}$ are the $(n-1)$ -th and n -th Fresnel zone radii.

If the Soret zone plate comprises N_o odd open Fresnel zones the total field at point P is easily found

$$E(P) = \sum_{n=1}^{N_o} E_n(P) \quad (4.4)$$

The equation for the total diffraction field can be approximated, and the field intensity $I(w)$ along the plate axis, proportional to squared $E(P)$, can be expressed as a simple trigonometric equation [10]

$$I(w) = C \frac{1 - \cos(2N_o w)}{w^2(1 + \cos w)} \quad (4.5)$$

where C is an undetermined constant, and $w = \pi F/z$.

An examination of (4.5) shows that $I(w)$ has maxima for the following values of w

$$w = \pm(2k + 1)\pi, \text{ for } k = 0, 1, 2, \dots \quad (4.6)$$

These maxima are termed zone plate foci.

For $k = 0$, $w = \pm\pi$, and $z = \pm d_1$; for $k = 1$, $w = \pm 3\pi$, and $z = \pm d_1/3$; and for $k = 2$, $w = \pm 5\pi$, and $z = \pm d_1/5$; and so forth. The plus sign of w corresponds to real foci P_1, P_3, P_5, \dots , located on the zone plate axis at positive z coordinates. In this case, the zone plate behaves as a multifocal converging lens. On the contrary, the minus sign of w relates to foci P'_1, P'_3, P'_5, \dots , which are images of the real foci. These are virtual foci, and they correspond to diverging rays. Thus, the Soret zone plate acts as two multifocal lenses: ray-converging and ray-diverging (Figure 4.15).

The points P_1 and P'_1 are first-order or primary foci, P_3 and P'_3 are third-order foci, and so on. In principle, they are infinite in number. Note that these are odd foci. The half-open zone plate has no foci of even order because the fields radiated by the even zones cancel along the axis.

The primary focus $z = +d_1$ is that for which the zone plate has been designed. It occurs when each annulus is exactly equal to one Fresnel zone. The high-order foci correspond to 3, 5, 7, etc. Fresnel zones, which fit into each clear zone.

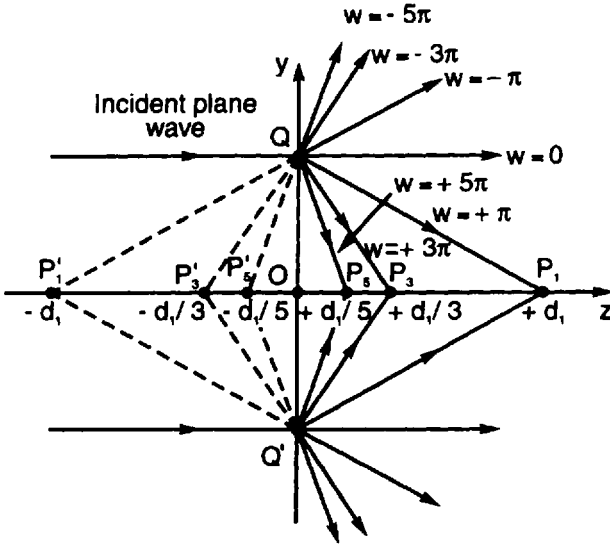


Figure 4.15 Converging and diverging diffraction properties of multifocal zone plate.

For instance, consider the creation mechanism of the third-order focus at $z = +d_1/3$. Now, (4.1) becomes $b_n = \sqrt{n\lambda d_1/3}$, and therefore, each opening aperture contains three half-wave zones, of which the first two cancel, leaving only the third one to contribute to point P_3 .

The normalized intensity function was calculated for $N_o = 7$ and drawn in Figure 4.16 versus the real focus number. It is evident that the high-order foci ($w = +3\pi$, or no. 3, $w = +5\pi$, or no. 5, and so on) are much less intensive than the primary one ($w = +\pi$, or no. 1), or more specific, $I(w = \pi): I(w = 3\pi): I(w = 5\pi) \dots = 1:1/9:1/25 \dots$

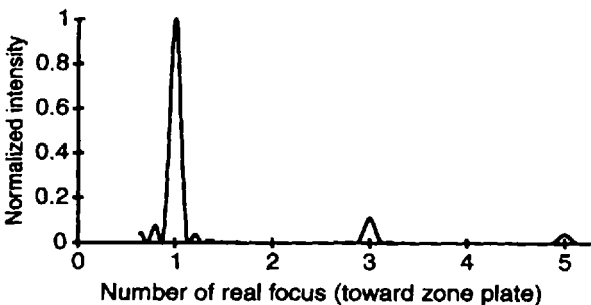


Figure 4.16 Normalized intensity of zone plate versus number of real focus (in direction to Fresnel zone plate), calculated for $N_o = 7$ (number of open zones).

The focusing intensity at the primary focus of the paraxial Soret zone plate is $1/\pi^2$ times smaller than the focusing intensity of the ordinary condensing lens (see Section 4.3.1.4). It is curious to quote at this place the physical explanation of the multiple focusing phenomenon as made for the first time by Wood [1]:

We may regard the zone plate as a circular grating in which the grating space becomes less and less as we proceed outward from the centre, consequently the bending or deviation of the diffracted ray from the normal becomes greater as we near the edge, and the change in the grating is such as to bring all the deviated rays of a single colour together in point. The principal real focus of the plate corresponds to the superimposed spectra of the first order; the second order spectra being bent more come together at a point nearer the plate, forming a second focus, and so on—the different foci corresponding to spectra of different orders. There are also spectra of the first order bent outwards, or away from the centre, and these rays projected backwards behind the plate will meet, forming a virtual focus in a position corresponding to that of the real focus on the opposite side of the plate; the second order spectra are bent out more, consequently the virtual focus of these rays is nearer to the plate, and we thus see, that for every real focus on the one side of the plate, there is a corresponding virtual focus on the other.

Now, let us consider more particularly the focusing operation of the microwave and millimeter-wave Soret zone plate. It is normally built as a grating of concentric metal rings at which transmission, reflection, and diffraction (or bent) waves arise. On the illumination side, the reflected and diffracted waves correspond to the so-called reflection zone plate mode with an infinite number of virtual (image) foci. On the other side the transmitted and diffracted waves form the transmission zone plate mode with an infinite number of real foci.

If the fields at two principal foci, the one for transmission (at $z = +d_1$) and another for reflection (at $z = -d_1$), are received and brought together in antiphase, the focusing efficiency (or focusing gain) of the Soret zone plate will be increased almost twice. This can be done by one of the following techniques:

1. Feed-line power combining, by use of two feed antennas, feed lines, a phase shifter, and a power combiner;
2. Free-space power combining, by means of plane metal reflector located behind the Soret zone plate that brings back the wave transmitted

through the open zones. The two waves, the one reflected from the Soret zone plate and another reflected from the metal reflector, are focused and interfere in phase at the principal focus for reflection. The Soret zone plate constructed in this manner was shown in Figure 4.13(a) and is known as zone plate reflector or simply a folded zone plate. (Its working mechanism is better illustrated in Chapter 5, in Figure 5.35.)

4.3.1.2 Resolution

The resolution power (or simply resolution) of the circular lens, illuminated normally by a plane wave, is defined as an angle between the lens axis and direction to the first minimum in the focal plane field pattern. For optical planar zone plates, it was studied in several publications [2, 16, 17, 22].

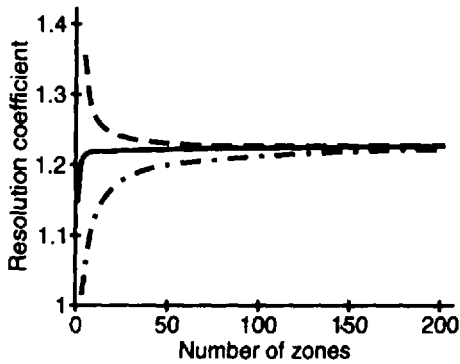
For illustration we shall use here Figure 2.22. Since the zone plate amplitude-phase distribution is almost constant and circularly symmetric, without loss of generality we may assume that the observation point P_2 lies in the zy plane, or $\vartheta_x = 0$ and $\vartheta = \vartheta_y$. Let us then mark the angle measuring the resolution with ϑ_o . According to [2] it is approximated as

$$\vartheta_o = \Delta_o \frac{\lambda}{2a_o} \quad (4.7)$$

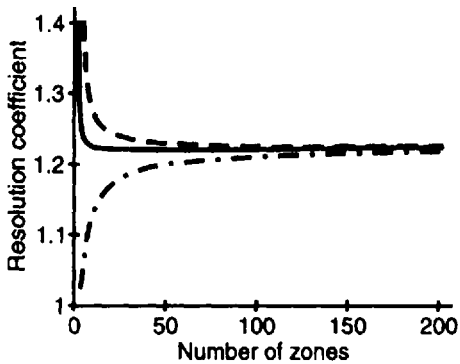
where $\Delta_o = 1.22$ is called a resolution coefficient, and $2a_o$ is the zone plate diameter. The same resolution equation is found for a circular aperture or ordinary lens illuminated normally by a plane wave.

More precise analysis shows, however, that this approximation is valid for a very large number of Fresnel zones (say, for zone plates with a total number of zones N higher than 200). This is a typical case for optical wavelengths, but not for microwave/millimeter wavelengths, where N is usually less than $15 \div 20$. The resolution coefficient Δ_o differs from 1.22 by an amount that depends on N . This is well-illustrated in Figure 4.17, taken from [17].

Figure 4.17(a) is referred to the primary focal plane at $z = d_2$ and shows the resolution coefficient Δ_o versus the number of zones N , for three different Fresnel zone plates: positive Soret zone plate (dashed line), negative Soret zone plate (dotted line), and phase-reversal or Wood zone plate (solid line). It is seen that for a small number of zones the negative Soret zone plate has a slightly better resolution ($\Delta_o < 1.22$) while the positive Soret zone plate has a slightly worse resolution ($\Delta_o > 1.22$) compared to the ordinary lens resolution. The resolution performance of the Wood zone plate is essentially identical to that of an ordinary lens once there are more than a few zones.



(a)



(b)

Figure 4.17 Resolution coefficient versus number of zones for: positive Soret zone plate (dashed line), negative Soret zone plate (dotted line), and phase-reversal Soret zone plate (solid line). (After: [17], © 1989 OSA Press.)

Similar graphs are plotted in Figure 4.17(b), but they are referred to as the third-order focal plane at $z = d_1/3$. Here the curve for the negative Soret zone plate is essentially unchanged but the curves for positive Soret zone plate and Wood zone plate show a resolution reduction below about 20 zones.

4.3.1.3 Aberrations

In optics and microwave/millimeter wave quasi-optics the lenses are commonly considered under the following ideal conditions:

- The waves are incident onto the lens plane as a bundle of paraxial rays, normally or at small angles toward the lens axis.

- The lens is without frequency dispersion, or the wave is monochromatic.

Lenses are transforming the incident wave front from one to another form. For example, the front of a spherical diverging wave can be changed into a spherical converging wave front. In practice, after passing throughout the real lens the waves become aberrated. The Gaussian or paraxial optics and quasi-optics are no longer valid, and such departures from the ideal Gaussian behavior are known as lens aberrations.

There are many kinds of wave aberrations, but in discussing the Fresnel zone plate-focusing properties we will restrict ourselves to three cases only: on-axis or axial spherical aberration, off-axis aberrations, and chromatic aberration, following mainly [4].

Axial Spherical Aberration Consider a Soret zone plate that transforms a monochromatic plane wave into a spherical wave converging to an axial point P (Figure 4.18). Expand the ray path difference (RPD) $RPD = r - F$ in a binomial power series

$$RPD = r - F = \sqrt{F^2 + b_n^2} - F = n \frac{\lambda}{2} \equiv \frac{b_n^2}{2F} - \frac{b_n^4}{8F^3} + \dots \quad (4.8)$$

According to Huygens' principle the peripheral point Q_n on the zone plate is a source of a secondary spherical wave, with a wave-front radius r , while the central point O is viewed as a source of another spherical wave with

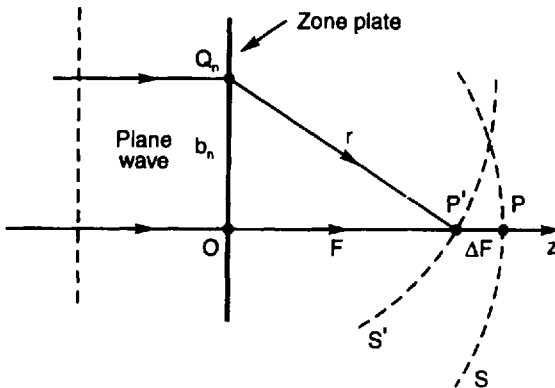


Figure 4.18 Illustration of axial spherical aberration due to peripheral and axial ray path difference. (After: [4], © 1972 OSA Press.)

$$\text{RPD} = b_n \sin \psi_i + F \sqrt{1 + \left(\tan \psi_i - \frac{b_n}{F} \right)^2} - F \sqrt{1 + \tan^2 \psi_i} \quad (4.11)$$

If we approximate the square roots by their binomial expressions and $\sin \psi_i$ and $\tan \psi_i$ by their respective power series, we may write

$$\text{RPD} \cong \frac{b_n^2}{2F} - \frac{b_n^4}{8F^3} + \frac{b_n^3}{2F^2} \psi_i - \frac{3b_n^2}{4F} \psi_i^2 \quad (4.12)$$

The terms in the above RPD approximate expression have a different aberration interpretation:

1. The first term $b_n^2/2F$ is equal to $n\lambda/2$ and is a first order, paraxial or aberration-free approximation.
2. The second term $b_n^4/8F^3$, as it was shown above, determines the axial spherical aberration.
3. The third term $b_n^3\psi_i/2F^2$ describes in optics the coma lens aberration. In this case the image of a point source is not a focal point but a transverse focal segment.
4. The fourth term $3b_n^2\psi_i^2/4F$ corresponds both to astigmatism and field curvature. These two aberrations are closely related. The lens astigmatism means that the image of a point source consists of two transverse mutually perpendicular (or crossed) line segments. The astigmatism disappears when the focal region is located not on plane but on a single curved surface known as the Petzwal surface. This corresponds to a so-called curved field (i.e., a field on the above curved surface).

It is still possible to calculate the maximum incidence angle $\psi_{i\max}$ for which the off-axis aberrations are negligible and good-focusing with the following inequality [9]

$$\left| \pm \sqrt{2\lambda NF} \frac{N\lambda}{F} \sin \psi_{i\max} - N\lambda \sin^2 \psi_{i\max} \right| < \frac{\lambda}{4} \quad (4.13)$$

Here N is the number of all open zones in the Soret zone plate.

Frequency Aberration As it is seen from (4.1) and (4.2) the focal length of a given Fresnel zone plate is inversely proportional to the wavelength, or

$F(\lambda) = b_n^2/n\lambda$. Therefore, the zone plate focusing quality is frequency-dependent, and this sets bounds to its frequency bandwidth. Consider a zone plate designed for a particular wavelength λ_o , for which $\text{RPD} = r - F$ (Figure 4.18) is exactly equal to $n\lambda_o/2$, $n = 1, 2, 3, \dots$

In optics it is assumed that the frequency (chromatic) aberration is not substantial to some other wavelength λ for which $\text{RPD} = N\lambda_o/2 \pm \lambda/4$, or $N/\omega_o = N/\omega \pm 1/2\omega$, where $\omega_o = 2\pi c/\lambda_o$, $\omega = 2\pi c/\lambda$. Thus, we may write

$$N\left(\frac{1}{\omega_o} - \frac{1}{\omega}\right) \equiv \pm \frac{1}{2\omega} \quad (4.14)$$

Denote with $2\Delta\omega = |\omega_o - \omega|$ the radian frequency band of the zone plate. We easily find that it depends directly on the total zone number N

$$\frac{2\Delta\omega}{\omega_o} \equiv \frac{1}{N} 100, \% \quad (4.15)$$

or

$$N \equiv \frac{\omega_o}{2\Delta\omega} \quad (4.16)$$

As an example, let us consider a zone plate with $N = 10$ Fresnel zones. Such a zone plate will have a relative frequency bandwidth roughly equal to 10%.

The frequency bandwidth of the microwave zone plates and antennas is limited by a variety of electromagnetic characteristics: focusing and resolution quality, polarization degradation, impedance matching, and so on. Therefore, the above relation for the zone plate bandwidth has to be viewed as initial approximation. In Section 4.3.1.4, we will give a relation that determines more precisely the Soret zone plate frequency bandwidth.

The zone plate frequency bandwidth can be increased by making a doublet of two coaxial Soret zone plate elements, separated by a distance d [4]. For a given wavelength bandwidth $2\Delta\lambda = \lambda - \lambda'$ the zone plate doublet can be designed as follows: The focal length of the first element is $F_1 = b_{n_1}^2/n_1\lambda$ at one extreme wavelength λ , and $F_1' = b_{n_1}^2/n_1\lambda'$ at the other extreme wavelength λ' , while the corresponding focal lengths of the second zone plate element are $F_2 = b_{n_2}^2/n_2\lambda$ at λ and $F_2' = b_{n_2}^2/n_2\lambda'$. Evidently, the two zone plate elements are different in zone number and zone radii ($n_1 \neq n_2$, and $b_{n_1} \neq b_{n_2}$).

Requiring the total transmission power at λ to equal that at λ' , the equivalent focal length F_e of the doublet can be expressed in terms of F_1 , F_2 , and d as follows

$$\frac{1}{F_e} = \frac{1}{F_1} + \frac{1}{F_2} - \frac{d}{F_1 F_2} \quad (4.17)$$

The zone plate doublet is achromatized (to the first order) in the wavelength bandwidth $2\Delta\lambda = \lambda - \lambda'$ if the distance between the two elements is taken as

$$d = \frac{F_1 + F_2}{1 + \lambda/\lambda'} \quad (4.18)$$

There is another, simpler configuration for achromatizing the zone plate doublet at two wavelengths, say λ_1 and λ_2 [9]. The first doublet element adjoins the other one, so we may assume that the two elements have the same focal distances $F_1 = F_2 = F$, and are sized as follows: $b_n^2(\lambda_1) = nF\lambda_1$ and $b_n^2(\lambda_2) = nF\lambda_2$. Now n takes all values between 0 and 1, 2 and 3, 4, and 5, and so on, for odd open zones, or between 1 and 2, 3 and 4, 5, and 6, and so on, for even open zones. It is clear that the lens doublet will have annular diaphragms smaller in area than the half-wave Fresnel zones. Thus, the increase of the frequency bandwidth of the doublet comes to the expense of its focusing quality, compared to the single zone plate element.

4.3.1.4 Transmission Function

The transmission function of zone plates describes the variation of transmission coefficients within the zone plate aperture. It determines the amplitude and phase distribution of aperture field, and thus, the focusing properties of the zone plate.

Transmission Function of Circular Soret Zone Plate Consider a plane wave incident normally into a circular aperture of radius a_o (Figure 2.22). The Fresnel diffraction field at an axial point was expressed in the form

$$E(\chi) = j\pi E_o \int_0^{\chi_o} e^{-j\frac{\pi}{2}\chi^2} \chi d\chi \quad (4.19)$$

where $\chi = r'\sqrt{2/\lambda z}$, $\chi_o = a_o\sqrt{2/\lambda z}$, and with a_o was marked the circular aperture radius. Then, suppose a circular plane-convex lens with a focal length

$z = F$ located in the aperture. This will cause a replacement of the integrand in (4.19) by the expression $\chi \exp(-j\pi\chi^2/2) \exp(j\pi\chi^2/2)$, and then the diffraction field will be given by [61]

$$E(F) = j \frac{\pi\chi_o^2}{2} E_o = j \frac{\pi a_o}{\lambda F} E_o \quad (4.20)$$

The focusing gain at the primary focal point can be expressed by

$$G_f = \left| \frac{E(F)}{E_o} \right|^2 = \left(\frac{\pi a_o^2}{\lambda F} \right)^2 \quad (4.21)$$

From (4.19) and (4.20), we conclude that the usual converging lens brings to the inclusion in the diffraction integrand the factor $\exp(\pi\chi^2/2)$, which cancels its complex conjugate $\exp(-j\pi\chi^2/2) = \cos(\pi\chi^2/2) - j\sin(\pi\chi^2/2)$.

A similar result can be achieved, if the negative parts of the function $\cos(\pi\chi^2/2)$ or $\sin(\pi\chi^2/2)$ are canceled, by making certain Fresnel zones in the diffraction aperture opaque (i.e., by putting a positive Soret zone plate [Figure 4.2(a)] in the aperture with the following transmission function)

$$T(\chi) = U \left[\cos \left(\frac{\pi\chi^2}{2} \right) \right] = \begin{cases} 1, & \text{for } \cos[(\pi/2)\chi^2] \geq 0 \\ 0, & \text{for } \cos[(\pi/2)\chi^2] < 0 \end{cases} \quad (4.22)$$

Replacing χ^2 with $(2/\lambda F)r'^2$ the transmission function equation is rewritten in the form given in [51]

$$T(r') = U \left[\cos \left(\frac{\pi r'^2}{2\sigma^2} \right) \right] = \begin{cases} 1, & \text{for } \cos(\pi r'^2/2\sigma^2) \geq 0 \\ 0, & \text{for } \cos(\pi r'^2/2\sigma^2) < 0 \end{cases} \quad (4.23)$$

where $U \left[\cos \left(\frac{\pi r'^2}{2\sigma^2} \right) \right]$ is a rectangular unit function, $\sigma = \sqrt{\lambda F_1/2\pi} = b_1/\sqrt{2\pi}$ is a parameter characterizing the zone plate, b_1 is the first Fresnel zone radius, and F_1 is the primary focal length.

Let the total number of open zones be N'_o and let them be limited in the radial interval $b_{n-1} \leq r' \leq b_n$, with $n = 1, 3, 5, \dots, N'_o$, (odd or positive phase zones). The open zones are alternated by N''_o opaque zones ($n = 2, 4, 6, \dots, N''_o$, even or negative phase zones).

As shown in Figure 4.20(a) its transmission function $T(r')$ is of rectangular or binary shape. It was calculated for $\lambda = 1$ cm, $F = 40$ cm, and $N_o = N'_o = N''_o = 12$.

The radius of the last clear ring b_N is found by

$$b_{N_o} \equiv \sigma \sqrt{2\pi N_o} = \sqrt{\lambda F_1 N_o} \quad (4.24)$$

It can be proved [61] that the diffraction field at the primary focus is

$$E(F_1) = E_o(N_o + j) \quad (4.25)$$

From (4.21) and (4.25) the equation for the focusing gain can be rewritten in the form

$$G_f = \left| \frac{E(F)}{E_o} \right|^2 = N_o^2 + 1 = \left(\frac{a_o^2}{\lambda F_1} \right)^2 \quad (4.26)$$

Now, we can compare the focusing properties of the plane wave-illuminated Soret zone plate and ordinary lens that occupy the same aperture and have the same focal length ($F_1 = F$) and wavelength. The relation between the focusing gain expressions (4.26) and (4.21) gives a relative focusing intensity or gain exactly equal to $1/\pi^2$. Here we proved the value given in Table 4.1.

From (4.26) the number of the open zones N_o is expressed as follows

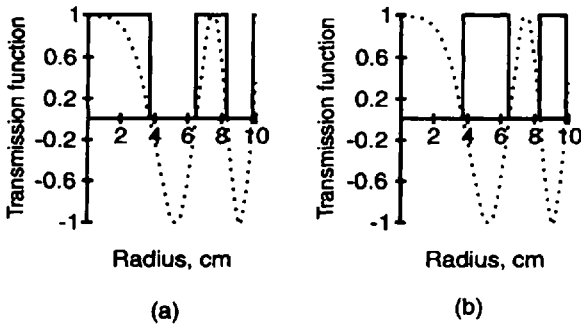


Figure 4.20 Rectangular or binary-type transmission function of the Soret zone plate calculated for $\lambda = 1$ cm, $F = 40$ cm, and $N_o = 12$ in case of (a) odd zones open and (b) even zones open.

$$N = \sqrt{\left(\frac{\pi a_o^2}{\lambda F}\right)^2 - 1} = \sqrt{\left(\sqrt{\pi} \frac{a_o}{b_1}\right)^4 - 1} \quad (4.27)$$

where $b_1 = \sqrt{\lambda F}$ is the radius of the first Fresnel zone.

Another, complementary Soret zone plate configuration can be formed by interchanging the positions of the open and opaque zones. The transmission function of this zone plate is found simply by altering the sign in front of the argument of the rectangular unit function U , or $T(r') = U[-\cos(\pi r'^2/2\sigma^2)]$. The latter was calculated for the same parameters ($\lambda = 1$ cm, $F = 40$ cm, and $N_o = 12$) and plotted in Figure 4.20(b).

Transmission Function of Soret Zone Plate With Straight Fresnel Zones Let us consider first an infinite slit cut along the x -axis (see Section 2.4.4.3). In this case, if $b_1 = b_2 = b$ the focal Fresnel diffraction field at a distance z from the slit plane can be determined by

$$E = \frac{j}{2} E_o \int_{-v}^{+v} e^{-j\frac{\pi}{2}v'^2} dv' = j(1-j) \frac{E_o}{\sqrt{\lambda z}} \int_{-b}^{+b} e^{-j\frac{\pi x'^2}{\lambda z}} dx' \quad (4.28)$$

where $2b$ is the slit width, $v_1 = v_2 = v = b\sqrt{2/\lambda z}$, and $v' = x'\sqrt{2/\lambda z}$.

Then assume an ordinary plane-convex lens with a focal length $z = F$ located in the slit aperture. This is equivalent to replacing the integrand in (4.28) with the expression $\exp(-j\pi\chi'^2/\lambda z)\exp(j\pi\chi'^2/\lambda z)$. Therefore, the diffraction field by the slit comprising an ordinary kind of lens is given by the following simple expression [61]

$$E(F) = j \frac{\pi\chi_o^2}{2} E_o = j \frac{\pi a_o}{\lambda F} E_o \quad (4.29)$$

From (4.29), we may easily find the focusing gain of a slit covered by an ordinary cylindrical lens

$$G_f = \left| \frac{E(F)}{E_o} \right|^2 = \frac{4b^2}{\lambda F} \quad (4.30)$$

In an analogy with the classical Soret zone plate, the transmission function of the parallel straight-line Soret-type zone plate [Figure 4.1(b), positive zones open], also depends only on one coordinate (the rectangular coordinate y') and may be written like (4.23)

$$T(y') = U \left[\cos \left(\frac{\pi y'^2}{2\sigma^2} \right) \right] = \begin{cases} 1, & \text{for } \cos(\pi y'^2/2\sigma^2) \geq 0 \\ 0, & \text{for } \cos(\pi y'^2/2\sigma^2) < 0 \end{cases} \quad (4.31)$$

where $y' \leq b$ and again $\sigma^2 = \lambda F/2\pi$.

As it is shown in [61], the diffraction field plate on the primary focal line of the straight-strip zone is given by

$$E \equiv \frac{\sqrt{2}E_o}{\pi} \sqrt{2N_o - 1} = \frac{2E_o}{\pi\sqrt{\lambda F}} \quad (4.32)$$

Here with N_o we denote the number of the straight open zones in the Soret-type zone plate.

From (4.32) the zone plate focusing gain is found as

$$G_f = 2(2N_o - 1) = \frac{4b^2}{\lambda F} \quad (4.33)$$

In addition, the number of the open zones may be expressed as $N_o = b^2/\lambda F + 1/2$.

Frequency Bandwidth: Further Discussion Let us consider now the spectral characteristics of a paraxial Soret zone plate on the basis of its transmission function. For a given zonal geometry $\sigma = \sqrt{\lambda F/2\pi}$ is a constant because the focal length is inversely proportional to the wavelength λ , or $F(\lambda) = b_N^2/N\lambda$, where $b_N = a_o$ is the Soret zone plate aperture radius.

The pulse response t_p of the paraxial Soret zone plate is given by (4.34) [64]

$$t_p \equiv 2.44 \frac{\lambda F}{2a_o} \quad (4.34)$$

If a_o is taken as constant and λF is an invariant product, a much unexpected conclusion follows: The paraxial Soret zone plate has a broadband transmission function.

Consider next a nonparaxial Soret zone plate (a short-focal Fresnel zone plate, for example) illuminated by a plane wave. Now its zone aperture radius b_N is calculated by a more complicated equation from which the primary focal length can be written in the form: $F = b_N^2/N\lambda - N\lambda/4$ [see (4.46)]. From the latter expression it is evident that the increase in wavelength leads to significant

diminishing of the first (paraxial) term or the zone plate paraxiality is getting worse. As it is shown in [64] the condition for a good Soret zone plate paraxiality or small frequency dependence is given as

$$\frac{2a_0}{F} \leq \frac{1.856}{\sqrt[3]{\frac{2a_0}{\lambda}}} \quad (4.35)$$

It is easily calculated from (4.35) that for $2a_0 > 100\lambda$, $2a_0/F \rightarrow 0.3$, or to keep good frequency bandwidth for the large aperture Soret zone plate a long-focal length is necessary, or $F \geq 6a_0$.

With the above criterion in mind, the frequency bandwidth can be determined as follows

$$\frac{2\Delta\omega}{\omega_0} \cong \frac{40F}{Na_0}, \% \quad (4.36)$$

Equation (4.36) is more precise than (4.15) because it takes into account not only N , but a_0 and F , as well.

The relative frequency bandwidth (in percent) of a Soret zone plate versus the ratio between the aperture and focal length a_0/F was calculated from (4.36) and drawn in Figure 4.21, with a solid line for $N = 10$ and a dashed line for $N = 30$. It is evident that for a small number of zones and a big focal length, the Soret zone plate is a paraxial lens, and its bandwidth becomes too large—more than 15–20%. On the other hand, with the increase in the number of zones (or zone plate diameter) the frequency bandwidth is only a few percent.

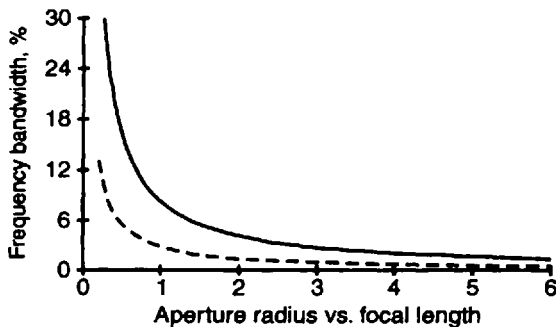


Figure 4.21 Frequency bandwidth of Soret zone plate versus ratio a_0/F .

4.3.1.5 Illumination by Spherical Wave and Comparison With Ordinary Lens

In the more general case, where a spherical wave front of radius d_1 is transformed by the Fresnel zone plate into spherical wave of radii d_{2n} , $n = 1, 2, 3, \dots$, we may rewrite (2.11) in the following form (for ρ_o and r_o replaced by d_1 and d_2 , respectively)

$$\frac{n\lambda}{b_n^2} = \frac{1}{F_n} = \frac{1}{d_1} + \frac{1}{d_{2n}} \quad (4.37)$$

The ordinary thin converging lens is described by a similar equation, the so-called lensmaker's formula [14, 15]

$$\frac{1}{F} = \frac{1}{d_1} + \frac{1}{d_2} \quad (4.38)$$

where

$$\frac{1}{f} = (\sqrt{\epsilon_r} - 1) \left(\frac{1}{R_1} - \frac{1}{R_2} \right) \quad (4.39)$$

In (4.39) ϵ_r is the relative permittivity of the lens, and R_1 and R_2 are the radii of its refracting surfaces.

From (4.37)–(4.39) we reach a conclusion that the zone plate has focusing properties similar to those of the ordinary converging lens, except for the multiple values of F .

The Soret zone plate is designed for plane wave incidence but is illuminated by a spherical wave. To maintain good-focusing quality of the zone plate the maximum number of the open zones must not exceed n_{\max} [2], or

$$n_{\max} < \frac{d_1}{\sqrt{|6\lambda(d_1 - F)|}} \quad (4.40)$$

It is seen from (4.40) that if the incident wave is not spherical, but plane one, then $d_1 = \infty$, and $n_{\max} < \infty$, or the number of zones, is theoretically unlimited. This is, however true, if the Fresnel zone plate is designed according to the exact formula for b_n , not to (4.3.1). Table 4.1 summarizes the basic properties of circular condensing lens and Soret zone plate [2, 9].

The most specific features of the Soret zone plate are listed as follows:

Table 4.1
Comparison Between Ordinary Converging Lens and Soret Zone Plate

Properties	Converging Lens	Soret Zone Plate
Focusing mechanism	Refraction plus interference	Diffraction plus interference
High-order foci	None	Odd foci (3, 5, 7 . . .)
Lensmaker's equation	$\frac{1}{F} = \frac{1}{d_1} + \frac{1}{d_2}$	$\frac{1}{F_n} = \frac{1}{d_1} + \frac{1}{d_{2n}}$
Focal length	$\frac{1}{F} = (\sqrt{\epsilon_r} - 1) \left(\frac{1}{R_1} - \frac{1}{R_2} \right)$	$\frac{1}{F_n} = \frac{2n+1}{F}$, $n = 0, 1, 2, \dots$
Thickness	Big	Small
Relative focusing intensity	1	$1/\pi^2$ (at primary focus)
Resolution	$\vartheta_o = 1.22 \frac{\lambda}{2a_o}$, radians	$\vartheta_o \cong 1.22 \frac{\lambda}{2a_o}$, radians
Chromatism	Present	Pronounced

- Multiple diffraction foci;
- π^2 times smaller focusing power intensity (at the primary focus) compared to that of the same diameter ordinary condensing lens;
- Approximately the same angular resolution.

4.3.1.6 Dimensioning of Circular Soret Zone Plate

At microwave/millimeter-wave frequencies more exact equations for Fresnel zone radii and areas are required, especially for short-focal and large-aperture zone plates. Here we shall derive such more precise equations for the Fresnel zone radii, areas, and widths.

Figure 4.22(a) is a geometry for dimensioning of the half-wave planar zone plate and, in particular, the planar Soret zone plate if a spherical wave radiated from a point source at $P_1(0, 0, z = -d_1)$ is focused by the Soret zone plate at the observation point $P_2(0, 0, z = +d_2)$.

For the Soret zone plate the half-wave RPD has to be applied, or

$$\text{RPD} = n \frac{\lambda}{2} = (\sqrt{d_1^2 + b_n^2} + \sqrt{d_2^2 + b_n^2}) - (d_1 + d_2) \quad (4.41)$$

where b_n is the n -th Fresnel zone circle radius ($n = 1, 2, 3, \dots, N$, with N the total number of the Fresnel zones).

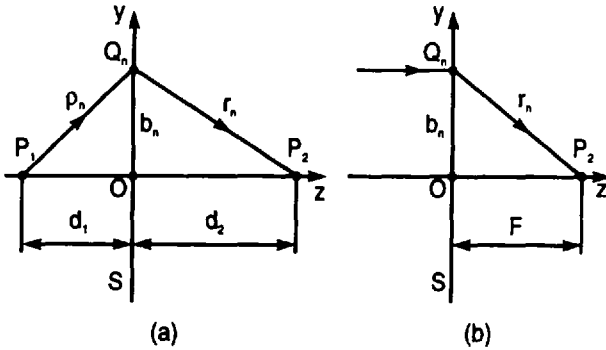


Figure 4.22 Geometry for deriving zone radii equation for Soret zone plate, illuminated by (a) spherical and (b) plane wave front.

Equation (4.41) can be solved for b_n as follows. Using the factorization expression for the difference of two squares, we can write $\rho^2 - r^2 = (\rho - r)(\rho + r)$, or

$$(\sqrt{d_1^2 + b_n^2} - \sqrt{d_2^2 + b_n^2})(\sqrt{d_1^2 + b_n^2} + \sqrt{d_2^2 + b_n^2}) = d_1^2 - d_2^2 \quad (4.42)$$

As $\rho - r$ is equal to

$$\sqrt{d_1^2 + b_n^2} - \sqrt{d_2^2 + b_n^2} = \frac{d_1^2 - d_2^2}{d_1 + d_2 + n\lambda/2} \quad (4.43)$$

from (4.41) and (4.43) we find that

$$2\sqrt{d_1^2 + b_n^2} = d_1 + d_2 + n\lambda/2 + \frac{d_1^2 - d_2^2}{\rho_1 + r_2 + n\lambda/2} \quad (4.44)$$

From (4.44) it is not difficult to obtain b_n , or

$$b_n = \frac{1}{2} \sqrt{(d_1 + d_2 + n\lambda/2)^2 + \left(\frac{d_1^2 - d_2^2}{d_1 + d_2 + n\lambda/2}\right)^2 - 2(d_1^2 + d_2^2)} \quad (4.45)$$

If the Soret zone plate is illuminated by a plane wave, or if $d_1 \rightarrow \infty$, and $d_2 = F$ is the zone plate focal length, (4.45) becomes

$$b_n = \sqrt{n\lambda F + \left(\frac{n\lambda}{2}\right)^2} \quad (4.46)$$

Finally, for the paraxial case, which is typical for optical and quasi-optical Soret zone plates, $F \gg \lambda$, $(n\lambda/2)^2 \ll n\lambda F$, and thus, the known approximation (2.24) for b_n is found again, or $b_n \equiv \sqrt{n\lambda F}$.

Computations for the Fresnel zone radius b_n as a function of the zone number n are illustrated in Figure 4.23. They were performed for the case of plane incident wave by use of (4.45), solid line, and the approximated one, or (2.24), dashed line, for a constant focal length $F = 40$ cm.

Figure 4.23(a) is relevant to a microwave Soret zone plate ($\lambda = 3$ cm) and Figure 4.23(b) to a submillimeter Soret zone plate ($\lambda = 0.3$ mm). In the former case, the Soret zone plate works under nonparaxial conditions, and (2.24) and (4.45) for b_n give different results, especially for large n . The error curve, drawn with a dotted line, shows a relative error of 15%, for $n = 0$. In the latter or paraxial case, however, the two formulas offer almost the same accuracy (the solid and dashed curves are merged, and the error is less than 0.25% for $n = 20$).

Figure 4.24(a) shows the Fresnel zones of a circular half-wave zone plate illuminated by a spherical wave [Figure 4.21(a)]. The zones are bounded in a square with sides of 60 cm. The calculations were made by (4.45) for $\lambda = 3.2$ cm, $d_1 = 40$ cm, and $d_2 = 60$ cm.

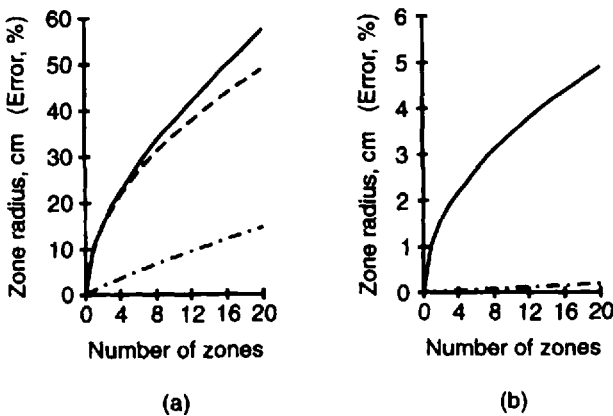


Figure 4.23 Fresnel zone radius versus zone number, for $F = 40$ cm, computed from exact (solid line) and approximate (dashed line) equations: (a) $\lambda = 3$ cm and (b) $\lambda = 0.3$ mm (dash-dot line)—approximation error in percent.

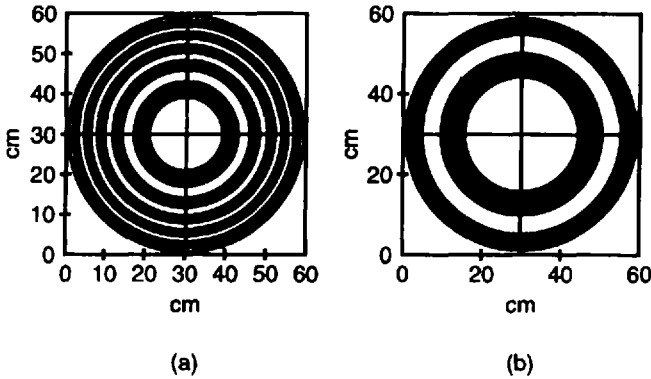


Figure 4.24 Fresnel zone patterns of a 3-cm circular Soret zone plate for two shapes of incident wave front: (a) spherical, with $d_1 = 40$ cm and $d_2 = 60$ cm, and (b) plane, with $F = 60$ cm.

Similar calculations were performed by (4.46) for a plane wave incidence, $\lambda = 3.2$ cm and $d_2 = F = 60$ cm. The zones for this case are contoured in Figure 4.24(b).

It is evident that the two zone patterns are rather different. While the Soret zone plate illuminated by a plane wave comprises four wide Fresnel zones in total, the Soret zone plate lighted by a spherical wave has eleven much narrower zones. For better clearness, the closed zones are blackened.

The zone radius (solid line) and zone area (dashed line) variation versus zone number for the above exemplary zone plate is illustrated in Figure 4.25(a, b), for spherical and plane wave incidence, respectively. The radius and area curves in the two cases are quite similar in shape, but correspond to very different values. From the area plots it is concluded that the Fresnel zones of the microwave Soret zone plate are not equal in area. This is an assumption for paraxial optical and quasi-optical zone plates that comprise hundreds or thousands more Fresnel zones. Instead, the zone area versus zone number increases almost linearly.

4.3.1.7 Focusing Properties of the Soret Zone Plate

For calculation of the Soret zone plate focusing characteristics, we apply the Fresnel-Kirchhoff diffraction theory for apertures with circular symmetry discussed in Section 2.4.6. Off-axis and on-axis field analysis are considered separately. Also discussed are the optimization of focal length and frequency bandwidth of the zone plate.

Off-Axis Field Analysis Let us consider a similar coordinate geometry as that given in Figure 2.22 and suppose that a point source (or isotropic radiating

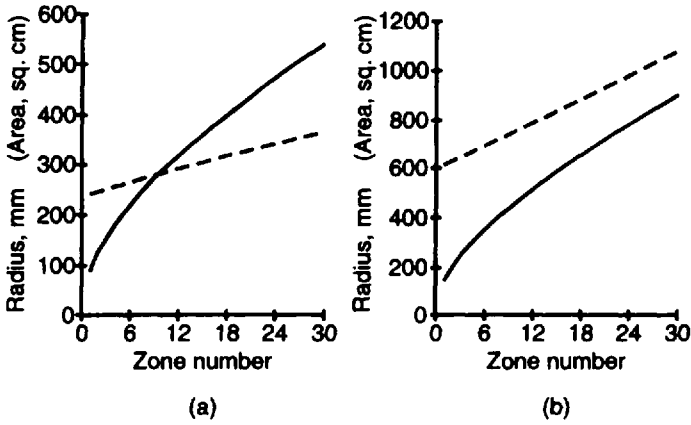


Figure 4.25 Zone radius (solid line) and zone area (dashed line) versus number of zones for: (a) spherical wave incidence ($d_1 = 40$ cm, $d_2 = 60$ cm, and $\lambda = 3.2$ cm) and (b) plane wave incidence ($d_2 = F = 60$ cm and $\lambda = 3.2$ cm).

antenna) is located at point $P_1(0, 0, -d_1)$. The observation point $P_2(x_2, 0, d_2)$ is placed in the xz -plane.

We shall examine here the Soret zone plate field amplitude variation with x_2 coordinate, in the transverse plane $z = d_2 = \text{const}$. We did a similar analysis in Section 2.4.6 for a single annular slot and in Section 3.2.1 for a metal ring director.

Suppose a positive Soret zone plate with a first Fresnel zone open. The complex field produced by the zone plate at the observation point can be written as a sum of all odd open zones, or

$$E(P_2) = j\pi E_o(P_2) \left[\sum_n \int_{\chi_{n-1}}^{\chi_n} e^{-j\frac{\pi}{2}\chi^2} J_o(k\chi) \chi d\chi - \frac{1}{2} \int_{\chi_{N-1}}^{\chi_N} e^{-j\frac{\pi}{2}\chi^2} J_o(k\chi) \chi d\chi \right] \quad (4.47)$$

where $n = 1, 3, 5, \dots, N$, and N is the number of the outer open zone, bordering the last opaque zone (metal or absorbing ring). Note that in (4.47) the inclination factor $I(\vartheta)$ is neglected.

As it was explained in Section 2.2.4, the second term in the above equation represents half of the diffraction field created by the outer open zone. This is a correction field term, which is accurate only for the field at axial point $P_2(0, 0, d_2)$. Therefore, it may give a proper correction only for a small off-axial deviation.

As in Chapters 1–3, the inclination factor $I(\vartheta) = 0.5(1 + \cos \vartheta)$ is taken to be constant and equal to unity because the calculations are usually made for small diffraction angles. For example, if $\vartheta = 15$ degrees, $I(\vartheta) = 0.983$.

Remember that since $\chi_{n,n-1} = \sqrt{2}b_{n,n-1}/b_1$, and the zone radii b_1 , b_n and b_{n-1} are calculated by (4.45). The equivalent focal length is $F_e = d_1 d_2 / (d_1 + d_2)$.

The focusing gain G_f of the zone plate is calculated in decibels from (4.47), or

$$G_f = 20 \log [E(P_2) / E_o(P_2)]$$

As a computational example for spherical wave illumination, we took the same X band Soret zone plate, whose Fresnel zones were dimensioned and plotted in Figure 4.24(a). From all eleven zones, six were considered open, and five opaque. The focusing gain pattern G_f , in decibels, was plotted by a solid line in the transverse plane $z = d_2$ versus the observation angle ϑ (Figure 4.26). The maximum focusing gain is on the zone plate axis ($\vartheta = 0$ degrees) and has a value of 17.3 dB.

If the Soret zone plate is illuminated by a plane wave front we may use the same field equation as for the spherical wave illumination, or (4.47), provided that $d_1 \rightarrow \infty$, $d_2 = F$, and the zone radii are calculated by (4.46).

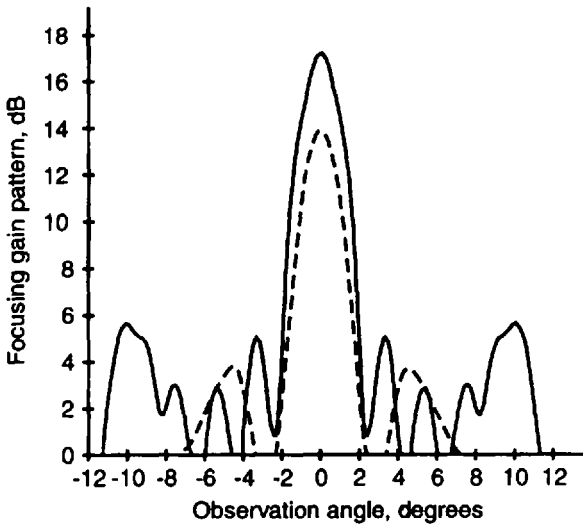


Figure 4.26 Focusing gain pattern of Soret zone plate as a function of the observation angle for spherical (solid line) and plane (dashed line) wave illumination.

Figure 4.26 plots also, with a dashed line, the focusing gain pattern of the Soret zone plate in case of plane wave illumination. From all Fresnel zones bounded in the 60-cm aperture, two and a half were taken in the summation procedure. Actually, this zone plate consists of only two opaque rings and has a maximum focusing gain of 13.8 dB.

As it was expected, the focusing gain of the two Soret zone plates depends mainly on the number of the open rings. Though the above two configurations are bounded in the same size aperture, they have much different focusing powers.

On-Axis Field Analysis for Plane Wave Incidence The analysis here closely follows [55, 56]. The geometry in Figure 4.27 is a section of the Soret zone plate with a primary focal point $P(0, 0, F)$ and a current point $P'(0, 0, z')$.

The Fresnel-Kirchhoff diffraction field contribution of an elementary circular strip (dr' in width) toward the total field at P' is given by

$$dE(P) = \frac{j}{\lambda} E_o(P) I(\vartheta) \frac{e^{-j\beta r}}{r} dS' \tag{4.48}$$

where $I(\vartheta) = 0.5(1 + \cos \vartheta) = 0.5(1 + z/r)$ is the Huygens' source inclination factor, $dS' = r' dr' d\varphi'$, with φ' current azimuth angle.

The integral field at P' due to the n -th Fresnel zone will be

$$E_n(P) = \frac{j}{\lambda} E_o(P) \int_0^{2\pi} \int_{b_{n-1}}^{b_n} I(\vartheta) \frac{e^{-j\beta r}}{r} r' dr' d\varphi' \tag{4.49}$$

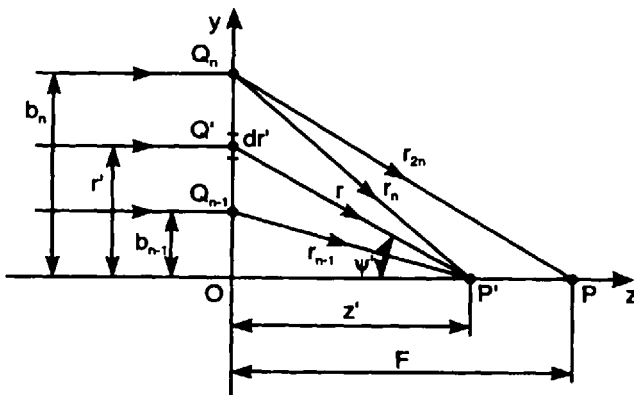


Figure 4.27 Geometry of Soret zone plate section. (After: [55].)

Integration with respect to the radial coordinate r' may be replaced with integration with respect to the ray coordinate r , as $r' dr' = r dr$, and because of the angular symmetry φ' , integration gives 2π . Therefore, (4.49) will be changed by the following one-dimensional integral

$$E_n(z) = \frac{j}{\lambda} \pi E_o(P) \int_{r_{n-1}}^{r_n} \left(1 + \frac{z}{r}\right) e^{-j\beta r} dr \quad (4.50)$$

where

$$r_n = \sqrt{z^2 + b_n^2} \quad (4.51)$$

with b_n calculated by (4.46).

The total field at the current axial point is a sum of the fields produced by all the open Fresnel zones, odd, for example, or

$$E(z) = \sum_n E_n(z), \text{ for } n = 1, 3, 5, \dots \quad (4.52)$$

Figure 4.28 illustrates the axial focusing gain or field intensity distribution along the zone plate axis for two sizes of the plane wave-illuminated Soret zone plate, with a same focal length $F = 40$ cm and for a wavelength $\lambda = 3$ cm. The solid line curve refers to a Soret zone plate with five zones open, and the dashed line curve to a Soret zone plate with one and a half zones open

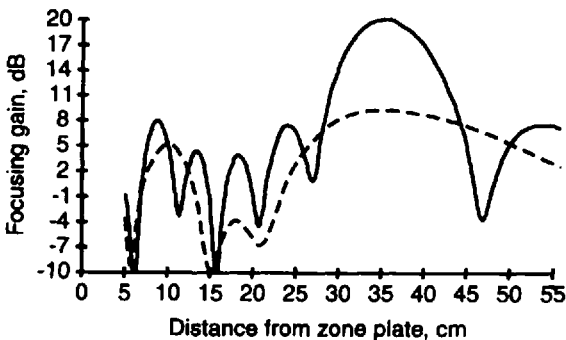


Figure 4.28 Focusing gain as function of axial distance from the Soret zone plate (with the solid line indicating that five zones are open and with the dashed line indicating that one and a half zones are open); $F = 40$ cm, $\lambda = 3$ cm.

zones open. The latter is actually a single opaque ring, illuminated by a normally incident plane wave.

Focal Length Optimization In [65] the focal length of an X -band Soret zone plate model was optimized to obtain maximum field intensity for two types of wave illumination: plane and spherical. The theoretical study was made in two steps: first, by calculation of the zone radii b_n for different focal lengths, and second, by computation for each focal length of the respective field amplitude at the primary focus. Figure 4.29 shows the variation of the relative field intensity with the focal length.

In the two cases, plane and spherical wave incidence, the field oscillates with the focal length. It is too low for small focal lengths (let us say smaller than 2–3 wavelengths). With the growth of the focal length, the field progressively increases, reaching asymptotically a medium relative value of about 0.8 for focal length around 10 wavelengths. It was concluded that for the plane wave of 3.2 cm in wavelength an optimized zone plate could be designed with focal length 32 cm.

A similar behavior of the field versus focal length was found for the spherical wave illumination with the only difference that after reaching field intensity maxima, the values go on decreasing much more slowly with a further increase in focal length. The optimum focal length was determined to be 25.4 cm for the same wavelength and a source distance of 60 cm.

Frequency Bandwidth of Microwave Soret Zone Plate (Experimental Study) The effect of the variation of frequency in X -band on the field intensity

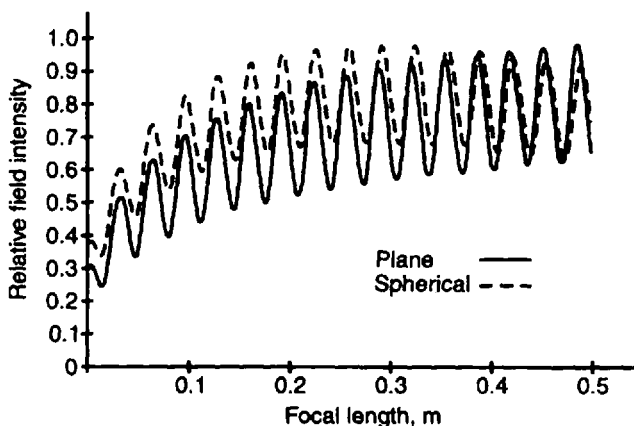


Figure 4.29 Variation of field intensity with focal length for plane (solid line) and spherical (dashed line) wave incidence. (After: [65].)

at the primary focal point of the Soret zone plate was studied theoretically and experimentally in [65], for both the plane and spherical wave incidence. The results of the study are seen in Figure 4.30.

For the two wave fronts, there is very good agreement between theory and experiment. It is evident that the curve for the spherical wave front is sharper, which indicates a smaller frequency bandwidth. This effect is easily explained with the higher number of Fresnel zones in the case of spherical wave incidence.

4.3.2 Phase-Corrected Zone Plates

The microwave/millimeter-wave phase-corrected or Wood-type zone plate finds much larger application compared to the Soret-type zone plate because of its enhanced focusing characteristics. This is attained, however, at the expense of more complicated zone plate designs and methods of analysis.

Here we explain visually the phase correction mechanism of the phase-reversal and quarter-wave zone plates and summarize their phase correction theory. Also studied are the focusing efficiency and focusing gain of the phase-corrected zone plate. Examined in detail are practical and theoretical design considerations for different zone plate constructions and zonal phase-shifters.

4.3.2.1 Phase Correction Mechanism

In principle, the Fresnel zone plates do not make as smooth a transformation from spherical to spherical or plane wave front (or vice versa) as do the ordinary lens and reflector focusing devices. Instead, the zoned plate is a stepwise phase

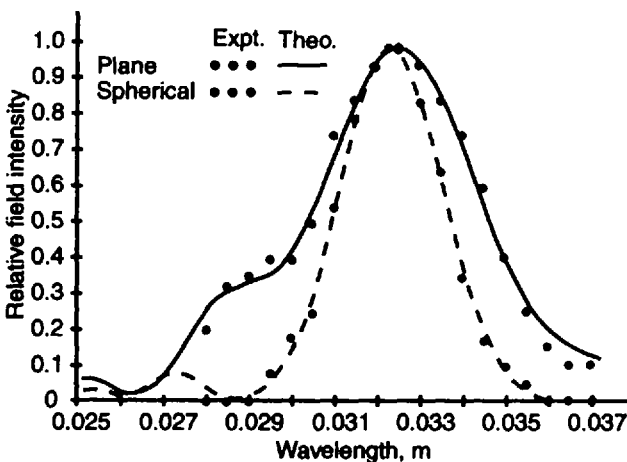


Figure 4.30 Frequency response of the X-band Soret zone plate model. (After: [65].)

front converter, where each full-wave Fresnel zone is divided into half-wave, quarter-wave, eighth-wave subzones, and so on.

Consider first the phase correction procedure for the half-wave or Wood's phase-reversal zone plate. Suppose the plate is illuminated by a spherical wave front from a point source at a distance F . The radial phase variation (or phase error) in the plane of the zone plate is described by a quadratic equation, which can be expressed as a function of Fresnel zone number as follows

$$\Phi_1(n) = -\frac{2\pi}{\lambda} \left(\sqrt{F^2 + b_n^2} - F \right) \quad (4.53)$$

where b_n is the Fresnel zone radius, calculated for given F and λ by (4.46). The calculated quadratic function of n is drawn in Figure 4.31 as a dash-dotted (dadot) line.

The conversion of the spherical phase front into a plane one makes zero phase error in the aperture. Ideally, this is attained by an ordinary, convex-plane dielectric lens, for example, which creates a phase-reversed quadratic function $\Phi_2(n) = -\Phi_1(n)$, with a graph shown in Figure 4.31 (dashed line). Therefore, the sum of the initial phase function and the lens phase correction function will be zero, and thus the spherical phase error in the lens aperture will be totally compensated.

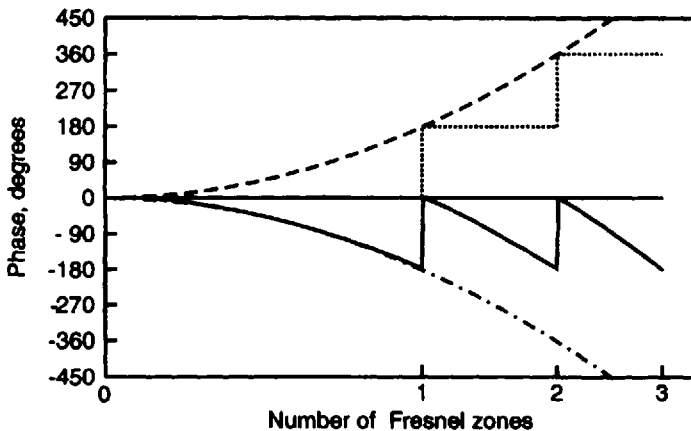


Figure 4.31 Illustration of stepwise phase-front transformation in Wood zone plate: spherical phase-error curve (dadot line), ideal compensation curve (dashed line), 180-degree staircase compensation curve (dotted line), and resultant tooth-type phase front (solid line).

Zoned plates, however, make partial phase compensation. In the phase-reversal zone plate or Wood zone plate, for example, an approximate, staircase compensation function (dotted line) with steps of 180 degrees each is created by the 180-degree phase-shifting transparent structures that replace the opaque zones in the Soret zone plate. The algebraic summation of the spherical phase-error function and staircase compensation function give the resultant tooth-type phase error function in the zone plate aperture, which vary within each Fresnel zone from 0 to -180 degrees. A similar explanation is valid for the quarter-wave-zoned plate, and it is illustrated graphically in Figure 4.32, where it is seen that within each subzone the resultant aperture phase error does not exceed -90 degrees.

4.3.2.2 Focusing Efficiency and Focusing Gain

The overall focusing efficiency of the real zone plate depends on amplitude, phase, polarization, and other factors. However, in the case of the idealized stepwise phase-corrected Fresnel zone plate illuminated by a point source, the focusing efficiency e_p depends only on the phase increment in the staircase compensation function. It is normally defined as a ratio between its focused intensity I (or squared focused field amplitude $|E|^2$) and that of the ideal lens I_L (or $|E_L|^2$) at the primary focal point, so that

$$e_p = \frac{I}{I_L} = \left| \frac{E}{E_L} \right|^2 100, \% \quad (4.54)$$

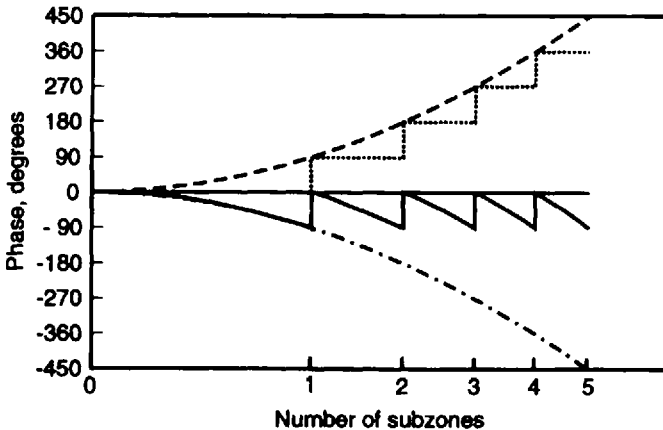


Figure 4.32 Illustration of stepwise phase-front transformation in quarter-wave zone plate: spherical phase-error curve (dash-dot line), ideal compensation curve (dashed line), 90-degree staircase compensation curve (dotted line), and resultant tooth-type quasi-plane phase front (solid line).

or, in decibels, $e_p = 10 \log(I/I_L)$, dB, for a plane wave illumination and the same focal distance F .

There are different approaches in the phase efficiency analysis, but we quote here only the following simple expression for planar phase-corrected zone plates taken from [6]

$$e_p = \frac{\sin^2(\Delta\Phi/2)}{(\Delta\Phi/2)^2} \quad (4.55)$$

where $\Delta\Phi$ is the increment of the staircase phase correction function.

A plot of the above efficiency function versus the phase increment in degrees is shown in Figure 4.33. The phase-reversal zone plate $\Delta\Phi = 180$ degrees, and this corresponds to an efficiency of 40.5%. The focusing efficiency of the quarter-wave zone plate ($\Delta\Phi = 90$ degrees) is 81%, and that of the eighth-wave zone plate ($\Delta\Phi = 45$ degrees) reaches 95%. If $\Delta\Phi \rightarrow 0$, the zone plate efficiency tends to unity [66]. For microwave/millimeter-wave frequencies, the zone plates, however, are normally made with phase corrections equal to or bigger than 45 degrees. Except for the focusing efficiency, the focusing action is measured by the focusing gain.

Focusing gain expressions and graphical illustrations for the Wood's phase-reversal zone plate as a function of the zone number and frequency were published in [39]. For a working frequency ω , not equal to the design frequency ω_0 , and total Fresnel zone number N , the focusing gain G_f for plane wave illumination is expressed as

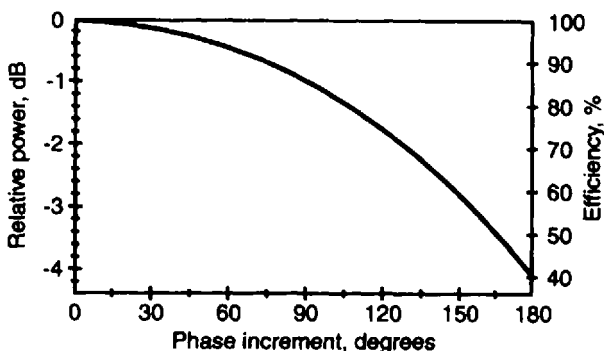


Figure 4.33 Efficiency of phase-corrected zone plate as function of phase increment. (After: [6].)

$$\begin{aligned}
G_f(N, \omega) = & \left(\sum_{n=1}^N A(n) \left\{ \left[2\text{GIV}\left(\frac{n-1}{2} + 1\right) \right] \cos\left(\pi \frac{\omega}{\omega_o}\right) \right. \right. \\
& - \left. \left. \left[2\text{GIV}\left(\frac{n-1}{2}\right) \right] \cos\left(\pi \frac{\omega}{\omega_o}\right) \right\} \right)^2 \\
& + \left(\sum_{n=1}^N A(n) \left\{ \left[2\text{GIV}\left(\frac{n-1}{2} + 1\right) \right] \sin\left(\pi \frac{\omega}{\omega_o}\right) \right. \right. \\
& - \left. \left. \left[2\text{GIV}\left(\frac{n-1}{2}\right) \right] \sin\left(\pi \frac{\omega}{\omega_o}\right) \right\} \right)^2
\end{aligned} \tag{4.56}$$

where $\text{GIV}\left(\frac{n-1}{2}\right)$ is the largest integer that is less than or equal to $(n-1)/2$, and the coefficients $A(n)$ are given by

$$A(n) = \frac{8F/\lambda_o + (2n-1)}{8F/\lambda_o + 2(2n-1)} \tag{4.57}$$

Equation (4.56) is greatly simplified if $f = f_o$, or

$$G_f = 4 \left(\sum_{n=1}^N \frac{8F/\lambda_o + (2n-1)}{8F/\lambda_o + 2(2n-1)} \right)^2 \tag{4.58}$$

and finally, for $F/\lambda_o \gg N$, the following rough approximation applies: $G_f(N) \cong 4N^2$. Because $N^2 \cong G_{f\text{SZP}}$, where with $G_{f\text{SZP}}$ we denote the focusing gain of the Soret zone plate, it follows that $G_f \cong 4G_{f\text{SZP}}$, and

$$G_{f\text{SZP}} = \left(\sum_{n=1}^N \frac{8F/\lambda_o + (2n-1)}{8F/\lambda_o + 2(2n-1)} \right)^2 \tag{4.59}$$

The calculated focusing gain in decibels versus frequency is illustrated in Figure 4.34. The two curves correspond to the phase-reversal zone plate (dashed line) with half-wave zones, and quarter-wave (solid line) zone plate with quarter-wave zones. The focal length of the two zone plates equals 50 wavelengths at medium frequency ω_o . The deep minima in the frequency characteristics suggest that the zone plate can be applied as a frequency filter. In addition, it is seen that a quarter-wave zone plate designed for the frequency ω_o acts as a half-period plate at the second harmonic.

A near-field axial intensity distribution (or relative gain), in decibels of a phase-reversal or Wood zone plate, is plotted after [67] in Figure 4.35 (solid

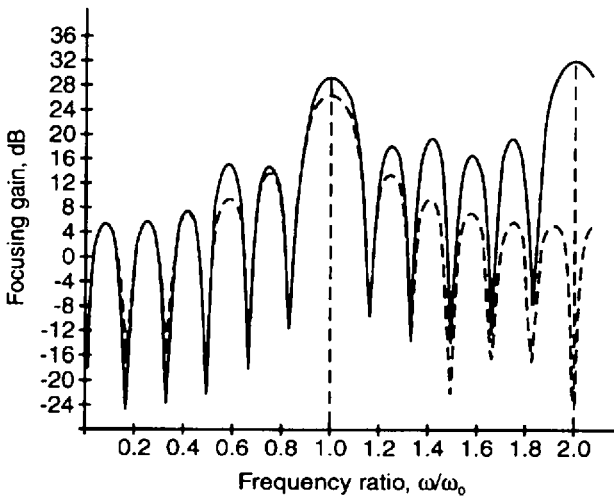


Figure 4.34 Frequency characteristic of zone plate of quarter-wave zone plate with 48 zones (solid curve) and phase-reversal zone plate with 24 zones (dashed curve), for $F = 50\lambda$. (After: [39], © 1987 IEEE.)

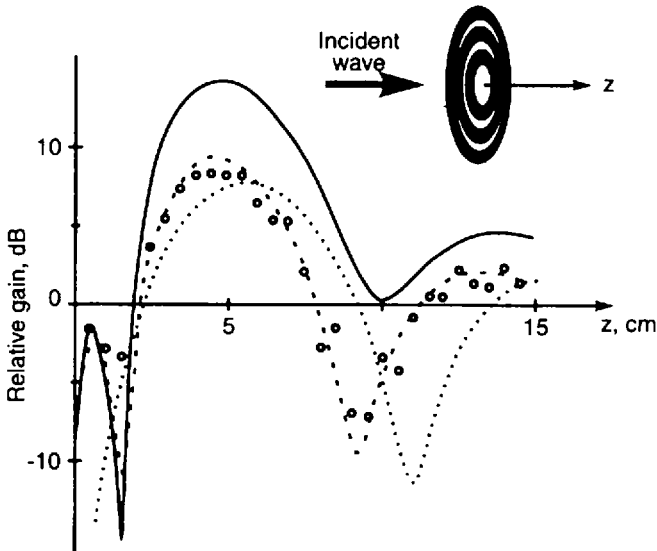


Figure 4.35 Near-field intensity distribution along focal axis of Wood zone plate (solid line), odd zone Soret zone plate (dashed line), and even zone Soret zone plate (dotted line). Experimental values for odd Soret zone plate are marked by o's. (After: [67].)

line). The zone plate is designed for 9,375 MHz and consists of six Fresnel zones. It has a focal length of 4 cm (or 1.25λ , short-focal zone plate) and maximum zone radius of 13 cm (or 1.25λ). This plot is compared to two other plots for the same-in-size Soret zone plate with odd zones open (positive Soret zone plate, dashed line) or even zones open (negative Soret zone plate, dotted line).

The axial field intensity contribution of each Fresnel zone is computed by (4.60), a near-field equation [67] similar to (4.50)

$$E_n(P) = j \frac{\pi}{\lambda} E_o(P) \int_{b_{n-1}}^{b_n} \frac{z}{r^2} e^{-j\beta r} \left[1 + \left(1 + \frac{1}{j\beta r} \right) \right] r' dr' \quad (4.60)$$

The zone plate coordinate geometry is the same as in Figure 4.26. The total field due to the odd or positive zones, $E_+(P)$, or that due to the even or negative zones only, $E_-(P)$, is calculated as

$$E_+(P) = \sum_{n=1,3,5} E_n(P) \text{ or } E_-(P) = \sum_{n=2,4,6} E_n(P) \quad (4.61)$$

respectively. In this case the zone plate comprises in total six Fresnel zones.

The field $E(P)$ radiated by the phase-reversal zone plate is found as a sum of $E_+(P)$ and $e^{j\pi}E_-(P)$, or

$$E(P) = E_+(P) + e^{j\pi}E_-(P) \quad (4.62)$$

From Figure 4.35 it is concluded that there is a significant difference between the near-field relative gains at primary focus of the odd zone Soret zone plate (9.4 dB) and even zone Soret zone plate (7.0 dB). The focal gain of the phase reversal zone plate is much higher (14 dB).

The dielectric zone plates have been studied here without taking into account the complicated diffraction phenomena inside the solid phase-correcting ring. Such studies were accomplished by Van Houten and Herben [46] using a modified GTD approach, and by Popov, Kopilov, and Vinogradov [68], who simulated diffraction fields on the basis of the parabolic equation (PE) diffraction method.

4.3.2.3 Phase Correction Theory of Zone Plate

Until a short time ago, the phase correction in the zone plates was executed based on simple physical considerations as it was done by Wood a hundred years ago. To the author's knowledge the only comprehensive theoretical treatment on

the phase correction of the electromagnetic Fresnel zone plates was published by Guo and Barton in 1993 [43]; it will be summarized here.

The total field at the primary focal point P produced by all zones of Fresnel zone plate, for plane wave illumination, is expressed on the basis of the Kirchhoff's diffraction integral in the form

$$E(P) = j\pi E_o \sum_{k=1}^K \int_{b_{k-1}}^{b_k} \frac{e^{j[\Phi(r')-\beta r]}}{r} \left(1 + \frac{1}{r}\right) r' dr' \quad (4.63)$$

where r' is the current radial coordinate, F is the focal distance, $r = \sqrt{F^2 + r'^2}$ is the ray distance from a current point on the zone plate to the axial focal point P , $\Phi(r')$ is a phase-correction function, and $\beta = 2\pi/\lambda$ is the wave number.

The k -th zone radius satisfies the full-wave zone RPD equation

$$\sqrt{F^2 + b_k^2} - F = k\lambda, \quad (k = 0, 1, 2, \dots, K) \quad (4.64)$$

Equation (4.63) is then approximated to become

$$E(P) \cong j\pi E_o(P) \sum_{k=1}^K \int_{b_{k-1}}^{b_k} \frac{1}{r} e^{j[\Phi(r')-\beta r]} \left(1 + \frac{F}{F + (k - \lambda/2)}\right) r' dr' \quad (4.65)$$

Next, a closed form of this equation is derived

$$E(P) \cong \frac{j}{2} E_o(P) e^{-j\beta F} \sum_{k=1}^K \left(1 + \frac{F}{F + (k - \lambda/2)}\right) \int_0^{2\pi} e^{j[\Phi'(\theta) - \theta]} d\theta \quad (4.66)$$

where

$$\theta = \beta(\sqrt{F^2 + r'^2} - [F - (k - 1)\lambda]), \quad (b_{k-1} \leq r' \leq b_k) \quad (4.67)$$

and $\Phi'(\theta) = \Phi[r'(\theta)]$.

The contributions from different full-wave zones with the same phase-correction function $\Phi'(\theta)$ differ only with the multiplier

$1 + F/[F + (k - \lambda/2)]$, which is an approximate expression of the Huygens' inclination factor.

For the ideally phase-corrected zone plate $\Phi'(\theta) - \theta = 0$, since for this condition (4.66) gives maximum field at P , or

$$|E(P)|_{\max} \cong \pi |E_o(P)| \sum_{k=1}^K \left(1 + \frac{F}{F + (k - \lambda/2)} \right) \quad (4.68)$$

The ideal smooth phase-correcting function in the r' domain is

$$\Phi_{\text{opt}}(r') = \beta(\sqrt{F^2 + r'^2} - [F - (k - 1/2)\lambda]) \quad (4.69)$$

In practice instead of a smooth phase-error-compensation, a discrete (stepwise) subzone phase-correction is employed, as illustrated in Section 4.3.2.1. The subzone phase correction techniques make use of discrete phase shifters in each full-wave zone in order to realize a stepwise phase-correcting function approximating $\Phi_{\text{opt}}(r')$.

Maximum of $|E(P)|$ is found for the following discrete conditions

$$\theta_{km} = 2\pi q/Q, \text{ and } \Phi'_{kp} = 2q\pi/Q + \alpha, \quad (q = 1, 2, 3, \dots, Q) \quad (4.70)$$

where k is the full-wave zone number, q is the subzone number, and α is an arbitrary initial phase, which must be the same for all full-wave zones.

From (4.67) and (4.70) the equation for finding the outer radius of the q -th subzone in the k -th full-wave zone is obtained

$$\sqrt{F^2 + b_{kq}^2} = F + [(k - 1) + q/Q]\lambda, \quad (4.71)$$

for $k = 1, 2, \dots, K; q = 1, 2, \dots, Q$

Using (4.67) and (4.71) two requirements have to be taken into account: (1) Q subzones must be equally divided in the θ domain, and (2) the phase difference between two adjacent phase shifters must be $2\pi/Q$.

Figure 4.36 illustrates two types of stepwise level approximation (quantization) in the quarter-wave zone plate ($Q = 4$) of the optimum quadratic phase function (dotted line), completed for different values of the initial phase angle α : first, for $\alpha = 0$ (solid line), and second, for $\alpha = 45$ degrees (dashed line). In the latter case the mean square quantization error is zero. To this point, we have discussed the case in which the number of subzones and the staircase

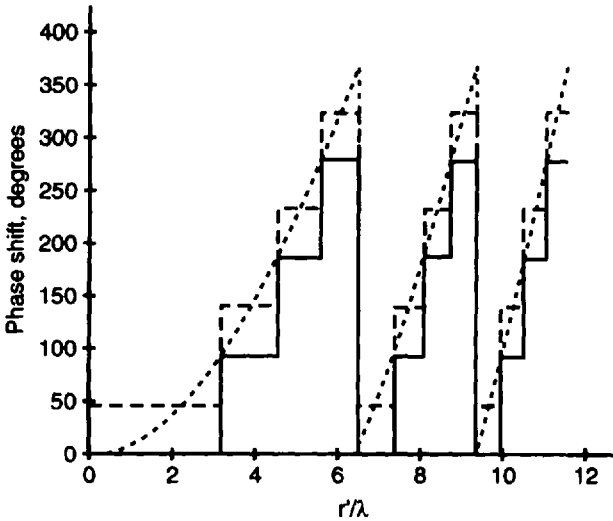


Figure 4.36 Ideal phase-correcting function (dotted line) for zone plate with $F = 20\lambda$ and its two equivalent stepwise approximations for: (a) $\alpha = 0$ (solid line) and (b) $\alpha = 45$ degrees (dashed line). (After: [43]).

approximation function are the same in each full-wave zone. In other words, this is the case of a periodic phase correction mechanism.

However, for a big number of zones in the zoned plate the widths of the outermost full-wave zones become too small. Practically, it is not possible to place the same number of phase shifters in the outer full-wave zones as in the inner ones. The problem can be solved by a compromise. For example, we can make a quarter-wave phase correction in the inner full-wave zones and a half-wave phase correction in the outer ones. This phase-correction technique, named aperiodic, was also described and studied theoretically in [43].

4.3.2.4 Design Considerations for Dielectric Phase-Reversal and Quarter-Wave Zone Plates

In this section we discuss practical experience and theoretical relations for designing phase-corrected zone plates as focusing elements in Fresnel zone plate antennas. Equations are given for the dimensions of phase-reversal and quarter-wave zone plates. Discussed are numerical examples for the transmission coefficients of solid, multilayer, and composite (metal-dielectric) phase-shifting plates provided they are infinite in extension. Finally, the equivalent-circuit transmission theory of circular ring array printed on a dielectric plate is considered.

Design of Single-Dielectric Zone Plates Consider first the basic points in designing the classical single-dielectric zone plate. Two possible profiles of the zone plate were shown in Figure 4.11(a, b). In Figure 4.37 [39], a millimeter-wave Wood zone plate is compared visually with two conventional plano-convex lenses for use at 140 GHz. The lenses and zone plates are of the same diameter, but the hyperbolic lens and the lens with spherical surface are much thicker than the Wood zone plate, about eight and eleven times, respectively. They are also much heavier, lossier, and more difficult to manufacture. Also, the Wood zone plate's focusing efficiency is only two and a half times smaller than the focusing efficiency of the hyperboloid lens.

From (4.71) we can obtain the following simple formula for calculation of the outer radius b_n of the n -th zone in a Fresnel zone plate with Q subzones in each full-wave zone

$$b_n = \sqrt{\frac{2nF}{Q} + \left(\frac{n\lambda}{Q}\right)^2} \quad (4.72)$$

where $Q = 2$ for the half-wave Soret and Wood zone plates. In this particular case, (4.72) reduces to (4.46). $Q = 4, 8, \dots$ for the quarter-wave, eighth-wave, and so on zone plates, respectively. The equation for zone radii is derived on the assumption that the zone plate has a negligibly small thickness that is true for the Soret zone plate. However, this is not the case for the dielectric Wood

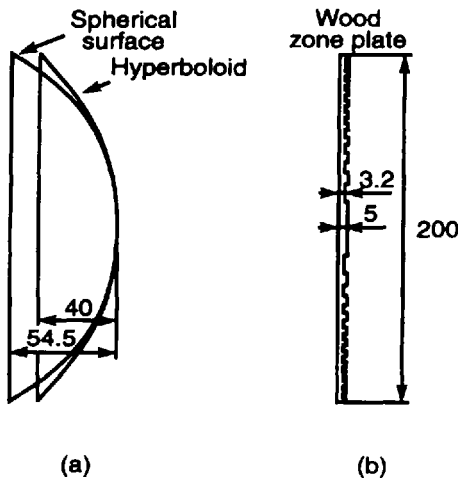


Figure 4.37 Comparison of polystyrene zone plate and lenses with 200-mm focal length designed for use at 140 GHz. (After: [39], © 1987 IEEE.)

zone plate-type zone plate, whose thickness is commensurate with the wavelength. If the focal length measured from the focus to the inside plate boundary is marked with F , the corresponding distance to the outside plate boundary will be $F + w$, where w is the plate thickness. For this focal length, (4.72) has to be rewritten, or $b_n(F + w) = \sqrt{2n\lambda(F + w)/Q + (n\lambda/Q)^2}$. Therefore, the following equation for b_n might be a good compromise for calculating the Wood zone plate zone radii [49]

$$b_n = \sqrt{\frac{2n\lambda(F + w/2)}{Q} + \left(\frac{n\lambda}{Q}\right)^2} \tag{4.73}$$

As we have discussed, the phase-reversing effect in the initial Wood zone plate is realized by forming annular grooves in a flat plate of low-loss dielectric material, such as polystyrene or teflon. The cross-section geometry of the Wood zone plate is shown in Figure 4.38, where the plane incident wave is focused at point P . The zone plate grooves have an equal depth w that can be found by taking into account that the rays from points A and B have to meet in phase at point P , or $(2\pi/\lambda)(\sqrt{\epsilon_r}t + B'P) - (2\pi/\lambda)[(t - w)\sqrt{\epsilon_r} + w + A'P] = 2\pi$.

However, from the half-wave Fresnel zone condition $(B'P - A''P) = \lambda/2$, and thus, w is easily found as

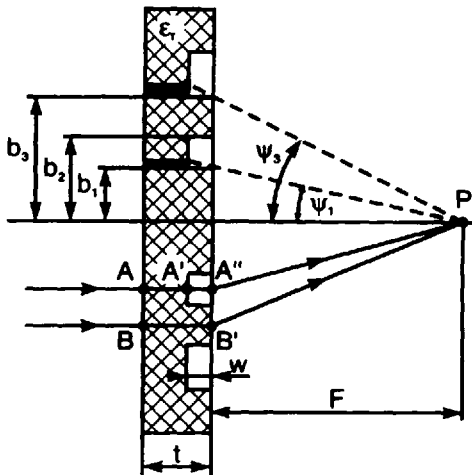


Figure 4.38 Geometry for finding depth of grooves and shadowed part in Wood zone plate. (After: [39], © 1987 IEEE.)

$$w = \frac{\lambda}{2\sqrt{\epsilon_r - 1}} \quad (4.74)$$

which is strictly valid only for a normal plane wave incidence. Nevertheless, in the nonparaxial zone plates, there are also rays coming to the plate obliquely, under an incidence angle ψ_i . For taking into account the influence of the incidence angle on the plate thickness, ray-tracing analysis through a dielectric phase-shifting plate was completed in [49 and Hristov, Selected Bibliography]. It gives the following more general formula for the plate thickness

$$w = \frac{\lambda}{2\sqrt{\epsilon_r - \sin^2 \psi_i - \cos \psi_i}} \quad (4.75)$$

For $\psi_i = 0$, (4.75) reduces to (4.74).

The thickness of a zone plate calculated by (4.75) for several values of the incidence angle is given in Table 4.2. The zone plate comprises dielectric phase-reversing rings with $\epsilon_r = 4$ and is designed for $\lambda = 5$ mm.

If the zone plate half-opening angle is $\psi_{i\max}$, the thickness w can be calculated by (4.75) for an average incidence angle ψ_{iav} , which is equal to $\psi_{i\max}/2$. The total thickness t of the classical Wood zone plate is bigger than the depth w of grooves.

For the quarter-wave dielectric zone plate, 0-, 90-, 270-, and 360-degree phase steps in each full-wave zone (staircase curve in Figure 4.31) are produced by successive zone grooves that are 0, w' , $2w'$, and $3w'$ in depth, correspondingly, where w' is given by

$$w' = \frac{\lambda}{4\sqrt{\epsilon_r - 1}} \quad (4.76)$$

More precise ray tracing through the flat structure of the Wood zone plate requires knowledge of the multiple complex transmission and reflection coefficients, given by (1.72) and (1.73), which are valid for oblique wave incidence and different polarizations.

Table 4.2
Zone Plate Thickness for Different Incident Angles

Angle of incidence ψ_i (degrees)	0	20	40	60	80
Zone plate thickness w (mm)	2.50	2.42	2.22	1.92	1.60

Let us consider next the effect of ray shadowing in the Wood zone plate. Figure 4.38 also illustrates the geometry of the shadowing situation. It shows that rays passing through the odd zones will be shadowed by the even zones. The percentage of the total plate that is shadowed is given by [39]

$$\text{Percentage shadowed} = \sum_{n=0}^{\text{GIV}[(n-1)/2]} \pi w \tan^2 \psi_{2n+1} / A \quad (4.77)$$

where A is the total zone plate area.

Design of Multidielectric Zone Plates In another method, by grooves in a single-dielectric plate, the phase correcting can be done by allocating within the zones concentric dielectric rings having equal thickness but different, properly chosen permittivity. In this way, a bilaterally planar multiple-dielectric zone plate is obtained.

These totally-flat zone plates have several considerable advantages compared to the grooved single-dielectric ones: (1) no accumulation of rain, snow, and dirt; (2) an aerodynamically smooth structure; and (3) lower spurious sidelobes because there are no edges in the zone structure.

The necessity of using two or more solid dielectrics with rather distinct permittivities and heat-expansion coefficients is the main disadvantage of the flat zone plates. In addition, the multiple-dielectric zone plates are heavier and more difficult to manufacture.

The thickness w'' of the double-dielectric zone plate is found with an equation similar to (4.74), or

$$w'' = \frac{\lambda}{2(\sqrt{\epsilon_{r1}} - \sqrt{\epsilon_{r2}})} \quad (4.78)$$

where ϵ_{r1} and ϵ_{r2} are the relative permittivities of the two dielectrics. Indeed, if the second dielectric is air, $\epsilon_{r1} = 1$ and (4.78) reduces to (4.74).

A family of graphs for selecting the thickness of the double-dielectric zone plate, in inches, is given by Black and Wietse in Figure 4.39 [39]. The thickness is plotted versus frequency, in gigahertz, for different material combinations. For example, a 35-GHz zone plate with a Rexolite/foam combination will be 7.11 mm in thickness.

We consider next some design considerations for the four-dielectric, quarter-wave zone plate, whose cross-section is sketched in Figure 4.12(b). Here, the central subzone of the first full-wave zone is open, and the other three subzones are filled up by solid dielectric rings with different permittivities. The next full-wave zones have a similar arrangement.

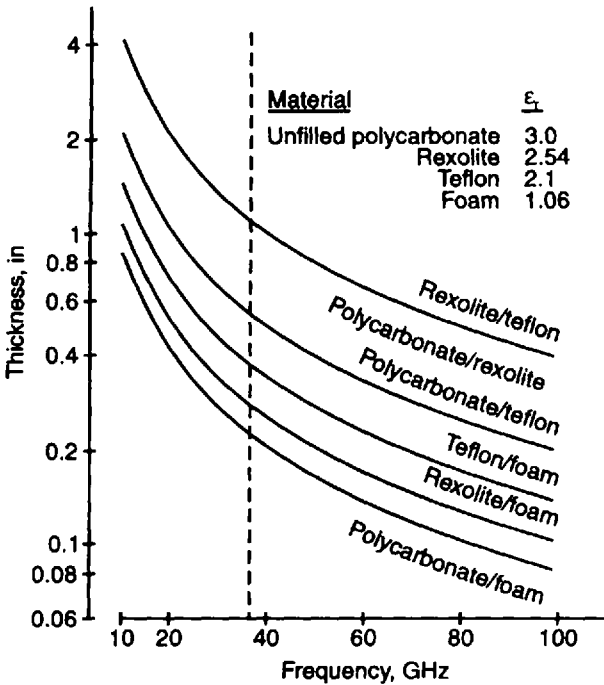


Figure 4.39 Double-dielectric zone plate thickness versus frequency for different dielectric combinations. (After: [39], © 1987 IEEE.)

To accomplish a quarter-wave step correction in this zone plate construction, or phase shift values in the four zone apertures $\Delta\Phi_1 = 0$, $\Delta\Phi_2 = 90$ degrees, $\Delta\Phi_3 = 180$ degrees, and $\Delta\Phi_4 = 270$ degrees (or -90 degrees), the relative permittivities of the corresponding rings were found as follows [49 and Hristov, Selected Bibliography]: $\epsilon_{r1} = 1$, $\epsilon_{r2} = 6.25$, $\epsilon_{r3} = 4$, and $\epsilon_{r4} = 2.25$. Note that this is a special case, where one of the four ring permittivities is deliberately chosen to be 4, or the value for which the “ideal” phase-reversing is obtained ($T = -1$), and the plate thickness is exactly $\lambda/2$.

The ring with $\epsilon_r = 2.25$ has good amplitude and phase transmission characteristics, while the ring with $\epsilon_r = 6.25$ makes proper phase shifting but transmits only about 50% of the normally incident power. This shortcoming could be removed by replacing all solid rings having $\epsilon_r = 6.25$ with three-layered sandwich-type rings designed for $|T| \approx 1$ and $\psi_T = 90$ degrees [51].

Solid (or Single-Layer) Phase-Shifting Dielectric Plate In the single- or multiple-dielectric zone plates, the planar dielectric steps or rings operate as

electromagnetic phase shifters. It is supposed here that their reflection and transmission properties do not much differ from those of the infinite dielectric plate. The lossless phase-reversing dielectric phase-shifter has a transmission coefficient $T = -1$, which is obtained for a normal plane wave incidence ($\psi_i = 0$ degrees), $\epsilon_r = 4$, and the plate thickness is $\lambda/2$. The increase of the dielectric constant leads to a rapid fall in the transmission coefficient magnitude, and the phase-shifting effect also changes for the worse. Here, this phenomenon is demonstrated graphically only for a normal wave incidence (Figure 4.40), for frequency of 12.1 GHz, $\epsilon_r = 4$, and $\tan \delta = 0.015$. If ϵ_r is less than 4, the phase-reversal zone plate becomes too thick and heavy. On the other hand, from Figure 4.40(a), it is seen that for ϵ_r bigger than 5–6 the amplitude-transmission coefficient is less than 0.75, or for such values of ϵ_r , the plate phase shifter will reflect more than 50% of the incident power.

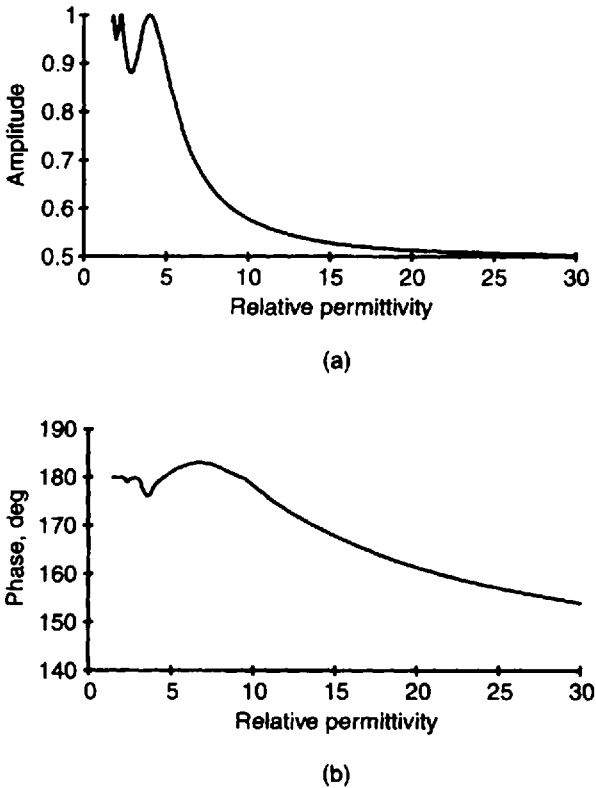
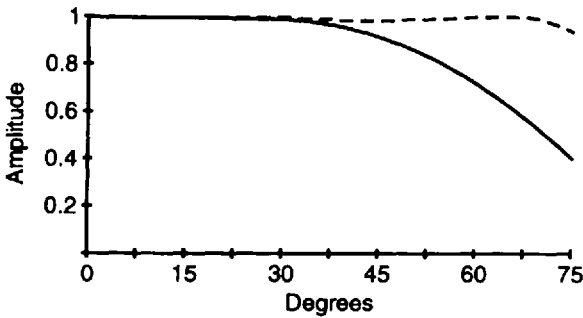


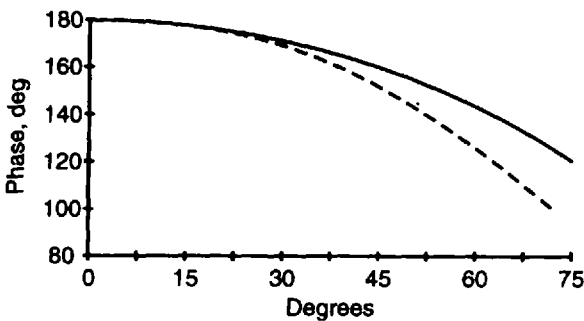
Figure 4.40 Transmission coefficients versus relative dielectric constant for phase reversing single-layer dielectric plate ($f = 12.1$ GHz, $\epsilon_r = 4$, $\tan \delta = 0.015$, normal plane wave incidence): (a) amplitude-transmission coefficient and (b) phase-transmission coefficient.

Next, we show the variation of the complex transmission coefficient as a function of the incidence angle (Figure 4.41). The dielectric plate has a thickness equal to 12.4 mm and the same frequency, permittivity, and loss tangent as in Figure 4.40. The wave transmission through the dielectric plate is characterized not only by magnitude and phase changes. Another phenomenon is the alteration in the wave polarization. The incident plane electromagnetic wave with linear polarization can be resolved into two orthogonal in-phase components—electric or perpendicular (solid line) and magnetic or parallel (dashed line).

For a normal incidence, the zone plate does not change the wave polarization. However, as it is seen from Figure 4.41 for angles of incidence bigger than 45 degrees, the transmitted electric (solid line) and magnetic (dashed line)



(a)



(b)

Figure 4.41 (a) Amplitude and (b) phase transmission coefficients versus incidence angle for phase-reversing single-layer dielectric plate ($f = 12.1$ GHz, $\epsilon_r = 4$, $\tan \delta = 0.0001$, and plate thickness of 12.4 mm). Electric polarization is represented by a solid line and magnetic polarization is represented by a dashed line.

polarization components obviously have different magnitudes and phases, and thus, the resultant outgoing wave will be elliptically polarized.

The single-layer phase shifter designed for 12.1 GHz shows very good amplitude-transmission and phase-reversing characteristics for the whole 11.7–12.5-GHz DBS frequency band, for angles of incidence 0–45 degrees. Polarization change of the transmitted wave is expected to be too small because the phase difference between the two orthogonal components does not exceed $\pi/10$ up to an incidence angle of 60 degrees.

The influence of the dielectric losses on the transmission characteristics is negligible for $\tan \delta \leq 0.001$. It is concluded that the amplitude of the transmitted wave depends mostly on the dielectric loss tangent.

Multilayer Phase-Shifting Dielectric Plate The electromagnetic properties of the high-frequency multilayered structures are well examined in the electromagnetic theory of the microwave/millimeter-wave antenna radomes [69–71].

The radomes have to satisfy specific aerodynamic, structural, and electromagnetic requirements. The electromagnetic characteristics could call for certain limits to transmission loss, polarization, pattern distortion, and so forth. While most of the radome electromagnetic characteristics are similar to those of the Fresnel dielectric plates (transmission losses, reflection levels, depolarization properties), the transmission phase shift demands are different. For both radomes and zone plates, it is important to have small and constant phase differences between the two orthogonal polarizations in the whole range of the incidence angles or frequencies. The transmission phase shift in radomes has to be small, while there may be significant prescribed values for the Fresnel zone plate.

As an example of a multiple-layer phase shifter, we consider here a phase-reversing plate with two skin layers and one core layer (or a sandwich-type plate). For a frequency of 12.1 GHz the following optimum parameters are obtained: a skin-layer's thickness and permittivities of 4.2 and 2.4 mm, and a core-layer thickness and permittivity of 6.2 mm and 5, respectively.

The dielectric loss tangent is chosen to be 0.001. The calculated amplitude- and phase-transmission coefficients are very good in the entire frequency region 11.7–12.5 GHz. Figure 4.42 shows the amplitude- and phase-transmission coefficients calculated as functions of the incidence angle of this three-layer plate, at the medium frequency 12.1 GHz.

The three-layer phase-shifting plate is thicker than the single-layer one (14.6 mm versus 12.4 mm, calculated for the above medium frequency), but it is lighter due to the sandwich combination of two dielectrics with different specific gravity. In some cases, the three-layer structure may be preferred as it has a higher strength-to-weight ratio and a wider bandwidth.

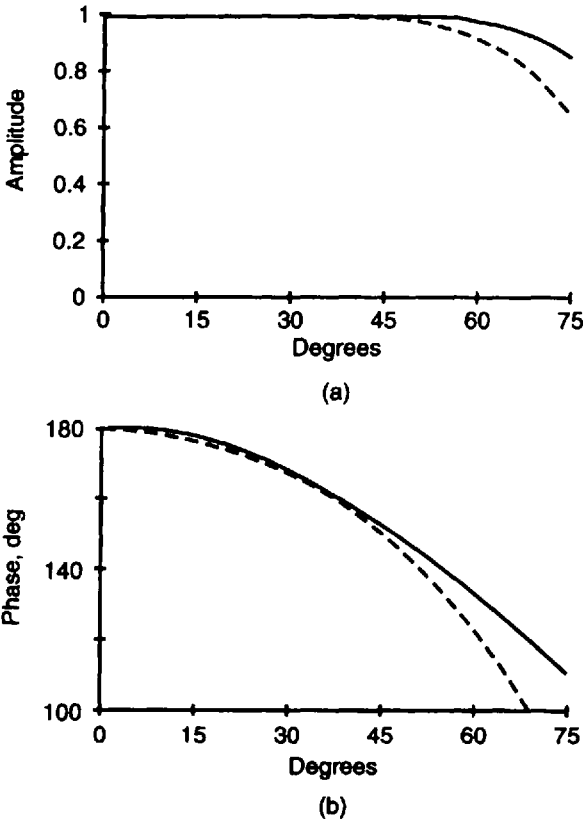


Figure 4.42 (a) Amplitude-transmission and (b) phase-transmission coefficient of the three-layer plate versus incident angle ($f = 12.1$ GHz, skin-layer thickness = 4.2 mm, core-layer thickness = 6.2 mm, skin-layer permittivity = 2.4, core-layer permittivity = 5.0, and loss tangent = 0.001).

Gridded Phase-Shifting Dielectric Plate The gridded phase-shifter is made as a single or multilayer metal grid of small metal elements imbedded in or printed on a high-frequency dielectric plate. From a polarization point of view the ideal grid structure plate has to be axially isotropic. This is not possible in practice but many grid arrangements have satisfactory polarization symmetry (e.g., circular ring array, square or double-square array, and Jerusalem cross array).

The circular ring array in the form of an equilateral triangular grid, shown in Figure 4.43(a), is usually printed on a dielectric substrate. It is an example of a transmissive phase shifter. If the substrate is taken to be $\lambda/(4/\sqrt{\epsilon_r})$ in thickness, and the ring grid is backed by a metal screen a reflective-type phase

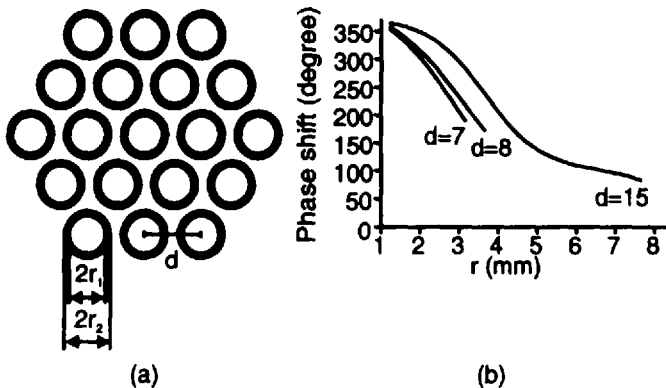


Figure 4.43 Reflective planar phase shifter made by printed circular ring array: (a) ring array configuration and (b) phase shift change as function of medium ring radius for different distances d between rings. (After: [45], © 1993 IEE.)

shifter is realized [45]. In Figure 4.43(b) the phase shift of the reflective phase shifter versus the medium ring radius $r = (r_1 + r_2)/2$ is plotted, for three different distances between ring centers, $d = 7, 8,$ and 16 mm. Note that the substrate thickness and ring width is fixed. The phase shift is mainly determined by the ring circumference. Small rings are capacitive and large ones are inductive. With the distance $d = 16$ mm, a phase shift in the range 0 to $3\pi/2$ can be obtained by adjusting the ring radii. The phase-shifter grids can be examined by use of approximate equivalent-circuit models [72–75] or by application of analytical and numerical wave diffraction methods [69, 70, 76, 77].

An equivalent circuit model for a transmissive grid of square loops, shown in Figure 4.44(a) was proposed in [73]. The square-loop grid is assumed to be derivative of two parallel orthogonal grids of thin wires and is represented by a single series LC circuit [Figure 4.44(c)] shunted across a transmission line of admittance Y_0 equal to the free-space admittance, or $Y_0 = 1/Z_0$, where $Z_0 = 120\pi, \Omega$. Though the equivalent circuit model is simple, it has enough accuracy for the practical design procedure.

Values for L and C in the equivalent circuit can be determined using the following equations [73]. Consider a plane wave polarized parallel to the strip incident obliquely on an infinite grid of narrow, perfectly conducting strips. The equivalent shunt reactance, normalized to the free space impedance Z_0 of the grid, is given by

$$\bar{X}(s) = F(p, s, \lambda) = \frac{p}{\lambda} \cos \psi_i \left[\ln \left(\operatorname{cosec} \frac{\pi s}{2p} \right) + G(p, s, \lambda) \right] \quad (4.79)$$

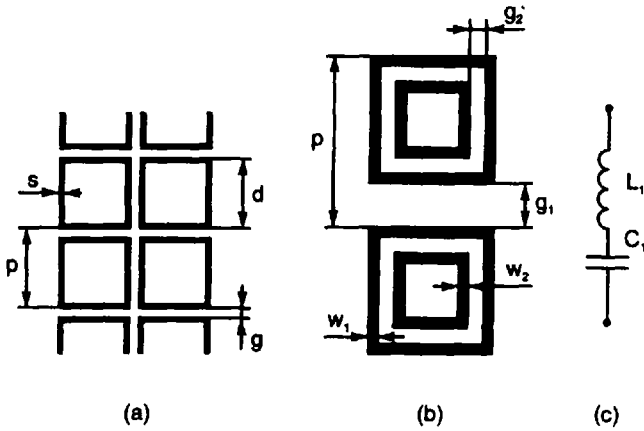


Figure 4.44 Planar phase-shifting arrays of single squares (a) and double squares (b). With (c) is marked equivalent circuit of single square element. (After: [74], © 1982 IEE.)

where ψ_i is the angle of incidence and

$$G(p, s, \lambda) = \frac{1}{2} \frac{(1 - \nu^2)^2 [(1 - \nu^2/4)(A_+ + A_-) + 4\nu^2 A_+ A_-]}{(1 - \nu^2/4) + \nu^2(1 + \nu^2/2 - \nu^4/8)(A_+ + A_-) + 2\nu^6 A_+ A_-}$$

with

$$A_{\pm} = \frac{1}{\sqrt{\left[1 \pm \frac{2p \sin \psi_i}{\lambda} - \left(\frac{2p \cos \psi_i}{\lambda} \right)^2 \right]}} - 1$$

and $\nu = \sin(\pi s)/2\pi$.

If the incident wave is polarized perpendicular to the conductors, the grid has a normalized capacitive susceptance given by

$$\bar{B}(g) = \frac{d}{p} F(p, g, \lambda) \tag{4.80}$$

where g is the width of the gap between the conducting strips.

For the square-loop grid, shown in Figure 4.44(a), the normalized reactance X_L of the inductance L is found from

$$\bar{X}_L = \frac{d}{p} F(p, 2s, \lambda) \tag{4.81}$$

where \bar{X}_L is reduced by a factor d/p due to the conductor not being continuous. The susceptance \bar{B}_C of the capacitance C is

$$\bar{B}_C = 4 \frac{d}{p} F(p, g, \lambda) \quad (4.82)$$

Denote with $\bar{B}_g = \bar{B}_{gL} + \bar{B}_{gC}$ the total grid-circuit susceptance. For the resonance frequency, the grid is totally transmissive ($\bar{B}_g = 0$) or totally reflective ($\bar{B}_g = \infty$) to an incident wave. In the two cases, the grid is acting as a frequency selective surface or FSS. For known grid inductance L and capacitance C , the resonance frequency f_o of the FSS is easily calculated by means of the resonant circuit equation $f_o = 1/(2\pi\sqrt{LC})$. For example, the square-loop grid configuration of dimensions $p = 5.25$ mm, $s = 0.47$ mm, $d = 5$ mm, and $g = 0.25$ mm has a resonance frequency of 15.2 GHz [73]. The double-square grid shown in Figure 4.44(b) has a larger bandwidth and better phase-shifting characteristic.

After finding the total normalized grid susceptance, which is a purely imaginary admittance, $j\bar{B}_g$, the next step is to obtain the grid's phase-shifting quality. The phase shift Φ_g as a function of \bar{B}_g is then disclosed by means of the simple circuit theory or more rigorous wave transmission concept. In terms of the circuit elements, the total normal normalized admittance of the grid equivalent circuit \bar{Y}_e may be found simply by adding to the normalized grid susceptance $\bar{B}_g = B_g/Y_o$ the purely real normalized admittance of the free space $\bar{Y}_o = 1$, or $\bar{Y}_e = 1 + j\bar{B}_g$.

The complex transmission coefficient T of the single layer grid in terms of the admittance \bar{B}_g is [40]

$$T = \frac{1}{1 + \frac{1}{2}j\bar{B}_g} \quad (4.83)$$

and the corresponding phase-shift is found as

$$\Phi_g = \arctan(T) = -\arctan(\bar{B}_g/2) \quad (4.84)$$

The phase shift has a positive sign if the grid susceptance is negative and vice versa. The practical single-layer grid phase shifter has an intolerably big reflection and an overly small phase shift (less than 45 degrees). These imperfections can be greatly avoided by using multilayer phase-shifting grids.

For a two-layer structure comprising only two equal planar grids with a susceptance \overline{B}_g each stacked $\lambda/4$ apart, (4.85), a simple formula for the phase shift, is derived in [40]

$$\Phi_g = \arctan\left(\frac{2\overline{B}_g^2\sqrt{2 + \overline{B}_g^2} - (1 - \overline{B}_g^2)}{B_g[2 + (1 - \overline{B}_g^2)\sqrt{2 + \overline{B}_g^2}]}\right) \quad (4.85)$$

Finally let us consider a simple example of a thin gridded plate in regard to its phase-shifting properties. Metallic grid is represented by an equivalent susceptance \overline{B}_g , which is supposed to be constant with the change of the incident angle and wave polarization.

Regard a thin-gridded, one-layer dielectric phase-shifter. Its structure is the same as that shown in Figure 4A.1(a), with a grid imbedded in the middle of the dielectric plate. Using the matrix transmission theory and more particularly the expressions given in Appendix 4A, a thin, 45-degree phase-shifting gridded plate for parallel (magnetic) polarization was designed. Its total thickness is 2 mm or 0.08λ for the optimum frequency $f = 12.1$ GHz. The calculated amplitude and phase transmission coefficients of this gridded dielectric plate structure for a permittivity $\epsilon_r = 2.5$ and grid normalized susceptance $\overline{B}_g = -j2.2$ are drawn in Figure 4.45.

It is seen that the magnitude and phase of the transmission coefficient are almost one and -45 degrees, respectively, for an angle of incidence in the range between 0 and 45 degrees. Several layers of this basic structure can be used in designing a phase shifter with a larger phase shift.

4.4 Curved Fresnel Zone Plates

Fresnel zone patterns are made not only on a planar plate. If the half-wave ray-path difference condition is applied to a curvilinear surface, the so-called curved zone plates (or shells) can be constructed.

Here we give equations for Fresnel zone radii of three types of axially symmetric convex/concave zone plates—spherical, parabolic, and conical. Their axial focusing properties for zone plates the same in zone number or aperture diameter are studied and compared to those of the corresponding planar zone plates. In a similar way we could examine zone plates of arbitrary axially symmetric surface shapes (e.g., elliptical, hyperbolic).

4.4.1 Introduction

It is hard to say exactly when the thought of introducing curved instead of planar zone plates arose. However, already in the Huygens' and Fresnel's studies

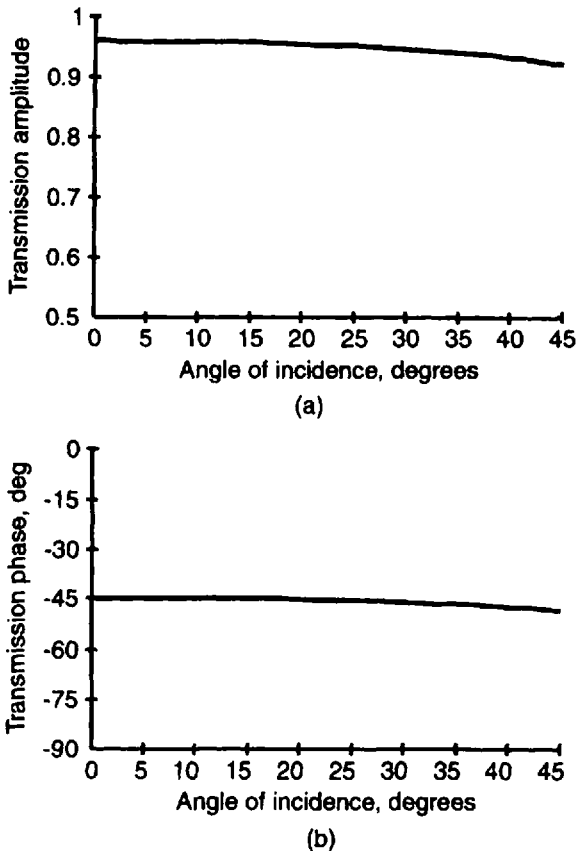


Figure 4.45 Amplitude- and phase-transmission coefficients of gridded plate: (a) amplitude and (b) phase shift versus angle of incidence.

the secondary diffraction sources and zone construction were supposed on the surface of the spherical wave front. Fresnel zones on a sphere are considered in Section 2.2.2.1, only for the specific cases in which the point source and center of the sphere coincide.

As far as we know, the first publication that describes spherical zone plates for optical wavelengths was put out by Raiski in 1952 [9]. To make Fresnel zones wider, he proposed a reflective spherical zone plate, whose geometry is shown in Figure 4.46(a). An aluminum zone plate model with a source distance $d_1 = 100$ cm, observation point distance $d_2 = 98$ cm, and sphere radius $R = 100$ cm was manufactured and studied experimentally for the visible light. For a diameter of 10 cm this spherical zone plate had only 100 broad zones while the planar Soret zone plate had 100 times more Fresnel zones, or 10,000.

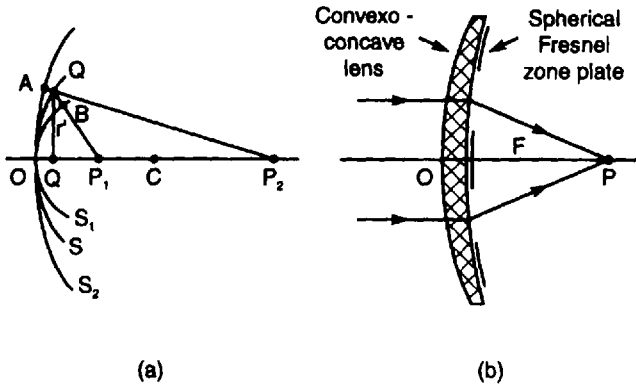


Figure 4.46 Spherical reflective and transmissive Soret zone plate. (After: [9].)

Again in [9], a transmissive zone plate working in combination with a convex-concave lens was proposed and examined. The Fresnel zones were cut on the spherical concave surface of a silver-plated glass lens [Figure 4.46(b)].

In the microwave region, the first curvilinear zone plate was probably the cylindrical one with straight parallel zones [Figure 4.8(b)] patented by Bruce [30] in 1936.

However, real advancement in the field of the curved zone plates was made in the early 1970s with the theoretical investigations of Dey and Khastgir [53–55, 57, 58]. They and their research associates proposed the spherical and parabolic Fresnel zone plates for microwave frequencies. They created a comprehensive theory for dimensioning of the curved zone plates, studied their focusing properties, and compared them with the planar zone plate. In the course of their investigation, the focusing superiority of curved zone plates over plane ones was convincingly proven.

Microwave/millimeter-wave curved zone plates were developed mainly as elements of lens or reflector aperture antennas [37, 59, 78, 79], which will be considered in Chapter 5.

4.4.2 Dimensions of Curved Fresnel Zone Plates

We give here equations for the zone radii and zone areas of curved Fresnel zones projected on a plane. The projection plane is transverse to the zone plate focal axis.

4.4.2.1 Dimensions of the Spherical Zone Plate

Figure 4.47(a) is a cross-sectional geometry of a spherical zone plate of a radius R and sphere center at point C illuminated by a diverging spherical wave. Let

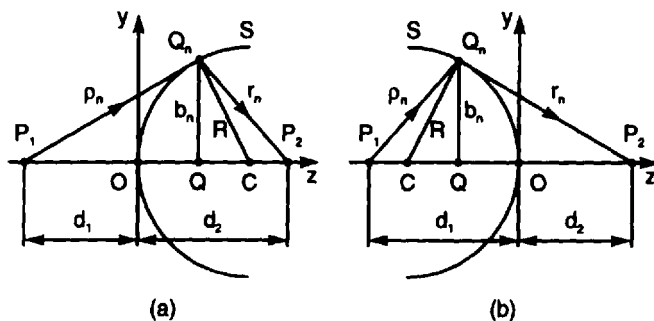


Figure 4.47 Geometry of spherical zone plate, (a) convex side or (b) concave side facing the spherical incident wave.

the zone plate be of a Soret type, with positive or negative zones blocked by reflecting or absorbing elements. If the zone plate is turned to the incident wave by its convex side, we will call it a convex zone plate.

The first task in zone plate design is to find an equation for the zone radii. Its derivation is based on the half-wave RPD condition [53, 54]. The spherical wave radiated by a point source $P_1(0, 0, z = -d_1)$ is converged by the spherical zone plate to the principal diffraction maximum at point $P_2(0, 0, z = +d_2)$. For the zone plate under consideration the RPD condition is expressed as

$$\rho_n + r_n = d_1 + d_2 + n \frac{\lambda}{2} \quad (4.86)$$

where

$$\rho_n = \sqrt{[d_1 + (R - \sqrt{R^2 - b_n^2})]^2 + b_n^2} \quad (4.87)$$

and

$$r_n = \sqrt{[d_2 - (R - \sqrt{R^2 - b_n^2})]^2 + b_n^2} \quad (4.88)$$

If $b_n^2 \ll R^2$, $\sqrt{R^2 - b_n^2} \cong R - b_n^2/2R$, the following approximations of (4.87) and (4.88) are taking place

$$\rho_n \cong \sqrt{d_1^2 + d_1 b_n^2/R + b_n^2} \quad (4.89)$$

and

$$r_n \cong \sqrt{d_2^2 - d_2 b_n^2 / R + b_n^2} \quad (4.90)$$

After placing (4.89) and (4.90) into (4.86) the RPD zone plate condition becomes

$$\sqrt{d_1^2 + d_1 b_n^2 / R + b_n^2} + \sqrt{d_2^2 - d_2 b_n^2 / R + b_n^2} = d_1 + d_2 + n\lambda / 2 \quad (4.91)$$

The solution of (4.91) for b_n gives

$$b_n = \sqrt{\frac{R}{d_2 - R}} \sqrt{d_2^2 - \frac{1}{2(d_1 + d_2)^2} [(d_2 - R)d_n + A_n]^2} \quad (4.92)$$

where

$$d_n = d_1 + d_2 + n\lambda / 2$$

$$A_n = \sqrt{4R^2(d_1 + d_2)^2 + n^2 \lambda^2 (R - d_2)(d_1 + R) + B_n}$$

$$B_n = 4n\lambda [d_1^2(R - d_2) - d_2^2(R + d_1) + R^2(d_1 + d_2)]$$

The general arrangement considered up to this point may be reduced to the following specific examples:

1. Convex spherical zone plate illuminated by a plane wave: The zone radii b_n in this case may be calculated from (4.92) after setting $d_1 \rightarrow \infty$ (plane wave front) and $d_2 = F$, or from another expression derived from a geometry of the spherical zone section illuminated by a plane wave. In the latter approach the equation for the Fresnel zone radii is found as [54]

$$b_n = \sqrt{R^2 - y^2} \quad (4.93)$$

where

$$y = -\frac{n\lambda}{2} + \sqrt{R^2 + n\lambda(R - F)}$$

If the wave is focused exactly at the center C of the sphere, or $R = F$, (4.93) becomes very simple and similar to that for the planar zone plate, illuminated by a plane wave (4.46)

$$b_n = \sqrt{n\lambda R - \left(\frac{n\lambda}{2}\right)^2} \quad (4.94)$$

For a paraxial arrangement, $n\lambda R \gg (n\lambda/2)^2$ (4.94) becomes equal to (4.46) Thus, in the case of paraxial plane wave incidence, the parabolic and planar zone plates will have identical zone patterns, for same focal distance.

2. Convex spherical zone plate transforming a spherical incident wave into a plane wave: For this specific case, the zone radii could be also found by (4.92) if one lets $d_2 \rightarrow \infty$.
3. Planar zone plate focusing a spherical incident wave at point P_2 . Equation (4.92) reduces to (4.45) if $R \rightarrow \infty$ (planar zone plate) and $d_2 = F$.
4. Plane incident wave transformed by a planar zone plate into a spherical wave: Equation (4.92) becomes the same as (4.46), if $d_1 \rightarrow \infty$ (plane wave), $R \rightarrow \infty$ (planar zone plate), and $d_2 = F$. Imagine that the zone plate is turned by its concave side to the incident spherical wave. Such a zone plate may be specified as a concave zone plate. The equation for the zone radii is obtained simply by interchanging d_1 with d_2 , and d_2 with d_1 in (4.91), as illustrated in Figure 4.47(b). Thus, for the zone plate radii in the present arrangement we obtain

$$b_n = \sqrt{\frac{R}{d_1 - R} \sqrt{d_1^2 - \frac{1}{2(d_1 + d_2)^2} [(d_1 - R)d_n + A_n]^2}}$$

$$d_n = d_1 + d_2 + n\lambda/2 \quad (4.95)$$

$$A_n = \sqrt{4R^2(d_1 + d_2)^2 + n^2\lambda^2(R - d_1)(d_2 + R) + B_n}$$

$$B_n = 4n\lambda [d_2^2(R - d_1) - d_1^2(R + d_2) + R^2(d_1 + d_2)]$$

The limiting arrangement, where $d_1 \rightarrow \infty$ and $d_2 = F$, corresponds to the spherical zone plate, concave side facing a plane incident wave. Now, (4.95) for b_n is easily reduced to

$$b_n = \frac{1}{2} \sqrt{C_n + \frac{A_n}{F + 2R} \left[F + R + \frac{n\lambda}{2} - \frac{A_n}{16(F + 2R)} \right] - 4F(F + R)} \quad (4.96)$$

where

$$A_n = 4[2(F + R)(F + R + n\lambda/2) - B_n]$$

$$B_n = \sqrt{4R^4 - n^2\lambda^2R(R + F) - 4n\lambda(R^3 + F^2 + 2FR^2)}$$

$$C_n = -4n\lambda(F + R + n\lambda/4)$$

The areas of the spherical segments s_n and s_{n-1} bounded by the n -th and $(n-1)$ -th Fresnel zone circles are found by $s_n = 2\pi R[R - \sqrt{R^2 - b_n^2}]$ and $s_{n-1} = 2\pi R[R - \sqrt{R^2 - b_{n-1}^2}]$, correspondingly. Thus, the area S_n of the n -th Fresnel zone is calculated as a segment area difference $S_n = s_n - s_{n-1}$.

It is important to note that the projections of the actual curved zones in the focal plane $z = F$, or in some other aperture plane, are planar circular rings that have the same radii b_n but different areas S'_n , or $S'_n = \pi(b_n^2 - b_{n-1}^2) \neq S_n$.

Figure 4.48(a) illustrates the projection view of the Fresnel zone pattern in the case of a spherical zone plate, convex side turned to a spherical incident wave. The zone plate distances and sphere radius are chosen as $d_1 = 40$ cm, $d_2 = 60$ cm, and $R = d_2 = 60$ cm [more correctly, $R \cong d_2$, because of the singularity in (4.92) and (4.95)]. The design wavelength is $\lambda = 3.2$ cm. The Fresnel zones are bounded within a square, which determines a zone plate of 60 cm in diameter. The source and observation point distances d_1 and d_2 , wavelength, and aperture diameter are purposely taken to be the same as those

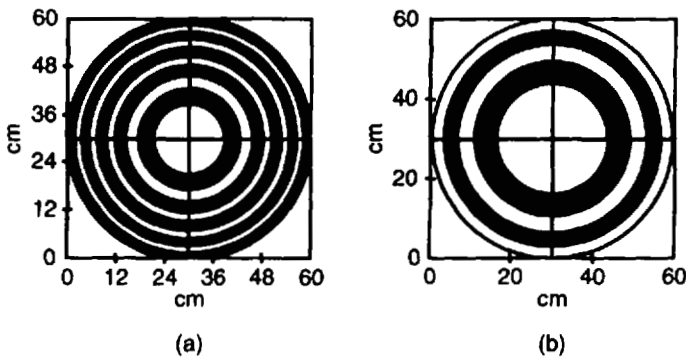


Figure 4.48 Fresnel zone patterns of spherical half-wave zone plate of radius $R = d_2 = 60$ cm for two shapes of incident wave: (a) spherical, $d_1 = 40$ cm and $d_2 = 60$ cm, and (b) plane, for $d_2 = F = 60$ cm.

for the planar zone plate, whose zone patterns were shown in Figure 4.24. Ten Fresnel zones are numbered within the 60-cm aperture, one less than in the planar zone plate, illuminated by a spherical wave. Five of them are open and five are blocked (the blackened ones).

The Fresnel zone pattern for the specific case of the plane wave illuminating the same spherical zone plate ($R \cong d_2 = 60.1$ cm and $d_2 = F = 60$ cm) is drawn in Figure 4.48(b). The 60-cm aperture boundary contains five wide Fresnel zones, one more than in the planar zone plate, illuminated by a plane wave.

4.4.2.2 Dimensions of the Paraboloidal Zone Plate

The cross-sectional geometry of the paraboloidal zone plate illuminated by a spherical wave is shown in Figure 4.49. All points and dimensions have the same meaning as those in the Figure 4.47(a) for the spherical zone plate. Of course, the curvature of the parabolic surface is characterized by its focal length, marked here by f_p . Let us find first an equation for the Fresnel zone radii using the half-wave RPD condition [55], or

$$\rho_n + r_n = d_1 + d_2 + n \frac{\lambda}{2} \quad (4.97)$$

where

$$\rho_n = \sqrt{\left[d_1 + \frac{b_n^2}{4f_p} \right]^2 + b_n^2} \text{ and } r_n = \sqrt{\left[d_2 - \frac{b_n^2}{4f_p} \right]^2 + b_n^2}$$

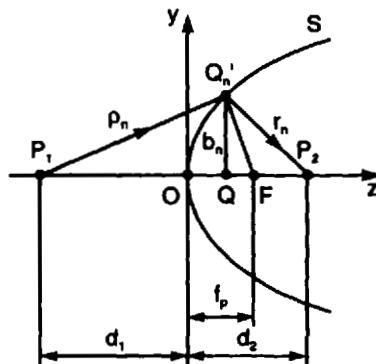


Figure 4.49 Geometry of a paraboloidal zone plate, convex side facing spherical incident wave.

The solution of (4.97) with respect to b_n gives

$$b_n = \frac{\sqrt{A_n + 2B_n d_n}}{\sqrt{8n\lambda(d_1 + d_2 + n\lambda/4)}} \quad (4.98)$$

where

$$d_n = d_1 + d_2 + n\lambda/2$$

$$A_n = 4f_p \{n\lambda[B_n + n\lambda(d_2 - d_1)] - 16f_p(d_1 + d_2)^2\}$$

$$B_n = 4[(d_2^2 - d_1^2) - 4f_p(d_1 + d_2 + n\lambda/4)]$$

$$C_n = 2f_p \sqrt{n\lambda[n\lambda D_n - 128f_p(d_1 + d_2)(d_2 - d_1 - 2f_p)] + 256f_p^2(d_1 + d_2)}$$

$$D_n = 16(d_1 + d_2)^2 + 8n\lambda(d_1 + d_2) + n^2\lambda^2 + 32f_p(d_2 - d_1 + 2f_p)$$

As in the case of the spherical zone plate, the general equation for the zone radii (4.98) can be reduced to several specific arrangements. Consider only one of them—the convex paraboloidal zone plate, illuminated by a plane wave, or if $d_1 \rightarrow \infty$ and $d_2 = F$. For this arrangement, (4.98) becomes very simple, or [56]

$$b_n = \sqrt{n\lambda f_p} \sqrt{\frac{F + n\lambda/4}{f_p + n\lambda/4}} \quad (4.99)$$

For $F = f_p$

$$b_n = \sqrt{n\lambda F} \quad (4.100)$$

Equation (4.100) is exactly the same as that for the zone radii of a paraxial planar zone plate, or (2.15). However, the latter is an optical/quasi-optical approximation while (4.100) is an exact one. If in (4.99) $n\lambda/4$ is much less than F and f_p , it again reduces to (4.100), but now approximately.

Figure 4.50(a) is a projection view of the zone pattern in the case of a paraboloidal zone plate turned by its convex side to a spherical incident wave for the specific case, where $d_1 = 40$ cm, $d_2 = R = 60$ cm, and $\lambda = 3.2$ cm. The Fresnel zones are bounded within an aperture of 60 cm in diameter. The source and observation point distances d_1 and d_2 , wavelength, and aperture diameter are chosen in the same manner as those for the planar and spherical zone plates, whose zone patterns were drawn in Figures 4.24 and 4.48, respec-

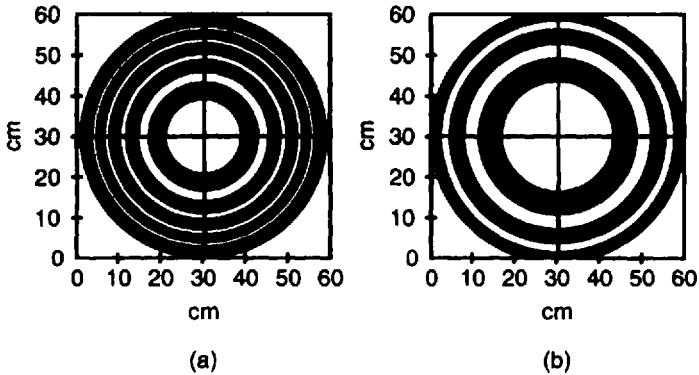


Figure 4.50 Fresnel zone pattern of a convex paraboloidal half-wave zone plate with focal length $f_p = 60$ cm for two shapes of incident wave: (a) spherical wave ($d_1 = 40$ cm and $d_2 = 60$ cm) or (b) plane wave ($d_1 \rightarrow \infty$, $d_2 = F = 60$ cm); the design wavelength is $\lambda = 3.2$ cm.

tively. Eleven Fresnel zones totally are numbered within the 60-cm aperture, six of them open.

The zone areas S_n can be calculated by use of the following relation [56]

$$S_n = \frac{8\pi f_p^2}{3} \left[\left(1 + \frac{b_n^2}{4f_p^2} \right)^{3/2} - \left(1 + \frac{b_{n-1}^2}{4f_p^2} \right)^{3/2} \right] \quad (4.101)$$

The Fresnel zone pattern for the specific case of plane wave illuminating the same paraboloidal zone plate is drawn in Figure 4.50(b). The 60-cm aperture boundary contains six Fresnel zones, open and closed, one more than in the spherical zone plate illuminated by a plane wave.

4.4.2.3 Dimensions of the Conical Zone Plate

The cross-section of a conical zone plate, convex side opposing the spherical wave produced at point P_1 , is shown in Figure 4.51. Here the specific parameter that determines the conical surface is the opening half-angle $\alpha = \arctan(b_n/OQ)$.

Let us find an equation for the zone radii of the conical zone plate using the half-wave RPD condition for the reinforcement of diffraction rays at the primary focal point P_2

$$\frac{n\lambda}{2} = \sqrt{\left(d_1 + \frac{b_n}{\tan \alpha} \right)^2 + b_n^2} + \sqrt{\left(d_2 + \frac{b_n}{\tan \alpha} \right)^2 + b_n^2} - d_1 - d_2 \quad (4.102)$$

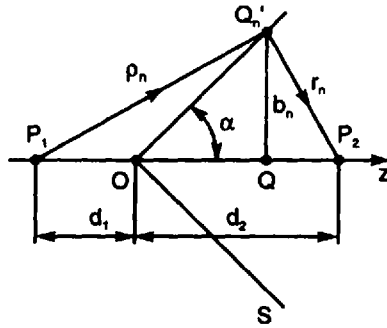


Figure 4.51 Geometry of conical zone plate, convex side looking at a spherical incident wave.

The solution of (4.102) with respect to b_n gives

$$b_n = B_n \left\{ C_n + \frac{2\sqrt{n\lambda}}{d_n \tan \alpha} \sqrt{\tan^2 \alpha [64d_1 d_2 (d_1 + d_2) + 16d_1 d_2 n\lambda + A_n] + A_n} \right\} \quad (4.103)$$

where

$$d_n = d_1 + d_2 + n\lambda/2$$

$$A_n = 4n\lambda \left[4(d_1 + d_2)^2 + 2n\lambda(d_1 + d_2) + \left(\frac{n\lambda}{2} \right)^2 \right]$$

$$B_n = \frac{\tan^2 \alpha}{8[1 + \tan^2 \alpha - (d_1 + d_2)^2/d_n^2]}$$

$$C_n = \frac{4(d_2 - d_1)}{\tan \alpha} \left[1 - \frac{(d_1 + d_2)^2}{d_n^2} \right]$$

If the convex conical zone plate is illuminated by a plane wave front the following simple equation for the zone radii is found

$$b_n = \sqrt{\left(\frac{n\lambda}{2 \tan \alpha} \right)^2 + \left(\frac{n\lambda}{2} \right)^2 + n\lambda F} = \sqrt{\left(\frac{n\lambda}{2 \tan \alpha} \right)^2 + (b_n^{(pl)})^2} \quad (4.104)$$

where $b_n^{(pl)} = \sqrt{\left(\frac{n\lambda}{2}\right)^2 + n\lambda F}$ marks the planar zone radius expression, given by (4.46). Sure enough, if $\alpha = \pi/2$, $b_n = b_n^{(pl)}$, or the conical zone plate is converted to a planar zone plate.

The areas of the Fresnel zones on the conical surface can be easily calculated by the next expression

$$S_n = \pi \left[b_n \sqrt{b_n^2 + \frac{b_n^2}{\tan^2 \alpha}} - b_{n-1}^2 \sqrt{b_{n-1}^2 + \frac{b_{n-1}^2}{\tan^2 \alpha}} \right] \quad (4.105)$$

The projection view of the zone pattern in the case of the convex conical zone plate illuminated by a spherical wave of wavelength $\lambda = 3.2$ cm is drawn in Figure 4.52(a). Here again $d_1 = 40$ cm and $d_2 = 60$ cm. The Fresnel zones are also bounded within an aperture of 60 cm in diameter. Ten Fresnel zones are numbered now within the 60-cm aperture, five open and five closed (the blackened ones). When a plane wave is illuminating the convex conical zone plate totally, six zones are produced, three of them open, as seen from Figure 4.52(b).

Figure 4.53 shows the variation of the zone radius versus the zone number for the four discussed zone plate configurations: planar (solid line), spherical (dotted line), parabolic (dadot line), and conical (dashed line) convex zone plates. All zone plates are lighted by a 9.375-GHz-plane wave and are designed for a same diffraction focal length of 60 cm. The spherical zone plate has a

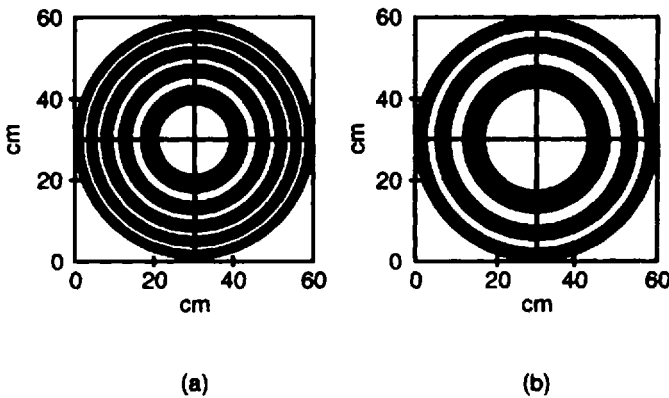


Figure 4.52 Fresnel zone pattern of convex conical half-wave zone plate with opening half-angle $\alpha = \pi/4$, illuminated by: (a) spherical ($d_1 = 40$ cm and $d_2 = 60$ cm) or (b) plane ($d_1 \rightarrow \infty$, $d_2 = F = 60$ cm). Design wavelength is $\lambda = 3.2$ cm.

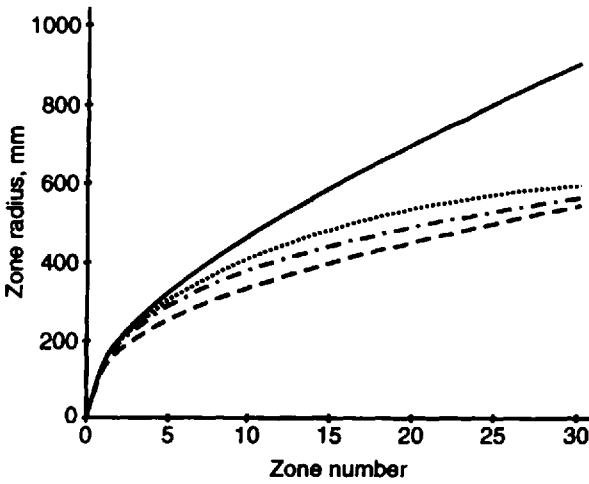


Figure 4.53 Zone radius versus zone number for plane (solid line), spherical (dot line), parabolic (dotted line), and conical (dash line) zone plate illuminated by plane wave-front.

radius equal to the focal length (or $R = F = 60$ cm), while the parabolic surface has a focal length for reflection $f_p = 15$ cm. The conical opening half-angle is chosen to be $\alpha = 45$ degrees.

4.4.3 Focusing Properties of Curved Zone Plates

The axial lens-like focusing action of the spherical and paraboloidal zone plates was originally studied in the early 1970s [53–56]. Later, a comparative study of the planar and paraboloidal zone plate was carried out in respect to off-axis field variation on a transverse plane [58, 78]. Here we will confine our discussion to the axial focusing properties of some spherical, parabolic, and conic zone plates.

4.4.3.1 Axial Focusing of the Spherical Zone Plate

The cross-sectional geometry of a Soret-type spherical zone plate of radius R , convex side facing a spherical or plane incident wave, is shown in Figure 4.54. We will give here the theory for the axial-focusing action of the convex spherical zone plate following [55] and the Kirchoff diffraction theory as described in Section 2.3. The elementary field amplitude at a point $P'(0, 0, z')$ may be expressed in the form

$$dE(P') = \frac{j}{\lambda} E_i(Q') I(\vartheta, \vartheta') \frac{e^{-j\beta r}}{r} dS' \quad (4.106)$$

$$E_n(P') = \frac{j\pi RA_1 e^{-j\beta d_1}}{\lambda(R-z')} e^{j\frac{\beta z'^2}{2(R-z')}} \int_{r_{n-1}}^{r_n} I(r, z') e^{-j\beta\left[\frac{r^2}{2(R-z')} + r\right]} dr \quad (4.109)$$

where

$$I(r, z') = 1 + \frac{2Rz' - r^2 - z'^2}{2r(R-z')} \quad (4.110)$$

and the integration limits r_n and r_{n-1} can be calculated by

$$r_n = \sqrt{z'^2 + 2(R-z')\left(R + \frac{n\lambda}{2} - \sqrt{R^2 + n\lambda(R-F)}\right)} \quad (4.111)$$

If the zone plate is illuminated by a spherical wave, produced at point P_1 , the field radiated by the n -th zone of the spherical zone plate is given by

$$E_n(P') = \frac{j\pi RA_1}{\lambda(R-z')} \int_{r_{n-1}}^{r_n} \frac{e^{-j\beta\left\{\sqrt{b_n^2 + \left[d_1 + \left(\frac{r^2 - z'^2}{2(R-z')}\right)^2\right]} + r\right\}}}{\sqrt{b_n^2 + \left[d_1 + \left(\frac{r^2 - z'^2}{2(R-z')}\right)^2\right]^2}} I(r, z') dr \quad (4.112)$$

where $I(r, z')$ is the inclination function given by (4.110).

The total field at point P' produced by all open zones is

$$E(P') = \sum_n E_n(P') \quad (4.113)$$

for $n = 1, 3, 5, \dots$ (odd zones) or $n = 2, 4, 6, \dots$ (even zones).

The numerical computations performed by Dey and Khastir [53] proved the focusing superiority of the spherical over plane zone plate. They considered a spherical zone plate with dimensions $d_1 = 60$ cm, $d_2 = 10$ cm, and $R = 40$ cm and a plane zone plate with a focal length $F = 10$ cm. The two plates were designed for a spherical wave incidence, at wavelength equal to 3.2 cm and had a total of 12 Fresnel zones. The axial field amplitude variations for the two zone plates are plotted in Figure 4.55 (dashed line representing the planar zone plate and solid line representing the spherical zone plate).

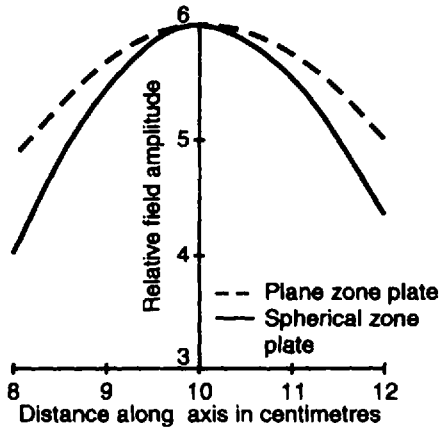


Figure 4.55 Axial variation of relative amplitude for spherical zone plate (solid line) and plane zone plate (dashed line) zone plates (12 zones, spherical wave incidence). (After: [53], © 1973 Taylor & Francis.)

The axial variation of the relative amplitude for spherical and planar zone plates illuminated by a plane wave of wavelength $\lambda = 3.2$ cm is given in Figure 4.56. The zone plate dimensions in this case are $d_2 = 15$ cm and $R = 50$ cm, for the spherical, and $F = 15$ cm, for the planar zone plate.

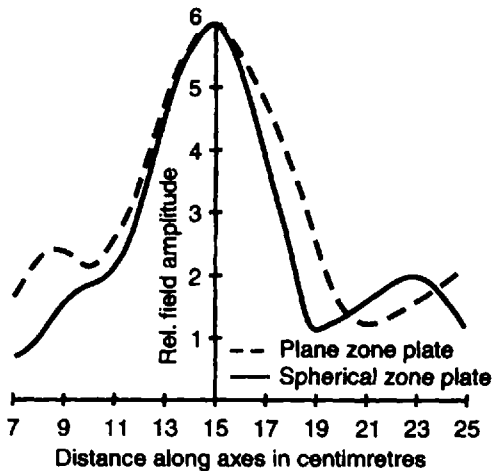


Figure 4.56 Axial variation of relative amplitude for spherical zone plate (solid line) and planar zone plate (dashed line), (12 zones each, plane wave incidence). (After: [53], © 1973 Taylor & Francis.)

From Figures 4.55 and 4.56 the domination of the spherical zone plate with respect to focusing is evident. The computations also show that the spherical zone plate retains its lens-like focusing quality almost irrespective of the source position.

4.4.3.2 Axial Focusing of a Curved Zone Plate: Universal Approximate Solution for Plane Wave Incidence

We describe next a general focusing theory valid for any axially symmetric curvilinear zone plate with a specified profile function. Let us consider the half-section geometry of a zone plate illuminated by a plane wave front (Figure 4.57). All open zone arcs are approximated by their adjacent chords as it is shown for the n -th zone. The curvature function may be generalized as $y(z)$; $P(z_p)$ is an axial running point, illuminated by the total elementary areas $dS = y(z)d\varphi(dz/\cos\alpha_n)$. The plane wave is traveling in the z direction and its electric field at point Q is defined as $E(Q) = E_o \exp(-j\beta z)$, where $E_o = E(z = 0)$.

According to the diffraction theory, the field produced by the n -th zone at point P can be written as

$$dE_n = \frac{j}{\lambda} E(Q) I(\vartheta_n, \vartheta'_n) \frac{e^{-j\beta r(z)}}{r(z)} dS \tag{4.114}$$

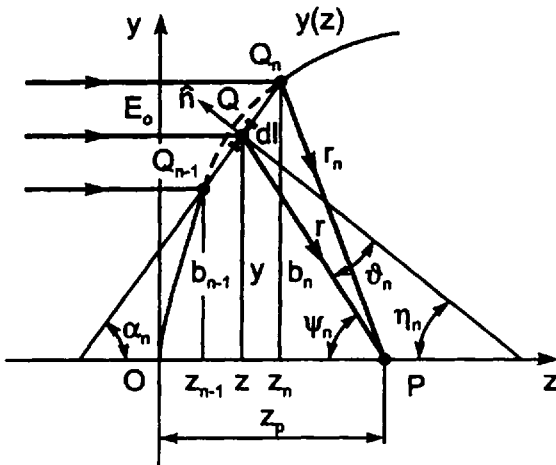


Figure 4.57 Geometry for the derivation of an approximate universal axial focusing theory.

where the inclination factor $I(\vartheta_n, \vartheta'_n)$ is approximated here as for the planar zone plate, or we assume that $I(\vartheta_n, \vartheta'_n) \equiv (1 + \cos \vartheta_n)/2$, $\beta = 2\pi/\lambda$, and $r(z)$ is given by

$$r(z) = \sqrt{(z_p - z)^2 + y^2(z)} \quad (4.115)$$

From geometrical considerations the angles ϑ_n , ψ_n , η_n , and α_n are related as follows

$$\vartheta_n = \psi_n - \eta_n \quad (4.116)$$

where

$$\psi_n = \arctan\left(\frac{y}{z_p - z}\right) = \arctan\left(\frac{b_n + b_{n-1}}{2z - z_n - z_{n-1}}\right)$$

and

$$\eta_n = \arctan\left(\frac{z_n - z_{n-1}}{b_n - b_{n-1}}\right)$$

Also, $dz/dl = \cos \alpha_n = \sin \eta_n$.

The total field at point P is found as a surface integral, which after integration with respect to the coordinate of rotation φ reduces to the following linear integral

$$E_n = j \frac{\pi E_0}{\lambda} \int_{z_{n-1}}^{z_n} y(z) \frac{1 + \cos \vartheta_n}{\cos \alpha_n} \frac{e^{-j\beta(r(z)+z)}}{r(z)} dz \quad (4.117)$$

where the integration limits z_n and z_{n-1} are calculated by the RPD condition

$$z_{n,n-1} + \sqrt{b_{n,n-1}^2 + (z_p - z_{n,n-1})^2} = z_p + \frac{(n-1)\lambda}{2} \quad (4.118)$$

numerically or if the approximation $b_{n,n-1}^2 \ll (z_p - z_{n,n-1})$ is valid, (4.118) is solved, and

$$z_{n,n-1} = z_p - b_{n,n-1} + \sqrt{(n, n-1)\lambda b_{n,n-1} - b_{n,n-1}^2} \quad (4.119)$$

where $b_{n,n-1}$ can be calculated in advance for each specific zone plate profile.

The total field at point P is created by all open zones, odd or even, by the sum equation (4.113).

The profile curve function $y(z)$ of the three curved zone plates, discussed in this section, are given by the following equations:

- For the spherical zone plate

$$y(z) = \sqrt{R^2 - (R - z)^2} \quad (4.120)$$

- For the paraboloidal zone plate

$$y(z) = \sqrt{4f_p z} \quad (4.121)$$

- For the conical zone plate

$$y(z) = z \tan \alpha \quad (4.122)$$

where $\alpha = \alpha_n = \text{const}$. The planar zone plate can be defined as a limiting case of the conical zone plate, where $\alpha \rightarrow \pi/2$.

The universal approximate equation (4.117) was applied for numerical computations and comparison between the planar, spherical, paraboloidal, and conical convex zone plates concerning their axial focusing characteristics.

Two different examples are considered:

1. Zone plates with the same number of odd open zones: The calculations are performed for $n = 1, 3, \dots, 13$, or for seven open zones. Also, all zone plates are chosen with an equal primary focal length $z_p = F = 60$ cm. The radius of the spherical zone surface is $R = 60.1$ cm, the focal length of the parabolic zone surface is $f_p = 15$ cm, and the opening half-angle of the conical zone plate is $\alpha = \pi/4$. The zone plate was studied on the base of the conical zone plate after setting $\alpha = \pi/2 - 0.001$. The zone plates are designed for $\lambda = 3.2$ cm. Figure 4.58 shows curves of the focusing gain G_f versus axial distance f_p , drawn with different lines: solid line corresponds to the conical zone plate ($G_f = 23.2$ dB at $f_p = 60$ cm), dashed line to the spherical zone plate ($G_f = 23.4$ dB at $f_p = 59$ cm), dotted line to the paraboloidal zone plate ($G_f = 23.8$ dB at $f_p = 59$ cm), and dadot line to the plane zone plate ($G_f = 22.3$ dB at $f_p = 60$ cm).
2. Zone plates with same-size apertures ($2b_n = 60$ cm): We take the same zone plate dimensions and wavelength as those in the previous

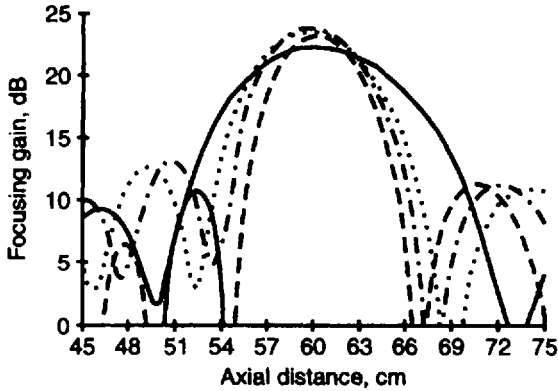


Figure 4.58 Focusing gain versus axial distance plotted for conical (solid line), spherical (dashed line), paraboloidal (dotted line), and planar (dadot line).

example. Two open zones are taken for the planar zone plate aperture, Figure 4.24, while the curved zone plate apertures contain three open zones, Figures 4.48(b), 4.50(b), and 4.52(b). Figure 4.59 shows curves of the focusing gain G_f versus the axial distance f_p , drawn with different lines: The dashed line corresponds to the conical zone plate ($G_f = 16.9$ dB at $f_p = 60$ cm), the dotted line to the spherical zone plate ($G_f = 16.8$ dB at $f_p = 58$ cm), the dadot line to the paraboloidal zone plate ($G_f = 17.1$ dB at $f_p = 59$ cm), and the solid line to the plane zone plate ($G_f = 11.9$ dB at $f_p = 60$ cm).

The numerical examples lead to the following basic conclusions:

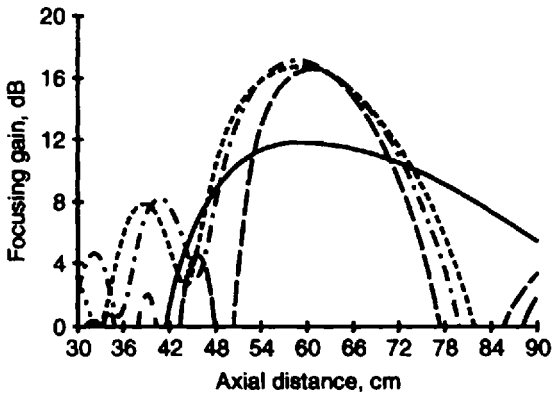


Figure 4.59 Focusing gain versus axial distance plotted for planar (solid line), spherical (dotted line), paraboloidal (dadot line), and conical (dotted line).

- The axial focusing gain of the curved zone plate illuminated by a plane wave depends mainly on the number of open zones and a little on the zonal surface curvature.
- For same-size apertures the focusing superiority of the curved zone plates over the planar ones is very well manifested, and again, there is not much difference in focusing gain between the curved zone plates.

References

- [1] Wood, R. W., "Phase-Reversal Zone Plates and Diffraction Telescopes," *Phil. Mag.*, S5, Vol. 45, No. 277, June 1898, pp. 511–523 (reprint in [24]).
- [2] Myers, O. E., "Studies of Transmission Zone Plates," *Am. J. Physics*, Vol. 41, 1951, pp. 359–365 (reprint in [24]).
- [3] Boivin, A., "On the Theory of Diffraction by Concentric Arrays of Ring-Shaped Apertures," *J. Opt. Soc. Am. (JOSA)*, Vol. 42, No. 1, Jan. 1952, pp. 60–64 (reprint in [24]).
- [4] Young, M., "Zone Plates and Their Aberrations," *J. Opt. Soc. Am. (JOSA)*, Vol. 62, No. 8, Aug. 1972, pp. 972–976 (reprint in [24]).
- [5] Wiltse, J. C., and J. E. Garrett, "The Fresnel Zone Plate Antenna," *Microwave J.*, Jan. 1991, pp. 101–114.
- [6] Garrett, J. E., and J. C. Wiltse, "Fresnel Zone Plate Antennas at Millimeter Wavelengths," *Int. J. Infrared and Millimeter Waves*, Vol. 12, No. 3, 1991, pp. 195–220.
- [7] Soret, J. L., "Ueber die durch Kreisgitter erzeugten Diffractionsphaenome." *J.C. Pogendorff's Annalen der Physik und Chemie*, Leipzig, Germany, Vol. 156, 1875, pp. 99–113 (reprint in [24]).
- [8] Wood, R. W., *Physical Optics* (3rd ed), New York: The MacMillan Co, 1934 (reprint in [24]).
- [9] Raiski, M. S., "The Zone Plate," *Uspehi Phys. Nauk*, Vol. XLVII, Aug. 4, 1952, pp. 515–536 (in Russian).
- [10] Sussman, M., "Elementary Diffraction Theory of Zone Plates," *Am. J. Physics*, Vol. 28, 1960, pp. 394–398.
- [11] Horman, M. H., "Efficiencies of Zone Plates and Phase Plates," *Applied Optics*, Vol. 6, Nov. 1967, pp. 2011–2013.
- [12] Kock, W. E., L. Rosen, and J. Rendeiro, "Holograms and Zone Plates," *Proc. IEEE*, Nov. 1966, pp. 1599–1601.
- [13] Borstema, M., "Fresnel Zone-Plate Diffraction Patterns," *J. Opt. Soc. Am (JOSA)*, 1969, pp. 1632–1638 (reprint in [24]).
- [14] Klein M. V., *Optics*, New York: John Wiley & Sons, 1970.
- [15] Nussbaum, A., and R. A. Phillips, *Contemporary Optics for Scientists and Engineers*, New Jersey: Prentice-Hall, 1976.
- [16] Stigliani, D. J., Raj Mittra, and R. G. Semonin, "Resolving Power of a Zone Plate," *J. Opt. Soc. Am. (JOSA)*, Vol. 57, No. 5, May 1967, pp. 610–613 (reprint in [24]).

- [17] Kearey, P. D., and A. G. Klein, "Resolving Power of Zone Plates," *Journal of Modern Physics*, Vol. 36, No. 3, 1989, pp. 361–367 (reprint in [24]).
- [18] Mottier, P., and S. Valette, "Integrated Fresnel Lens of Thermally Oxidized Silicon Substrate," *Applied Optics*, Vol. 20, No. 9, May 1, 1981, pp. 1630–1634.
- [19] Sahara, T., K. Kobayashi, H. Nishihara, and J. Koyama, "Graded-Index Fresnel Lenses for Integrated Optics," *Applied Optics*, Vol. 21, No. 11, June 1, 1982, pp. 1966–1971.
- [20] Kamiya, K., "Theory of Fresnel Zone Plate," *Science of Light*, Vol. 12, No. 2, 3, 1963.
- [21] Thompson, B. J., "Diffraction by Semitransparent and Phase Annuli," *J. Opt. Soc. Am. (JOSA)*, Vol. 55, Feb. 1965, pp. 145–149.
- [22] Sun, J.-A., and A. Cai, "Archaic Focusing of Fresnel Zone Plates," *J. Opt. Soc. Am. (JOSA), A*, Vol. 8, No. 1, Jan. 1991, pp. 33–35.
- [23] Goto K., and H. Banjo, "Angle Eikonals of Plane and Spherical Zone Plates," *J. Opt. Soc. Am., A*, Vol. 3, No. 12, December 1986 (reprint in [24]).
- [24] Ojeda-Castaneda, J., and C. Gomez-Reino (editors), Thomson, B. J (general editor), *Selected Papers on Zone Plates*, Washington: SPIE Opt. Engng Press, 1996.
- [25] Malyujinetz, G. D., "Diffraction Near Zone Plate Axis," *Dokladi Sov. Akademii Naik*, Vol. 54, No. 5, 1946, pp. 403–406 (in Russian).
- [26] Kanevski, I. N., *Focusing Sound and Ultrasound Waves*, Moscow: Nauka, 1977 (in Russian).
- [27] Hadimioglu, B., E. G. Rawson, R. Lujan, J. C. Zesch, B. T. Khuri-Yakub, and C. F. Quate, "High-Efficiency Fresnel Zone Acoustic Lenses," *IEEE Ultrasonic Symp.*, Baltimore, 31 Oct.–3 Nov. 1993, Symp. Proceedings, Vol. 1, pp. 579–582.
- [28] Skudrzyk, E., *The Foundations of Acoustics*, Springer-Verlag, 1971.
- [29] Clavier, A. G., and R. H. Darbord, "Directional Radio Transmission System," *U.S. Patent 2,043,347*, June 9, 1936.
- [30] Bruce, E., "Directive Radio System," *U.S. Patent 2,169,553*, Aug. 15, 1939.
- [31] Bruce, E., "Directive Radio System," *U.S. Patent 2,412,202*, Dec. 10, 1946.
- [32] Van Buskirk, L. F., and C. E. Hendrix, "The Zone Plate as a Radio Frequency Focusing Element," *IRE Trans. on Antennas and Propagat.*, Vol. AP-9, May 1961, pp. 319–320.
- [33] Hull, G. F., "Microwave Experiments and Their Optical Analogs," *Am. J. Physics*, Vol. 17, 1949, pp. 559–566.
- [34] Sobel, F., F. L. Wentworth, and J. C. Wiltse, "Quasi-Optical Surface Waveguide and Other Components for the 100- to 300-Gc Region," *IRE Trans. Microwave Theory Techn.*, Vol. 9, Nov. 1961, pp. 512–518.
- [35] Cohn, M., F. Wentworth, F. Sobel, and J. Wiltse, "Radiometer Instrumentation for the 1 to 2 Millimeter Wavelength Region," *Proc. IRE, 1962, Nat. Aerospace Electronics Conf.*, Dayton, OH, May 1962, pp. 537–541.
- [36] Huder, B., and W. Menzel, "Flat Printed Reflector Antenna for MM-Wave Applications," *Electronics Letts.*, Vol. 24, Mar. 1988, p. 318.
- [37] Delmas, J.-J., S. Toutain, G. Landrac, and P. Cousin, "TDF Antenna for Multisatellite Reception Using 3D Fresnel Principle and Multilayer Structure," *IEEE Int. Antennas and Propagat. Symp.*, Ann Arbor, MI, June 28–July 2, 1993, Symp. Digest, pp. 1647–1650.

- [38] Wiltse, J. C., "The Fresnel Zone-Plate Lens," *Proc. SPIE Symp.*, Arlington, VA, Vol. 544, Apr. 9–10, 1985, pp. 41–47.
- [39] Black, D. N., and J.C. Wiltse, "Millimeter-Wave Characteristics of Phase-Correcting Fresnel Zone Plates," *IEEE Trans. Microwave Theory Techn.*, Vol. 35, No. 12, Dec. 1987, pp. 1122–1128.
- [40] Griffiths, H. D., A. M. Veron, and K. Milne, "Planar Phase-Shifting Structures for Steerable DBS Antennas," *Int. Conf. Antennas Propagat.* (ICAP'89), Univ. Warwick, UK, Conf. Proc., Apr. 4–7, 1989, Part 1, pp. 45–49.
- [41] Garrett, J. E., and J. C. Wiltse, "Performance Characteristics of Phase-Correcting Fresnel Zone Plates," *IEEE Int. Microwave Symp.*, Vol. 11, pp. 797–799, 1990.
- [42] Guo, Y. J., S. K. Barton, and T. M. B. Wright, "Design of High-Efficiency Fresnel Zone Plate Antennas," *IEEE Int. Antennas Propagat. Symp.*, London, Ontario, June 1991, pp. 182–185.
- [43] Guo, Y. J., and S. K. Barton, "On the Subzone Phase Correction of Fresnel Zone Plate Antennas," *Microwave Opt. Techn. Letts.*, Vol. 6, No. 15, Dec. 1993, pp. 840–843.
- [44] Guo Y. J., and S. K. Barton, "Fresnel Zone Plate Reflector Incorporating Rings," *IEEE Microwave and Guided Wave Letts.*, Vol. 3, Nov. 1993, pp. 417–419.
- [45] Guo, Y. J., and S. K. Barton, "High-Efficiency Zone Plate Reflector Incorporating Printed Resonator," *Proc. Int. Conf. Antennas and Propagat.* (ICAP'93), Edinburgh, U.K., 1993, pp. 620–622.
- [46] Van Houten, J. M., and M. H. A. J. Herben, "Analysis of Phase-Correcting Fresnel-Zone Plate Antenna With Dielectric/Transparent Zones," *J. Electromagnetic Waves and Applications*, Vol. 8, No. 7, 1994, pp. 847–858.
- [47] Wiltse, J. C., "Millimeter-Wave Fresnel Zone Plate Antennas," Chapter 11 in *Millimeter and Microwave Engng. for Communications and Radar* (book), Critical Reviews of Optical Science and Technology, J. C. Wiltse, ed., SPIE Vol. CR54, Bellingham, WA, SPIE Press, 1994.
- [48] Guo, Y. J., and S. K. Barton, "Phase Correcting Zonal Reflector Incorporating Rings," *IEEE Trans. Antennas Propagat.*, Vol. 43, 1995, pp. 350–355.
- [49] Hristov, H. D., and M. H. A. J. Herben, "Millimeter-Wave Fresnel Zone Plate Lens and Antenna," *IEEE Trans. Microwave Theory and Techn.*, Vol. 43, Dec. 1995, pp. 2770–2785.
- [50] Hristov, H. D., and M. H. A. J. Herben, "Quarter-Wave Fresnel Zone Planar Lens and Antenna," *IEEE Microwave and Guided Waves Letts.*, Vol. 5, Aug. 1995, pp. 249–251.
- [51] Hristov, H. D., "The Multidielectric Fresnel Zone Plate Antenna—A New Candidate for DBS Reception," *IEEE Antennas and Propagat. Symp.*, Baltimore, MD, 1086, *Symp. Digest.*, Vol. 1, July 21–26, 1996, pp. 746–749.
- [52] Wiltse, J. C., "The Phase-Correcting Zone-Plate," *Proc. Int. Conf. Infrared Millimeter Waves*, Lake Buena Vista, FL, Dec. 1985, pp. 345–347.
- [53] Dey, K. K., and P. Khastgir, "Comparative Focusing Properties of Spherical and Plane Microwave Zone Plate Antennas," *Int. J. Electronics*, Vol. 35, No. 4, 1973, pp. 497–506.
- [54] Dey, K. K., and P. Khastgir, "A Study of the Characteristics of a Microwave Spherical Zone Plate Antenna," *Int. J. Electronics*, Vol. 35, No. 1, 1973, pp. 97–103.

- [55] Dey, K. K., and P. Khastgir, "A Theoretical Study of the Axial Field Amplitude of Microwave Paraboloidal, Spherical and Plane Zone Plate Antennas," *J. Inst. Electronics and Telecommunication Engineers, India*, Vol. 19, No. 12, 1973, pp. 697–700.
- [56] Khastgir, P., J. N. Chakravorty, and K. K. Dey, "Microwave Paraboloidal, Spherical & Plane Zone Plate Antennas: A Comparative Study," *Indian J. Radio & Space Physics*, Vol. 2, No. 1, 1973, pp. 47–50.
- [57] Chakravorty, S. C., P. Khastgir, and K. K. Dey, "Microwave Fresnel Zone Plates With Non-Uniform Aperture Excitation," *J. Inst. Electronics and Telecommunication Engineers, India*, Vol. 23, No. 3, 1977, pp. 145–147.
- [58] Khastgir, P., and K. N. Bhowmick, "Analysis of the Off-axis Defocus of Microwave Zone Plate," *Indian J. Pure & Applied Physics*, Vol. 16, Feb. 1978, pp. 96–101.
- [59] Cousin, P., G. Landrac, S. Toutain, and J. J. Delmas, "Calculation of the Focal Field Distribution and Radiation Pattern of a Parabolic Antenna With Fresnel Zones," *JINA'94*, Nice, France, Nov. 8–10, 1994, *Proc. of the Int. Symp. Antennas*, pp. 489–492 (in French).
- [60] Ji, Y., and M. Fujita, "A Cylindrical Fresnel Zone Antenna," *IEEE Trans. Antennas Propagat.*, Vol. 44, Sept. 1996, pp. 1301–1303.
- [61] Papulis, A., *Systems and Transforms with Applications in Optics*, New York: McGraw-Hill, 1968.
- [62] Jiang, G. Z., and W. X. Zhang, "The Effect of Layer Spacing on the Properties of Double-Layer Fresnel Zone Plate Lens," *IEEE Int. Symp. Antennas and Propagat.*, Vol. 1, Montreal, Canada, July 13–18, 1997, *Symp. Digest*, pp. 472–475.
- [63] Wilcockson, P. C., "Evaluation of Flat Reflectors for Space and Ground Station Antenna Applications," *Report, Eu. Space Agency, Order 142600*, Dec. 22, 1994, 46 pages + Appendix (MathCad Program).
- [64] Bazarsk'i, O. B., A. I. Kolesnikov, and Ya. L. Hlyavich, "Frequency Properties of Fresnel Zone Lenses," *Radiotekhnika i elektronika*, No. 12, 1980, pp. 2491–2497 (in Russian).
- [65] Shekhar, S., S. P. Ojha, and K. K. Dey, "Ray-Theoretic Characteristics of a Plane Microwave Zone Plate and Their Experimental Verification," *Nat. Acad. Sci. Lett.*, Vol. 14, No. 10, 1991, pp. 421–426.
- [66] Abella, C., et al, "Analysis and Synthesis of Planar Nonhomogenous Lenses," *Eu. Microwave Conf.*, 6–9 September 1993, Madrid, Conf. Proc. pp. 893–895.
- [67] Yamauchi, J., S. Honma, T. Honma, and H. Nakano, "Focusing Properties of Fresnel Zone-Plate and Its Application to a Helix Radiating a Circularly Polarized Wave," *Electronics and Communications in Japan, Part 1 (Communications)*, Vol. B-II, Vol. J72-B-II, No. 12, 1989, pp. 648–654 (in Japanese).
- [68] Popov, A. V., et al, "Computer Simulation of Diffraction and Focusing in Quasi-optics," *Eu. Microwave Conf.*, Sept. 6–9, 1993, Madrid, Conf. Proceedings, pp. 993–995.
- [69] Walton, J. D., Jr., *Radome Engineering Handbook*, New York: Marcel Dekker, 1970.
- [70] Kaplun, V. A., *Radomes for Microwave Antennas*, Moscow: Soviet Radio, 1974 (in Russian).
- [71] Rudge, A. W., et al. (editors), *The Handbook of Antenna Design*, Vol. 2, IEE Electromagnetic Waves Series 16, London: Peter Peregrinus, 1983.
- [72] Parker, E. A., and S. M. A. Hamdy, "Rings as Elements for Frequency Selective Surfaces," *Electronics Letts.*, Aug. 20, 1981, Vol. 17, No. 17, pp. 612–614.

- [73] Langley, R. J., and E. A. Parker, "Equivalent Circuit Model for Arrays of Square Loops," *Electronics Letts.*, Apr. 1, 1982, Vol. 18, No. 7, pp. 294–296.
- [74] Langley, R. J., and A. J. Drinkwater, "Improved Empirical Model for the Jerusalem Cross," *IEE Proc.*, Vol. 129, Pt. H, No. 1, Feb. 1982, pp. 1–6.
- [75] Langley, R. J., and C. K. Lee, "Design of Single-Layer Frequency Selective Surfaces," *Electromagnetics*, No. 5, 1985, pp. 331–347.
- [76] Chen, Ch.-Ch., "Diffraction of Electromagnetic Waves by a Conducting Screen Perforated Periodically with Circular Holes," *IEEE Trans. Microwave Theory Techn.*, 1971, Vol. MTT-19, pp. 403–409.
- [77] Chen, Ch.-Ch., "Transmission through a Coupling Screen Perforated Periodically with Apertures," *IEEE Trans. Microwave Theory Techn.*, Vol. 18, No. 9, Sept. 1970, pp. 627–632.
- [78] Ji, Yu, and M. Fujita, "Design and Analysis of a Folded Fresnel Zone Plate Antenna," *Int. J. Infrared and Millimeter Waves*, Vol. 15, Aug. 1994, pp. 1385–1406.
- [79] Minin, I. V., and O. V. Minin, "New Class Microwave Antennas Based on the Elements of the Diffraction Quasioptics: Advantages and Applications," *IEEE Int. Antennas and Propagat. Symp.*, Orlando, FL, July 11–16, 1999, Symp. Digest, Vol. 2, pp. 754–757.

Selected Bibliography

- Baibulatov, O., Minin, and O. V. Minin, "Investigation of Focusing Properties of Fresnel Zone Plate," *Radiotekhnika i Elektronika*, Vol. 30, No. 9, pp. 800–806 (in Russian).
- Garrett, J. E., and J. C. Wiltse, "Fresnel Zone Plate Antennas at Millimeter Wavelengths," *Int. J. Infrared and Millimeter Waves*, Vol. 12, No. 3, Mar. 1991, pp. 195–220.
- Guo, Y. J., et al., "Reflection Efficiency of a Phase Reversal Zone Plate Antenna Made of Thin Conducting Film," *IEE Colloq. Materials and Manufacturing Processes for Antennas*, London, United Kingdom, Digest No. 169, 29 November 1990, pp. 4/1–3.
- Guo, Y. J., and S. K. Barton, "Analysis on One-Dimensional Zonal Reflectors," *IEEE Trans. Antennas Propagat.*, Vol. 43, 1995, pp. 385–389.
- Hristov, H. D., *Analysis and Design of Transmissive Fresnel Zone Antennas for DBS Reception*, CEC CIPA 35 10CT926503 Report, Eindhoven Univ. Technology, Fac. Electr. Engineering, February 1994 (72 pages).
- Hristov, H. D., J. R. Urumov, and M. J. Semov, "Ring-Shaped Dielectric Antenna," *Eu. Microwave Conf.*, 6–12 September 1980, Warsaw, Conf. Proceedings, pp. 109–113. Reprint in *Advanced Antenna Technology*, ed. by P. J. B. Clarricoats, Reprint Vol. No. 1, *Conf. Exhibitions & Publishers*, United Kingdom, 1982, pp. 361–365.

- Jiang, G. Z., W. X. Zhang, and K. Kang, "The Focused Fields of Fresnel Zone Plate Lens," *Int. Sym. Antennas and Propagat. (ISAP '96)*, 1996, Chiba, Japan, Conf. Proc., pp. 57–59.
- Jiang, G. Z., and W. X. Zhang, "New Types of Fresnel Zone Plate Lens With Lower Backward Radiation," *IEEE Int. Symp. Antennas and Propagat.*, Atlanta, GA, Vol. 1, June 1998, *Symp. Digest*, pp. 166–169.
- Kopilov, Yu, A. V. Popov, and A. V. Vinogradov, "Diffraction Phenomena Inside Thick Fresnel Zone Plates," *Radio Science*, Vol. 31, No. 6, 1996, pp. 1815–1822.
- Lazarus, M. J., A. Silvertown, and S. Novak, "Fresnel-Zone Plate Aids Low-Cost Doppler Design," *Microwaves*, November 1979, pp. 78–80.
- Sanyal, G. S., and M. Singh, "Fresnel Zone Plate Antenna," *J. Inst. Telecommunication Engineers, India*, Vol. 14, 1968, pp. 265–281.
- Van Buskirk, L. F., "Zone Plate Radio Transmission System," *U.S. Patent 3,189,907*, June 15, 1965.

Appendix 4A: Transmission Through Dielectric Plate With Metal Grid

Here we apply the theory from Section 1.6.2 for the transmission through a dielectric plate with a planar metal grid (or a gridded plate), which can be examined as a three-layer sandwich (Figure 4A.1). The wave transmission through such a structure is accompanied with multiple reflections and transmissions and higher order spatial modes generated by the discontinuity at the conducting grid [70, 75].

Using a simple equivalent circuit of the grid it can be treated as a reactive two-port element $\bar{Z}_g = \pm j\bar{Z}_g$ connected in parallel to the equivalent transmission line. This simplified approach gives reasonably accurate predictions of the electromagnetic transmission/reflection characteristics.

The inductive grid increases the phase shift of the dielectric plate, and in this sense it has dielectric-like behavior. On the contrary, the capacitive grid reduces the total phase shift, and if the grid phase shift is equal to the dielectric phase shift the gridded slab gets compensated, or its resultant phase shift turns to zero.

The equivalent cascaded two-port transmission network of the gridded dielectric plate is shown in Figure 4A.2, and in accordance with (1.101) it is described by the following matrix equation

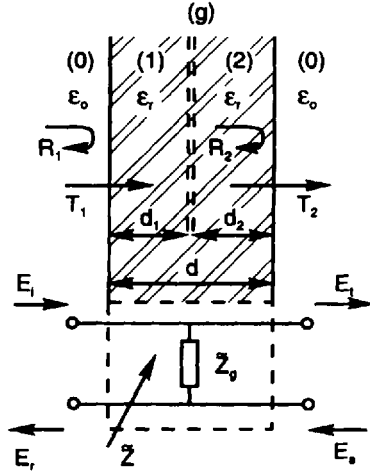


Figure 4A.1 Dielectric plate with metal grid. (After: [70].)

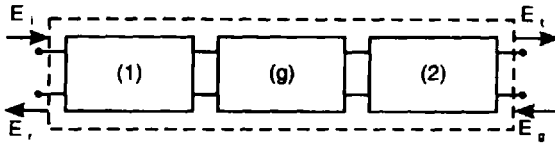


Figure 4A.2 Equivalent network of dielectric plate with metal grid.

$$\begin{aligned}
 \begin{bmatrix} E_i \\ E_r \end{bmatrix} &= \frac{1}{1 - R_1^2} \begin{bmatrix} 1 & R_1 \\ R_1 & 1 \end{bmatrix} \begin{bmatrix} e^{\dot{\phi}_1} & 0 \\ 0 & e^{-\dot{\phi}_1} \end{bmatrix} \begin{bmatrix} M_{g11} & M_{g12} \\ M_{g21} & M_{g22} \end{bmatrix} \\
 &\times \begin{bmatrix} e^{\dot{\phi}_2} & 0 \\ 0 & e^{-\dot{\phi}_2} \end{bmatrix} \begin{bmatrix} 1 & -R_1 \\ -R_1 & 1 \end{bmatrix} \begin{bmatrix} E_t \\ E_s \end{bmatrix} \\
 &= \begin{bmatrix} M'_{11} & M'_{12} \\ M'_{21} & M'_{22} \end{bmatrix} \begin{bmatrix} E_t \\ E_s \end{bmatrix}
 \end{aligned} \tag{4A.1}$$

Here $\phi_{1,2} \cong \frac{2\pi}{\lambda} d_{1,2} \left(\frac{\epsilon_r \tan \delta}{\sqrt{\epsilon_r - \sin^2 \psi}} + j \sqrt{\epsilon_r - \sin^2 \psi} \right)$, M_{g11} , M_{g12} ,

M_{g21} and M_{g22} are the grid matrix elements, and M'_{11} , M'_{12} , M'_{21} and M'_{22} are the total matrix elements. The thickness of the grid is assumed to be zero. T_1 , T_2 , and R_1 are the relevant transmission and reflection coefficients, for which the following relations are valid: $T_1 = 1 + R_1$ and $T_2 = 1 - R_1$.

According to (1.80) the normalized wave impedances are given by

$$\begin{bmatrix} \bar{\eta}_1^\perp \\ \bar{\eta}_1^\parallel \end{bmatrix} = \begin{bmatrix} 1/\sqrt{\epsilon_{r1} - \sin^2 \psi} \\ \sqrt{\epsilon_{r1} - \sin^2 \psi}/\epsilon_{r1} \end{bmatrix} \quad (4A.2)$$

Denote with R_{g1} and $R_{g2} = R_{g1}$ the reflection coefficients referred to as the grid two-port circuit input and output, respectively, and with T_{g1} the grid's transmission coefficient for a matched output. The coefficients R_{g1} and T_{g1} can be expressed by $\bar{\eta}_1$ and \bar{Z}_g as follows

$$R_{g1} = -\frac{\bar{\eta}_1^2}{\bar{\eta}_1^2 + 2\bar{\eta}_1\bar{Z}_g} \quad (4A.3)$$

$$T_{g1} = 1 + R_{g1} \quad (4A.4)$$

and from (1.87)–(1.90) the grid matrix elements are found as

$$M_{g11} = \frac{1}{T_{g1}} = 1 + \frac{\bar{\eta}_1}{2\bar{Z}_g} \quad (4A.5)$$

$$M_{g21} = \frac{R_{g1}}{T_{g1}} = -\frac{\bar{\eta}_1}{2\bar{Z}_g} \quad (4A.6)$$

$$M_{g12} = -M_{g21} = \frac{\bar{\eta}_1}{2\bar{Z}_g} \quad (4A.7)$$

$$M_{g22} = 1 - \frac{\bar{\eta}_1}{2\bar{Z}_g} \quad (4A.8)$$

The total transmission coefficient T of the gridded plate is found after placing (4A.5–4A.8) into (4A.1)

$$T = \frac{1}{M'_{11}} \quad (4A.9)$$

For the specific case of metal grid situated in the middle of a lossless dielectric plate $d_2 = d_1$, $\varphi_2 = \varphi_1$, and then

$$T = \frac{1 - R_1^2}{(M_{g11}e^{j\varphi_1} + M_{g21}R_1e^{-j\varphi_1}e^{j\varphi_1}) - (M_{g12}e^{j\varphi_1} + M_{g22}R_1e^{-j\varphi_1})R_1e^{-j\varphi_1}} \quad (4A.10)$$

or for $\bar{Z}_g = j\bar{X}_g$ it is obtained that

$$T = |T|e^{-j\psi_T} = \frac{1 - R_1^2}{Q_1} \quad (4A.11)$$

where

$$Q_1 = [(1 - R_1^2)\cos 2\varphi_1 + \frac{\bar{\eta}_1}{2\bar{X}_g}(1 - R_1^2)\sin 2\varphi_1] + j[(1 + R_1^2)\sin 2\varphi_1 - \frac{\bar{\eta}_1}{2\bar{X}_g}(1 + R_1^2)\cos 2\varphi_1 + R_1\frac{\bar{\eta}_1}{\bar{X}_g}] \quad (4A.12)$$

For a given $\bar{\eta}_g$, ϵ_r , and plate dimensions, it is not difficult to calculate the reflection and transmission coefficients.

The problem can be posed in a reverse manner: to find out Z_g for given dielectric plate characteristics and reflection (or transmission) coefficient. In [70] the problem is solved approximately using the transmission line equivalent circuit of the gridded plate structure, and the following expression for \bar{Z}_g is found

$$\bar{Z}_g = \frac{\bar{\eta}_1(\Omega \cos \varphi_1 + j \sin \varphi_1)[R(\Omega \cos \varphi_2 + j \sin \varphi_2) + (\Omega \cos \varphi_2 - j \sin \varphi_2)]}{-R[2\Omega \cos(\varphi_1 + \varphi_2)] + j \sin(\varphi_1 + \varphi_2)(1 + \Omega^2) + j(1 - \Omega^2)\sin(\varphi_1 + \varphi_2)} \quad (4A.13)$$

where $\Omega = \frac{\bar{\eta}_o}{\bar{\eta}_1}$ and $\varphi_{1,2} = \beta_{1,2}d_{1,2}\sqrt{\epsilon_r - \sin^2\psi}$.

All equations in Appendix 4A are valid for both polarizations: perpendicular and parallel.

This page intentionally left blank

5

Fresnel Zone Plate Antennas

5.1 Introduction

The Fresnel zone plate antenna is essentially a lens or reflector antenna, which consists of two basic elements—a transmission or reflection zone plate, respectively, and a feed. The feed (e.g., open waveguide, horn, dipole) is normally placed at the primary focus of the zone plate. The Fresnel zone plate converts the spherical wave radiated by the feed into a plane wave (transmitting antenna), or the sideways incident plane wave into a spherical wave focused at the feed (receiving antenna). Depending on the zone plate construction we may distinguish two different types of zone plate antennas: (1) the Soret-type antenna with a zone plate lens of open and blocked Fresnel zones and (2) the Wood-type antenna with a zone plate lens of phase-corrected zones.

The transmission zone plate antenna originated directly from the optical Soret- and Wood-type lenses, and it was hardly by chance that in radiowave engineering it was mostly applied to millimeter/submillimeter-wave systems [1–7]. As a radio antenna element, designed at 1.5 GHz, the reflection zone plate was first proposed in 1932 by Clavier and Darbord [8]. About thirty years later, Van Buskirk and Hendrix [9, 10] developed and studied an X-band reflector antenna, termed by them a folded or grounded zone plate antenna. It was then adjusted to the millimeter wave region [4, 7, 11–14]. Nevertheless, the applications of the reflection zone plate antennas are still mainly associated with the broadcast satellite reception at centimeter waves [15–23].

Both the transmission and reflection zone plate antennas can be also fed in an offset manner. The feed offsetting is usually made in the reflector antennas for beam scanning purposes and for avoiding the shading effect of the feed [21, 24–29].

On the base of the curvilinear zone-plate lenses effective and conformal antennas have already been studied and applied [21, 24, 30–39].

The scope of this chapter is the concise presentation of theory, properties, and typical applications of axially and offset-fed, transmission and reflector, planar, and curved zone plate antennas.

5.2 Planar Zone Plate Antennas: Transmission Versions

As the transmission zone plates are diffraction lenses the corresponding zone-plate antenna versions are actually lens antennas. Thus, the theoretical and design considerations that have to be taken into account are similar to those for the classical lens antennas. Here we deal with the far-field scalar/vector theory and the basic numerical and measured antenna characteristics: co-polar and cross-polar radiation patterns, directive gain, aperture efficiency, cross-polarization, and bandwidth of axially-fed, transmission-type planar zone plate antennas.

5.2.1 Soret Zone Plate Antenna

5.2.1.1 Far-Field Equations Based on Scalar Kirchhoff Diffraction Theory

Boivin [40] first obtained accurate expressions for the far-field of the half-open or Soret zone plate illuminated by a point source using the Lommel functions. While these expressions are completely suitable for optics where the zone plate focal length is very big compared to the zone plate diameter, they are not precise for the microwave and millimeter-wave region.

It is a common practice to express the aperture antenna far field as a function of the complex aperture field distribution. If the antenna aperture is placed at xy plane (as in Figure 2.22), the elementary Huygens area surrounding the running point $Q'(x', y')$ can be given as $dS' = dx' dy'$. For a known aperture field $E(x', y')$, the far field is easily obtained by the following Fresnel-Kirchhoff integral

$$E(\vartheta, \varphi) = j \frac{(1 + \cos \vartheta)}{2\lambda} \frac{e^{-j\beta r_0}}{r_0} \iint E(x', y') e^{j\beta \sin \vartheta (x' \cos \varphi + y' \sin \varphi)} dx' dy' \quad (5.1)$$

where ϑ , φ , and r_0 are spherical coordinates of a far-field point, and $\beta = 2\pi/\lambda$ is the free-space phase constant.

Using a similar far-field approximation Black and Wiltse [41] expressed the far field of the n -th ring-shaped aperture with an axially symmetric field function $f(r')$ in the form

$$E(\varphi, \vartheta) = j \frac{(1 + \cos \vartheta)}{2\lambda} \frac{e^{-j\beta r_o}}{r_o} e^{j\Phi_n} \int_{b_{n-1}}^{b_n} f(r') J_0(\beta r' \sin \vartheta) r' dr' \quad (5.2)$$

where Φ_n is the phase, and b_{n-1} and b_n are the radii of the n -th Fresnel zone; J_0 is the zero order Bessel function.

The aperture distribution depends on the feed radiation pattern. For a point feed source it is easily expressed

$$f(r') = \frac{e^{-j\beta\sqrt{F^2 + r'^2}}}{\sqrt{F^2 + r'^2}} \quad (5.3)$$

where F is the primary zone plate focal length.

In the case of a directive feed source with a normalized axially symmetric radiation pattern similar to that of (3.99) we can modify the feed function in the following form

$$f(r') = \cos^p \psi \frac{e^{-j\beta\sqrt{F^2 + r'^2}}}{\sqrt{F^2 + r'^2}} = \left(\frac{F}{\sqrt{F^2 + r'^2}} \right)^p \frac{e^{-j\beta\sqrt{F^2 + r'^2}}}{\sqrt{F^2 + r'^2}} \quad (5.4)$$

where p is the power number determining the amplitude feed pattern directivity.

5.2.1.2 Vectorial Far Field Equations Derived From the Kirchhoff Diffraction Theory

During the period 1991–1994 an extensive study of transmissive zone plate antennas for direct broadcast satellite (DBS) reception was carried out at the Eindhoven University of Technology by Herben and his graduate students Leyten, Baggen, Van Houten, et al. First, a vectorial far field theory for the Soret zone plate antenna was completed and published in [19, 42]. Since this theory will, from this point forward, often be used in its original or modified form, we shall summarize it in detail. Figure 5.1 illustrates the derivation procedure.

Let the feed gain pattern have an axially symmetric shape and be modeled by the cosine equation (3.99). Assume also that beside the axial radiation symmetry the antenna feed has Huygens' source polarization properties and

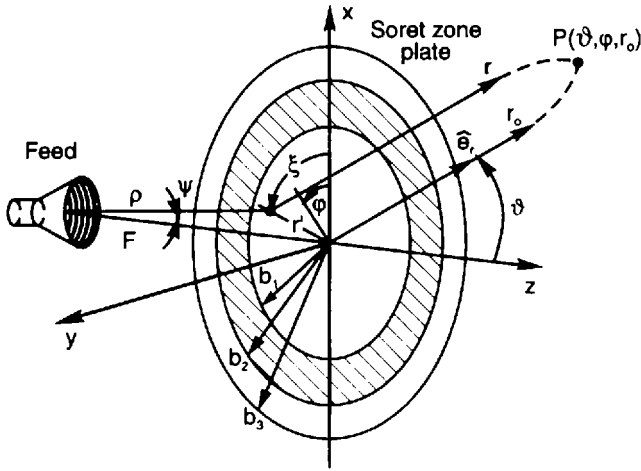


Figure 5.1 Geometry of a Soret zone plate antenna illuminated by an axially symmetric feed field. (After: [42].)

that the field at the zone plate plane xy has an electric vector, expressed as [43]

$$\mathbf{E}_f(\psi, \xi, m) = C_f \sqrt{G_f(\psi, m)} \frac{e^{-j\beta\rho(\psi)}}{\rho(\psi)} \quad (5.5)$$

where the amplitude constant C_f is

$$C_f = \sqrt{\frac{P_f \eta_0}{2\pi}} \quad (5.6)$$

and the polarization unit vector $\hat{\mathbf{e}}_f(\psi, \xi)$ is written as

$$\hat{\mathbf{e}}_f(\psi, \xi) = -\cos\xi \hat{\mathbf{e}}_\psi + \sin\xi \hat{\mathbf{e}}_\xi \quad (5.7)$$

In (5.6) P_f is the feed radiation power, $\eta_0 = 120\pi$, and Ω is the free-space wave impedance.

From geometrical considerations

$$\rho(\psi) = \frac{F}{\cos\psi} \quad (5.8)$$

Next, let us find equations for the far field starting from the vectorial Kirchhoff diffraction integral given by (2.141), for an aperture in an infinite

screen (Figure 2.28). For a zone plate illuminated by the electric vector field $\mathbf{E}_f(\psi, \xi, m)$ expressed by (5.5), (2.141) can be transformed to give [19, 42, 44].

$$\mathbf{E}(r, m) = C \hat{\mathbf{e}}_r \times \iint_S [\hat{\mathbf{n}} \times \hat{\mathbf{e}}_f(\psi, m)] \sqrt{G_f(\psi, m)} \frac{e^{-j\beta\rho(\psi)}}{\rho(\psi)} e^{j\beta(\hat{\mathbf{e}}_r \cdot \mathbf{r}')} dS' \quad (5.9)$$

where

$$C = j \frac{\beta e^{-j\beta r_0}}{2\pi r_0} \sqrt{\frac{P_t \eta_0}{2\pi}} \quad (5.10)$$

and the normal unit-vector $\hat{\mathbf{n}}$ is oriented along the z -axis (i.e., $\hat{\mathbf{n}} = \hat{\mathbf{e}}_z$).

The unit polarization vector $\hat{\mathbf{e}}_f(\psi, \xi)$ has rectangular coordinates given for short in the following matrix form

$$\hat{\mathbf{e}}_f(\psi, \xi) = \begin{pmatrix} -\cos^2 \xi \cos \psi - \sin^2 \xi \\ \sin \xi \cos \xi (1 - \cos \xi) \\ 0 \end{pmatrix} \quad (5.11)$$

and the vector product $\hat{\mathbf{n}} \times \hat{\mathbf{e}}_f(\psi, \xi)$ yields

$$\hat{\mathbf{n}} \times \hat{\mathbf{e}}_f(\psi, \xi) = \begin{pmatrix} (\cos \psi - 1) \sin \xi \cos \psi \\ -\cos^2 \xi \cos \psi - \sin^2 \xi \\ 0 \end{pmatrix} \quad (5.12)$$

The unit-vector $\hat{\mathbf{e}}_r(\varphi, \vartheta)$ points to the far-field region, and its rectangular components are given by

$$\hat{\mathbf{e}}_r(\varphi, \vartheta) = \begin{pmatrix} \sin \vartheta \cos \varphi \\ \sin \vartheta \sin \varphi \\ \cos \vartheta \end{pmatrix} \quad (5.13)$$

The vector \mathbf{r}' defines the position of the elementary area dS' point on the zone plate plane and can be written as

$$\mathbf{r}' = \begin{pmatrix} F \tan \psi \cos \psi \\ F \tan \psi \sin \psi \\ 0 \end{pmatrix} \quad (5.14)$$

The aperture elementary area dS' is easily found

$$dS' = \frac{F^2 \tan \psi}{\cos^2 \psi} d\xi d\psi \quad (5.15)$$

The scalar product in the phase factor $\exp(j\beta(\hat{\mathbf{e}}_r \cdot \mathbf{r}'))$ is given by

$$\hat{\mathbf{e}}_r \cdot \mathbf{r}' = F \sin \vartheta \tan \psi \cos(\varphi - \xi) \quad (5.16)$$

After substituting (5.10–5.16) into (5.9) and carrying out the ξ -integration in a closed form, only ψ -integral remains. Finally, the components E_ϑ and E_φ of the total far-field vector are obtained

$$E_\vartheta(\varphi, \vartheta) = -\pi C \cos \varphi \sum_n \int_{\psi_{n-1}}^{\psi_n} O(\psi, m) e^{M(\psi)} I_\vartheta(\vartheta, \psi) d\psi \quad (5.17)$$

and

$$E_\varphi(\varphi, \vartheta) = -\pi C \cos \varphi \cos \vartheta \sum_n \int_{\psi_{n-1}}^{\psi_n} O(\psi, m) e^{M(\psi)} I_\varphi(\vartheta, \psi) d\psi \quad (5.18)$$

where

$$O(\psi, m) = \sqrt{G_f(\psi, m)} \frac{F \tan \psi}{\cos \psi} \quad (5.19)$$

$$M(\psi) = -j\beta F / \cos \psi \quad (5.20)$$

$$\psi_n = \arctan\left(\frac{b_n}{F}\right) \quad (5.21)$$

$$I_\vartheta(\vartheta, \psi) = -(\cos \psi + 1)J_0(N(\vartheta, \psi)) + (\cos \psi - 1)J_2(N(\vartheta, \psi)) \quad (5.22)$$

$$I_\varphi(\vartheta, \psi) = (\cos \psi + 1)J_0(N(\vartheta, \psi)) + (\cos \psi - 1)J_2(N(\vartheta, \psi)) \quad (5.23)$$

The summation is made over the open Fresnel zones, odd ($n = 1, 3, 5, \dots$) or even ($n = 2, 4, 6, \dots$).

The electric far-field vector is expressed as

$$\mathbf{E}(\vartheta, \varphi) = E_{\vartheta}(\vartheta, \varphi)\hat{\mathbf{e}}_{\vartheta} + E_{\varphi}(\vartheta, \varphi)\hat{\mathbf{e}}_{\varphi} \quad (5.24)$$

and the antenna directive gain pattern is calculated by

$$G(\varphi, \vartheta) = 10 \log \left(\frac{2\pi r^2}{\eta_o P_t} |E(\varphi, \vartheta)|^2 \right) \quad (5.25)$$

For the transmitting antenna with an electric field polarized along the x -axis, the copolar and cross-polar field components can be defined as follows (see Appendix 1A)

$$E_{co}(\varphi, \vartheta) = E_x(\varphi, \vartheta) = 10 \log \left(\frac{2\pi r^2}{\eta_o P_t} |\cos \varphi E_{\vartheta}(\varphi, \vartheta) - \sin \varphi E_{\varphi}(\varphi, \vartheta)|^2 \right) \quad (5.26)$$

$$\begin{aligned} E_{cr}(\varphi, \vartheta) &= E_y(\varphi, \vartheta) \\ &= 10 \log \left(\frac{2\pi r^2}{\eta_o P_t} |-\sin \varphi E_{\vartheta}(\varphi, \vartheta) - \cos \varphi E_{\varphi}(\varphi, \vartheta)|^2 \right) \end{aligned} \quad (5.27)$$

5.2.1.3 Numerical Results

The antenna radiation pattern depends on the arrangement of the open zones in the Soret zone plate. In principle, the open zones can be odd (positive) or even (negative). We calculated the gain radiation patterns for the two alternative zone dispositions and the results were illustrated graphically (Figure 5.2). With a solid line is drawn the copolar or E -plane gain pattern of the Soret zone plate antenna with an aperture diameter $D = 1\text{m}$ and a focal length $F = 2\text{m}$. The antenna is designed for a frequency $f = 11.1\text{GHz}$. There is a notable difference between the two patterns, especially in their sidelobe regions.

The antenna with odd open zones has a 0.6 dB higher maximum gain, while that with even open zones has a narrower beamwidth and lower near sidelobes. The positive zone plate has a central zone open that ensures a minimum reflection from the plate to the feed, or better feed matching and larger frequency bandwidth.

Figure 5.2 also shows the gain radiation pattern of the same size phase-reversal or Wood zone plate antenna (dotted line). It has a 5.7 dB higher

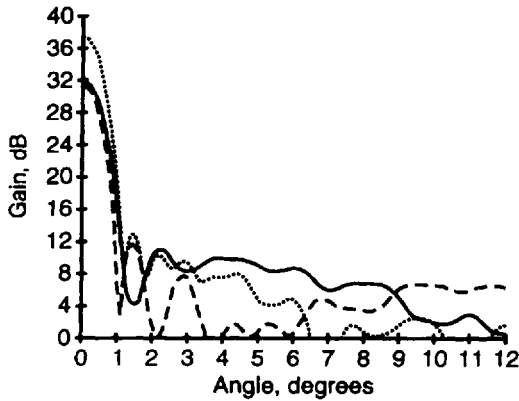


Figure 5.2 Gain radiation patterns of Soret zone plate antenna, for odd zones open (solid line) and even zones open (dashed line). Also shown for comparison is a gain pattern of same-size phase-reversal or Wood zone plate antenna (dotted line), ($f = 11.1$ GHz, $D = 1$ m, $F = 2$ m).

maximum gain compared to the gain of the Soret zone plate antenna with odd zones open.

Numerical study on the influence of the total full-wave zone number N_1 on the sidelobe performance of the positive and negative zone plates was completed by Guo and Barton [45]. Their analysis was based on the Kirchhoff scalar diffraction integral for a feed illumination pattern given by (3.99). Figure 5.3 shows the normalized radiation patterns of (a) positive and (b) negative Soret zone plate antennas for four different values of N_1 : $N_1 = 3$ (solid line), $N_1 = 5$ (dotted line), $N_1 = 7$ (dashed line), and $N_1 = 9$ (dotted line). The antennas are designed at 12 GHz for an aperture diameter of 0.75 m and an edge illumination of -11 dB. It is found that when N_1 is increased from 3 to 9 the focal distance to aperture diameter ratio F/D is reduced from 1.2 to 0.27, and the sidelobe level is significantly decreased. This means that with a given zone plate diameter and a constant edge amplitude taper, a small F/D is favorable to obtain low close-in sidelobes.

If it is not explicitly specified, we normally have in mind Soret zone plate antennas with odd open zones. Numerical comparison between two Soret zone plate antennas (SZPA-1 and SZPA-2) with odd zones open and a parabolic reflector antenna (PRA) designed for the reception of DBS signals is given in [25]. The antennas are chosen with approximately the same diameter of 1 m and a focal length of 0.5 m for the PRA and SZPA-1, and of 2 m for the SZPA-2. The antenna design is $f = 11.1$ GHz. Though with the same aperture size the two Soret zone plate antennas have very distinct numbers of open

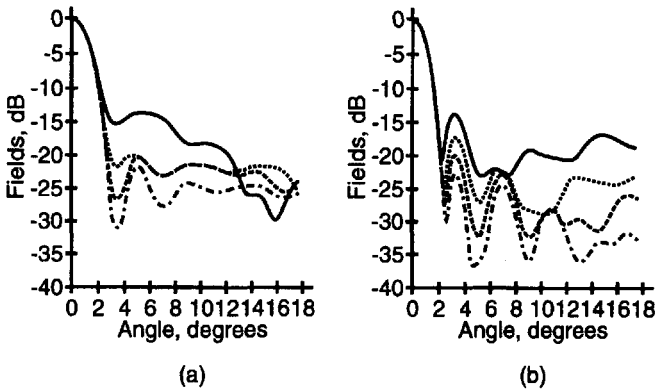


Figure 5.3 Far-field patterns for (a) positive and (b) negative Soret zone plate antennas of diameter 0.75m, $EIL = -11$ dB, and varying full-wave Fresnel zone number N_1 : $N_1 = 3$ (solid line), $N_1 = 5$ (dotted line), $N_1 = 7$ (dash line), and $N_1 = 9$ (dadot line). (After: [45], © 1992 IEEE.)

Fresnel zones: eight in the SZPA-1 and three in the SZPA-2, due to the big difference in their focal lengths. The feed illumination for all antennas is shaped according to (3.99) in a way that the same edge taper of -10 dB is kept.

The gain radiation patterns of these antennas are plotted in Figure 5.4 with a solid line for the PRA, a dashed line for SZPA-1, and a dadot line for SZPA-2 [19]. The radiation parameters of the three antennas are compared

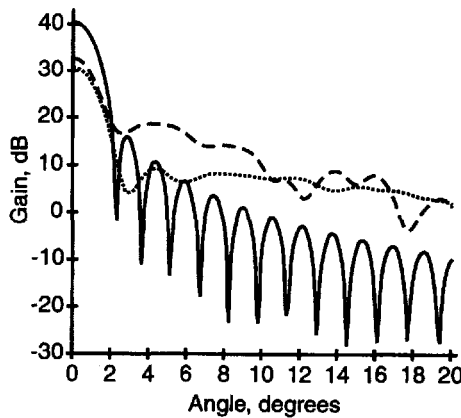


Figure 5.4 Theoretical gain radiation patterns of PRA (solid line), SZPA-1 (dotted line), and SZPA-2 (dashed line). The angle refers to ϑ in degrees, $\varphi = 0$ (E-plane). (After: [19].)

in Table 5.1 [19]. The PRA has 9.3 and 6.7 times greater efficiency and 9.8 and 7.85 dB higher gain, respectively, than the SZPA-1 and SZPA-2.

The calculated normalized copolar and cross-polar gain patterns of the PRA and SZPA-1 are drawn in Figure 5.5 [26]. In principle, the parabolic antenna has much better sidelobe and cross-polar performance than the Soret zone plate antennas. In particular, the maximum cross-polar level of the studied PRA, calculated at $\varphi = 45$ degrees is -54 dB, while that of the Soret zone plate antenna-1 is -30 dB.

However, the SZPA-2's cross polar level is -51 dB, or commensurable with that of the PRA. On the other hand, the SZPA-2 has very high near sidelobe level (-13.8 dB, as seen in Table 5.1). It is interesting to compare the copolar radiation patterns of the Soret zone plate antennas for the two main planes: $\varphi = 0$ degrees or E -plane (solid line), and $\varphi = 90$ degrees or H -plane (dotted line), drawn in Figure 5.6 [26]. These are theoretical radiation patterns of the SZPA-1. Though the feed pattern is axially symmetric, there

Table 5.1
Comparison of Soret Zone Plate Antennas With Parabolic Reflector Antennas

Antenna	Focal Distance (m)	Directive Gain (dBi)	Aperture Efficiency (%)	3-dB Beamwidth (degrees)	Maximum Sidelobe (dB)
PRA	0.5	40.4	81.9	1.9	-24.3
SZPA-1	0.5	30.6	8.8	1.9	-21.3
SZPA-2	2.0	32.6	12.2	1.9	-13.8

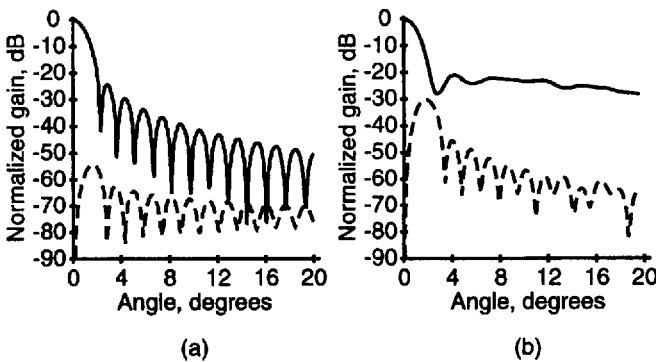


Figure 5.5 Theoretical normalized copolar (solid line) and cross-polar (dotted line) gain patterns of (a) PRA and (b) SZPA-1. (After: [26].)

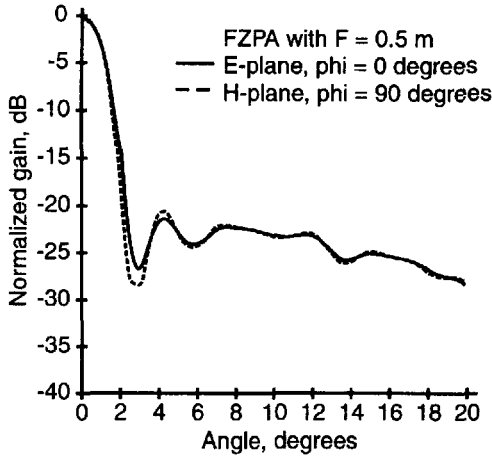


Figure 5.6 Copolar radiation patterns SZPA-1 for the two main planes: $\varphi = 0$ degrees or E-plane (solid line), and $\varphi = 90$ degrees or H-plane (dotted line). (After: [26].)

is some shape difference between the two orthogonal patterns due to the diffraction polarization anisotropy.

The partial and overall aperture efficiencies of the zone plate antenna are usually calculated for illumination by the already adopted axially symmetric feed pattern. On the base of antenna efficiency definitions, suitable equations were derived in [25, 26, 41]. In contrast with the parabolic reflector antenna, the most prominent characteristic of the Fresnel zone plate antenna is its phase efficiency.

Figure 5.7 plots the calculated overall and three partial efficiency curves (spillover, amplitude-taper, and phase ones) as functions of the primary focal distance F , for the Soret zone plate antenna with a diameter $D = 1$ m and design frequency of 11.1 GHz [46].

As is seen from the efficiency curves, the overall efficiency ν is too small, only about 10%. It depends mainly on the product of phase efficiency ($\nu_{ph} \approx 40\%$) and taper or illumination efficiency ($\nu_{tp} \approx 25\text{--}30\%$). Because the spillover efficiency ν_{sp} is higher than 90%, it does not significantly influence the overall efficiency.

Looking at curves in Figure 5.7 local extremes of the efficiency curves are detected. To better illustrate them the overall efficiency graph $\nu(F)$ is drawn magnified in Figure 5.8. It is seen that efficiency maxima are obtained for specific values of the focal distance, corresponding to some optimum power numbers m of the feed radiation pattern [46].

Actually, maximum efficiency is found for all cases in which the outer aperture zone is open, so that the number of the closed Fresnel zones is one

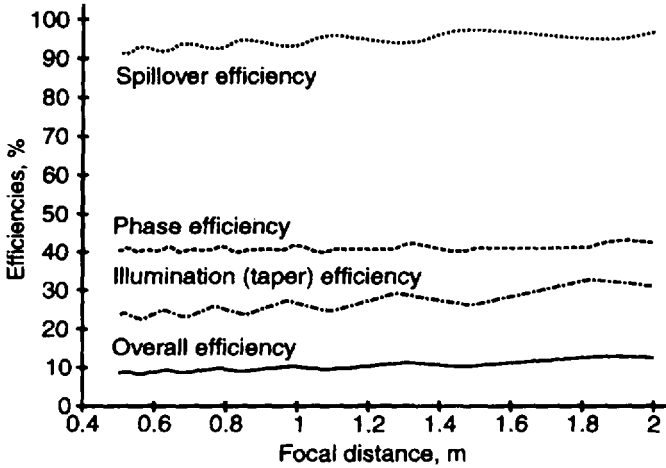


Figure 5.7 Efficiency curves of Soret zone plate antenna versus focal distance for aperture diameter of 1m and design frequency of 11.1 GHz. Curve traces: Solid line represents overall efficiency; dashed line represents phase efficiency; dash-dot line represents taper efficiency; and dotted line represents spillover efficiency. (After: [46].)

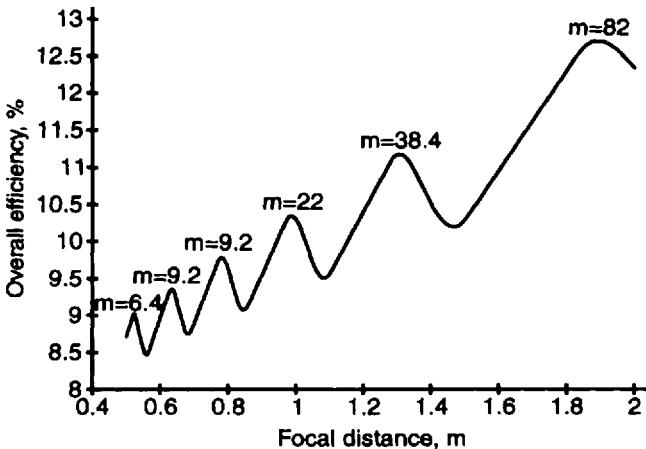


Figure 5.8 Magnified overall efficiency curve versus focal distance. (After: [46].)

less than the open zone number. In contrast, minimum efficiency and gain values occur at some focal distances for which the outer aperture zone is blocked. The theoretical curves of the total antenna gain G , feed gain G_f , and additional gain $G_{add} = G - G_f$ of the Soret zone plate antenna, designed for

$f = 11.1$ GHz, $D = 1$, and EIL = -10 dB, are plotted versus the focal length F in Figure 5.9, with solid, dotted, and dashed lines, correspondingly [26].

Figure 5.10 shows the antenna gain (solid line) and the aperture efficiency (dashed line), drawn as functions of the edge illumination level (EIL) [47]. The antenna is designed for an aperture diameter $D = 0.9$ m, a focal distance of $F = 0.6$ m, and a frequency of $f = 10$ GHz. The maximum antenna gain

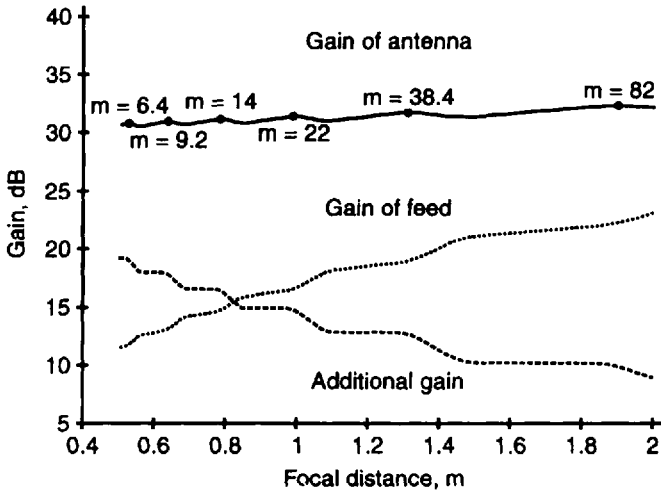


Figure 5.9 Gain versus focal length of Soret zone plate antenna with aperture diameter of 1 m and design frequency of 11.1 GHz: Total antenna gain (solid line), feed gain (dotted line), and additional gain (dashed line). (After: [26].)

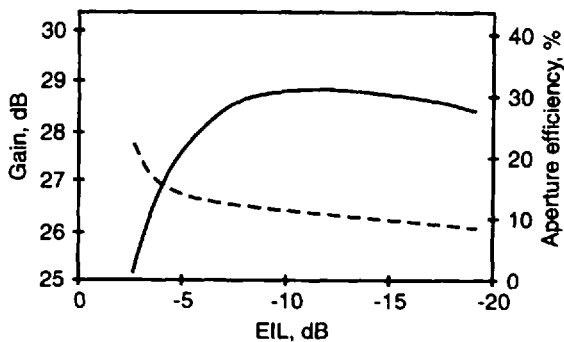


Figure 5.10 Gain (solid line) and aperture efficiency (dashed line) of Soret zone plate antenna as function of EIL, for $D = 0.9$ m, $F = 0.6$ m, and $f = 10$ GHz. (After: [47], © 1994 IEEE.)

appears when the EIL is within $-9 \div -12$ dB. It differs from the optimum EIL for the parabolic reflector antenna due to the distinction in the free-space loss L and imperfect phase-front transformation by the zone plate antenna.

The next numerical analysis is made for four Soret zone plate antenna models with different zone numbers $N = 3, 5, 7,$ and 9 , all designed for a frequency $f = 11.1$ GHz, focal distance $F = 0.54$ m, and EIL = -10 dB. Figure 5.11 shows (a) the gain feed patterns calculated according to (3.99), and (b) the antenna gain patterns of antennas [48].

Suppose that the feed of the same antenna models is moved along the axis from $F = 15\lambda$ to $F = 50\lambda$. For the design focal length $F = 20\lambda$ each model has a maximum gain while with the change of the focal length other extremes occur (Figure 5.12).

If the feed of the antenna model with seven Fresnel zones is located at the focal point $F_{lmax} \approx 36\lambda$, which corresponds to the first secondary maximum on the right, the antenna radiation pattern takes the form shown in Figure 5.13(a). The main lobe is again pointing to the zero direction, but the gain is about 11.5 dB less, and the sidelobes are very high compared to the antenna with a feed at the primary focal point.

Another interesting numerical simulation takes place when the feed of the same SZPA is put at the axial point $F_{lmin} \approx 29\lambda$, which corresponds to the first right minimum. Now the main lobe of the gain pattern becomes split, with a minimum at zero degrees as seen from Figure 5.13(b). Such a pattern

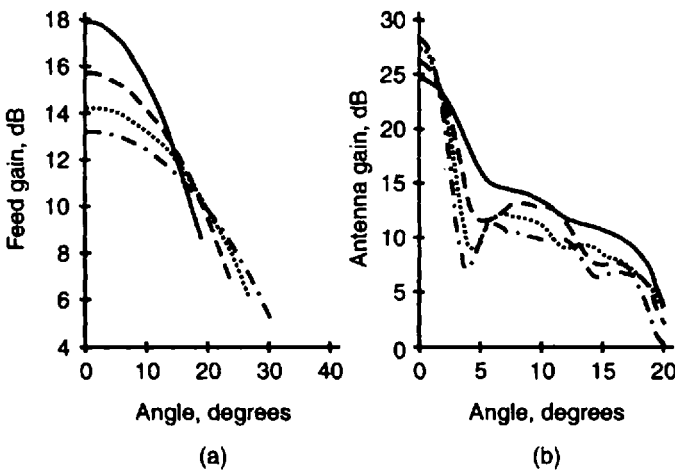


Figure 5.11 (a) Feed radiation patterns and (b) antenna radiation patterns of four designs with three (solid line), five (dashed line), seven (dotted line), and nine (dadot line) half-wave Fresnel zones ($f = 11.1$ GHz, $f = 20\lambda = 0.54$ m, EIL = -10 dB, $\varphi = 45$ degrees) [48].

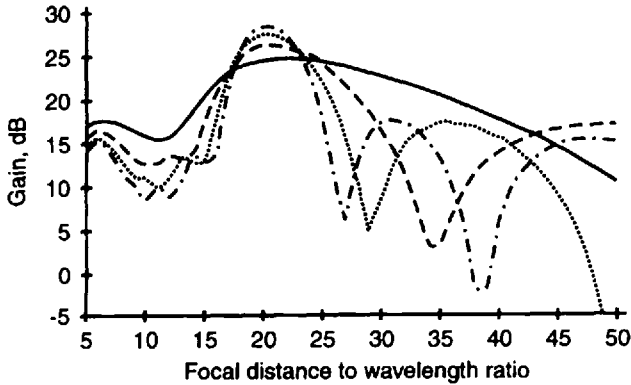


Figure 5.12 Gain patterns of four antenna models versus variation of feed position for the four antenna models depicted in Figure 5.11 [48].

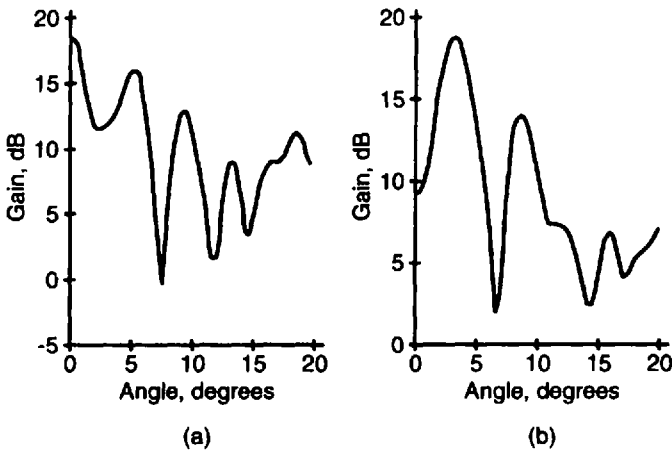


Figure 5.13 Radiation pattern of Soret zone plate antenna with seven (dotted line) Fresnel zones in case of feed disposition at: (a) second right maximum (Figure 5.11, $F_{\text{Imax}} \approx 36\lambda$) and (b) first right minimum (Figure 5.11, $F_{\text{Imin}} \approx 29\lambda$) [48].

shape might be useful for radio tracking purposes. Note that the minimum becomes deeper when the zone number increases.

The gain of Soret zone plate antenna can be raised by use of a specially shaped feed radiation pattern having deep minima in direction to the closed zones. In fact, this is an amplitude instead of phase correction.

In [49] the amplitude-correction technique is applied to a plate comprising three zones only. The feed radiation pattern is modeled by the following function

$$G_{fi}(\psi) = \frac{A}{p_i} |\cos^m(\psi - \psi_{ci})| \tag{5.28}$$

where A is calculated by the condition $\int_0^\pi G_{fi}(\psi) \sin \psi d\psi = 2$, and $p_i = A_1/A_i$ is a ratio between the field maximum A_1 in the first (central) open zone and the field maximum A_i in the i -th open zone.

The numerical analysis of a three-zone amplitude-corrected zone plate was completed for a frequency of 11.1 GHz and focal distance of 0.5m. The diameter of the third Fresnel zone, which is also an equivalent diameter of the zone plate is found to be 0.41m. The feed gain pattern calculated by (5.28), for $p_i = 3.1$ and EIL = -10 dB, is drawn by a solid line in Figure 5.14(a). Also in Figure 5.14(a), the feed gain pattern calculated by (3.99) is plotted (dashed line) for an EIL = -10 dB. Figure 5.14(b) shows the copolar and cross-polar gain patterns for the two feed illumination functions. Again a solid line is used for the amplitude-corrected zone plate antenna and a dashed line for the antenna with an ordinary feed pattern. The comparison between the radiation characteristics of the two antenna versions shows that the amplitude correction technique leads to a gain increase of 2 dB. On the other hand, the maximum cross-polar level is worsened by 4 dB.

Next we examine the frequency bandwidth of the Soret zone plate antenna designed at 30 GHz for an edge illumination level of -11 dB and a focal length of 26.4 cm. Figure 5.15 plots the (a) computed gain and (b) efficiency as functions of frequency for SZP antennas of different zone number N (open

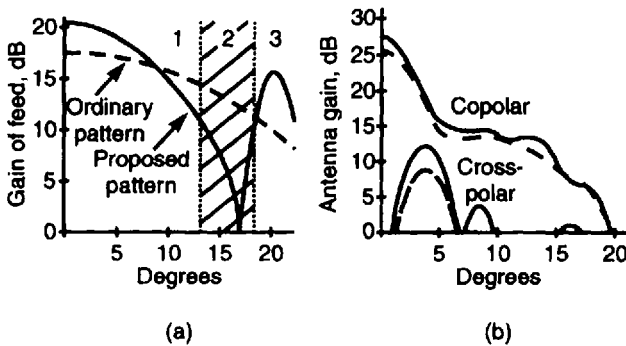


Figure 5.14 Gain patterns for usual (dash line) and amplitude-corrected (solid line) three zone plate antenna: (a) feed gain patterns and (b) antenna gain patterns. (After: [49].)

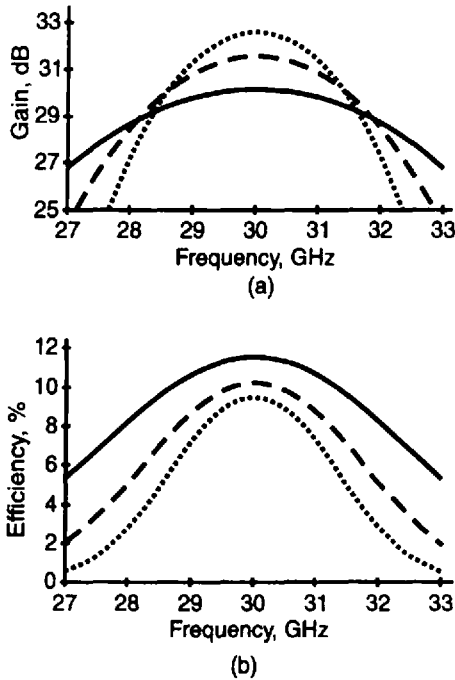


Figure 5.15 (a) Gain and (b) efficiency versus frequency of Soret zone plate antenna for $N = 8$ (solid line), $N = 12$ (dashed line), and $N = 16$ (dotted line).

and blocked): $N = 8$ (solid line), $N = 12$ (dashed line), and $N = 16$ (dotted line). The antenna size and parameters are given in more detail in Table 5.2.

From Figure 5.15 and Table 5.2 we may conclude that for a constant focal length and EIL the increase in the zone number (or aperture diameter) leads to a growth in antenna gain and to a reduction of its aperture efficiency and bandwidth.

Because the zone plate is acting as a diffraction array of discrete elements (the zone rings) with almost the same areas, its interference radiation pattern

Table 5.2
Antenna Diameter and Radiation Parameters

Soret Zone Plate Antenna With:	Aperture Diameter (cm)	Directive Gain (dB)	Aperture Efficiency (%)	3-dB Gain Bandwidth (%)
8 zones	30	30.1	11.5	19.5
12 zones	37.5	31.5	10.2	13.3
16 zones	44.6	32.6	9.5	10.7

has a periodical spectral behavior. This phenomenon is illustrated in Figure 5.16 for a Soret zone plate antenna designed for a frequency of $f_0 = 30$ GHz, a focal length of $F = 264$ mm, an aperture diameter of $D = 301.5$ mm, and $EIL = -10$ dB. In Figure 5.16 the curves correspond to the gain (solid line) and aperture efficiency (dashed line) plotted as functions of the frequency.

Figure 5.16 confirms the expected frequency periodicity in the gain and efficiency curves. Equal gain and much different efficiency maxima occur at frequencies 30, 90, or 150 GHz, or the Soret zone plate antenna behaves as a multiple or frequency-selective antenna with a multiple frequency ratio 1:3:9, The latter is equal to the multiple focal-length ratio characterizing focusing action of the SZP along its axis (see for comparison Figure 4.16). The antenna aperture efficiency is 11.5% at the design frequency of 30 GHz

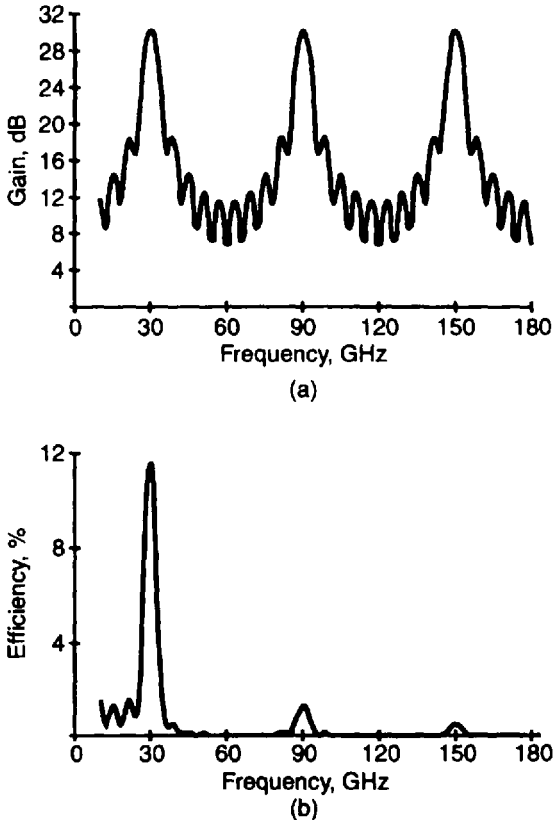


Figure 5.16 Gain and aperture efficiency of Soret zone plate antenna plotted versus frequency ($f_0 = 30$ GHz, $F = 264$ mm, $D = 301.5$ mm, $EIL = -10$ dB).

(a typical efficiency value for Soret zone plate antenna), only 1.28% at 90 GHz, and 0.46% at 150 GHz.

Zhang and others (see [50] and Selected Bibliography) proposed varieties of the classical Soret zone plate—a double-layer and multiple-layer one, which have much better focusing efficiency. The double-layer zone plate was analyzed as a receiving antenna using the spectral domain technique (SDT) based on the vector Hankel transform.

At the primary focus a gain growth of $2 \div 2.5$ dB over the gain of the single-layer zone plate was found in a 30% frequency bandwidth, for a distance between the two layers of about $(2m + 1)\lambda/4$, $m = 0, 1, 2$. However, the double-layer configuration has a relatively high back-lobe level (BLL) of -7 dB compared to the main lobe maximum. These numerical results were verified experimentally.

A four-layer zone plate was also developed and studied by means of the same SDT. As a result of a layer positioning optimization, the four-layer zone plate was designed with a gain increase of 3.1 dB over the single-layer zone plate. Besides, the BLL was decreased to -14 dB.

5.2.1.4 Some Experimental Designs and Measurements

Experimental verification of the radiation characteristics calculated on the basis of the Kirchhoff diffraction integral was reported by Hull in 1949 [51], Sanyal and Singh in 1968 [52].

Van Buskirk and Hendrix from the Michelson Laboratory, U.S. Naval Ordnance Test Station were among the pioneers who studied the Soret zone plate as a radio-frequency lens [9]. Using the Huygens' principle they derived simple gain equations for the zone plate with odd or even zones open. They pointed out that any metallic zone plate had a primary foci for transmission and for reflection. The latter corresponds to the first virtual focus in the optical zone plate.

On the basis of this zone plate effect they suggested two practical radio-frequency antenna constructions of doubled aperture efficiency:

- A zone plate antenna with two feeds, the first put at the focus for transmission and the second at the focus for reflection;
- A zone plate with a ground plane or so-called folded zone plate [9, 10].

The authors designed and studied an experimentally usual X-band zone plate with one, two, and three open Fresnel zones. Two types of feeds, a half-wave dipole and a turnstile, were used.

Figure 5.17 plots the measured 0-degree + 360-degree radiation pattern of the zone plate of 16.6 wavelengths in diameter and three zones open. The pattern consists of a forward (0-degree – 180-degree) or transmission and of a backward (180-degree – 360-degree) or reflection fragments with almost equal maxima [9].

The 3-dB width of each beam is about 4 degrees, which is nearly identical to that of a reflector parabolic antenna of the same diameter. However, the gain of the zone plate is 15 + 20 dB down. The authors stress that where a narrow beamwidth is required and the overall gain can be increased by active amplification, it is feasible to use the zone plate. This would be valid if there is no special signal to noise requirement in the radio wave system because the pattern side lobes of the usual half-open zone plate antenna are too high.

Ye and Zhang [47] give a comparison between the theoretical (solid line) and experimental (dotted line) (a) *E*-plane and (b) *H*-plane radiation patterns of the Soret zone plate antenna shown in Figure 5.18. The calculated curves are obtained through the Kirchhoff integral method. The zone plate is designed at a frequency of 9,375 MHz as a 50 cm × 50 cm square transmissive structure with four full-wave zones, a focal distance $F = 20$ cm, and EIL = -10.5 dB. The antenna feed is an *E*-plane sectoral horn, whose average of *E*- and *H*-plane phase centers coincides with the primary focus.

The comparison between the theoretical and experimental patterns shows that the main lobes coincide very well and that the near sidelobes are close. As the authors state, a bigger difference arises mainly in the more distant sidelobe regions because (1) the Kirchhoff diffraction theory neglects the contribution of the edge diffraction from the zones that become important for the zone width

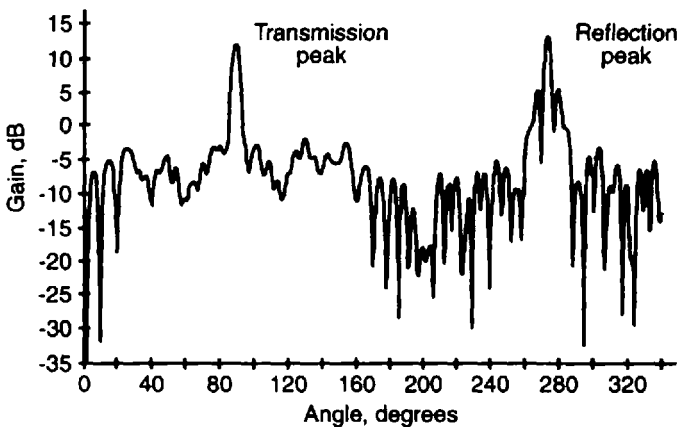


Figure 5.17 Zone-plate patterns showing transmission and reflection maxima. (After: [9].)

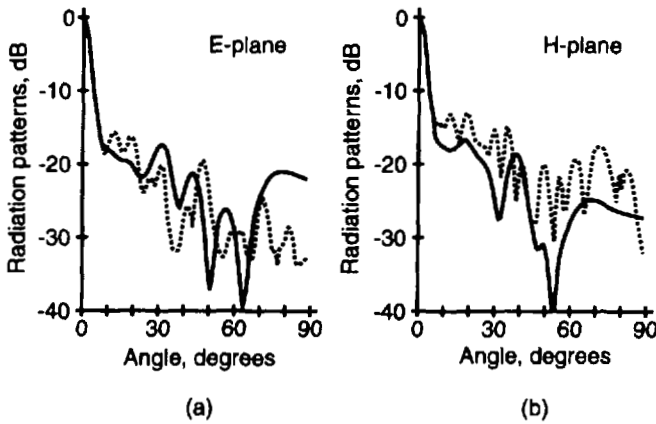


Figure 5.18 Radiation theoretical (solid lines) and experimental patterns (dotted line) of Soret zone plate antenna fed by *E*-plane sectoral horn: (a) *E*-plane patterns and (b) *H*-plane patterns. (After: [47], © 1994 IEEE.)

less than one wavelength, (2) the incomplete zones at the four corners of the square plate are not taken into account in numerical calculations, and (3) measurement errors.

More exact electromagnetic modeling of Soret zone plate antenna by combination of the Kirchhoff diffraction theory, for the main lobe region, and the uniform theory of diffraction (UTD) [53], for the sidelobes, leads to much closer theoretical and experimental results [25, 46, 53–54]. This is well validated in [59] for an *X*-band SZPA with an aperture diameter $D = 1.12\text{m}$ and focal distance $F = 0.71\text{m}$. The antenna is designed at 11.5 GHz and fed by a dual-mode conical Potter horn. In Figure 5.19, the measured *E*-plane field pattern (solid line) is compared with the computed one (dotted line). The latter is based on the UTD supplemented with the Kirchhoff diffraction theory for obtaining the pattern in the main lobe region [55].

In [56] the theoretical gain versus frequency behavior is checked experimentally for the Soret zone plate antenna with an aperture diameter of 1.12m and a focal length of 0.71m. The antenna is designed at a frequency of 11.5 GHz. Figure 5.20 shows the theoretical (solid line) and measured (dots) antenna gain as a function of frequency. It is evident that the experimental gain values are scattered close to the computed graph [56].

For a strong DBS signal even the low effective Soret zone plate antenna can be successfully applied for normal TV and radio program reception. Such lens antennas were designed and manufactured in the late 1980s by the Mawzones Ltd., UK. Mawzones Ltd. proposed a zone-plate matrix, a modular, flush-mounted flat reflector plate, which permits the construction of large, high-gain

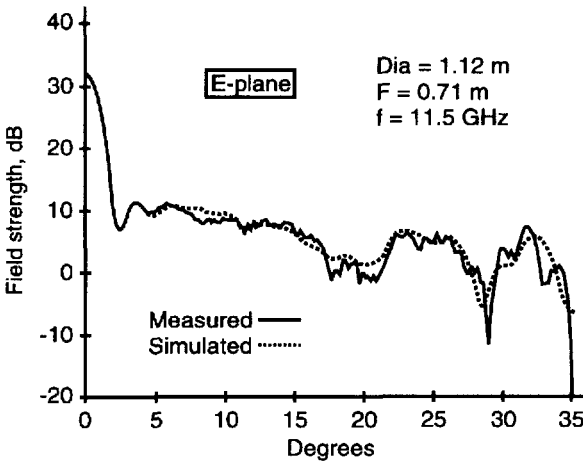


Figure 5.19 Experimental (solid line) and theoretical (dotted line) *E*-plane field pattern of Soret zone plate antenna with a diameter of 1.12m and a focal distance of 0.71m at 11.5 GHz. (After: [55].)

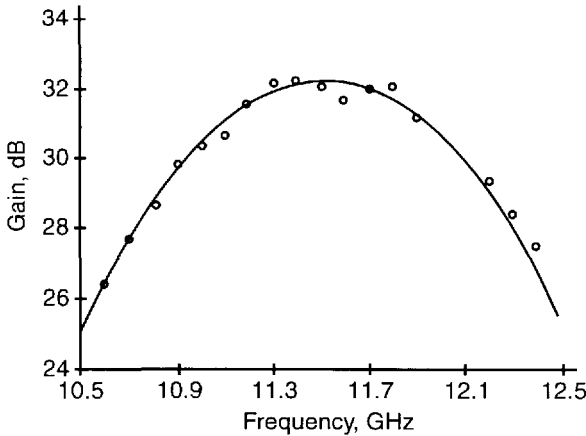


Figure 5.20 Gain of Soret zone plate antenna as function of frequency: theoretical (solid line) and measured (dots). (After: [56].)

microwave antennas on the flat roofs of buildings without raising environmental objections [57]. Very large UHF modular zone plate antennas could be easily transported and erected in remote areas.

A metallic zone plate using a planar lens configuration was constructed for use in the aperture of an *X*-band and *H*-plane sectoral horn [58]. The dimensions of the sectoral horn aperture with the zone plate is $9.13\lambda_o \times 0.852\lambda_o$. Here, λ_o is the free space wavelength at the zone plate



The Mawzones Matrix

Figure 5.21 Mawzones modular matrix for construction of very large zone plate reflectors on flat roofs and remote areas. (After: [57], © Mawzones.)

design frequency. The focal length of the zone plate is $6.84\lambda_0$. Quarter-wave phase correction at a depth of $1.56\lambda_0$ is achieved by placing machined metal steps into the sectoral horn. In production, these steps would be machined from the body of the horn. The step for the 90 degree correction zone is $0.894\lambda_0$ wide and $0.192\lambda_0$ high. For the 180 degree zone, the step is $0.708\lambda_0$ wide and $0.276\lambda_0$ high, and for the 270 degree zone, the step is $0.615\lambda_0$ wide and $0.319\lambda_0$ high. The 0 degree zones do not require correction steps.

The 3 dB gain bandwidth of the zone plate is around 9.5%. The measured reflection coefficient of the horn with the zone plate in place is around -15 dB. The close in sidelobes is about 13 dB down as expected for the uniform illumination of a rectangular aperture. The resulting gain is around 1.2 dB below the gain achieved using a classical dielectric lens in the same sectoral horn. The 3 dB beamwidth ranges from 6 to 7 degrees over the band. This value is about 0.3 degrees wider than the dielectric lens case and is consistent with the measured gain numbers, which are about 0.3 dB below prediction.

5.2.2 Phase-Corrected (Wood-Type) Zone Plate Antennas

5.2.2.1 Double-Dielectric Phase-Reversal Zone Plate Antenna

We will extend here the design considerations for the double-dielectric zone plate [59, 60] discussed in Section 4.3.2.4 and will apply them to a numerical analysis and optimization of the corresponding transmissive zone plate antenna. The Soret zone plate sketched in Figure 5.1 can be modified into a phase-reversal one simply by replacing the metal/absorbing rings by phase-reversing dielectric or dielectric-like rings. As a result, each full-wave zone will consist

of a free-space inner half-wave zone ($\epsilon_{r1} = 1$), and a solid dielectric ring with $\epsilon_r = \epsilon_{r2} = 4$ filling the outer half-wave zone. In this case, the zone plate has a half-wave thickness that is easily checked by (4.74).

Another, more general configuration can be built by using two solid dielectrics of relative permittivities ϵ_{r1} and ϵ_{r2} . Given the two permittivities and the wavelength the zone plate thickness d can be calculated by (4.78) or $d = \lambda/2(\sqrt{\epsilon_{r2}} - \sqrt{\epsilon_{r1}})$. Alternatively, given the one permittivity, say ϵ_{r1} , it is practical to find the optimum plate thickness d and the second permittivity ϵ_{r2} .

For a normal incidence, the dielectric plate with a permittivity ϵ_{r1} becomes fully transparent for

$$d = \frac{k\lambda}{2\sqrt{\epsilon_{r1}}} \quad (5.29)$$

where $k = 1, 2, 3, \dots$ accounts for the number of standing half-waves in the dielectric medium.

From (5.29) it is obtained that $\sqrt{\epsilon_{r1}} = k\lambda/2d$. Placing the latter expression into (4.78) gives

$$d = \frac{(k+1)\lambda}{2\sqrt{\epsilon_{r2}}} \quad (5.30)$$

From (5.29) and (5.30) a relationship between ϵ_{r2} and ϵ_{r1} is easily found [48]

$$\epsilon_{r2} = \epsilon_{r1} \left(\frac{k+1}{k} \right)^2 \quad (5.31)$$

Let us next analyze the aperture field distribution and far-field equations of the phase-reversal zone plate. Suppose again a feed of axially symmetric pattern modeled by (3.99). The incident free-space ray $\rho(\psi)$ associated with the feed spherical wave extends through the phase-correcting dielectric ring as a refraction ray. The focal distance-to-aperture diameter ratio is assumed to be large enough that we can treat the incident spherical wave as a local plane wave. Ray tracing through the Fresnel zone plate comprising solid-dielectric and air-transparent zones is illustrated in Figure 5.22.

The transmission through the dielectric ring for the linear orthogonal polarizations is characterized by the multiple complex transmission coefficients: $T^{\parallel} = |T^{\parallel}| e^{j\phi_i^{\parallel}} \equiv T_M$ (for parallel or magnetic polarization) and

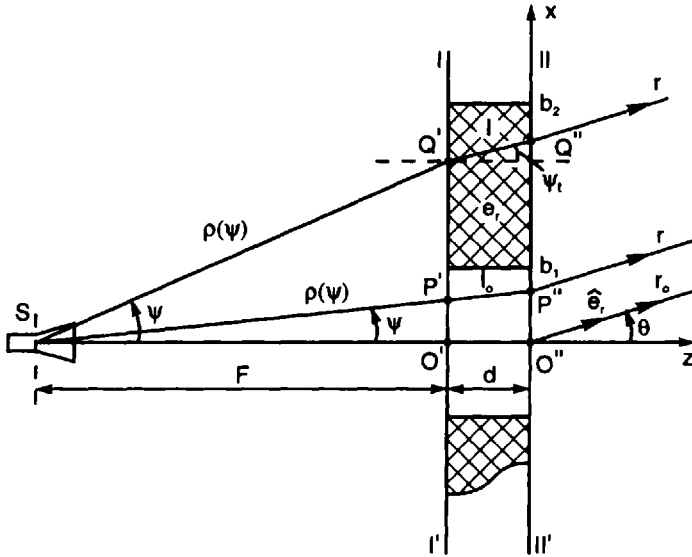


Figure 5.22 Ray tracing through solid-dielectric/air-transparent zone plate. (Source: [65].)

$T^\perp = |T^\perp| e^{j\phi_i^\perp} \equiv T_E$ (for perpendicular or electric polarization). The vectorial field at the input plane $I - I'$ (point Q') is given by (5.5). At point Q' in the output or aperture plane $II - II'$ the refracted ray gives rise to an electric field $E_d(\psi, \xi, m)$, which can be expressed as [25, 61–63]

$$E_d(\psi, \xi, m) = C_f \sqrt{G_f(\psi, m)} \frac{e^{-j\beta(\psi)}}{\rho''(\psi)} (-|T^\parallel| e^{j\phi_i^\parallel} \cos \xi \hat{e}_\psi + |T^\perp| e^{j\phi_i^\perp} \sin \xi \hat{e}_\xi) \tag{5.32}$$

or

$$E_d(\psi, \xi, m) = C_f \sqrt{G_f(\psi, m)} \frac{e^{-j\beta(\psi)}}{\rho''(\psi)} P_d(\psi, \xi) \tag{5.33}$$

where

$$P_d(\psi, \xi) = -|T^\parallel| e^{j\phi_i^\parallel} \cos \xi \hat{e}_\psi + |T^\perp| e^{j\phi_i^\perp} \sin \xi \hat{e}_\xi = -T^\parallel \cos \xi \hat{e}_\psi + T^\perp \sin \xi \hat{e}_\xi \tag{5.34}$$

If the multiple reflection transmission coefficient of a dielectric ring is approximately assumed to be the same as that of the infinite dielectric plate, it is computed according to (1.73), which may be rewritten in the form

$$T^{\parallel,\perp} = \frac{\rho_t \rho_d [1 - (R_1^{\parallel,\perp})^2]}{1 - (R_1^{\parallel,\perp})^2 \rho_d^2 \rho_a} \quad (5.35)$$

where R_1^{\parallel} and R_1^{\perp} are calculated by (1.44) and (1.48), respectively. For a dielectric medium, these equations are easily simplified to become

$$R_1^{\parallel} = \frac{\epsilon_r \cos \psi - \sqrt{\epsilon_r - \sin^2 \psi}}{\epsilon_r \cos \psi + \sqrt{\epsilon_r - \sin^2 \psi}} \quad (5.36)$$

and

$$R_1^{\perp} = \frac{\cos \psi - \sqrt{\epsilon_r - \sin^2 \psi}}{\cos \psi + \sqrt{\epsilon_r - \sin^2 \psi}} \quad (5.37)$$

The phase factors, ρ_a , ρ_d , and ρ_t are given by (1.70), (1.71), and (1.73), correspondingly.

The dielectric phase shifters are designed by (5.35–5.37) for $\psi = \psi_t = 0$ degrees. If in addition, the zone plate thickness is chosen equal to $\lambda/2$, the transmission coefficient formula (5.35) is greatly simplified, or

$$T = T^{\parallel} = T^{\perp} = \frac{e^{-j\pi\sqrt{\epsilon_r}} \left[1 - \left(\frac{1 - \sqrt{\epsilon_r}}{1 + \sqrt{\epsilon_r}} \right)^2 \right]}{1 - \left(\frac{1 - \sqrt{\epsilon_r}}{1 + \sqrt{\epsilon_r}} \right)^2 e^{-j2\pi\sqrt{\epsilon_r}}} \quad (5.38)$$

The phase difference between two adjacent Fresnel zones or subzones is

$$\Delta\Phi_{i,i-1} = \arg T_i(\epsilon_{r,i}) - \arg T_{i-1}(\epsilon_{r,i-1}) \quad (5.39)$$

For a chosen $\epsilon_{r,i}$, the solution of this equation gives $\epsilon_{r,i-1}$. Equation (5.31) is a special case of (5.39).

The amplitude divergence factor $1/\rho''(\psi)$ may be approximated as [66]

$$\frac{1}{\rho''(\psi)} \cong \frac{F + d}{\cos \psi} \quad (5.40)$$

Putting $\rho(\psi)$ and $\rho''(\psi)$ from (5.8) and (5.40), respectively, into (5.32) we find

$$E_d(\psi, \xi, m) = C_f \sqrt{G_f(\psi, m)} \frac{e^{-j\beta F \cos \psi}}{F + d} \cos \psi \mathbf{P}_d(\psi, \xi) \quad (5.41)$$

Equation (5.41) gives the vector field distribution over the dielectric-zone apertures. It accounts for the amplitude, phase, and polarization changes due to the multiple transmission (refraction) process.

Referring to Figure 5.21 and (5.2) a similar expression can be written for the vector field over the air-zone apertures

$$E_d(\psi, \xi, m) = C_f \sqrt{G_f(\psi, m)} \frac{e^{-j\frac{\beta(F+d)}{\cos \psi}}}{F + d} \cos \psi \hat{\mathbf{e}}_f(\psi, \xi) \quad (5.42)$$

For the far-field vector radiated by a dielectric ring aperture (Figure 5.1) we may write an equation similar to (5.9), or

$$\mathbf{E}_d(\varphi, \vartheta) = C \hat{\mathbf{e}}_r(\varphi, \vartheta) \times \iint_{S_a} [\hat{\mathbf{n}} \times \mathbf{P}_d(\psi, \xi)] \cos \psi \frac{\sqrt{G_f(\psi, m)}}{F + d} \dots e^{-j\beta \rho(\psi)} e^{j\beta \hat{\mathbf{e}}_r \cdot \mathbf{r}'} dS' \quad (5.43)$$

The vector product $\hat{\mathbf{n}} \times \mathbf{P}_d(\psi, \xi)$ projected in a rectangular coordinate system can be represented in matrix form as

$$\hat{\mathbf{n}} \times \mathbf{P}_d(\psi, \xi) = \begin{pmatrix} (T^{\parallel} \cos \psi - T^{\perp}) \sin \xi \cos^2 \xi \\ -T^{\parallel} \cos^2 \xi \cos \psi - T^{\perp} \sin^2 \xi \\ 0 \end{pmatrix} \quad (5.44)$$

The unit-vector $\hat{\mathbf{e}}_r(\varphi, \vartheta)$, the vector \mathbf{r}' , the aperture elementary surface dS' and the phase factor $\exp(j\beta \hat{\mathbf{e}}_r \cdot \mathbf{r}')$ are the same as in Section 5.2.1.2.

After setting

$$M_d(\psi) = -jkL(\psi) \quad (5.45)$$

$$N_d(\theta, \psi) = k \sin \theta \left(F \tan \psi + \frac{\epsilon_r d \sin \psi}{\sqrt{\epsilon_r - \sin^2 \psi}} \right) \quad (5.46)$$

$$O_d(\psi, m) = \sqrt{G_f(\psi, m)} \frac{F^2 \tan \psi}{(F + d) \cos \psi} \quad (5.47)$$

and performing ξ -integration in a closed form, the spherical components of the far-field vector $E_d(\varphi, \vartheta)$ due to all dielectric-zone apertures are

$$E_{\vartheta}^{(d)}(\varphi, \vartheta) = -\pi C \cos \varphi \sum_n \int_{\psi_{n-1}}^{\psi_n} e^{M_d(\psi)} O_d(\psi, m) I_{\vartheta}^{(d)}(\vartheta, \psi) d\psi \quad (5.48)$$

$$E_{\varphi}^{(d)}(\varphi, \vartheta) = -\pi C \sin \varphi \cos \vartheta \sum_n \int_{\psi_{n-1}}^{\psi_n} e^{M_d(\psi)} O_d(\psi, m) I_{\varphi}^{(d)}(\vartheta, \psi) d\psi \quad (5.49)$$

where

$$I_{\varphi}^{(d)}(\vartheta, \psi) = -(T^{\parallel} \cos \psi + T^{\perp}) J_0[N_d(\vartheta, \psi)] \\ + (T^{\parallel} \cos \psi - T^{\perp}) J_2[N_d(\vartheta, \psi)] \quad (5.50)$$

and

$$I_{\vartheta}^{(d)}(\vartheta, \psi) = (T^{\parallel} \cos \psi + T^{\perp}) J_0[N_d(\vartheta, \psi)] \\ + (T^{\parallel} \cos \psi - T^{\perp}) J_2[N_d(\vartheta, \psi)] \quad (5.51)$$

The far-field components radiated by the air-transparent apertures are given by (5.17–5.23), with only F replaced by $F + d$.

Finally, the total far-field scalar components $E_{\vartheta}(\varphi, \vartheta)$ and $E_{\varphi}(\varphi, \vartheta)$ are found

$$E'_{\vartheta}(\varphi, \vartheta) = E_{\vartheta}^{(o)}(\varphi, \vartheta) + E_{\vartheta}^{(d)}(\varphi, \vartheta) \quad (5.52)$$

$$E'_{\varphi}(\varphi, \vartheta) = E_{\varphi}^{(o)}(\varphi, \vartheta) + E_{\varphi}^{(d)}(\varphi, \vartheta) \quad (5.53)$$

or in a vectorial form, the far-field intensity can be written as follows

$$\mathbf{E}(\varphi, \vartheta) = \hat{\mathbf{e}}_{\vartheta} E_{\vartheta}(\varphi, \vartheta) + \hat{\mathbf{e}}_{\varphi} E_{\varphi}(\varphi, \vartheta) \quad (5.54)$$

5.2.2.2 Four-Dielectric Quarter-Wave Zone Plate Antenna

Consider a transmissive Fresnel zone plate antenna comprising the phase-corrected quarter-wave zone plate described in Section 4.3.2.4. In Figure 5.23, the geometry of such a four-dielectric zone plate antenna is illustrated [61, 62, 64, 65]. The ϑ - and φ -components of the far field of the quarter-wave zone plate antenna can be calculated also by means of (5.52) and (5.53), respectively. For the case of odd zones open the zone number n runs as follows: $n = 0, 4, 8, \dots$ for the first quarter-wave subzones, $n = 1, 5, 9, \dots$ for the second quarter-wave subzones, $n = 2, 6, 10, \dots$ for the third quarter-wave subzones, and $n = 3, 7, 11, \dots$ for the fourth quarter-wave subzones.

5.2.2.3 Numerical Results for Quarter-Wave and Phase-Reversal Dielectric Zone Plate Antennas

As a first illustration, we shall examine numerically a quarter-wave and phase-reversal zone plate antenna, with an ideal phase shifting element. In this case, the total far field of the quarter-wave zone plate antenna, for example, can be expressed as a sum of the partial fields radiated by all quarter-wave odd subzones, or

$$E = \sum_{n_1} E_n + e^{j\frac{n\pi}{2}} \sum_{n_2} E_n + e^{jn\pi} \sum_{n_3} E_n + e^{j\frac{3n\pi}{2}} \sum_{n_4} E_n \quad (5.55)$$

where E_n is the field created by the n -th quarter-wave subzone, with $n = n_1 = 1, 5, \dots$, $n = n_2 = 2, 6, \dots$, $n = n_3 = 3, 7, \dots$, and $n = n_4 = 4, 8, \dots$.

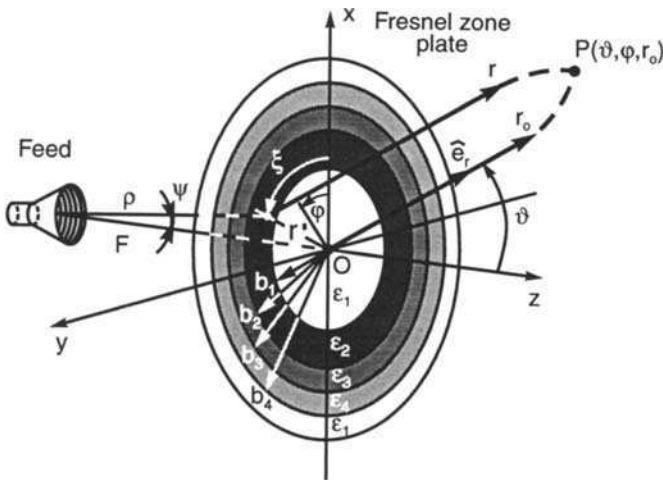


Figure 5.23 Geometry of four-dielectric quarter-wave zone plate antenna.

The real phase-corrected zone plate antennas differ from the ideal ones. The real zone phase shifters do not produce the exact phase-difference ratio $0: \pi/2: \pi: 3\pi/2$, for the quarter-wave antenna, and $0: \pi$, for the phase-reversal antenna.

Figure 5.24 shows the gain radiation patterns of (a) phase-reversal and (b) quarter-wave zone-plate antennas, ideal (dashed line), and real (solid line). The ideal pattern curves were taken from [46], and the real patterns were computed by the author. The computations were based on the far-field Kirchhoff diffraction equations given in Sections 5.2.1.2, 5.2.2.1, and 5.2.2.2 for the following design parameters: $f = 11.1$ GHz, $D \approx 1$ m, EIL = -11 dB, and $F = 0.58$ m and 0.52 m for the phase-reversal and the quarter-wave, respectively.

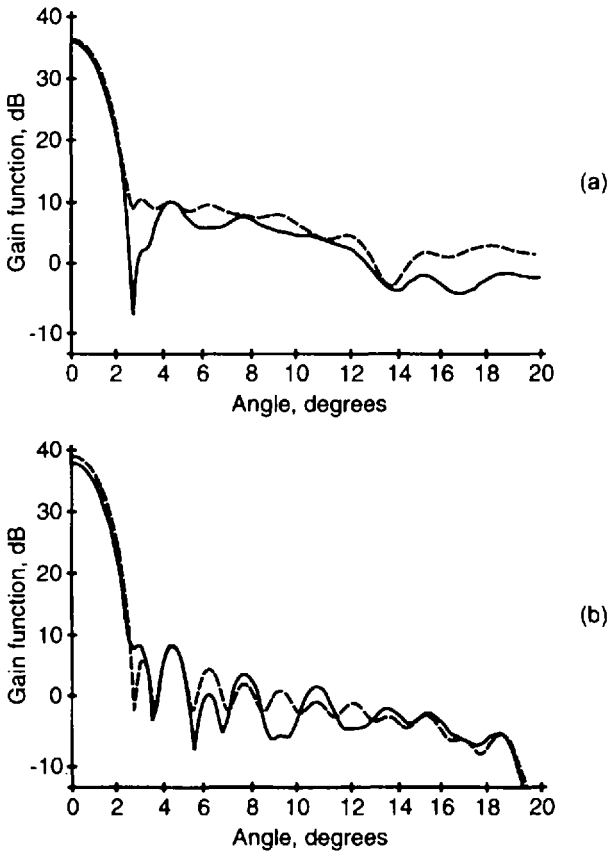


Figure 5.24 Gain patterns of (a) phase-reversal and (b) quarter-wave zone plate antennas, with ideal (dashed line) and real (solid line). Ideal curves are redrawn from [46].

The loss tangent of the real-dielectric zone plate antenna was chosen as 0.001. Table 5.3 gives the values of antenna gain and efficiency, for the ideal and real phase-reversal and quarter-wave zone plate antennas.

As seen in Figure 5.24 and Table 5.3 the parameters of the ideal and real phase-reversal antenna are very close ($\Delta G = G_{ideal} - G_{real} = 0.3$ dB) because the half-wave-in-thickness dielectric rings have a permittivity $\epsilon_r = 4$ and behave as ideal π phase-shifters. Therefore, the difference in gain ΔG is due to the losses only in the real plate.

It is not the same for the quarter-wave antenna, where the phase-rings with $\epsilon_r = 6.25$ and 2.25 have an amplitude-transmission coefficient $|T^{\parallel, \perp}|$ less than 1. This leads to a much bigger gain difference ΔG equal to 0.9.

Next we make a numerical comparison between three antenna models—Soret-type, phase-reversal, and quarter-wave—for design parameters $f_o = 30$ GHz, $F = 150$ mm, $D = 180$ mm, $F/D = 1.2$, EIL = -10 dB, and $N = 10$. If the zone plate thickness is equal to $\lambda/2$, and two of the dielectrics are taken with permittivities equal to 1 (free space) and 4 (ideal phase-reversing plate), the other two permittivities are easily calculated by (5.39). Note that four different sequences of permittivities are possible for the quarter-wave zone plate (antenna models A1, A2, A3, and A4), and two for the phase-reversal zone plate (A5 and A6). The values of the relative permittivities and calculated antenna parameters—directive gain, maximum sidelobe level (SLL), and aperture efficiency—are given in Table 5.4. All dielectrics are taken with a loss tangent equal to 0.001. For comparison, Table 5.4 also adds the same parameters of the Soret zone plate antenna (A7) with odd zones open. Figure 5.25 plots the normalized radiation patterns of the three antenna models, A3, A5, and A7.

From Table 5.3 and Figure 5.25, we may conclude the following:

- There is no substantial difference between the parameters of the four quarter-wave antenna models (A1–A4). The A3 has slightly better gain (32.4 dB) and efficiency (53.3%), while A4 holds a lower sidelobe level (-28.4 dB). A more precise comparison between the four antenna

Table 5.3
Gain and Efficiency of Ideal and Real Fresnel Zone Plate Antennas

Antennas Parameters	Ideal Quarter-Wave	Ideal Phase-Reversal	Real Quarter-Wave	Real Phase-Reversal
Antenna gain (dB)	39.1	36.5	38.2	36.2
Aperture efficiency (%)	60	33.3	44.5	28

Table 5.4
Comparison Between Quarter-Wave, Phase-Reversal, and Soret-Type Antennas

Zone Plate Antenna Models		Gain (dB)	Max. SLL (dB)	Efficiency (%)
Quarter-wave	A1: $\epsilon_r = 1, 6.25, 4, 2.25$ (Lens I in Figure 5.25)	32.2	-26	51
	A2: $\epsilon_r = 6.25, 4, 2.25, 1$	32	-24	48.7
	A3: $\epsilon_r = 4, 2.25, 1, 6.25$	32.4	-27.8	53.3
	A4: $\epsilon_r = 2.25, 1, 6.25, 4$	32.3	-28.4	52.6
Phase-reversal	A5: $\epsilon_r = 1, 4$	30.3	-19.7	33
	A6: $\epsilon_r = 4, 1$	30.2	-19.5	32
Soret-type	A7: odd zones open	26.1	-13.7	12.6

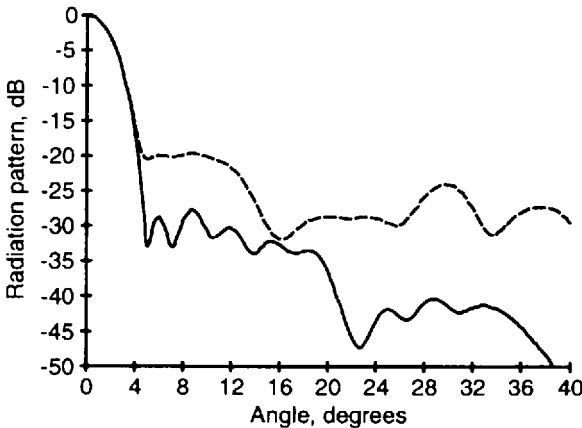


Figure 5.25 Radiation patterns of quarter-wave (A3, solid line), phase-reversal (A5, dashed line), and Soret-type (A3, dotted line) zone plate antennas ($f_0 = 30$ GHz, $F = 150$ mm, $D = 180$ mm, $F/D = 1.2$, EIL = -10 dB, $N = 10$).

configurations requires knowledge about their polarization and feed-matching properties.

- Similar conclusions are valid for the two phase-reversal antenna models (A5 and A6). In comparison with the quarter-wave versions, phase-reversal ones have at least a 2 dB lower gain and a much higher sidelobe level.

The radiation patterns of all antenna models listed in Table 5.4 have almost the same beamwidth of about 3.8 degrees \div 4 degrees.

The half-wave-in-thickness plate-type phase shifters made of dielectrics with relative permittivities of 4 and 2.25 have amplitude-transmission coefficients very near to one, while for a permittivity value of 6.25 the dielectric phase-shifter transmits only about 50% of the normally incident power. This undesirable effect decreases gain of the quarter-wave zone plate antenna and can be removed by replacing all 6.25-permittivity rings with multilayer dielectric structures. A three-layer, B-type sandwich plate according to the radome wall classification (lens II in Figure 5.26), with two skin layers ($\epsilon_{rs} = 2.25$, $d_s = 2.4$ mm) and one core layer ($\epsilon_{rc} = 10$ and $d_c = 7.6$ mm), has an amplitude-transmission coefficient very close to one and a phase-transmission coefficient of nearly 90 degrees at all angles of incidence [64].

The calculations proved that for design parameters $f_o = 30$ GHz, $F = 150$ mm, $D = 180$ mm, $F/D = 1.2$, EIL = -10 dB, and $N = 10$, the aperture efficiency of the quarter-wave antenna with lens II almost reached 60%.

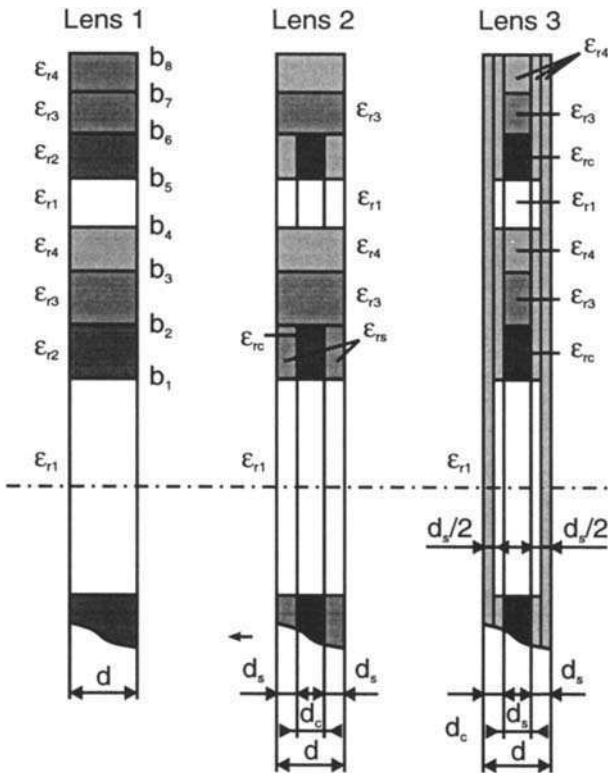


Figure 5.26 Three types of planar dielectric lenses of quarter-wave configuration: lens I (with air and solid rings), lens II (with air, solid, and sandwich-type rings), and lens III (with air and sandwich-type rings). (After: [64], © 1996 IEEE.)

Lens II is a modification of lens I that is used in the antenna model A1. As Table 5.3 shows, the antenna A1 has around a 10% smaller aperture efficiency.

Another, more practical and technological B-type sandwich zone plate is sketched in Figure 5.26 and marked as lens III. The lens is packed by two thin disk-plate skin layers of thickness $d_s/2 = 1.2$ mm and a permittivity of 2.25 each. The lens core rings are equal in thickness ($d_c = 7.6$ mm) but have different permittivities $\epsilon_r = 1, 10, 5.8,$ and 2.25 as shown in lens III. The antenna made of sandwich-type lens III has an efficiency of about 55%. In addition, it has a smaller weight, higher strength, and wider frequency bandwidth compared to the antennas made of lenses I and II.

We also examined numerically another model of phase-reversal antenna that comprises only solid dielectric rings—the double-ring or Wood-Wiltse zone-plate [59]. If we chose a value of 2.25 for the first ring permittivity ϵ_{r1} , the permittivity ϵ_{r2} and the plate thickness d of the second ring is easily calculated from (5.31).

Figure 5.27 plots the theoretical antenna gain as a function of the second permittivity ϵ_{r2} , for $\epsilon_{r1} = 2.25$ and zone number N equal to three (solid line), five (dashed line), and seven (dotted line). The other design parameters are: $f = 11$.GHz, $F = 0.54$ m, and EIL = -10 dB [48].

There are maxima in the gain curves for $k = 1, 2, 3, \dots$. For $k = 1$, $d = 9$ mm, and $\epsilon_{r2} = 9$, which corresponds to the last, broadest gain maxima shown in Figure 5.27. With these optimum zone plate parameters the gain radiation patterns of three- (solid line), five- (dashed line), and seven- (dotted line) phase-reversal zone plate antennas were calculated and plotted in Figure 5.28: (a) feed patterns and (b) antenna patterns. The corresponding aperture diameters of these antennas are 0.42m, 0.54m, and 0.64m.

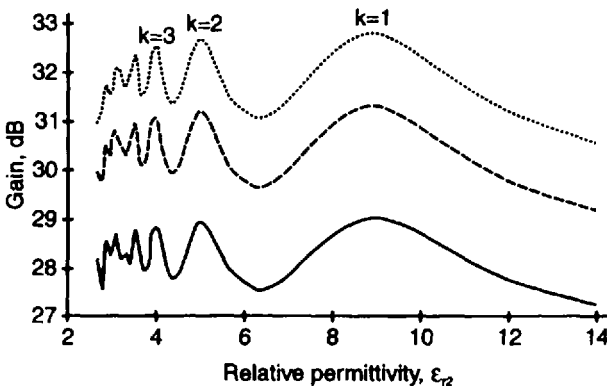


Figure 5.27 Gain as function of second permittivity ϵ_{r2} , for $\epsilon_{r1} = 2.25$ and $N = 3$ (solid line), 5 (dashed line), and 7 (dotted line). (Source: [48].)

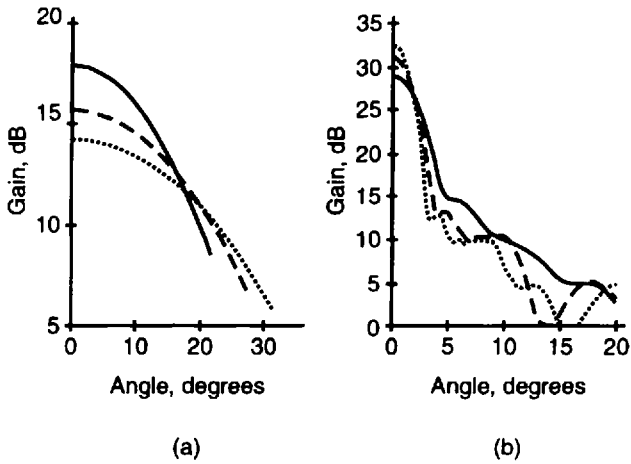


Figure 5.28 (a) Feed gain patterns and (b) antenna gain patterns for three antenna zone plate configurations with three zones (solid line), five zones (dashed line), and seven zones (dotted line). (Source: [48].)

The gain and efficiency periodicity of the phase-reversal and quarter-wave zone plate antennas within a broad frequency band was studied for design parameters $f = 30$ GHz, $F = 264$ mm, $D = 301.5$ mm, and EIL = -10 dB, or the same as for the Soret zone plate antenna described at the end of Section 5.2.1.3. The frequency curves of the (a) gain and (b) efficiency are drawn in Figure 5.29, with solid lines for the phase-reversal antenna and dashed lines for the quarter-wave antenna. Almost equal gain and different efficiency maxima occur at frequencies 30, 90, 150, and so on gigahertz for the phase-reversal zone plate antennas, or the antenna multiple-frequency ratio is again 1:3:9, . . . as in the case of Soret zone plate antennas. The efficiency at 30 GHz is 38.2%, and for 90 GHz only 4.1%.

Quite different is the frequency behavior of the quarter-wave zone plate antenna, where the first group of three gain maxima take place at 30 GHz (37.3 dB), 60 GHz (41.3 dB), and 90 GHz (37.2 dB). This determines a local multiple-frequency ratio 1:2:3. The next group of similar three maxima happen at 150 GHz, 180 GHz (40.1 dB), and 210 GHz, or the next local multiple ratio is 5:6:7. The antenna has an efficiency of about 60% at 30 GHz and of 37.3% at 60 GHz.

5.2.2.4 Some Designs and Applications of Transmission Phase-Corrected Zone Plates and Antennas

In 1958 Brandt and others [66] used two equal-in-size zone plates of 5–6 Fresnel zones each as transmitting and receiving lens antennas A and B for

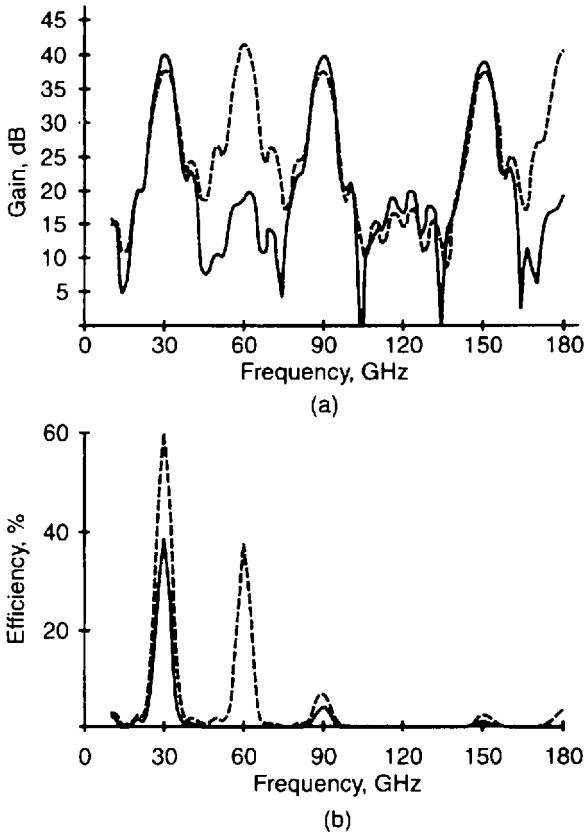


Figure 5.29 (a) Gain and (b) efficiency versus frequency of phase-reversal (solid line) and quarter-wave (dashed line), for $f = 30$ GHz, $F = 264$ mm, $D = 301.5$ mm, and $EIL = -10$ dB.

achieving a plane uniform field in the dielectric measurement system shown in Figure 5.30.

In 1961 Sobel, Wentworth, and Wiltse reported about the feasibility of using millimeter-wave phase-corrected zone plates as antennas in wireless transmission systems and interferometer lenses [1]. Several zone plates were machined from polystyrene sheet stock and successfully tested at frequencies of 140, 210, and 280 GHz. To facilitate the development of millimeter-wave components and to permit measurements of different properties of materials at frequencies from 100 to 300 GHz, a modified version of the Michelson interferometer was constructed (Figure 5.31). The permittivities and loss tangents of a number of plastics have been measured with the interferometer, and a method of frequency filtering by zone plate focal isolation was demonstrated.

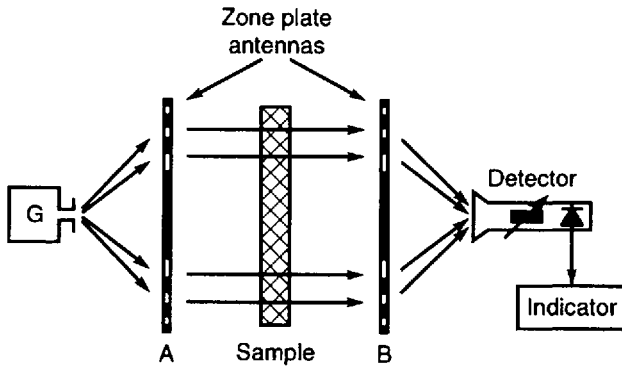


Figure 5.30 System for measurement of complex dielectric permittivity comprising transmitting and receiving zone plate antennas. (After: [66].)

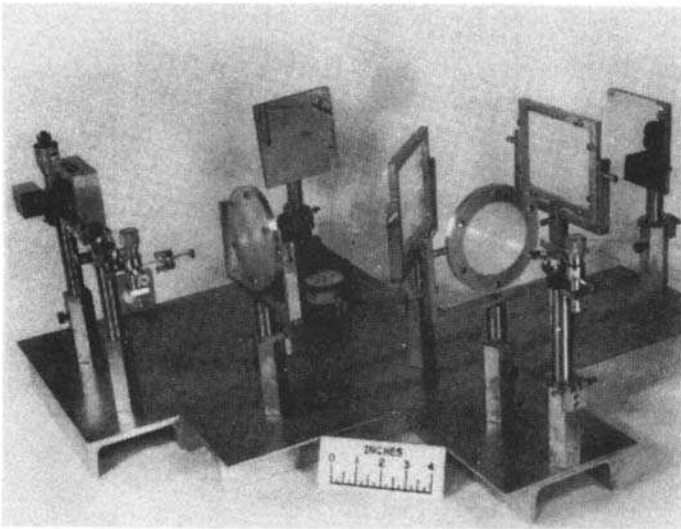


Figure 5.31 Millimeter-wave Michelson interferometer with polystyrene phase-corrected zone plates about 0.5 cm thick and 20 cm in diameter. (Source: [1], © 1961 IEEE.)

A 21-inch (in diameter) single-dielectric quarter-wave zone plate antenna was used in the Norden millimeter-wave radio transceiver, Series 3800 [67]. At 37.8 GHz, the antenna, pictured in Figure 5.32 has the following parameters: gain of 41.5 dB, 3-dB beamwidth of 1.1 degrees, and sidelobes more than 24 dB below peak.



Figure 5.32 Norden millimeter-wave radio transceiver. (Source: [67], © Norden Systems.)

A polyethylene phase-reversal zone plate antenna fed by a rectangular horn integrated in a 33- and 66-GHz low-cost homodyne Doppler radar (Figure 5.33) was designed and studied by Lazarus et al. [2, 3]. The plate lens designed for 33 GHz had the following dimensions: a thickness of 9 mm, a focal length of 180 mm, and an aperture diameter of 300 mm.

A compact single-ring phase-reversal zone plate antenna, termed as a ring-shaped dielectric antenna, was proposed and examined by Hristov, Urumov, and Semov [68]. Figure 5.34(a) is a sketch of a 10-GHz antenna model that consists of a second zone phase-reversing dielectric ring of rectangular cross-section (1), a waveguide-dielectric primary feed (2, 4, 5), and four metal struts (3). With an outer ring diameter of 120 mm, a focal length of 140 mm, and a relative permittivity of 2.6 the antenna has a 3-dB beamwidth of about 11 degrees in the E - and H -planes and a gain of 22 dB. The theoretical (dashed line) and experimental (solid line) E -plane radiation patterns are drawn in Figure 5.34(b). The ring-shaped dielectric antenna has a simple and chip construction with a small wind resistance. It has a radiation pattern with a good axial symmetry and high gain for relatively small dimensions and weight.

5.3 Planar Zone Plate Antennas: Reflection Versions

The reflection versions of the planar zone plate antenna resemble the classical reflector antenna, but they have a planar instead of curved (dish) reflector. We summarize below the state-of-art in the reflection Fresnel zone antennas with

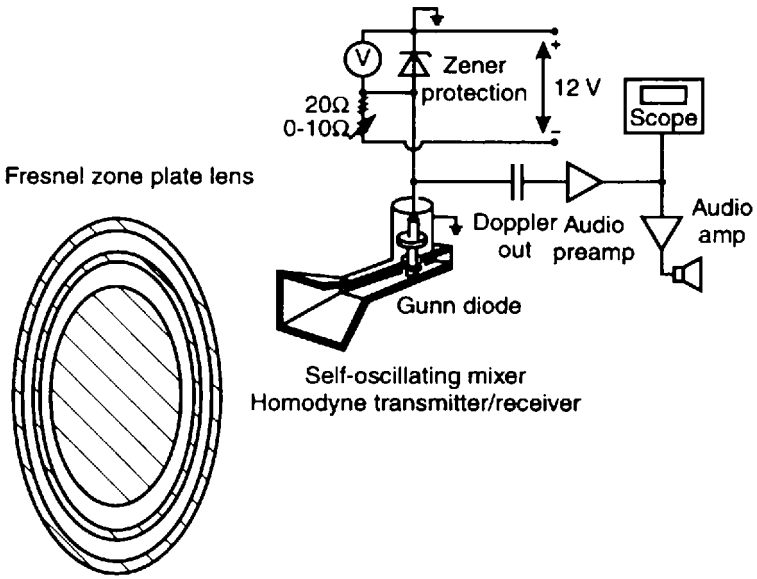


Figure 5.33 Doppler radar schematics and horn-fed phase-reversal dielectric lens. (After: [2], © Hayden Press.)

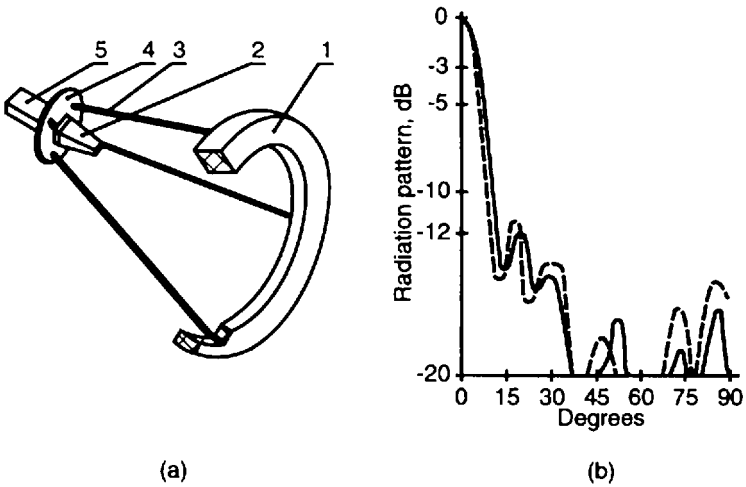


Figure 5.34 (a) Ring-shaped dielectric antenna and (b) *E*-plane radiation patterns, drawn with solid line (experiment) and dashed line (theory). (Source: [68].)

air-grounded (folded) or printed single layer and multilayer zone plate reflectors for microwave and millimeter wavelengths.

5.3.1 Folded Phase-Reversal Zone Plate Antenna

The classical or Soret zone plate with metallic rings is a simple but ineffective lens. As we already emphasized, the zone plate has two principal foci: one for transmission, at point P_2 [Figure 5.35(a)] and one for reflection, at point P_1 [Figure 5.35(b)]. The latter corresponds to the so-called virtual focus, where the backward diffraction rays interfere in phase.

By placing a plane reflector quarter-wavelength behind the metal zone plate the incident plane wave transmitted through the open zones is turned

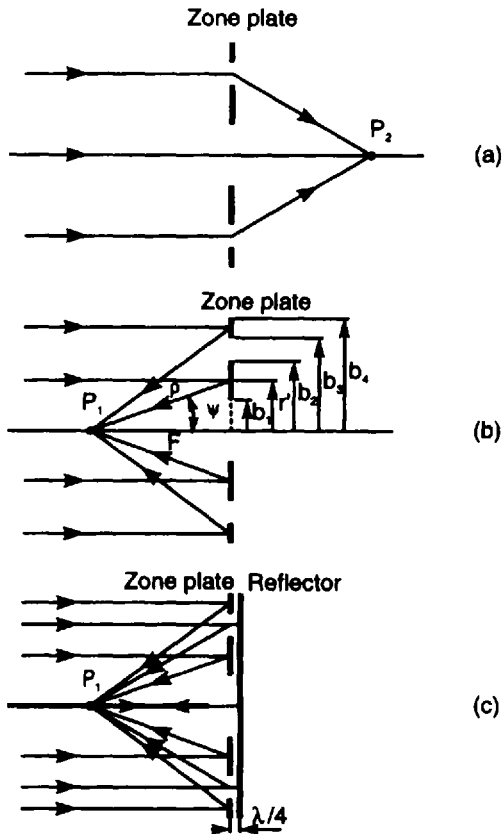


Figure 5.35 Illustrations concerning folded zone plate antenna: (a) focusing by transmission, (b) focusing by reflection, and (c) reflector or folded zone plate antenna. (After: [13], © 1992 IEEE.)

back and interferes constructively at the receiving point P_1 (the focus for reflection) as illustrated in Figure 5.35(c). Essentially, this technique brings two foci in coincidence and leads to a doubling of signal amplitude in the receiving feed antenna. Thus, the reflector-type or folded Soret zone plate construction acts as a phase-reversal zone plate antenna. It was described by Van Buskirk and Hendrix in 1961 [9], and in 1965 was patented by the first of two authors [10].

They experimented a folded X -band metal antenna of three zones open and proposed a possible configuration of a simple and cheap radio telescope based on the folded zone plate system, an artistic view of which is shown in Figure 5.36. It consists of a metal zone plate fixed at a quarter wavelength above the ground plane and a feed antenna that is moved over an arch up to about ± 20 degrees away from the zenith.

A simple scalar expression of the far field of the folded zone plate antenna derived from the Kirchhoff diffraction integral is given in [69, 70]

$$E(\vartheta) = j\frac{\beta}{2} \frac{e^{-j\beta r_o}}{r_o} \sum_{n=1}^N (-1)^n \int_{b_{n-1}}^{b_n} \frac{F}{\rho} \left(\cos \vartheta + \frac{F}{\rho} \right) J_0(\beta r' \sin \vartheta) \frac{e^{-j\beta \rho}}{\rho} r' dr' \quad (5.56)$$

where according to Figure 5.35(b), $\rho = \sqrt{F^2 + r'^2}$ and $F/\rho = F/\sqrt{F^2 + r'^2} = \cos \psi$ is the radiation pattern of a dipole feed; J_0 is the first kind, zero-order Bessel function.

To obtain a vectorial solution $\mathbf{E} = E_\vartheta \hat{\vartheta} + E_\varphi \hat{\varphi}$ for the far field of the folded zone plate antenna we may use (5.17) and (5.18) in a slightly modified form

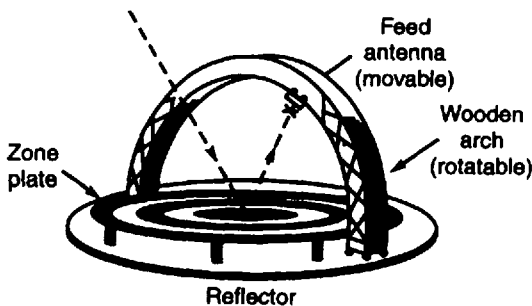


Figure 5.36 Artistic view of fixed radio telescope based on folded zone plate. (After: [9], © 1961 IEEE.)

$$E_{\vartheta}(\varphi, \vartheta) = -\pi C \cos \varphi \sum_{n=1}^N (-1)^n \int_{\psi_{n-1}}^{\psi_n} O(\psi, m) e^{M(\psi)} I_{\vartheta}(\vartheta, \psi) d\psi \quad (5.57)$$

and

$$E_{\varphi}(\varphi, \vartheta) = -\pi C \cos \varphi \sum_{n=1}^N (-1)^n \int_{\psi_{n-1}}^{\psi_n} O(\psi, m) e^{M(\psi)} I_{\varphi}(\vartheta, \psi) d\psi \quad (5.58)$$

with $n = 1, 2, 3, \dots, N$.

Application of the folded Soret zone plate (SZP) to an endfire-type antenna as a reflector or ground-plane was proposed by Yamauchi, Nakano, et al. [69, 71]. More specifically, they investigated the influence of the Soret zone plate structure to a couple of radiating helices: the backfire helical antenna (BHA) and the axial-mode or endfire helical antenna (AHA). The antennas are designed for a frequency of 9.375 GHz ($\lambda = 32$ mm).

Figure 5.37 shows a folded zone plate fed by a monofilar BHA with the following design parameters: pitch angle $\alpha = 26$ degrees, circumference of the helical cylinder $C = 0.833\lambda$, number of turns $N = 6$, and ground plane of diameter $D_1 = 7.9$ mm. The zone plate has a focal length $F = 40$ mm and a diameter $D = 260$ mm, or $F/D = 0.154$.

The radiation pattern of BHA is shown in Figure 5.38 for three cases: (a) with a folded zone plate and (b) and (c) without the zone plate, or with a ground-plane disk only at a distance $z = 40$ mm and $z = 165$ mm from the BHA center, respectively. The values of the gain, 3-dB beamwidth, front to back ratio, VSWR and polarization axial ratio at the design frequency are given

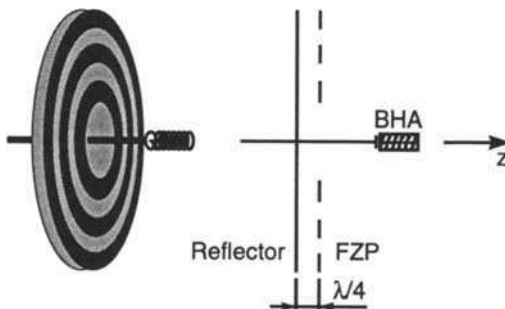


Figure 5.37 Configuration of folded zone plate fed by monofilar BHA. (After: [69].)

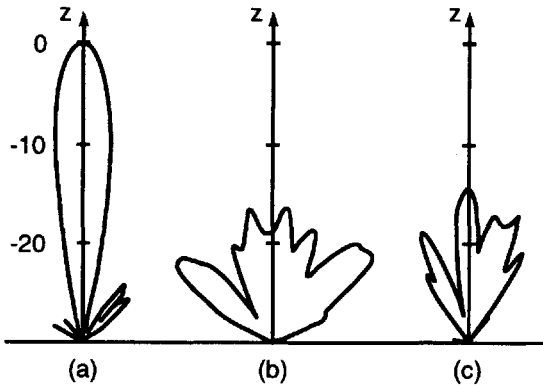


Figure 5.38 Radiation pattern of BHA with folded zone plate: (a) BHA with folded zone plate, (b) BHA with disk-reflector only, or zone plate removed, distance from BHA to disk $z = 40$ mm, and (c) BHA with disk-reflector only, or zone plate removed, $z = 165$ mm. (After: [69].)

in Table 5.5. Since the BHA operates over a wide band of frequencies, the proposed antenna system is broadbanded as well. It has an absolute gain of 21 dB at 9.375 GHz, and a gain greater than 20 dB is measured over a frequency range from 9 GHz to 9.8 GHz. The axial ratio is less than 1.5, and the VSWR is less than 1.6 over the same frequency range.

The second version of helix and folded zone plate combination is illustrated in Figure 5.39(a). The first Fresnel zone is a metal disk that serves as a ground plane of a two-turn AHA. The next odd zones (#3 and #5) are covered by metal rings. A disk reflector of about 175 mm is located at a distance of $\lambda/4$ behind the zone plate by means of a styrofoam spacer with $\epsilon_r \cong 1$, which determines a distance value of about 8 mm. Of course, it can be made thinner if the folded zone plate reflector is manufactured through a microstrip printed technology on a solid substrate as shown in the next section.

Table 5.5
Parameters of Helical Antennas With or Without Folded Fresnel Zone Plate

Parameters/Antennas	Gain (dB)	Beamwidth (degrees)	Front/Back Ratio (dB)	VSWR	Axial Ratio (dB)
AHA with folded FZP	12.2	31	25	1.25	1.5
(disk without FZP)	(8.7)	(69)	(23)	1.2	—
BHA with folded FZP	21	9	28	<1.5	1.3
(disk without FZP)	(6)	—	—	—	—

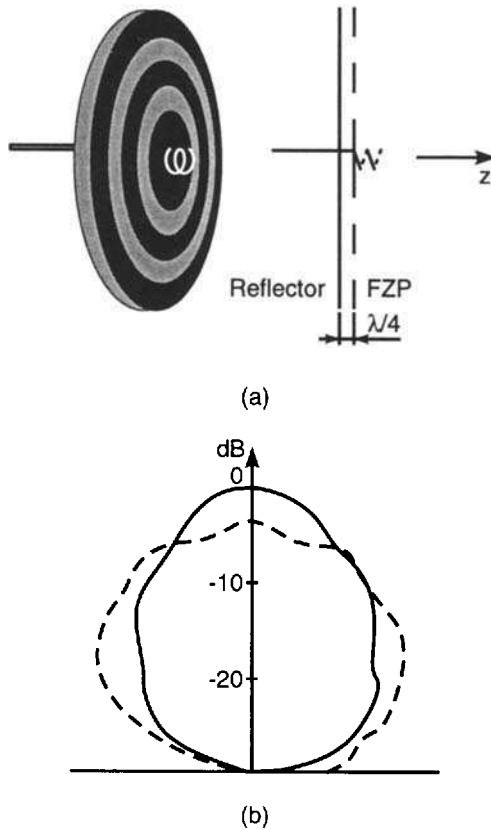


Figure 5.39 (a) Configuration and (b) radiation pattern of two-turn AHA with zoned ground plane solid line is zoned ground plane and dashed line is nonzoned disk ground plane. (After: [69].)

The radiation pattern of the AHA is drawn in Figure 5.39(b) by a solid line for AHA with a zoned ground plane and by a dashed line for AHA with a nonzoned ground plane. It is seen from Figure 5.39 that the zoning increases the gain by 3.5 dB. Other basic parameters are given in Table 5.5. The AHA with a zoned ground plane is also designed for a frequency of 9.375 GHz.

5.3.2 Printed Reflector Zone Plate Antennas

5.3.2.1 Single-Layer Zone Plate Construction

In 1988, Huder and Menzel [4] described a millimeter-wave folded zone plate configuration manufactured with a standard microstrip technology. It seems that this was the first printed reflector zone plate. Figure 5.40 shows a cross-

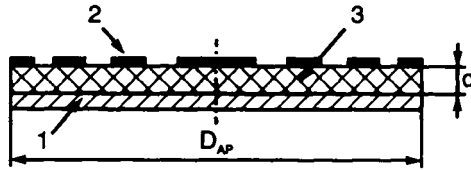


Figure 5.40 Cross-section of single-layer-printed reflector zone plate for millimeter waves. Ground plate is marked by (1), Fresnel zone metal rings by (2), and dielectric substrate by (3). (After: [4].)

sectional view of the reflector zone plate consisting of a ground plane (1) of diameter $D_{ap} = 125$ mm, and a number of etched Fresnel-zone metal rings (2) spaced from the ground plane by the dielectric substrate (3) of thickness $d = \lambda_o/4\sqrt{\epsilon_r}$. For a design frequency of 94 GHz and $\epsilon_r = 2.2$ (RT/Duroid 5850), the substrate thickness is of 0.508 mm. The antenna is fed by an open-ended waveguide WR-10 with an aperture placed at a focal distance of 80 mm. The calculated and measured antenna parameters for an amplitude taper of about -10 dB are listed in Table 5.6. The reflection losses measured at the input of the open ended waveguide feed are -15 dB.

Remarkable research and development results for printed reflector zone plate antennas have been achieved at the University of Bradford by Guo and Barton in collaboration with Wright and others of Flat Antenna Company Ltd. (former Mawzones Ltd.), UK (see, for example, [17, 18, 28, 73–78]).

A novel planar phase correcting technique based on printed reflective phase shifters was introduced in [72, 73]. This technique has been applied for development of a single-layer zone plate incorporating printed resonators in the form of circular rings and several models of reflector zone plate antennas for DBS reception and receive-only VSAT. (Some printed phase-shifting configurations and the equivalent-circuit shifter-design procedure were described in Section 4.3.2.4.)

Table 5.6

Calculated and Measured Parameters of Printed Reflection Zone Plate (After: [4])

Antenna Data	Calculated	Measured
Gain (dB)	41	35
Half-power beamwidth (degrees)	1.5	1.6
Sidelobe level (dB)	-19	<-19
Cross polarization level (dB)	—	<-25

The microstrip resonator-type circuitry printed on a dielectric substrate behaves as a frequency selective surface (FSS) or electromagnetic wave filter. Figure 5.41 illustrates the transmission line model (right above) of the reflective phase shifter, where Z is the intrinsic wave impedance of the free-space (equivalent to an infinite two-wire line) and Z_1 is the wave impedance of the short-ended two-wire line (equivalent circuit of the dielectric substrate) [72]. B is the shunt reactance of the free-standing FSS. If the substrate is without a ground plane, the FSS will act as a transmissive phase shifter, and if it is grounded the FSS becomes a reflective phase shifter. With a fixed operating frequency, any given phase shift can be achieved by adjusting the geometry of resonators or, equivalently, the reactance B . Figure 5.41 also shows the phase shift curves as functions of the normalized reactance B/Z of an exemplary reflective phase shifters, for a substrate permittivity of 2 and three different values of the normalized substrate thickness t/λ_s , where $\lambda_s \equiv \lambda/\sqrt{\epsilon_r}$. The solid, dashed, and dotted lines correspond to $t/\lambda_s = 0.225, 0.25$, and 0.275 , respectively. As it is seen from the graphs, a change of B/Z from -4 to 4 gives a more than 300-degree phase shift.

Two experimental reflective zone plate prototypes, a quarter-wave (marked as QW-1) and a phase-reversal (SR) are designed and tested [72]. Both QW-1 and SR zone plates are made equal to the first full-wave zone. To obtain the needed four phase shift values (0-degree, 90-degree, 180-degree, and 270-degree) in the QW-1 zone plate, the first quarter-wave subzone is left blank, the whole third subzone (with a 180-degree phase shift) is covered by a metal ring, and the second and fourth subzones are overlaid by printed arrays of small ring resonators of different radii. The SR zone plate consists of two-half-wave zones; the first is left blank while the second is blocked by metal ring. The basic zone plate antenna dimensions and parameters are given in Table 5.7. A similar quarter-wave zone plate reflector, marked as QW-2, is

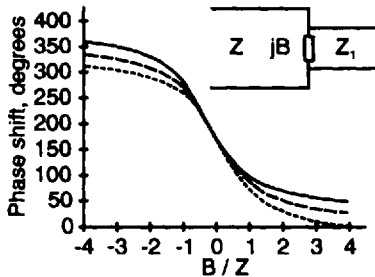


Figure 5.41 Transmission line model of reflective phase shifter (right above) and phase shift variation versus normalized reactance B/Z of free-standing phase-shift structure. (After: [72].)

Table 5.7
Parameters of Reflector Zone Plate Antennas for DBS Reception of TV Signals (After: [20, 23, 29, 72, 73])

Parameters Antennas	Aperture Diameter (mm)	Focal Distance (mm)	Gain (dB)	Aperture Efficiency (%)	Frequency (GHz)	Frequency Bandwidth (%)
Phase-reversal, SR	332	462	~27	~38	10.4	~12
Quarter-wave, QW-1	332	462	29.2	65	10.4	~12
Quarter-wave, QW-3	594	475.2	33.4	43	11.4	>10
Quarter-wave, QW-4	600	400	34.7	~55	11.8	13

reported in [73]. As seen in Figure 5.42, the ring arrangement there is different: The first three subzones are topped by arrays of different sized ring resonators, and the last one is left blank. The two quarter-wave reflectors, QW-1 and QW-2, and the SR reflector are illuminated by a same helical feed antenna, with 3 dB beamwidth of 39 degrees.

Another quarter-wave zone reflector antenna that is about the size of the parabolic dish for DBS application in part of Europe was designed and tested by the same authors [23, 29]. The reflector zone plate, labeled as QW-3, comprises three full-wave zones and one quarter-wave subzone. The reflector antenna utilizing this reflective zone plate is pictured in Figure 5.43, where the printout of the quarter-wave ring-resonator structures is shown.

The QW-3 dielectric substrate has thickness of 5 mm and permittivity of 2.08 (the same substrates employ QW-1, QW-2, and SR zone plate reflectors). The antenna is fed by a conical corrugated horn with a 47-mm aperture diameter. The other main antenna dimensions and radiation parameters are given in Table 5.7. Figure 5.44 draws the measured E -plane radiation pattern of the antenna at 11.2 GHz.

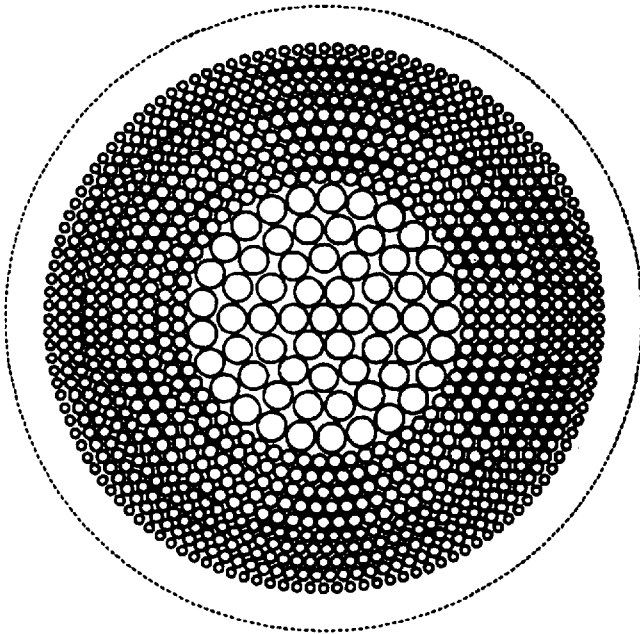


Figure 5.42 Ring arrangement of quarter-wave Fresnel zone plate reflector QW-2.

(Source: [73], © 1993 IEEE.)

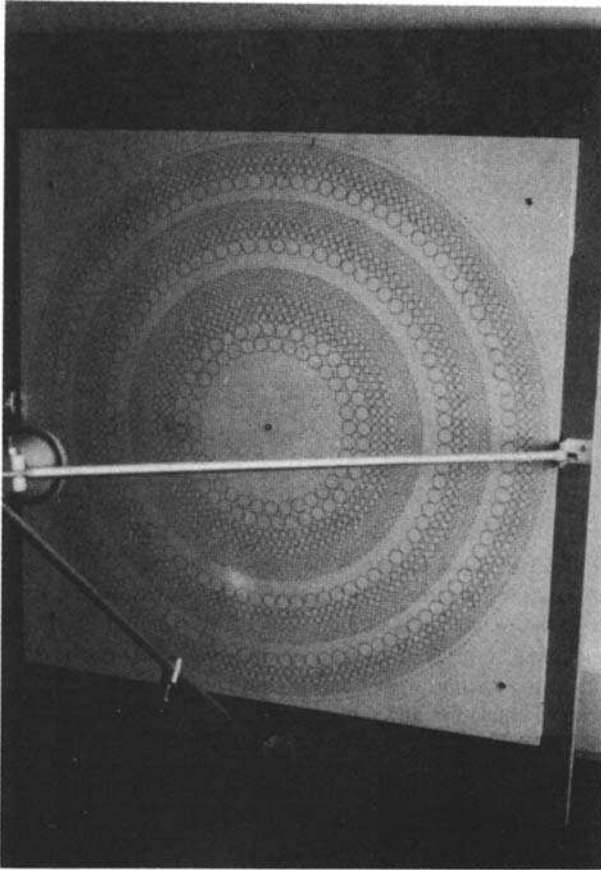


Figure 5.43 Reflector antenna utilizing reflector zone plate QW-3. (Source: [23], © 1995 IEEE.)

5.3.2.2 Multilayer Zone Plate Construction

Beside the quarter-wave reflector consisting of printed single-layer zonal phase-shifters, Guo, Barton, and Wright studied another, very efficient phase-correcting arrangement—the multilayered zone plate reflector [20, 77]. Let us label it for convenience as QW-4. It has a plane ground and three layers of concentric metal rings separated by three dielectric substrates, as seen in Figure 5.45. The rings are located at different interfaces. The substrate thickness is so determined that a normally incident wave experiences $2\pi/Q$ phase delay after transmission and reflection in it, or

$$d = \frac{\lambda}{2M\sqrt{\epsilon_r}} \quad (5.59)$$

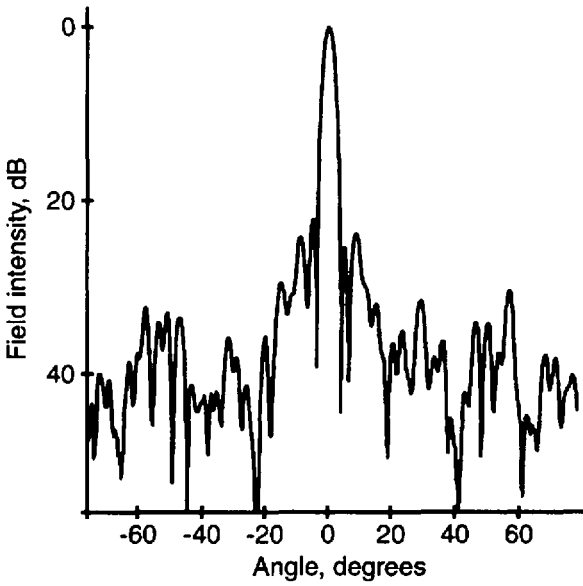


Figure 5.44 Experimental E-plane radiation pattern at 11.2 GHz (a) and gain bandwidth. (After: [23], © 1995 IEEE.)

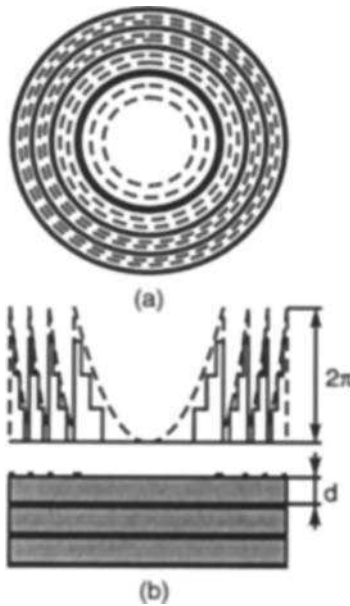


Figure 5.45 Printed three-layer zone plate reflector (QW-4): (a) front view and (b) sectional view and phase correction stepwise function. (After: [77], © 1992 IEEE.)

where Q is the number of subzones in each full-wave zone. For the quarter-wave zone plate $Q = 4$ and $d = \lambda/8\sqrt{\epsilon_r}$, and there are four constant phase shifts in each full-wave zone: 0 , $\pi/2$, π and $3\pi/2$.

The reflector antenna developed on the basis of the printed three-layer zone plate has a polyrod feed with a 43-degree beamwidth, which yields about -11 dB edge illumination level. The measured antenna gain in the DBS frequency band is plotted in Figure 5.46. A maximum gain of 34.75 dB occurs at 11.8 GHz and the 3-dB bandwidth estimated from the gain curve is about 13%. Table 5.7 summarizes the main dimensions and measured radiation parameters of antennas comprising the printed zone plate reflectors SR, QW-1, QW-2 or QW-4.

From Table 5.7, we may conclude the following.

1. The first two antennas, with reflectors SR and QW-1, and $F/D \approx 1.3$ have rather high gain and efficiency. This is typical for all relatively small-in-aperture FZP antennas, where mainly the feed determines the antenna gain.
2. Although having approximately the same apertures the multilayer zone plate antenna (with QW-4) surpasses in gain and efficiency the single-layer one (with QW-3). However, the single-layer antenna is lighter, cheaper, and simpler to manufacture.

5.3.2.3 Integrated-Circuit Antenna for Millimeter Waves Based on Fresnel Zone Plate

A new type of millimeter-wave integrated-circuit (IC) antenna system was proposed and studied in detail by Gouker and Smith [11–13]. It is composed

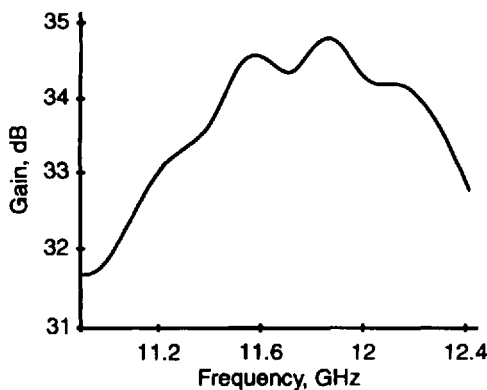


Figure 5.46 Measured antenna gain of versus frequency. (After: [77], © 1992 IEEE.)

of a Soret zone plate on one side of a dielectric substrate with a strip dipole at the focal point of the zone plate on the opposite side of the substrate as shown in Figure 5.47. The energy collected by the resonant dipole antenna at the focus is then detected by a bismuth bolometer at the terminals of the dipole.

All components are made using a simple fabrication technique for ICs: thin-film metal depositions on planar dielectric substrates. Another feature of this design is the small focal length F to aperture diameter D ratio (F/D ranges from 0.1 to 0.5). The antenna models described are designed for a frequency of 230 GHz ($\lambda \cong 1.3$ mm).

The authors developed a theory for predicting the antenna radiation parameters. First, the far field of the dipole, which is assumed infinitesimal, is determined within the substrate. This field is then used to obtain the current on the zone plate rings and reflector. Finally, the fields of the physical optics current is expressed as a plane wave spectrum and transformed through the substrate to the far-field region where it is combined with the field radiated directly by the dipole.

In Figure 5.48, the theoretical (a) E -plane and (b) H -plane gain patterns (solid line) of the IC zone plate antenna are compared with the measured ones (dotted line). There is good agreement on the main beam of the calculated and experimental patterns and on the on-axis gains. The measurements are made for an antenna system with a focal length of 10 mm and a zone plate diameter of 21.4 mm. The average experimental gain is found to be 23.3 dB, the E -plane 3-dB beamwidth to be 4.2 degrees, and the H -plane 3-dB beamwidth to be 3 degrees.

5.4 Off-Axis Scanning in Planar Antenna With Circular Zone Plate

A satisfactory off-axis signal is received (transmitted) for a small angle feed displacing (defocusing) instead of rotating the whole antenna system. In this

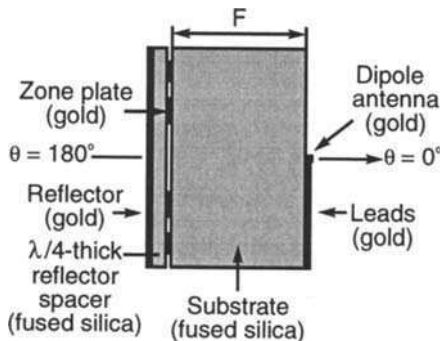


Figure 5.47 Cross-sectional view of IC zone plate antenna. (After: [12], © 1991 IEEE.)

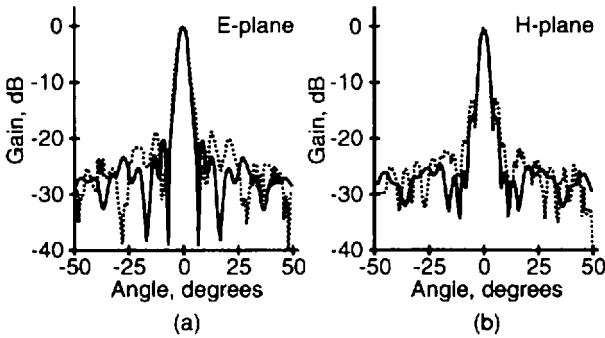


Figure 5.48 *E*-plane (a) and *H*-plane (b) theoretical (solid line) and measured (dashed line) gain radiation patterns. (After: [13], © 1992 IEEE.)

case, it is assumed that the Fresnel zones in the planar zone plate are kept circular. The main beam is approximately scanned at the angle of feed defocusing. First in this section are reviewed the experimental studies of off-axis scanning properties of some transmission and reflection zone plate antennas. The scanning feed trajectory and the far-field gain equation of defocused transmission zone-plate antenna are given. At the end, the off-axis scanning theory is illustrated by means of gain versus scan angle graphs and radiation patterns for different angles of feed defocusing.

5.4.1 Some Experimental Studies

A concise summary of the scanning performance of the Fresnel zone plates was produced by Wilcockson in a report on flat reflectors prepared for the European Space Agency [78]. The focusing aberrations characterizing the Soret zone plate whenever a plane wave is incident along an off-axis direction were studied theoretically by Young, and his results were shortly summarized in Section 4.3.1.3. Scanning properties of the folded zone plate were discussed by Van Buskirk and Hendrix in [9], where they supposed that the scan angles should not exceed ± 20 degrees.

Sanyal and Singh obtained a number of experimental results describing the on- and off-axis intensity variation in an *X*-band zone plate [52]. Measurements of the lateral focal pattern at 140 GHz are described in [6, 41, 79, 80]. They reported signal loss less than 6 dB to scan angles up to ± 20 degrees and concluded that multiple feed configurations were really possible.

The first application of a Fresnel lens antenna for ground-based satellite TV reception was believed to be that of Shuter, et al. from the University of British Columbia [15]. They described a 4-GHz 12 ft \times 12 ft zone plate with a feed horn that is scanned ± 15 degrees off-axis, and after refocusing the

measured signal, loss was not more than 1 dB. The authors concluded that satellites up to ± 10 degrees off antenna axis could be received by the plate with circular zones merely by moving the feed horn. They pointed out also the possibility of receiving signals from two or more satellites simultaneously by means of separate feed horns and low noise converters.

An experimental verification of the scanning and multifocal properties of reflector zone plate antennas was reported by Wright and Wilcockson in [74]. A set of zone plates each 0.95-m square and having offset angles of 0 degrees, 15 degrees, 30 degrees, 45 degrees, and 60 degrees were manufactured, and variations in strength of the received signals from the main European Ku-band satellites were recorded. A multiple feed configuration was investigated for a 1.2-m prime focus unit having a gain of 40 dB and a focal length of 0.84m using signals from Eutelsat satellites at 7 degrees, 10 degrees, 13 degrees, and 16 degrees E. The antenna azimuth and elevation were set correspondingly to the mid-value (11.5 degrees E) and in all cases good pictures were obtained with 1.2 dB LNBs. In conclusion, the authors state that the Ku-band-measured and -computed results predict significantly improved scanning performance compared to a similar in size conventional parabolic reflector.

5.4.2 Scanning Feed Trajectory

A comprehensive theoretical study comparing the scan performance of the Soret zone plate antenna and parabolic reflector antenna was completed by Baggen, Jeronimus, and Herben [27, 46]. The feed is moved over a particular scan surface so that the gain of the antenna is as large as possible. Scanning as illustrated in Figure 5.49 means receiving signals from different satellites by displacing the feed instead of rotating the whole antenna system. For simplicity,

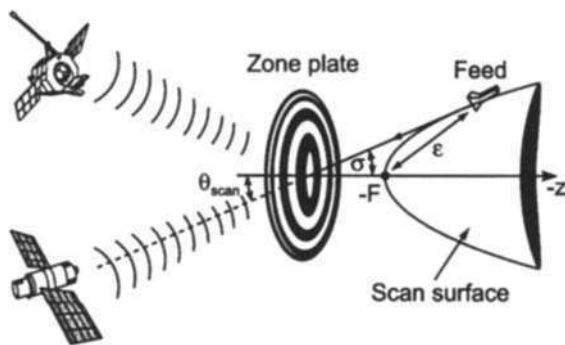


Figure 5.49 Defocused zone plate antenna system used for satellite scan purposes.

(After: [46].)

if the feed is displaced in the xz -plane only the scan surface is transformed to scan curve, as shown in Figure 5.50.

The scan surface of the parabolic reflector antenna is the Petzval curve that is given by the parabolic equation

$$z - F = \frac{x^2}{2F} \tag{5.60}$$

The scan curve of the Soret zone plate antenna is approximated by a circle expressed as

$$x^2 + z^2 = F^2 \tag{5.61}$$

5.4.3 Far-Field Gain Patterns

The scalar far-field gain equation of the Soret zone plate antenna, derived for the xz -plane (or $\varphi = 0$ degrees), is found given in the form [27]

$$G = \frac{m + 1}{2\lambda^2} \left| \sum_n \int_0^{2\pi} \int_{b_{n-1}}^{b_n} g(\varphi', r') e^{j\beta h(\varphi', r')} r' dr' \right|^2 \tag{5.62}$$

where

$$g(\varphi', r') = E'_{feed} [\cos \vartheta + (\hat{n} \cdot \hat{s}')] r' \tag{5.63}$$

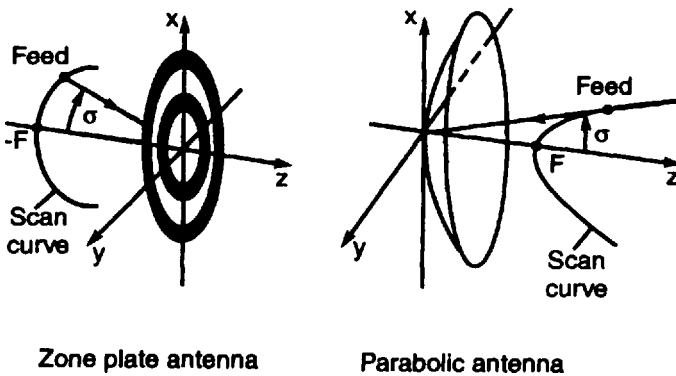


Figure 5.50 Scan curves of Soret zone plate antenna and parabolic reflector antenna. (After: [46].)

with

$$E'_{feed} = \sqrt{\frac{(F - r' \sin \sigma \cos \varphi')^m}{(F'^2 + r'^2 - 2r'F' \sin \sigma \cos \varphi')^{(n/2)+1}}}$$

$$\mathbf{n}' \cdot \hat{\mathbf{S}}' = \frac{F' \cos \sigma}{\sqrt{F'^2 + r'^2 - 2r'F' \sin \sigma \cos \varphi'}}$$

and

$$h(\varphi', r') = N \sqrt{1 - W \cos \varphi' + U \cos \varphi'}$$

$$N = \sqrt{F'^2 + r'^2} \quad (5.64)$$

$$W = \frac{2r'F' \sin \sigma}{N^2}$$

$$U = r' \sin \vartheta$$

Here the summation sequence $n = 1, 3, 5, \dots$ determines the odd open zones, and m is the power integer to the cosine feed function, given by equation $G_f(\psi', m) = 2(m+1) \cos^m \psi'$. Figure 5.51 illustrates the solution for the far-field and directive gain.

5.4.4 Numerical Results

In Figure 5.52, the gain patterns of two 11.1-GHz, 1-m in diameter Soret zone plate, and parabolic reflector antennas are plotted. The upper two curves

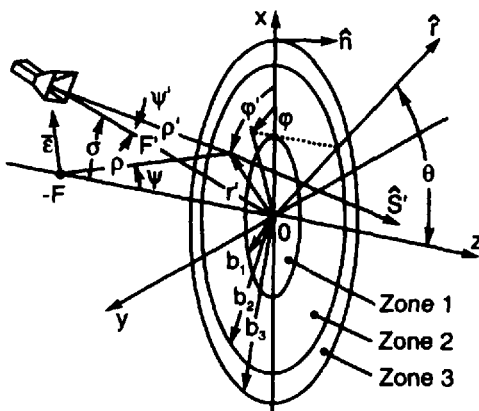


Figure 5.51 Geometry of defocused zone plate antenna. (After: [27].)

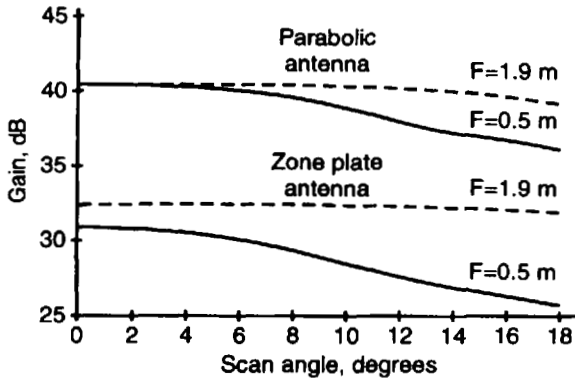


Figure 5.52 Antenna gain as function of scan angle of Soret zone plate antenna and PRA. (After: [27].)

are for the parabolic antenna and the lower curves are for the Soret zone plate antenna. Solid lines correspond to a focal length of about 0.5m, while the dashed line corresponds to a focal length of about 1.9m. From Figure 5.52, it is seen that the scan loss increases in case the focal distance decreases.

Figure 5.53 shows the computed radiation patterns of an on-axis and off-axis focused 1-m in diameter Soret zone plate antenna with $F \cong 1.9\text{m}$ and $f = 11.1\text{ GHz}$. It can be seen that if the satellite spacing is 6 degrees, the isolation due to this antenna between the signals from two adjacent satellites is approximately 15 dB. This rather poor beam isolation can be improved by using a zone plate lens with phase-correcting zones.

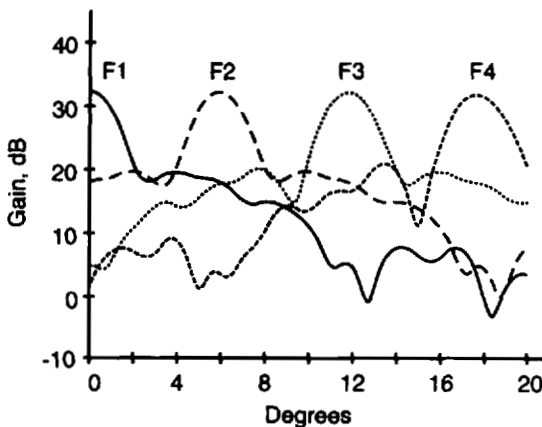


Figure 5.53 Patterns of on-axis focused (F_1) and off-axis focused (F_2 , F_3 , and F_4) Soret zone plate antenna. (After: [27]).

5.5 Planar Offset Antenna With Elliptical Zone Plate

For realizing more efficiency in a larger sector off-axis scanning we need to redesign the zone plate construction. Such a zone plate will comprise a set of elliptical zones and the corresponding antenna is termed here an offset antenna with elliptical zone plate. We begin with the design equations of elliptical zones and then we give the equations for the far field components of transmission zone plate antenna. The section ends with a review of a number of offset antenna zone plate designs for DBS TV signal reception from one or more than one satellite.

5.5.1 Geometry Formulation and Design of Elliptical Zones

As we discussed in Section 3.1.4.1, the wave path is related to a set of confocal ellipsoids of revolution. The intersection curves of these ellipsoids with the antenna plane inclined to the propagation path are ellipses, and the zone plate comprises a set of elliptical zones. Several publications deal with the theory of the offset plate antennas with elliptical zones [25, 75, 76, 81, 82] but here we shall mostly summarize the problem on the basis of a study completed by Van Houten and Herben [25, 81].

Figure 5.54 is a geometry illustrating the far-field solution for such an elliptical zone plate. The antenna aperture is defined in the xy -plane. Its axis lies in the xz -plane, points through the origin O of the coordinate system (xyz) , and is tilted with respect to z -axis. The feed is located at point S at a focal distance F from the origin. A feed-fixed (x', y', z') coordinate system is

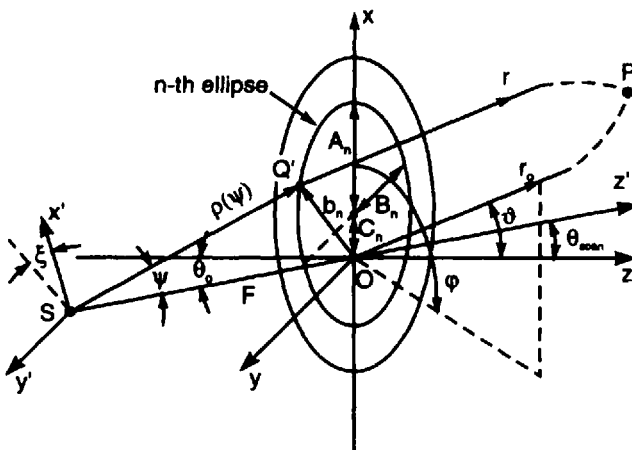


Figure 5.54 Geometry illustrating far-field of solution offset elliptical zone plate.

introduced which appears when the (xyz) system is rotated over the offset angle θ_0 around the x -axis. The accompanying spherical coordinates are ρ , ψ , and ξ .

Two orthogonal polarization patterns of the feed will be considered, namely those of a linearly x' - and y' -polarized Huygens source with unit polarization vectors written as

$$\hat{\mathbf{f}}_{x'} = -\hat{\boldsymbol{\psi}} \cos \xi + \hat{\boldsymbol{\xi}} \sin \xi \quad (5.65)$$

$$\hat{\mathbf{f}}_{y'} = \hat{\boldsymbol{\psi}} \sin \xi + \hat{\boldsymbol{\xi}} \cos \xi \quad (5.66)$$

The gain function of the feed is again assumed to be cosine-shaped.

Let the major semi-axis of the n -th Fresnel elliptical zone be specified by A_n , and the minor semi-axis by B_n , and let C_n be the distance from the center of the ellipse to the origin. The equation of the elliptical zones can be expressed as

$$\left(\frac{x - C_n}{A_n}\right)^2 + \left(\frac{y}{B_n}\right)^2 = 1 \quad (5.67)$$

Given n , λ , F , and θ_0 the dimensions A_n , B_n and C_n can be found by

$$A_n = \frac{\sqrt{n\lambda(F\cos^2\theta_0 + n\lambda/4)}}{\cos^2\theta_0} \quad (5.68)$$

$$B_n = |\cos\theta_0| A_n \quad (5.69)$$

$$C_n = \frac{m\lambda \sin\theta_0}{2\cos^2\theta_0} \quad (5.70)$$

5.5.2 Far-Field Analysis of Offset Elliptic Zone Plate Antenna: Transmission Case

The far field is found by means of the Kirchhoff diffraction integral. In case of x' -polarized feed the ϑ - and φ -components of the field radiated by a single open zone are given by [81]

$$\begin{aligned} \begin{bmatrix} E_{\vartheta, x'}(\vartheta, \varphi) \\ E_{\varphi, x'}(\vartheta, \varphi) \end{bmatrix} &= j \sqrt{\frac{P_t \eta}{2\pi}} \frac{e^{-j\beta r}}{\lambda r} \iint \sqrt{2(m+1)\cos^m\psi} \frac{e^{-j\beta\rho}}{\rho} \\ &\cdots \begin{bmatrix} e^{j\beta\rho' \sin\vartheta \cos(\varphi - \varphi') W_{x1}} \\ e^{j\beta\rho' \sin\vartheta \cos(\varphi - \varphi') W_{x2}} \end{bmatrix} \rho' d\rho' d\varphi' \end{aligned} \quad (5.71)$$

where

$$\begin{aligned}
 W_{x'1} &= (\cos^2 \xi \cos \psi \cos \theta_o - \cos \xi \sin \xi \sin \theta_o + \sin^2 \xi \cos \theta_o) \cos \varphi \\
 &\quad + \sin \xi \cos \xi \sin \varphi (\cos \psi - 1) \\
 W_{x'2} &= -(\sin^2 \xi \cos \theta_o + \cos^2 \xi \cos \xi \cos \theta_o - \sin \xi \cos \xi \sin \theta_o) \sin \varphi \cos \vartheta \\
 &\quad + \sin \xi \cos \xi \cos \varphi \cos \vartheta (\cos \psi - 1)
 \end{aligned}$$

In case of y' -polarized feed similar component equations are obtained

$$\begin{aligned}
 \begin{bmatrix} E_{\vartheta, y'}(\vartheta, \varphi) \\ E_{\varphi, y'}(\vartheta, \varphi) \end{bmatrix} &= j \sqrt{\frac{P_t \eta}{2\pi}} \frac{e^{-j\beta r}}{\lambda r} \iint \sqrt{2(m+1) \cos^m \psi} \frac{e^{-j\beta \rho}}{\rho} \\
 &\quad \cdot \cdot \cdot \begin{bmatrix} e^{j\beta \rho' \sin \vartheta \cos(\varphi - \varphi')} W_{y'1} \\ e^{j\beta \rho' \sin \vartheta \cos(\varphi - \varphi')} W_{y'2} \end{bmatrix} \rho' d\rho' d\varphi' \quad (5.72)
 \end{aligned}$$

where

$$\begin{aligned}
 W_{y'1} &= -(\sin \xi \cos \xi \cos \theta_o (\cos \psi - 1) - \sin \xi \sin \psi \cos \theta_o) \cos \varphi \\
 &\quad - \sin \varphi (\cos \psi \sin^2 \xi + \cos^2 \xi) \\
 W_{y'2} &= ((\cos \psi - 1) \sin \xi \cos \xi \cos \theta_o - \sin \xi \sin \psi \sin \theta_o) \cos \vartheta \sin \varphi \\
 &\quad - \cos \vartheta \cos \varphi (\cos \psi \sin^2 \psi + \cos^2 \psi)
 \end{aligned}$$

A specific, nondirect procedure is used for solving the double integral. Because of the elliptic shape of zone borders the integration limits of ρ' depends on φ' . This means that the ρ' integration has to be carried out from $\rho_{n-1}(\varphi')$ to $\rho_n(\varphi')$, and φ' -integration from 0 to 2π . Finally, the total field at the far-field observation point is easily obtained by summing the contributions from all open zones ($n = 1, 3, 5, \dots$ for odd zones open).

5.5.3 Offset Antenna Designs: Numerical and Experimental Characteristics

The early studies on offset reflector zone plates were aimed mainly toward development and fabrication of antennas for strong signal DBS TV reception comparable in efficiency to the classical parabolic reflector antennas. Years ago the Mawzones specialized in production of cheap and simple Fresnel zone plate antennas giving a very good reception of the strong-signal Astra satellite and some other European satellites transmitting weaker signals. Well-known are

their numerous concepts of such antennas and real constructions for domestic use. For example, a possible application of the Sorer-type plate made of metal (foil) zone rings attached to a window or rolled up when not in use is illustrated in Figure 5.55 [57]. A reflective type of Mawzones' offset zone plate antenna made of a sheet material similar to the corrugated plastics sandwich used for estate agents' placards, with the ring pattern on one side and a metallized backing on the reverse, is shown in Figure 5.56 [57, 73].

Sazonov reported for a simple $1.5\text{m} \times 1.5\text{m}$ offset antenna with a phase-reversing zone plate that was named a reflect-type holographic antenna [83] (Figure 5.57). The antenna receives 12.5-GHz DBS signals with the same quality as a standard 1.2-m parabolic dish.

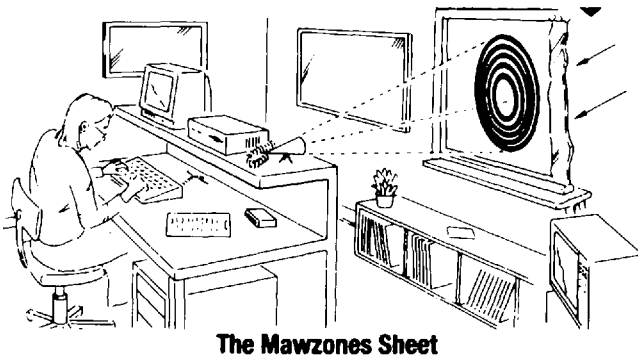


Figure 5.55 Artistic view of attached to window transmissive offset zone plate intended for direct computer satellite link. (Source: [57], © Mawzones.)

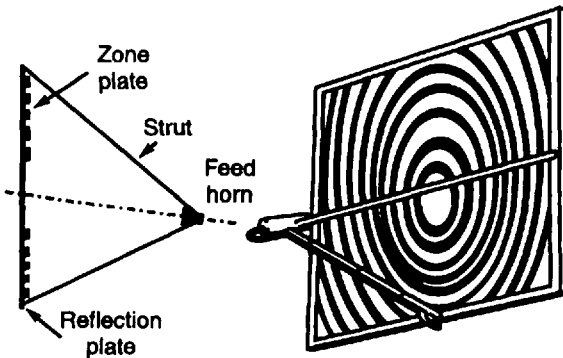


Figure 5.56 Mawzones' reflective offset zone plate antenna. (After: [57], © Mawzones.)

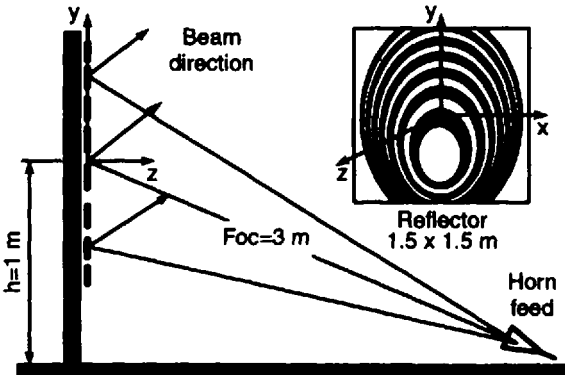


Figure 5.57 Reflective offset zone plate antenna for 12.5 GHz DBS TV reception for outside installation. (Source: [83], © 1999 IEEE.)

Using the far-field theory Houren and Herben [81] investigated numerically an offset elliptical antenna for a satellite TV reception at 11.1 GHz. The antenna focal distance was chosen as 1 m and the maximum (or vertical) antenna size $2A_{max}$ was initially restricted to about 1 m. For offset angles of 10 degrees and 30 degrees, the maximum size $2A_{max}$ and the minimum (or horizontal) size $2B_{max}$ were numerically specified to $2A_{max} = 1.0325\text{m}$ and 1.0357m , and $2B_{max} = 1.017$ and 0.897m , respectively. From the numerical results for linear feed polarization and $\xi = 90$ degrees it is concluded that: (1) for x' -polarization the copolar gain decreases from 31.3 dB to 31.1 dB, and the maximum cross-polar radiation increases from -38 dB to -31 dB for offset angles 10 degrees and 30 degrees, correspondingly; (2) for y' -polarization the cross-polar level is much higher (-2 dB and $+8$ dB for offset angles 10 degrees and 30 degrees, respectively). In case of circular polarization, both the copolar and cross-polar pattern shifts, and the cross-polar pattern lies between the patterns for linear x' - and y' -polarization.

Guo and Burton studied both the transmission and reflection offset zone plate antennas [75, 76]. For reflection mode, the zone plate is taken as a flat phase-correcting mirror, and the main beam is on the same side of the plate with the same angle from the normal. In this case, the authors change the coordinate system so that the z -axis is pointed to the direction of maximum radiation and the origin is at the focal point.

Beside theory, they produced many experiments with offset zone plate antennas. For example, an experimental prototype of offset phase-reversal zone plate reflector with a focal length of 85 cm and an offset angle of 30 degrees, operating at 11.85 GHz, was fabricated [75]. The antenna feed with almost

symmetric E - and H -plane symmetric feed pattern gave about -10 -dB edge illumination level. The reflector plate aperture contained four full-wave zones.

Figure 5.58 shows the experimental and theoretical E -plane radiation patterns of the antenna prototype. As expected, the main beam is tilted at the design angle (30 degrees). There is a good agreement for the main beam and close-in sidelobes.

A very effective X -band four-layer offset construction was designed and measured by Guo, Sassi, and Barton [28]. Figure 5.59 shows the front and sectional view of this antenna. It produces five phase shifts ($Q=5$) in each full-wave zone: 0 degrees, 72 degrees, 144 degrees, 216 degrees, and 288 degrees. The thickness of the substrate layer, d_s is calculated by

$$d = \frac{\lambda \sqrt{1 - \sin^2 \theta_0 / \epsilon_r}}{2Q\sqrt{\epsilon_r}} \quad (5.73)$$

The measured prototype of the four-layer offset reflector antenna was designed to operate at 10.39 GHz. The reflector had a 0.32-m by 0.34-m elliptical aperture, a 20-degree offset angle, and a 0.19-m focal length. The substrate permittivity and loss tangent were $\epsilon_r = 2.1$ and $\tan \delta = 0.0069$. A pyramidal horn with aperture dimension 4.1 cm by 2.8 cm was used as the feed.

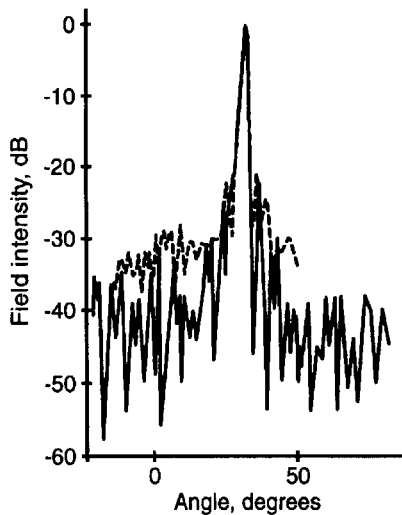


Figure 5.58 E -plane radiation patterns of offset phase-reversal zone plate antenna: theoretical (solid line) and measured (dotted line). (After: [75].)

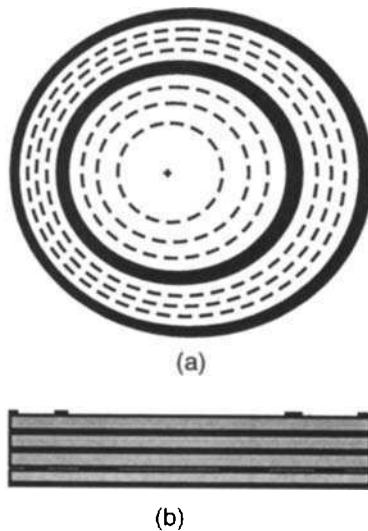


Figure 5.59 Illustration of multilayer offset zone plate reflector: (a) front view and (b) sectional view. (Source: [28], © 1994 IEEE.)

Figure 5.60 shows the measured E -plane (dashed line) and H -plane (solid line) patterns of the antenna at the design frequency. The patterns are very close, with a sidelobe level below -20 dB. The antenna has an efficiency of 61%, which is a very good value for such a complicated design.

A design method for an offset Fresnel zone-plate reflector intended for DBS reception was proposed by Onodera and Hoashi [82]. Figure 5.61(a)

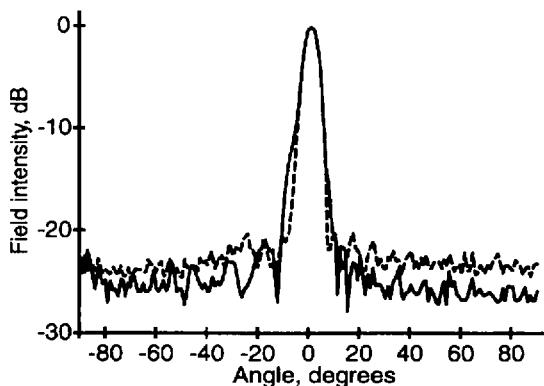


Figure 5.60 E - (dashed line) and H -plane (solid line) patterns of four-layer offset zone-plate reflector antenna at 10.39 GHz. (After: [28], © 1994 IEEE.)

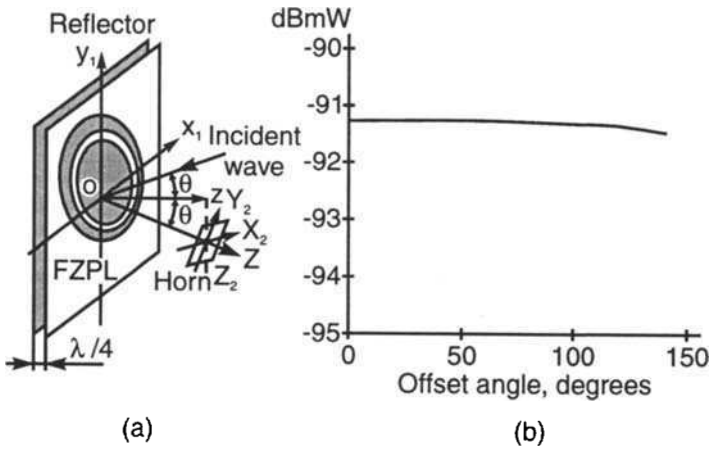


Figure 5.61 Reflector offset antenna: (a) geometry and (b) level of received power calculated as function of offset angle. (Source: [82], © 1999 IEEE.)

illustrates the geometry for the offset antenna model analysis. The coordinates $(x_1, y_1, 0)$ determine any point on the zone plate aperture. By means of Kirchhoff diffraction integral the authors determine the power flux density (PFD) at a point (X_2, Y_2, Z_2) on the feed horn aperture in the form

$$\text{PFD}(X_2, Y_2, Z_2) = \frac{|U_0|^2}{\lambda^2} \left\{ \left[\sum_{i=1}^n (-1)^i A_i \right]^2 + \left[\sum_{i=1}^n (-1)^i B_i \right]^2 \right\} \quad (5.74)$$

where A_i and B_i are real quantities found from the following integrals

$$A_i = \iint_{S_i} \left[\left(\cos \theta + \frac{z_2}{R} \right) \frac{1}{2R} \cos(2\pi r/\lambda) \right] dx_1 dy_1 \quad (5.75)$$

and

$$B_i = \iint_{S_i} \left[\left(\cos \theta + \frac{z_2}{R} \right) \frac{1}{2R} \sin(2\pi r/\lambda) \right] dx_1 dy_1 \quad (5.76)$$

with $R = \sqrt{(x_1 - x_2)^2 + (y_1 - y_2)^2 + z_2^2}$

The phase of the complex field amplitude at the same point is given by

$$\Phi(X_2, Y_2, Z_2) = (180/\pi) \tan^{-1} \left\{ \left[\sum_{i=1}^n (-1)^i A_i \right] \div \left[\sum_{i=1}^n (-1)^i B_i \right] \right\} \quad (5.77)$$

If the phase distribution over the feed horn aperture is taken constant, the power received is given by

$$W'_a(Z_2) = \nu \iint_{S_2} \text{PFD}(X_2, Y_2, Z_2) dX_2 dY_2 \quad (5.78)$$

where ν is the horn aperture efficiency, and S_2 is the aperture area.

Based on the above equations a method for designing and optimization of the phase-reversal offset zone plate antenna was developed. Four Fresnel zone plate reflectors with a 90-degree offset angle (here the authors call 2θ an offset angle) and focal lengths = 0.3m, 0.4m, 0.5m, and 0.6m were built and measured. Aluminum foil was used as reflecting material and an acrylic sheet 4-mm-thick was put as a spacer between the zone plate and reflector. A commercial conical horn of 68 mm in diameter and a frequency converter with a gain of 55.45 dB were used for receiving TV signals at 11.92 GHz.

Figure 5.61(b) shows calculated power level in the feed horn as a function of the offset angle. From Figure 5.61, it is seen that the received power keeps almost constant up to $2\theta = 120$ degrees.

The authors conclude that in comparison with the offset paraboloidal reflector, the offset Fresnel zone plate reflector shows better offset and oblique incidence characteristics. The studied antenna has an aperture efficiency of 24%, which is a typical value for the phase-reversal zone plate antenna.

The proposed design method was used also for building a multibeam offset zone plate antenna with three receivers for receiving simultaneously three DBS satellites. Some calculated and measured data taken from [82] are included in Table 5.8.

5.6 Curved Zone Plate Antennas

The microwave planar zone plate antenna has the advantage of being of flat construction that is cheap, light, and easy to manufacture. With the purpose

Table 5.8

Received Power and Horn Position in Offset Zone Plate Reflector Antenna for Different Focal Lengths

Focal length, m	0.3	0.4	0.5	0.6
Power, dBmW, calculated	-92.6	-91.5	-90.7	-90.0
(measured)	(-94.3)	(-93.5)	(-92.8)	(-92.0)
Position of horn, m, calculated	0.31	0.41	0.51	0.62
(measured)	(0.27)	(0.40)	(0.51)	(0.62)

of maintaining the beauty of the urban environment, a flat antenna that conforms to a building wall can be used instead of a classical parabolic one.

However, to increase the focusing, resolving, and scanning properties and to create differently shaped radiation patterns the Fresnel zone plate and antenna can be assembled on a curved, commonly rotational 3D surface. Moreover, the curved Fresnel zone plate antenna is not limited to a specific surface as in the case of a parabolic antenna and can be made conformal to a curvilinear natural or man-made formation.

The main disadvantage, both of planar and curved zone plate antenna, is that compared to the parabolic reflector antenna, it is frequency-sensitive and has lower radiation efficiency. The microwave/millimeter-wave curved zone plate antenna is still little-known in practice, and it is no a wonder that there is no more than a score or so publications on the subject [5, 21, 24, 30–39, 48, 84–91].

The lens-like properties of the curved zone plates were discussed briefly in Section 4.1.2, and after that were studied in Section 4.4.3.

Here we consider in more detail first X-band elliptical zone plate backed by a parabolic reflector and cylindrical zone plate antenna, and after that we summarize briefly some results of millimeter-wave antennas with curved single-dielectric zone plates.

5.6.1 Paraboloidal Zone Plate Antenna

A new, three-dimensional antenna comprising a rotational parabolic reflector and zone plate of concentric metal rings arranged on a parabolic surface in parallel at a quarter-wavelength above the reflector was proposed and studied by Delmas and others [21, 24, 89], Figure 5.62(a). In principle, this configuration acts as a single-layer phase-reversal zone plate antenna with a calculated aperture efficiency of 27% (measured at about 20%). The three-layered metal zone plate backed by a parabolic reflector [Figure 5.62(b)] has more than twice higher efficiency (56%).

A paraboloidal zone plate was designed to provide two symmetrical diffraction focal points F_1 and F_2 with an angular spacing of about 40 degrees. An antenna prototype was built and used for a simultaneous reception of TV programs from two different geostationary satellites: TDF 1/2 (19.2 degrees O) and Astra (19.2 degrees E), Figure 5.62(c). The basic antenna dimensions and parameters of a 12-GHz single-layer zone plate with a parabolic reflector of 90 cm in diameter are: focal distance of the parabolic surface = 29 cm, lateral focal length of the diffraction foci = 62 cm, number of zones = 10, zone elevation above the reflector = 6.25 mm, gain = 35 dB, 3-dB beamwidth = 2 degrees, sidelobe level = -20 dB, and crosspolar level = -22 dB.

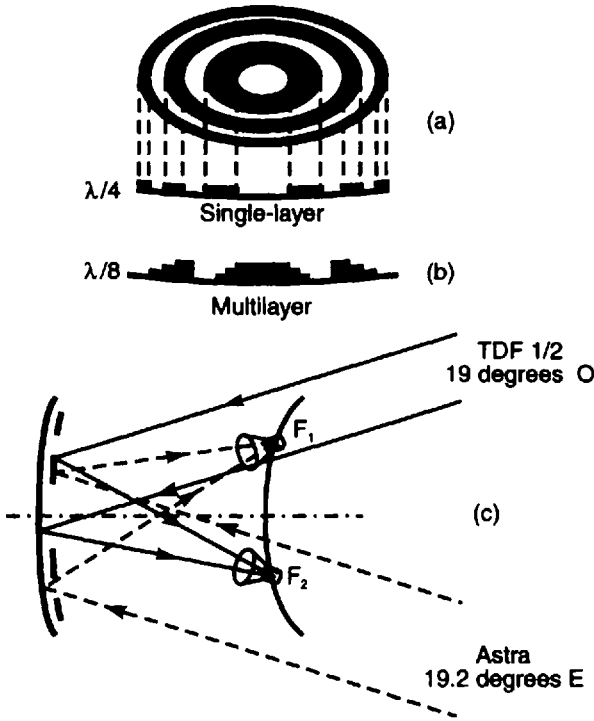


Figure 5.62 Zone plate antenna with parabolic reflector: (a) single-layer configuration, (b) three-layer configuration, and (c) simultaneous reception of TV programs from two different geostationary satellites. (After: [86].)

5.6.2 Cylindrical Zone Plate Antenna

Recently, Ji and Fujita proposed a cylindrical Fresnel zone plate antenna with an omnidirectional radiation pattern [87]. This is a low-efficiency, half-open (or Soret-type) zone plate antenna with a zone lens consisting of alternate open and opaque half-wave Fresnel zones. In the proposed construction the opaque zones are actually made as circular metal rings, and the feed is a strip dipole located at the midpoint O , Figure 5.63(a).

In case of vertical cylindrical zone plate (Figure 5.64), the antenna has a vertical field polarization and omnidirectional horizontal radiation pattern. Thus, it might be quite suitable as a base station and mobile antenna in the wireless communication and broadcasting systems.

The cylindrical zone plate antenna is designed for 9 GHz and is fabricated by bonding eight metal zone rings on cardboard, which is then bent into a cylinder with radius of 40 mm. The vertical (E -plane) pattern is directive as shown in Figure 5.63(a). The sidelobe discrepancy between the measured (solid

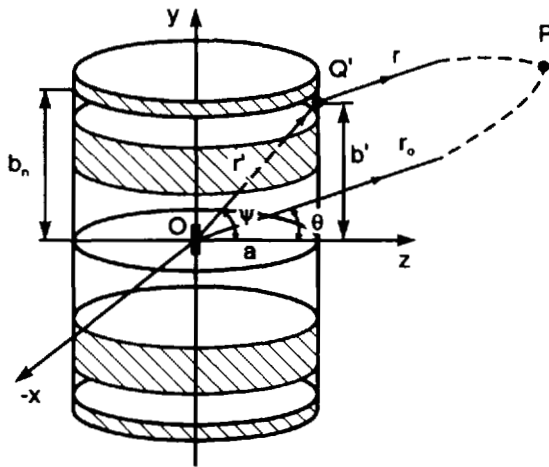


Figure 5.63 Geometry of half-open cylindrical zone plate antenna. (After: [87], © 1996 IEEE.)

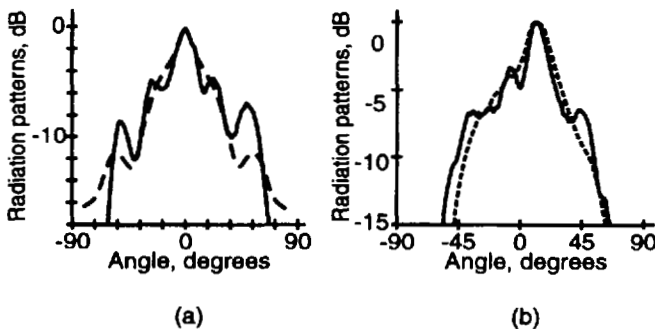


Figure 5.64 Measured (solid line) and calculated (dashed line) vertical radiation pattern of cylindrical zone plate at 9 GHz: (a) feed dipole centered at point O and (b) feed dipole moved axially 20 mm apart from point O . (After: [87], © 1996 IEEE.)

line) and computed (dashed line) radiation patterns the authors explain by the multiple diffraction and reflection from the inner sides of the metal rings. Moving in some extent the dipole axially leads to a main beam scanning in the vertical plane [Figure 5.63(b)].

Based on the above antenna configuration we considered several varieties (symmetrical and nonsymmetrical) of cylindrical zone plate antennas with much enhanced aperture efficiency [48, 91]. As in the planar zone plate this is done by replacing the half-open zone plates with phase correcting ones (half-

wave or quarter wave) and by optimizing the antenna dimensions and radiation feed pattern.

In the phase-reversal zone plate, the metal rings are replaced by dielectric rings with permittivity $\epsilon_r = 4$. In the quarter-wave zone plate each half-wave zone is divided into two subzones and covered by dielectric 90-degree phase rings with equal thicknesses but different permittivities: $\epsilon_{r1} = 1$, $\epsilon_{r2} = 6.25$, $\epsilon_{r3} = 4$, and $\epsilon_{r4} = 2.25$ [Figure 5.65(a)].

The far field of the zone plate antenna with $2N$ ring zones totally (open and opaque) is found following the physical optics approach used in [50]. The Kirchhoff's integral equation for the far field in the xy -plane (Figure 5.63) is rewritten here in a more general form

$$E_{n(\pm)} = \frac{jka}{4\pi r_0} \sqrt{\frac{G_f P_f}{2}} e^{-j\beta r_0} \int_{\pm\psi_n}^{\pm\psi_{n+1}} F(\psi) T(\psi) \left(1 + \frac{\cos\theta}{\cos\psi}\right) \dots e^{j\beta a \left(\frac{1}{\cos\psi} - \tan\psi \sin\theta\right)} \int_{-\pi/2}^{\pi/2} e^{j\beta a \cos\theta \cos\alpha} d\alpha \quad (5.79)$$

where a is the radius of the circular cylinder equal to the lens focal distance F , G_f is the feed directive gain, P_f is the power radiated by the feed, η is the

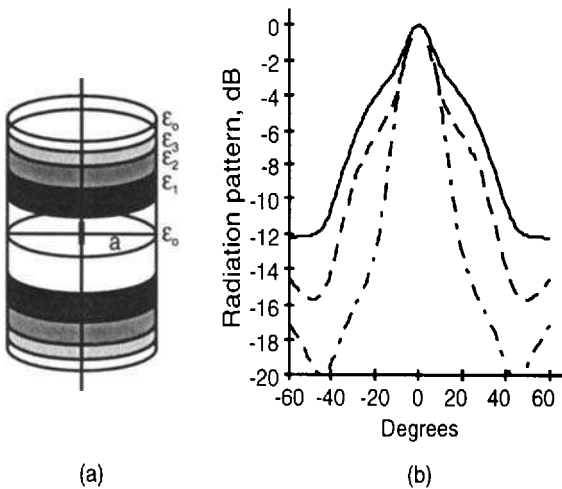


Figure 5.65 (a) Dielectric quarter-wave cylindrical zone plate antenna and (b) radiation pattern for: half-open zone plate (solid line), phase-reversal (dashed line), and quarter-wave (dadot line). (Source: [91], © 1999 IEEE.)

medium intrinsic impedance, $T(\psi)$ is the dielectric ring transmission coefficient, and $F(\psi)$ is the feed radiation pattern. Transmission through a dielectric ring may be calculated approximately using the equations for the dielectric plate multiple reflection/transmission coefficients.

In the symmetrical cylindrical zone plate antenna the ring zones are in number twice that in the planar Fresnel zone plate (N above and N below the xz -plane of symmetry). Thus, the vertical level y_n of the n -th ring circle may be calculated by the formula for the circular zone radii in the planar FZP, or $y_n = \pm(na\lambda + n^2\lambda^2/4)^{1/2}$. The (+) sign is for the upper, and the (-) sign for the lower Fresnel zones. The illumination angle $\pm\psi_n$ that corresponds to the $\pm n$ -th zone is found by the trigonometric relation $\psi_n = \arctg(y_n/a)$.

Thus, the total far field radiated by all open Fresnel zones can be calculated as follows

$$E = \sum_n E_n^+ + \sum_n E_n^- \quad (5.80)$$

We first calculated the radiation pattern and directive gain of the three symmetrical zone plate antennas, half-open (solid line), phase-reversal (dashed line), and quarter-wave (dotted line). The same frequency and antenna dimensions were used as those chosen in [87], and the total number of zones, N , was 4 or 8. The half-wave dipole centered at point 0 was also chosen as a feed. For the half-open zone plate antenna, we obtained results very similar to those displayed in [87].

The calculated vertical patterns of these antenna versions for $N = 8$ are shown in Figure 5.64(b). The directive gain at 9 GHz is given in Table 5.9 for two zone numbers, $N = 4$ and $N = 8$, and three different radii: $a = 4$ cm, 8 cm, and 12 cm. The gain increase for the phase-reversal and quarter-wave antennas was found to be considerable: 1.5 dB and 3.2 dB higher in comparison with the gain of the initial Ji and Fujita's half-open zone plate

Table 5.9
Gain of Various Cylindrical Zone Plate Antennas

	Radius: a (cm)	4	8	12
Gain of cylindrical zone plate antenna, dB	Half-open:	5.1	6.3	6.5
	$N = 4$ (or 8)	(5.3)	(6.7)	(7.0)
	Phase-reversal:	6.4	8.1	8.6
	$N = 4$ (or 8)	(6.8)	(8.8)	(9.7)
	Quarter-wave:	7.7	9.5	10.2
	$N = 4$ (or 8)	(8.5)	(10.5)	(11)

antenna (see the column for $a = 4$ in Table 5.9). The calculations also show a gain rise for the cylindrical zone plates of bigger radii: $a = 8$ cm and $a = 12$ cm. Another way to further increase antenna gain is to replace the half-wave dipole by a feed with a broader radiation pattern.

We proposed another version of the cylindrical zone plate—the nonsymmetrical one [91], shown in Figure 5.66(a). The radiation patterns of three nonsymmetrical antenna varieties fed by $\lambda/4$ -monopole radiator M, half-open (solid line), phase-reversal (dashed line), and quarter-wave (dadot line), are plotted in Figure 5.66(b). For this antenna model, the total far field was computed by summing the far fields of the upper rim zones only. It is seen that the nonsymmetric zone plate has an asymmetric vertical pattern, slightly tilted above the horizon.

5.6.3 Millimeter-Wave Antennas With Curved Single-Dielectric Zone Plate

The most substantial practical progress in antennas with curved dielectric zone plates was made at the Novosibirsk Institute of Applied Physics Problems, Russia, by Minin and Minin [5, 38, 39, 85, 88–90]. They developed and studied experimentally a whole nomenclature of curvilinear Fresnel zone plates and antennas: spherical, parabolic, conical, and so forth.

The authors considered the millimeter-wave zone plate lens as specific case of the so-called quasioptical diffraction elements (QDE). They proposed and studied a lot of attractive practical applications of the millimeter-wave zone plate lenses, as for example, in plasma diagnostics, quasioptical holography

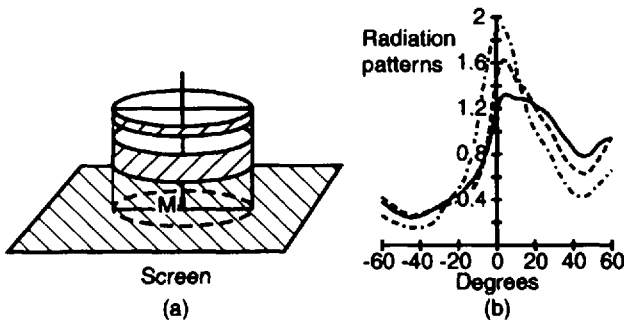


Figure 5.66 Half-open nonsymmetrical zone plate antenna with two metal rings and fed by monopole radiator (a) and radiation pattern (b) for three nonsymmetrical antenna versions: half-open (solid line), phase-reversal (dashed line), and quarter-wave (dadot line). (Source: [91], © 1999 IEEE.)

("radiovision"), shock-wave focusing, measurement instrumentation, and zone plate antennas.

The authors designed and examined experimentally various prototypes of millimeter-wave antennas with curved single-dielectric zone plates in the frequency range 40–95 GHz. Most of them were made as polystyrene shells with phase-reversing or quarter-wave phase grooves machined on their surface.

One of the antenna constructions has a half-wave parabolic zone plate lens with $D/\lambda = 16$ and $D/F = 0.9$, where D is the aperture diameter and F is the lens focal length. The antenna measurement shows a gain $G = 27.5$ dB, and sidelobe levels less than $-18 \div -20$ dB. Off-axis source defocusing of about ± 25 degrees does not diminish the antenna gain more than 2.5 dB.

Another antenna prototype comprises a spherical half-wave zone plate with $D/\lambda = 36$ and $D/F = 1.48$ or 0.98 . The authors claim a measured antenna gain of about 34 dB, and sidelobe levels less than -28 dB in the H -plane and -18 dB in the E -plane.

References

- [1] Sobel, F., F. L. Wentworth, and J. C. Wiltse, "Quasi-optical Surface Waveguide and Other Components for the 100- to 300-Gc Region," *IRE Trans. Microwave Theory Techn.*, Vol. 9, Nov. 1961, pp. 512–518.
- [2] Lazarus, M. J., A. Silvertown, and S. Novak, "Fresnel-Zone Plate Aids Low-Cost Doppler Design," *Microwaves*, Nov. 1979, pp. 78–80.
- [3] Lazarus, M. J., F. R. Pantoja, S. Novak, and M. A. Somekh, "Sensitivity to Direction of Motion of a Self-Oscillating-Mixer Doppler Radar," *IEE Proc.*, Vol. 129, Pt. F, No. 4 Aug. 1982, pp. 233–240.
- [4] Huder, B., and W. Menzel, "Flat Printed Reflector Antenna for MM-Wave Applications," *Electronics Letts*, Vol. 24, Mar. 1988, p. 318.
- [5] Minin, I. V., and O. V. Minin, "Diffraction Lenses on Parabolic Surfaces," *Computer Optics*, No 3. 1988, pp. 21–29.
- [6] Wiltse, J. C., *Millimeter-Wave Fresnel Zone Plate Antennas*, Chapter 11 in *Millimeter and Microwave Engng. for Communications and Radar* (book), Critical Reviews of Optical Science and Technology, J.C. Wiltse, ed., SPIE Vol. CR54, Bellingham, WA, Nov., 1994, pp. 272–293.
- [7] Wiltse, J. C., "History and Evolution of Fresnel Zone Plate Antennas for Microwaves and Millimeter Waves," *IEEE Int. Antennas and Propagat. Symp.*, Special Session "Status and Future of Fresnel Zone Plate Antenna," Orlando, FL, July 11–16, Symp. Digest, vol. 2, 1999, pp. 722–725.
- [8] Clavier, A. G., and R. M. Darbord, "Directional Radio Transmission System," *U.S. Patent 2,043,347*, June 9, 1936.

- [9] Van Buskirk, L. F., and C. E. Hendrix, "The Zone Plate as a Radio Frequency Focusing Element," *IRE Trans. Antennas and Propagat.*, Vol. AP-9, May 1961, pp. 319–320.
- [10] Van Buskirk, L. F., "Zone Plate Radio Transmission System," *U.S. Patent 3,189,907*, June 15, 1965.
- [11] Gouker, M. A., and G. S. Smith, "A Millimeter-Wave Integrated-Circuit Antenna Based on the Fresnel Zone Plate," *IEEE MTT-S Digest*, Boston, MA, June 1991, pp. 157–160.
- [12] Gouker, M. A., and G. S. Smith, "A Millimeter-Wave Integrated-Circuit Antenna Based on the Fresnel Zone Plate," *IEEE MTT-S Int. Symp. Digest*, Boston, Mass., June 1991, pp. 157–160.
- [13] Gouker, M. A., and G. S. Smith, "A Millimeter-Wave Integrated-Circuit Antenna Based on the Fresnel Zone Plate," *IEEE Trans. Microwave Theory and Techn.*, Vol. 40, No. 5, May 1992, pp. 968–977.
- [14] Hristov, H. D., and M. H. A. J. Herben, "Millimeter-Wave Fresnel Zone Plate Lens and Antenna," *IEEE Trans. on Microwave Theory and Techn.*, Vol. 43, Dec. 1995, pp. 2770–2785.
- [15] Shuter, W. L. H., C. P. Li, and A. K. C. Yeung, "A Metal Plate Fresnel Lens for 4 GHz Satellite TV Reception," *Trans. Antennas Propagat.*, Vol. AP-32, No. 3, Mar. 1984, pp. 306–307.
- [16] Griffiths, H. D., A. M. Veron, and K. Milne, "Planar Phase-Shifting Structures for Steerable DBS Antennas," *Int. Conf. Antennas Propagat. (ICAP'89), Conf. Proc.*, Apr. 4–7, 1989, Part 1, pp. 45–49.
- [17] Wright, T. M. B., "Large Reflecting Zone Plates for Satellite Signal Reception," *IEE Colloq Mechanical Aspects of Antenna Design Digest*, Apr., 1989, pp. 12/1–12/4.
- [18] Guo, Y. J., K. Barton, and T. M. B. Wright, "Phase Reversal Reflection Efficiency of Zone Plate Antenna," *IEE Colloq. on Materials and Manufact. Process for Antennas*, London, UK, Digest No. 169, Nov. 29, 1990, pp. 4/1–3.
- [19] Leyten, L., *Fresnel Zone Plate Antenna Versus Parabolic Reflector Antenna*, Report of Special Task for the Inst. for Continuing Education, Supervisor: M. H. A. J. Herben, Eindhoven Univ. Technology, Fac. Electrical Engineering, Apr. 1991 (60 pages).
- [20] Guo, Y. J., S. K. Barton, and T. M. B. Wright, "Design of High-Efficiency Fresnel Zone Plate Antennas," *1991 IEEE Antennas Propagat. Symp.*, London, Ontario, June 1991, pp. 182–185.
- [21] Delmas, J.-J., and A. Sarremejean, "TDF Antenna for Multisatellite Reception Using Fresnel Principle in Three Dimensions," *Proc. Int. Symp Antennas Propagat., (ISAP 92)*, Sapporo, Japan, 1992.
- [22] Guo, Y. J., and S. K. Barton, "On the Subzone Phase Correction of Fresnel Zone Plate Antennas," *Microwave and Opt. Technology Letters*, Vol. 6, No. 15, Dec. 1993, pp. 840–843.
- [23] Guo, Y. J., and S. K. Barton, "Phase Correcting Zonal Reflector Incorporating Rings," *IEEE Trans. Antennas and Propagat.*, Vol. 43, No. 4, Apr., 1995, pp. 350–355.
- [24] Delmas, J.-J., S. Toutain, G. Landrac, and P. Cousin, "TDF Antenna for Multisatellite Reception Using 3D Fresnel Principle and Multilayer Structure," *IEEE Int. Antennas and Propagat. Symp.*, Ann Arbor, MI, June 28–July 2, 1993. Symp. Digest, pp. 1647–1650.

- [25] Van Houten, J. M., "Analysis of Phase Correcting and Elliptical Fresnel Zone Plate Antennas," Report of Graduation Work, Fac. Electr. Engineering, Eindhoven Univ. Technology, 1993, (107 pages).
- [26] Baggen, L. C. J., and M. H. A. J. Herben, "Design Procedure for a Fresnel Zone Plate Antenna," *Int. J. of Infrared and Millimeter Waves*, Vol. 14, No. 6, 1993, pp. 1341–1352.
- [27] Baggen, L. C. J., C. J. Jeronimus, and M. H. A. J. Herben, "The Scan Performance of the Fresnel Zone Plate Antenna: A Comparison with the Parabolic Reflector Antenna," *Microwave and Opt. Techn. Letts.*, Vol. 6, No. 13, 1993, pp. 769–774 (Correction in vol. 14, p. 138).
- [28] Guo, Y. J., I. H. Sassi, and S. K. Barton, "Multilayer Offset Fresnel Zone Plate Reflector," *IEEE Microwave and Guided Wave Letts.*, Vol. 4, June 1994, pp. 196–198.
- [29] Guo, Y. J., and S. K. Barton, "Flat Printed Lens and Reflector Antennas," *IEE Int. Conf. on Antennas and Propagat. (ICAP)*, Conf. Proc., Vol. 1, 1995, pp. 253–256.
- [30] Bruce, E., "Directive Radio System," *U.S. Patent 2,169,553*, Aug. 15, 1939.
- [31] Dey, K. K., and P. Khastgir, "A Study of the Characteristics of a Microwave Spherical Zone Plate Antenna," *Int. J. of Electronics*, Vol. 35, No. 1, 1973, pp. 97–103.
- [32] Dey, K. K., and P. Khastgir, "Comparative Focusing Properties of Spherical and Plane Microwave Zone Plate Antennas," *Int. J. of Electronics*, Vol. 35, No. 4, 1973, pp. 497–506.
- [33] Khastgir, P., J. N. Chakravorty, and K. K. Dey, "Microwave Paraboloidal, Spherical & Plane Zone Plate Antennas: A Comparative Study," *Indian J. of Radio & Space Physics*, Vol. 2, No. 1, 1973, pp. 47–50.
- [34] Dey, K. K., and P. Khastgir, "A Theoretical Study of the Axial Field Amplitude of Microwave Paraboloidal, Spherical and Plane Zone Plate Antennas," *J. Inst. Electronics and Telecom. Engineers, India*, Vol. 19, No. 12, 1973, pp. 697–700.
- [35] Chakravorty, S. C., P. Khastgir, and K. K. Dey, "Microwave Fresnel Zone Plates With Non-Uniform Aperture Excitation," *J. Inst. Electronics and Telecom. Engineers, India*, Vol. 23, No. 3, 1977, pp. 145–147.
- [36] Khastgir, P., and K. N. Bhomwick, "Analysis of the Off-Axis Defocus of Microwave Zone Plate," *Indian J. Pure & Applied Physics*, Vol. 16, Feb. 1978, pp. 96–101.
- [37] Dey, K. K., and P. Khastgir, "Off-Axis Field Amplitude Variation for Plane and Paraboloidal Zone Plate: Comparative Study," *J. Sc. Research, Banaras Hindu University*, Vol. XXVIII(1), 1977–78, Supplement, pp. 15–24.
- [38] Minin, I. V., and O. I. Minin, "Elements of Diffraction Quasioptics and Systems for Millimeter Waves," *Collection of Papers "Radio Systems for Millimeter Waves"*, Harkov, UA, 1991, pp. 102–109 (in Russian).
- [39] Minin, I. V., and O. I. Minin, "Antenna Systems for Based on Elements of Diffraction Quasioptics," *Collection of Papers "Radio Systems for Millimeter Waves"*, Harkov, UA, 1991, pp. 120–127 (in Russian).
- [40] Boivin, A., "On the Theory of Diffraction by Concentric Arrays of Ring-Shaped Apertures," *J. Opt. Soc. Am. (JOSA)*, Vol. 42, No 1, Jan. 1952, pp. 60–64.
- [41] Black, D. N., and J. C. Wiltse, "Millimeter-Wave Characteristics of Phase-Correcting Fresnel Zone Plates," *IEEE Trans. Microwave Theory and Techn.*, Vol. 35, No. 12, Dec. 1987, pp. 1122–1128.

- [42] Leyten, L., and M. H. A. J. Herben, "Vectorial Far-Field of the Fresnel-zone Plate Antenna: A Comparison with the Parabolic Reflector Antenna," *Microwave and Opt. Techn. Letts.*, Vol. 5, No. 2, pp. 49–56, 1992.
- [43] Silver, S., *Microwave Antenna Theory and Design*, London: Peter Peregrinus, 1984.
- [44] Balanis, C. A., *Advanced Engineering Electromagnetics*, New York: John Wiley & Sons, 1989.
- [45] Guo, Y. J., and S. K. Barton, "On the Sidelobe Performance of Fresnel Zone Plate Antennas," *IEEE Int. Antennas Propagat. Symp.*, Chicago, IL, July 1992, Symp. Digest, pp. 2175–2178.
- [46] Baggen, L. C. J., *The Fresnel Zone Plate Antenna: Design and Analysis*, Report of Graduation Work (Supervisor: M. H. A. J. Herben), Eindhoven Univ. Technology, Fac. Electr. Engineering, 1992 (139 pages).
- [47] Ye, Ch. F., and W. X. Zhang, "On the Radiation Characteristics of Fresnel Zone Plate Antenna," *IEEE Int. Antennas and Propagat. Symp.*, Vol. 3, June 1994, Symp. Digest, pp. 2236–2239.
- [48] Hristov, H., G. Kirov, J. Urumov, B. Boyanov, L. Kamburov, and I. Nedelchev, *Miniaturization of Microwave Antennas for Satellite Communications*, Research Report TN-701/97, Nat. Scientific Fund, TU-Varna, 1998, 85 pages (in Bulgarian).
- [49] Kamburov, L. P., J. R. Urumov, and H. D. Hristov, "Fresnel Zone Plate Antenna With Enhanced Aperture Efficiency," *Electrotechnics and Electronics*, Sofia, No. 5–6, 1997, pp. 32–35 (in Bulgarian).
- [50] Jiang, G. Z., W. X. Zhang, and K. Kang, "The Focused Fields of Fresnel Zone Plate Lens," *Int. Symp. Antennas Propagat. (ISAP)*, Chiba, Japan, Conf. Proc., 1996, pp. 57–59.
- [51] Hull, G. F., "Microwave Experiments and Their Optical Analogs," *American J. of Physics*, Vol. 17, 1949, pp. 559–566.
- [52] Sanyal, G. S., and M. Singh, "Fresnel Zone Plate Antenna," *J. Institution Telecom. Engineers, India*, Vol. 14, 1968, pp. 265–281.
- [53] Baggen, L. C. J., and M. H. A. J. Herben, "Calculating the Radiation Pattern of a Fresnel Zone Plate Antenna: A Comparison Between UTD/GTD and PO," *Electromagnetics*, Vol. 15, 1995, pp. 321–345.
- [54] McNamara, D. A., C. W. I. Pistorius, and J. A. G. Malherbe, *Introduction to Uniform Geometrical Theory of Diffraction*, Norwood, MA: Artech House, 1989.
- [55] Sluijter, J. M. H., A. J. Herben, and O. J. G. Vullers, "Experimental Validation of PO/UTD Applied to Fresnel Zone Plate Antennas," *Microwave and Opt. Techn. Letts.*, Vol. 9, No. 2, 1995, pp. 111–113.
- [56] Van Houten, J. M., and M. H. A. J. Herben, "The Bandwidth of Fresnel Zone Plate Antennas," *J. Electromagn. Waves and Applications*, Vol. 11, 1997 pp. 175–183.
- [57] Mawzones Ltd. (U.K.) Leaflet, "Mawzones Zone Plate Antennas: A Revolution in Antenna Design."
- [58] Black, D. N., and C. Nguen, "Metallic Zone Plates for the Sectoral Horns," *IEEE Int. Antennas and Propagat. Symp.*, Orlando, FL, July 11–16, Symp. Digest, Vol. 2, 1999, pp. 730–733.
- [59] Wiltse, J. C., "The Fresnel Zone-Plate Lens," *Proc. SPIE Symp.*, Arlington, VA, Vol. 544, Apr. 9–10, 1985, pp. 41–47.

- [60] Wiltse J. C., "Recent Developments in Fresnel Zone Plate Antennas at Millimeter Wavelengths," *16th Int. Conf. Infrared and Millimeter Waves*, Lausanne, Switzerland, Vol. 1576, Aug. 1991, pp. 497–498.
- [61] Hristov, H. D., and M. H. A. J. Herben, "Millimeter-Wave Fresnel Zone Plate Lens and Antenna," *IEEE Trans. Microwave Theory and Techn.*, Vol. 43, Dec. 1995, pp. 2770–2785.
- [62] Hristov, H. D., *Analysis and Design of Transmissive Fresnel Zone Antennas for DBS Reception*, CEC CIPA 35 10CT926503 Report, Eindhoven Univ. Technology, Fac. Electr. Engineering, Feb. 1994 (72 pages).
- [63] Van Houten, J. M., and M. H. A. J. Herben, "Analysis of Phase-Correcting Fresnel-Zone Plate Antenna With Dielectric/Transparent Zones," *J. Electromagnetic Waves and Applications*, Vol. 8, No. 7, 1994, pp. 847–858.
- [64] Hristov, H. D., "The Multidielectric Fresnel Zone Plate Antenna—A New Candidate for DBS Reception," *IEEE Antennas Propagat. Symp. Digest*, Baltimore, MD, Vol. 1, July 21–26, 1996, pp. 746–749.
- [65] Herben, M. H. A. J., and H. D. Hristov, "Some Developments in Fresnel Zone Plate Lens Antennas," *IEEE Int. Antennas and Propagat. Symp.*, Orlando, FL, July 11–16, Symp. Digest, vol. 2, 1999, pp. 726–729.
- [66] Brandt, A. A., Yu. N. Pashin, and V. G. Petelin, "Study of Focusing Properties of Zone Antenna in Centimeter Wavelength Band," *Scientific Reports of Higher Schools*, No. 6, 1958, pp. 201–207 (in Russian).
- [67] Millimeter-Wave Radio Series 3800, Data Sheet, Norden Systems, Inc., Norwalk, CT.
- [68] Hristov, H. D., J. R. Urumov, and M. J. Semov, "Ring-Shaped Dielectric Antenna," *Eu. Microwave Conf.*, 6–12 Sept. 1980, Warsaw, Conf. Proc., pp. 109–113 / Reprint in *Adv. Antenna Technology*, (ed. P. J. B. Clarricoats), Reprint Vol. No. 1, Conf. Exhibitions & Publishers, UK, 1982, pp. 361–365.
- [69] Yamauchi, S., S. Honma, T. Honma, and H. Nakano, "Focusing Properties of Fresnel Zone-Plate and Its Application to a Helix Radiating a Circularly Polarized Wave," *Electronics and Communications in Japan*, Part 1, Vol. 73, No. 9, 1990, pp. 107–113.
- [70] Ji, Y., and M. Fujita, "Design and Analysis of a Folded Fresnel Zone Plate Antenna," *Int. J. Infrared and Millimeter Waves*, Vol. 15, Aug. 1994, pp. 1385–1406.
- [71] Yamauchi, J., and N. Nakano, "Theoretical and Experimental Investigations on Focusing Properties of the Fresnel Zone Lens and Plate," *IEEE Int. Antennas and Propagat. Symp.*, Orlando, FL, July 11–16, Symp. Digest, Vol. 2, 1999, pp. 746–749.
- [72] Guo, Y. J., and S. K. Barton, "High-Efficiency Zone Plate Reflector Incorporating Printed Resonators," *Proc. Int. Conf. on Antennas and Propagat. (ICAP'93)*, Edinburgh, UK, 1993, pp. 620–622.
- [73] Guo Y. J., and S. K. Barton, "Fresnel Zone Plate Reflector Incorporating Rings," *IEEE Microwave and Guided Wave Letts*, Vol. 3, Nov. 1993, pp. 417–419.
- [74] Wright, T. M. B., and P. C. Wilcockson, "Experimental Verification of Reflecting Zone Plate Antennas," *Int. Conf. on Antennas and Propagat. (ICAP'95)*, Apr. 4–7, 1995 IEE Conf. Publ. No. 407, Vol. 1, pp. 291–294.
- [75] Guo, Y. J., and S. K. Barton, "Offset Fresnel Zone Plate Antennas," *Int. J. of Satellite Communications*, Vol. 12, 1994, pp. 381–385.

- [76] Guo, Y. J., I. H. Sassi, and S. K. Barton, "Offset Fresnel Lens Antenna," *IEE Proc.-Microw. Antennas Propagat.*, Vol. 141, No. 6, Dec. 1994, pp. 517-522.
- [77] Guo, Y. J., and S. K. Barton, "A High-Efficiency Quarter-Wave Zone Plate Reflector," *IEEE Microwave Guided Wave Letts*, Vol. 2, No. 12, Dec. 1992, pp. 470-471.
- [78] Wilcockson, P. C., *Evaluation of Flat Reflectors for Space and Ground Station Antenna Applications, Report, Eu. Space Agency (ESA), Order 142600*, Dec. 22, 1994, (46 pages).
- [79] Garrett, J. E., and J. C. Wiltse, "Performance Characteristics of Phase-Correcting Fresnel Zone Plates," *IEEE MTT-S Int. Microwave Symp.*, Vol. 11, 1990, pp. 797-799.
- [80] Garrett, J. E., and J. C. Wiltse, "Fresnel Zone Plate Antennas at Millimeter Wavelengths," *Int. J. Infrared and Millimeter Waves*, Vol. 12, No. 3, 1991, pp. 195-220.
- [81] Van Houten, J. M., and M. H. A. J. Herben, "The Elliptical Fresnel Zone Plate Antenna," *Int. Conf. Antennas Propagat. (ICAP'95)*, Conf. Publ. No. 407/IEE, 1995, pp. 97-100.
- [82] Onodera, T., and T. Hoashi, "A Design Method of Offset Fresnel Zone Plate Reflector as Receiving Antenna," *IEEE Int. Antennas and Propagat. Symp.*, Orlando, FL, July 11-16, Symp. Digest, Vol. 2, 1999, pp. 742-745.
- [83] Sazonov, D. M., "Computer-Aided Design of Holographic Antennas," *IEEE Int. Antennas and Propagat. Symp.*, Orlando, FL, July 11-16, Symp. Digest, Vol. 2, 1999, pp. 738-741.
- [84] Sazonov, D. M., B. A. Mishustin, and V. I. Sergeev, "Radioholographic Antennas for Satellite Television Reception," *Proc. Int. Conf. on Antennas, Radiocommunication Systems and Means (ICARSM'97)*, Voronezh, Russia, May 1997, Vol. 2, pp. 82-85.
- [85] Minin, I. V., and O. V. Minin, "Invariant Properties of Elements of Diffraction Quasiopitics," *Computer Optics*, No. 6, 1989, pp. 89-97 (in Russian).
- [86] Cousin, P., G. Landrac, S. Toutain, and J. J. Delmas, "Calculation of the Focal Field Distribution and Radiation Pattern of a Parabolic Antenna with Fresnel Zones," *JINA '94*, Nice, France, 8-10 Nov., 1994, *Proc. Int. Symp. on Antennas*, pp. 489-492 (in French).
- [87] Ji, Y., and M. Fujita, "A Cylindrical Fresnel Zone Antenna," *IEEE Trans Antennas and Propagat.*, Vol. 44, Sept. 1996, pp. 1301-1303.
- [88] Minin, I. V., and O. V. Minin, "New Class Microwave Antennas Based on the Elements of the Diffraction Quasiopitics: Advantages and Applications," *IEEE Int. Antennas and Propagat. Symp.*, Orlando, FL, July 11-16, Symp. Digest, Vol. 2, 1999, pp. 754-757.
- [89] Minin, I. V., and O. V. Minin, "Antenna Systems for Millimeter-Wave Range Based on the Quasioptical Elements," *Conference on Optical Wireless Communications*, SPIE, Vol. 3532, 1998.
- [90] Minin, I. V., and O. V. Minin, *Diffraction Quasioptics and its Applications*. Novosibirsk, 1999 (in Russian).
- [91] Hristov, H. D., "Variety of Cylindrical Fresnel Zone Plate Antennas," *IEEE Int. Antennas and Propagat. Symp.*, Orlando, FL, July 11-16, Symp. Digest, Vol. 2, 1999, pp. 750-753.

Selected Bibliography

Hirsch, H. L., and D. C. Grove, *Practical Simulation of Radar Antennas and Radomes*, Norwood, MA: Artech House, 1988.

- Hristov, H. D., and M. H. A. J. Herben, "Quarter-Wave Fresnel Zone Planar Lens and Antenna," *IEEE Trans. Microwave and Guided Wave Letters*, Vol. 5, No. 8, 1995, pp. 249–251.
- Hristov, H. D., and M. H. A. J. Herben, "Millimeter-Wave Fresnel Zone Planar Lens and Antenna," *IEEE MTT-S 1995 Int. Microwave Symposium*, Mar. 16–20, Orlando, FL, *Symp. Digest*, Vol. 2, 1995, pp. 553–556.
- Jiang, G. Z., W. X. Zhang, and K. Fang, "The Focused Fields of Fresnel Zone Plate Lens," *Int. Symp. Antennas Propagat. (ISAP)*, Chiba, Japan, Conf. Proc., 1996, pp. 57–59.
- Jiang, G. Z., W. X. Zhang, and T. H. Liu, "New Types of Fresnel Zone Plate Lens With Lower Backward Radiation," *IEEE Int. Antennas Propagation Symp.*, Atlanta, GA, *Symp. Digest*, Vol. 1, June 1998, pp. 166–169.
- Lambley, R., "Fresnel Antenna," *Electronics and Wireless World*, Aug. 1989, p. 792.
- Wiltse, J. C., "The Phase-Correcting Zone Plate," *Proceedings of Tenth International Conference on Infrared and Millimeter Waves*, Lake Buena Vista, FL, Dec. 1985, pp. 345–347.
- Wiltse, J. C., "Dual-Band Fresnel Zone Plate Antennas," *Proceedings of SPIE*, Vol. 3062, 1997, pp. 181–185.
- Wiltse, J. C., "High Efficiency, High Gain Fresnel Zone Plate Antennas," *Proceedings of SPIE*, Vol. 3375, 1998, pp. 286–290.
- Wiltse, J. C., "Recent Developments in Fresnel Zone Plate Antennas at Microwave/Millimeter Wave," *Proceedings of SPIE*, Vol. 3464, 1998, pp. 146–154.
- Wiltse, J. C., and D. N. Black, "Millimeter-Wave Characteristics of Fresnel Zone Plates," *Proc. IEEE MTT-S Int. Microwave Symp.*, Las Vegas, NV, June 1987, pp. 437–440.
- Wiltse, J. C., and J. E. Garrett, "Recent Developments in Phase-Correcting Fresnel Zone Plate Antennas," *SPIE Intl. Conf. Infrared and Millimeter Waves*, Orlando, FL, Vol. 1514, Dec. 1990, pp. 608–610.
- Zhang, W. X., and G. Z. Jiang, "Review of the Layered Fresnel Zone Plate Lens Antenna," *IEEE Int. Antennas and Propagat. Symp.*, Orlando, FL, July 11–16, *Symp. Digest*, Vol. 2, pp. 734–737.

This page intentionally left blank

About the Author

Hristo D. Hristov is a graduate of the Sofia Technical University, Bulgaria. He holds Ph.D. and D.Sc. degrees in wireless communications. Dr. Hristov is now a professor at the Technical University of Varna, Bulgaria. He was a research fellow at the Strathclyde University, Glasgow; Queen Mary College, London University; and the Eindhoven University of Technology, the Netherlands, where he studied novel types of microwave antennas.

He is an observer-expert to the European Cooperation in Science and Technology (COST) research program on smart antennas for satellite and mobile communications. His current research interests include microwave/millimeter-wave conformal antennas, quasi-optical systems, and solar concentrators. Dr. Hristov is the co-author (with A. Kumar) of *Microwave Cavity Antennas*, Artech House, 1989.

This page intentionally left blank

Index

- π -phase shifting ring, 128
- Aberrations, 158–63
 - axial spherical, 159–60
 - frequency, 161–63
 - off-axis, 160–61
 - See also* Soret zone plates
- Amplitude, 14
 - axial field, 215, 216
 - back-lobe (BLL), 249
 - divergence factor, 256
 - equations, 7–8
 - of gridded plate, 202
 - ground media data, 8
 - interference field, 98
 - properties in boundless space, 6–12
 - radio link equations, 8–12
- Antenna(s)
 - aperture efficiency, 119
 - axial-mode helical (AHA), 272
 - backfire helical (BHA), 272
 - curved zone plate, 296–303
 - cylindrical zone plate, 298–302
 - defocused zone plate, 284, 286
 - dielectric ring as director, 126–29
 - directive properties, 119, 121
 - double-dielectric phase-reversal zone plate, 253–58
 - elevated over flat earth, 97–99
 - folded phase-reversal zone plate, 270–74
 - four-dielectric quarter-wave zone plate, 259
 - Fresnel zone plate, 231–303
 - integrated-circuit, 281–82
 - metal ring as director, 119–26
 - millimeter-wave, 302–3
 - paraboloidal zone plate, 297–98
 - phase-corrected, 253–68
 - planar (off-axis scanning), 282–87
 - planar (reflection), 268–82
 - planar (transmission), 232–68
 - planar offset, 288–96
 - polarization parameters, 32–34
 - printed reflector zone plate, 274–82
 - radiation field, 32
 - ring-shaped, 269
 - Soret zone plate, 232–53
 - spherical half-wave zone plate, 303
 - systems, 121, 122
 - transmission losses, 12
 - See also* Radiation patterns
- Antenna gain, 98
 - cylindrical zone plate, 301
 - diffraction pattern, 128
 - directive pattern, 237
 - as function of scan angle, 287
 - in ground radio systems, 119
 - rise in, 119
 - Soret zone plate, 245, 252
- Aperture
 - boundary condition, 56
 - circular, 62–64, 72–77

- distribution, 233
- efficiency, 119, 248–49, 299
- elementary area, 236
- in infinite plane screen, 58–62
- rectangular, 66–67, 69–72
- Asymmetric Fresnel zone plates, 142, 143
- Attenuation factors, 116–17
- Axial field distribution, 214
- Axial focusing, 213–21
 - approximate universal theory, 217
 - of curved zone plate, 217–21
 - gain, 221
 - of spherical zone plate, 213–17
- Axial-mode helical antenna (AHA), 272
 - configuration, 274
 - radiation pattern, 274
- Axial spherical aberration, 159–60
 - defined, 160
 - illustrated, 159
 - wavelengths, 160
 - See also* Aberrations
- Axial variation, 215, 216
- Babinet's principle, 64, 78
- Backfire helical antenna (BHA), 272
 - frequency operation, 273
 - radiation pattern, 272, 273
 - See also* Antenna(s)
- Back-lobe amplitude (BLI), 249
- Bessel functions, 64
- Boundary conditions
 - aperture, 56
 - approximate, 55
 - field, 13
- Brewster angle, 17
- Circular apertures, 62–64
 - Fresnel diffraction by, 72–77
 - Fresnel diffraction patterns, 76, 78, 79
 - infinite, 76
 - radiation pattern comparison, 77
- Circular polarization, 6
- Conical zone plates, 144, 145
 - convex, 211
 - cross-section, 210
 - dimensions of, 210–13
 - Fresnel zone pattern, 212
 - geometry, 211
 - profile curve function, 219
 - zone radii equation, 211
 - zone radius vs. zone number, 213
 - See also* Curved Fresnel zone plates
- Co-polar gain pattern, 33
- Cross-polar field pattern, 33
- Cross-polar gain pattern, 34
- Cross-polar isolation, 34
- Curved Fresnel zone plates, 142–46, 201–21
 - arbitrary, 144
 - axial focusing, 213–21
 - conical, 144, 145, 210–13
 - cylindrical, 144–46
 - dimensions of, 203–13
 - focusing properties, 213–21
 - introduction, 201–3
 - paraboloidal, 208–10
 - profile curve function, 219
 - pyramidal, 144, 145
 - spherical, 143–44, 202, 203–6
 - See also* Fresnel zone plates
- Curved zone plate antennas, 296–303
 - cylindrical, 298–302
 - disadvantage, 297
 - millimeter-wave, 302–3
 - paraboloidal, 297–98
 - spherical half-wave, 303
 - See also* Antenna(s); Fresnel zone plate antennas
- Cylindrical Fresnel zone plates, 144–46
 - aperture efficiency, 299
 - arrangements, 144
 - cross-type, 145, 146
 - nonsymmetrical, 145, 146
 - ring-type, 145, 146
 - strip-type, 145, 146
 - See also* Fresnel zone plates
- Cylindrical zone plate antenna, 298–302
 - fabrication, 298
 - far field, 300
 - gain, 301
 - geometry, 299
 - nonsymmetrical, 302
 - quarter-wave, 300
 - radiation pattern, 299, 301
 - symmetrical, 301
 - vertical zone plate, 298
 - See also* Antenna(s); Curved zone plate antennas

- Defocused zone plate antennas
 defined, 284
 geometry, 286
 illustrated, 284
- Design, 188–201
 gridded phase-shifting dielectric plate, 197–201
 multidielctric zone plates, 192–93
 multilayer phase-shifting dielectric plate, 196–97
 single-dielectric zone plate, 189–92
 solid phase-shifting dielectric plate, 193–96
See also Phase-corrected zone plates
- Dielectric layers
 electric thickness of, 28
 matrix, 31
- Dielectric losses, 28
- Dielectric plate
n-layer, 31
 phase-reversing, 127, 131
 structures, 129
 transmission loss, 127
- Dielectric ring, 126–29
 complex transmission coefficient, 127
 diffraction factor, 127
 diffraction pattern, 127
 phase-reversing, 128
See also Antenna(s)
- Diffraction
 by aperture in infinite plane screen, 58–62
 by rectangular aperture, 66–67
 factor, 120, 123, 127
 far-field, 64
 Fraunhofer, by circular aperture, 62–64
 Fresnel, 64–79
 Kirchhoff (scalar), 54–64
 Kirchhoff (vectorial), 80–82
 knife-edge, 88, 111–13
 multifocal zone plate properties, 155
 pattern, 120, 127, 134, 135
 physical theory of (PTD), 87–88
 radio wave, 106–8, 113–17
- Diffraction
 aperture efficiency, 119
 dielectric-type, 132
 focusing aperture, 51
 focusing properties, 50–54
 Fresnel zone, 118–35
 illustrated, 50, 51
 ring segment, 129–35
 single-ring lens-like, 51
- Dimensions, 203–13
 of conical zone plate, 210–13
 of paraboloidal zone plate, 208–10
 of spherical zone plate, 203–8
See also Curved Fresnel zone plates
- Doppler radar schematics, 269
- Double-dielectric phase-reversal zone plate antenna, 253–58
 amplitude divergence factor, 256
 configuration, 254
 dielectric phase shifters, 256
 far-field vector, 258
 feed gain patterns, 265
 focal distance-to-aperture diameter ratio, 254
 numerical results, 259–65
 radiation pattern, 262
 ray tracing, 255
 solid dielectric rings, 264
 total far-field scalar components, 258
See also Phase-corrected zone plate antennas
- Earth curvature
 accounting for, 101–4
 antenna heights and, 101
 interference ray scheme and, 102
- Electric field, 81, 123
 elementary, 85
 magnitude, 10
 strength, 10
 vectors, 2, 5, 20, 81
- Electromagnetic fields, linear superposition of, 19–21
- Electromagnetic waves, interference of, 19–25
- Elliptical polarization, 6
- Elliptical zones
 geometry formulation and design of, 288–89
 major semi-axis, 289
- Far-field
 approximation, 82

- defined, 62
- diffraction, 64
- elementary components, 85
- radiation of electric antenna sources, 4
- vector potential, 3
- wave equation solution, 3–5
- Feed-line power combining, 156
- Flat-earth scheme, 97–99
- Focal length
 - gain vs., 243
 - optimization, 178
- Focusing efficiency
 - dependent elements, 181
 - Fresnel zone plate, 54, 140
 - as function of phase increment, 182
 - phase-corrected zone plate, 181–85
- Focusing gain, 165, 167
 - axial, 177, 221
 - axial distance vs., 220
 - calculated, 183
 - phase-corrected zone plate, 181–85
 - Soret plate, 175, 176
 - for Wood's phase-reversal zone plate, 182
- Focusing properties
 - curved Fresnel zone plate, 213–21
 - diffractor, 50–54
 - Soret zone plate, 173–79
- Folded phase-reversal zone plate antenna, 270–74
 - AHA, 272, 274
 - BHA, 272, 273
 - configuration, 272
 - defined, 270–71
 - focusing illustration, 270
 - parameters, 273
 - Soret zone plate (SZP), 272
 - See also* Antenna(s); Planar zone plate antennas
- Four-dielectric quarter-wave zone plate antenna, 259
 - feed gain patterns, 265
 - gain patterns, 260
 - geometry, 259
 - numerical results, 259–65
 - planar dielectric lenses, 263
 - radiation pattern, 262
 - See also* Phase-corrected zone plate antennas
- Four-ray diffraction, 112–13
- Fraunhofer diffraction, 62–64
- Free-space power combining, 156–57
- Frequency aberration, 161–63
- Frequency bandwidth, 167–68
 - determining, 168
 - microwave Soret zone plate, 178–79
 - ratio vs., 168
 - relative, 168
 - Soret zone plate antenna, 246–47
- Frequency-selective structures (FSS), 152, 276
- Fresnel, Augustin, 37
- Fresnel diffraction, 64–79
 - by aperture in plane infinite screen, 59
 - by circular aperture, 72–77
 - dimensionless variables, 65–66
 - factors, 67, 77, 113
 - field, 64
 - by obstacles, 78–79
 - patterns, 73, 133
 - pure, 61
 - by rectangular aperture, 66–67
 - by slit, 72
 - by straight edge of semi-infinite screen, 70–72
- Fresnel integrals, 67–69
 - cosine, 67–68, 75
 - plots, 69
 - sine, 67–68, 75
- Fresnel-Kirchhoff diffraction theory, 35–86
 - derivation geometry, 55, 69–72
 - integral, 58
 - knife-edge hill diffraction and, 108
- Fresnel's biprism arrangement, 22
- Fresnel zone(s), 37–54
 - applied to radio communication links, 87–135
 - axial field intensity contribution, 185
 - boundaries, 44
 - construction, 40–45
 - construction geometry, 40
 - defined, 40
 - diffractor focusing properties, 50–54
 - in direct wave propagation, 89
 - equal, 50
 - field determination, 45–48

- fields, sum of, 48
- focusing coefficient, 51
- length of, 96
- lenses, 52, 54
- n -th space, 89
- obstructed by concentric disk obstacle, 49
- obstruction, 48–50
- on sea surface, 100, 101
- patterns, 173, 207, 208, 209, 210, 212
- plane, 42–45
- radio wave propagation and, 87–118
- radius, 65, 89, 172
- reflection and, 90–96
- rings, 52
- space, 44, 101
- spherical, 40–42
- total number of, 46
- Fresnel zone plate antennas, 231–303
 - curved, 296–303
 - defined, 231
 - gain and efficiency, 261
 - introduction, 231–32
 - millimeter-wave receiver with, 268
 - planar, 232–96
 - reflection, 231
 - transmission, 231
- Fresnel zone plates, 139–221
 - arbitrary shape, 144
 - asymmetric, 142, 143
 - classification by cross-sectional structure, 146–52
 - classification by shape of zonal surface, 141–46
 - curved, 142–46, 201–21
 - cylindrical, 144–46
 - first, 140
 - focusing efficiency, 54, 140
 - frequency bandwidth, 162
 - introduction, 139–40
 - linear, 141, 142
 - multiple phase-corrected, 149–50
 - phase-corrected, 179–201
 - planar, 141–42
 - polystyrene, 189
 - pyramidal, 144, 145
 - quarter-wave, 149, 184
 - reflectors, 150–52
 - short-focal microwave, 160
 - SI, 142, 143
 - Soret, 132, 141, 146–47, 153–79
 - spherical, 143–44
 - thickness, 191
 - transmission, 146–50
 - transmission function, 163
 - types of, 140–52
 - Wood, 147–49, 157
- Fresnel zone regions
 - applications, 87
 - free-space propagation and, 89–90
 - significant, 93, 94
- Fresnel zones in reflection, 90–96
 - application, 100–101
 - geometry, 91
 - homogeneous, 95
 - significant earth region and, 91–94
- Friis free-space equation, 11, 12
- Geometrical optics (GO), 87
- Geometrical theory of diffraction (GTD), 87
- Green theorem, 54
- Gridded phase-shifting dielectric plate, 197–201
 - amplitude/phase-transmission coefficients, 202
 - circular ring array, 197
 - complex transmission coefficient, 200
 - defined, 197
 - of double squares, 199
 - illustrated, 198
 - phase shift, 200
 - resonance frequency, 200
 - of single squares, 199
 - total grid-circuit susceptance, 200
 - transmission grid equivalent circuit model, 198
- Ground media, 8
- Ground-wave propagation paths, 88–89
 - illustrated, 88
 - propagation modes, 88–89
 - See also* Radio wave propagation
- Helmholz wave equation, 54
- Hilly terrain propagation, 87, 104–18
 - four-ray diffraction, 112–13
 - shape geometry, 106

- straight knife-edge approximation, 108–12
- terrain profile and link clearance, 105–6
- troposphere refraction influence, 117–18
- wave diffraction, 106–8, 113–17
 - See also* Radio wave propagation
- Huygen, Christiaan, 35, 37
- Huygens' element, 84
- Huygens'-Fresnel's principle, 38–39
- Huygen's principle, 35–37
 - classical construction illustration, 36
 - defined, 35
 - refraction law proof, 37
 - uses, 36
- Huygen's source, 57, 63, 83–86
 - defined, 83
 - illustrated, 84
 - polar radiation pattern of, 86
- Hyperbolic lens, 150
- Illumination angle, 123
- Inclination factor, 47
- Integrated-circuit antenna, 281–82
 - component fabrication, 282
 - cross-sectional view, 282
 - defined, 281–82
 - gain radiation patterns, 283
 - See also* Antenna(s)
- Interference, 19–25
 - amplitude, 98
 - arrangement for flat ground surface, 97
 - attenuation factor, 99
 - basis, 19
 - by coherent individual source, 25
 - by division of wave amplitude, 23–25
 - by division of wave front, 21–22
 - classical antenna array theory and, 25
 - factor, 99
 - line-of-sight schemes, 97–104
 - maxima, 99
 - methods, 21–25
 - optical/quasi-optical methods, 21–25
 - scheme with antenna elevated, 97–99
 - standing type patterns, 20–21
 - in summation, 21
 - term, 20, 21
- Isotropic antennas, 12
- Kirchhoff, Gustav, 54
- Kirchhoff's diffraction theory, 54–64
 - far-field equations based on, 232–33
 - integral, 54–58, 60, 186
 - scalar, 54–64
 - solution, 58
 - vectorial, 80–82
 - vectorial far field equations derived from, 233–37
- Knife-edge diffraction, 107
 - factor, 111
 - four-ray, 112–13
 - models, 88
 - total field, 112
 - See also* Diffraction
- Knife-edge hill, 106–8
 - geometry, 106
 - multiple, 116–17
 - problem approximation, 108–12
 - wave propagation, 107
 - See also* Hilly terrain
- Knife-edge loss, 108
- Kottler's equation, 80
- Lenses
 - converging, 169–70
 - Fresnel zone, 52, 54
 - hyperbolic, 150
 - Soret zone plate comparison, 170
- Lensmaker's formula, 169
- Linear Fresnel zone plates, 141, 142
- Linear polarization, 6
 - orthogonal, 16
 - ratio, 34
- Link clearance, 105–6
 - for negative refraction, 118
 - troposphere refraction influence on, 117–18
- Lommel functions, 232
- Mawzones offset zone plate antenna, 291
- Maxwell's equations, 1, 13
- Metal-dielectric phase-correcting plate structures, 152
- Metal grid
 - capacitive, 226
 - illustrated, 227
 - inductive, 226
 - matrix elements, 228

- transmission through dielectric plate
 - with, 226–29
- Metal ring, 119–26
 - diffraction factor, 120, 123
 - diffraction pattern, 120
 - illustrated, 121
 - See also* Antenna(s)
- Millimeter-wave antennas, 302–3
- Millimeter-wave Michelson interferometer, 267
- Minimum Fresnel propagation region, 90
- Multidielectric zone plates, 192–93
 - frequency vs. thickness, 193
 - thickness, 192
- Multilayer phase-shifting dielectric plate, 196–97
 - amplitude/transmission coefficients, 196, 197
 - example, 197
 - thickness, 196
- Multilayer zone plate construction, 279–81
- Near field region, 61–62
- Normalized co-polar field pattern, 33
- Normalized intensity function, 155
- Off-axis aberrations, 160–61
 - illustrated, 160
 - RPD, 160–61
 - See also* Aberrations
- Off-axis field analysis, 173–76
- Off-axis scanning, 282–87
 - defocused zone plate antenna system, 284
 - experimental studies, 283–84
 - far-field gain patterns, 285–86
 - feed trajectory, 284–85
 - numerical results, 286–87
- Offset elliptical zone plate antenna, 288–96
 - far-field analysis, 289–90
 - geometry formulation and design, 288–89
 - multilayer, 294
 - numerical/experimental characteristics, 290–96
 - phase-reversal, 293
 - reflective, 292
- transmission, 289–96
 - See also* Antenna(s); Planar zone plate antennas
- On-axis field analysis, 176–78
- Parabolic equation (PE) method, 88
- Parabolic reflector antenna, 285
- Paraboloidal zone plate, 208–10
 - convex, 209
 - Fresnel zone pattern, 209, 210
 - geometry, 208
 - profile curve function, 219
 - See also* Curved Fresnel zone plates
- Paraboloidal zone plate antenna, 297–98
 - defined, 297
 - dimensions/parameters, 297
 - illustrated, 298
 - See also* Antenna(s); Curved zone plate antennas
- Passive repeaters
 - dielectric-type, 131
 - grating, 132
 - illustrated, 129
 - ring segment diffractor as, 129–35
- Petzval curve, 285
- Phase, 14
 - equations, 7–8
 - function, 74
 - ground media data, 8
 - partial, compensation, 181
 - properties in boundless space, 6–12
 - radio link equations, 8–12
- Phase-corrected zone plate antennas, 253–68
 - designs/applications, 265–68
 - double-dielectric phase reversal, 253–58
 - four-dielectric quarter-wave, 259
 - numerical results, 259–65
 - See also* Antenna(s); Planar zone plate antennas
- Phase-corrected zone plates, 179–201
 - design considerations, 188–201
 - focusing efficiency, 181–85
 - focusing gain, 181–85
 - gridded phase-shifting dielectric, 197–201
 - multidielectric, 192–93
 - multilayer phase-shifting dielectric, 196–97

- phase correction mechanism, 179–81
- single-dielectric, 189–92
- solid phase-shifting dielectric, 193–96
- subzone technique, 187
- theory, 185–88
- thickness, 191
- See also* Fresnel zone plates
- Phase-correcting structures, 152
- Phase-reversing director, 126
- Physical optics (PO), 87
- Physical theory of diffraction (PTD), 87–88
- Planar Fresnel zone plates, 141–42, 153–201
 - asymmetric, 142, 143
 - cross, 142
 - dielectric permittivity measurement, 267
 - focusing optical wave, 142
 - hyperbolic, 142
 - illustrated, 141
 - linear, 141, 142
 - phase-corrected, 179–201
 - SI, 142, 143
 - Soret, 141, 153–79
 - See also* Fresnel zone plates
- Planar zone plate antennas, 232–96
 - for direct broadcast satellite (DBS), 233
 - disadvantage, 297
 - folded phase-reversal, 270–74
 - off-axis scanning in, 282–87
 - offset, with elliptical zone plate, 288–96
 - phase-corrected, 253–68
 - printed reflector, 274–82
 - reflection versions, 268–82
 - Soret, 232–53
 - transmission versions, 232–68
 - See also* Antenna(s)
- Plane Fresnel zones, 42–45
 - boundaries, 44
 - calculation geometry, 43
 - concentric, 43
 - defined, 42
 - radius, 42, 44
 - See also* Fresnel zone(s)
- Plane of incidence, 14
- Plane waves
 - incident on interface between mediums, 26
 - propagation of, 25
 - transmission matrix analysis, 25–31
- Poisson's bright spot, 79
- Polarization. *See* Wave polarization
- Polarization unit vector, 234, 235
- Power density
 - average, 20
 - total, 48
- Power flux density (PFD), 295
- Poynting vector, 10, 47
- Primary focal plane, 157
- Printed reflector zone plate antennas, 274–82
 - integrated-circuit, 281–82
 - multilayer construction, 279–81
 - parameters, 275, 277
 - quarter-wave zone plate reflector, 276–78
 - single-layer construction, 274–79
 - See also* Antenna(s); Planar zone plate antennas
- Profile curve function, 219
- Propagation. *See* Radio wave propagation
 - Pyramidal zone plates, 144, 145
- Quarter-wave zone plate reflector, 276–78
 - ring arrangement, 278
 - zone plate, 278
- Quarter-wave zone plates, 149
 - design considerations, 188–201
 - frequency characteristic, 184
- Quasioptical diffraction elements (QDE), 302
- Radiation near-field region, 62
- Radiation patterns, 121
 - approximated, 125
 - axial-mode helical antenna, 274
 - backfire helical antenna, 272, 273
 - cylindrical zone plate antenna, 299, 301
 - E*-plane, 280
 - experimental, 126
 - integrated-circuit antenna, 283
 - multiplication equation, 134
 - off-axis antenna, 287

- on-axis antenna, 287
- phase-reversal antenna, 262
- primary, 124, 125
- quarter-wave antenna, 262
- in Soret zone plate antenna, 237, 238, 244, 245, 251, 262
- for uniform aperture field, 134
- See also* Antenna(s)
- Radio relay links
 - Fresnel zone diffractors in, 118–35
 - over hilly terrain, 118
 - section illustration, 119
- Radio wave diffraction
 - four-ray, 112–13
 - by hill modeled as multiple knife-edge, 116–17
 - knife-edge, 108
 - by sharp hill with round ridge section, 113–16
 - significant segment, 108–12
 - by straight sharp hill, 106–8
 - See also* Diffraction
- Radio wave propagation
 - Fresnel zone regions important to, 89–90
 - Fresnel zones and, 87–118
 - ground-wave paths, 88–89
 - over hilly terrain, 87, 104–18
 - knife-edge hill, 107
- Rayleigh, Lord, 139–40
- Rayleigh's criterion, 100
- Rectangular aperture, 66–67
 - diffraction by, 69–72
 - with infinite dimensions, 70
 - with semi-infinite screen, 70–72
- Reflection
 - features, from flat earth, 94–96
 - Fresnel zones and, 90–96
 - law of, 13
 - matrix equation, 16–17
 - multiple, by dielectric slab, 24
 - at oblique wave incidence, 15
 - of plane electromagnetic waves, 13–17
 - at plane interface, 14
 - Rayleigh's criterion for, 100
 - of rough spherical earth, 104
 - special cases of, 17–19
 - total, surface wave resulting from, 18
 - wave, 18
 - See also* Transmission
- Reflection coefficient, 15, 18, 99, 227
 - calculation, 16
 - earth plane, 103
 - for smooth earth surface, 94
 - total, 25
 - voltage, 26
- Reflector offset antenna, 295
- Resonance frequency, 200
- Ring segment diffractor, 129–35
 - Fresnel diffraction pattern, 133
 - geometry, 130
 - horizontal diffraction pattern, 135
 - mounting, 134
 - normalized length, 130
 - ring segment widths/spacings, 132–33
 - vertical diffraction pattern, 134, 135
 - See also* Diffractors
- Ring-shaped dielectric antenna, 269
- Roughness
 - Rayleigh's criterion for, 100
 - reflectivity estimation, 104
- Scalar components, 4
- Scan curves, 285
- Semi-infinite screen, 70–72
 - defined, 70
 - diffraction factor of, 71
- Sharp hill diffraction, 113–16
 - round-shaped ridge segment, 115
 - variable ridge profile, 114
 - See also* Hilly terrain SI Fresnel zone plates, 142, 143
- Significant diffraction segment, 108–12
 - defined, 109
 - dimensionless chord, 110
 - illustrated, 109
- Significant propagation region, 90
- Single-dielectric zone plates, 189–92
 - profiles, 189
 - thickness, 191
 - See also* Fresnel zone plates
- Single-layer zone plate construction, 274–79
- Snell's law, 14, 17
- Solid phase-shifting dielectric plate, 193–96
 - amplitude vs. incidence angle, 195

- transmission coefficients vs. incidence angle, 195
- transmission coefficients vs. relative dielectric constant, 194
- Soret zone plate antenna, 232–53
 - amplitude-corrected, 246
 - antenna gain as function of scan angle, 287
 - aperture efficiency, 248–49
 - comparison with PRAs, 240
 - coplanar radiation patterns, 241
 - directive antenna gain, 243
 - efficiency curves, 241, 242
 - efficiency curve vs. focal distance, 242
 - experimental designs/measurements, 249–53
 - experimental/theoretical *E*-plane field pattern, 252
 - far-field equations, 232–33
 - far-field patterns, 239
 - feed radiation patterns, 244
 - folded, 272
 - frequency bandwidth, 246–47
 - frequency design, 237
 - gain, 245, 252
 - gain radiation pattern, 238, 239, 246
 - gain vs. focal length, 243
 - geometry, 234
 - numerical results, 237–49
 - off-axis, 287
 - on-axis, 287
 - radiation pattern, 237, 244, 245, 251
 - scan curves, 285
 - theoretical/experimental patterns, 251
 - vectorial far field equations, 233–37
 - See also* Antenna(s); Planar zone plate antennas
- Soret zone plates, 146–47
 - aberrations, 158–63
 - axial focusing gain, 177
 - circular, dimensioning of, 170–73
 - classical, 140, 146
 - concentric circular regions, 153
 - cross-sectional geometry, 213
 - cross-sectional view, 147
 - field intensity distribution, 177
 - focal length optimization, 178
 - focusing, 147
 - focusing gain, 175, 176
 - focusing intensity, 156
 - focusing operation, 156
 - focusing properties, 173–79
 - frequency bandwidth, 167–68, 178–79
 - half-wave RPD, 170
 - illumination by spherical wave, 169–70
 - millimeter-wave, 156
 - multiple focusing action, 153–57
 - multizone plate, 52
 - negative, 157
 - nonparaxial, 167
 - off-axis field analysis, 173–76
 - on-axis field analysis, 176–78
 - paraxial, 153, 156
 - positive, 157, 174
 - reflector, 150
 - resolution, 157–58
 - section geometry, 176
 - transmission function, 163–68
 - zone radii equation, 171
 - See also* Fresnel zone plates
- Spatial attenuation, 12
- Spectral domain technique (SDT), 249
- Spherical Fresnel zones, 40–42
 - calculation geometry, 41
 - n*-th, 45
 - radius, 40, 42
 - See also* Fresnel zone(s)
- Spherical half-wave zone plate antenna, 303
- Spherical zone plates, 143–44
 - axial focusing, 213–17
 - convex, 205–6
 - dimensions, 203–6
 - Fresnel zone patterns of, 207
 - geometry, 204
 - for optical wavelengths, 202
 - profile curve function, 219
 - reflective and transmissive, 203
 - zone radii equation, 209
 - See also* Curved Fresnel zone plates
- Subzone phase correction techniques, 187
- Time-harmonic fields, wave equations, 1–5
- Total gain pattern, 34
- Transmission
 - through dielectric plate with metal grid, 226–29

- law of, 14
- lines, 25–26
- through multilayer dielectric plates, 27–31
- multiple, by dielectric slab, 24–25
- at oblique wave incidence, 15
- of plane electromagnetic waves, 13–17
- at plane interface, 14
- special cases, 17–19
- See also* Reflection
- Transmission coefficient, 15
 - calculation, 16
 - of gridded plate, 202, 228
 - incidence angle vs., 195
 - multiple reflection, 255
 - relative dielectric constant vs., 194
 - of single layer grid, 200
 - of three-layer plate vs. incident angle, 197
 - total, 25
- Transmission Fresnel zone plates, 146–50
 - antenna, 231
 - multiple phase-corrected, 149–50
 - quarter-wave, 149, 184
 - Soret, 146–47
 - Wood, 147–49, 157
 - See also* Fresnel zone plates
- Transmission function, 163–68
 - binary-type, 165
 - of circular Soret zone plate, 163–66
 - defined, 163
 - equation, 164
 - of Soret zone plate with straight Fresnel zones, 166–67
- Transmission losses, 12
 - dielectric plate, 127
 - isotropic antenna, 12
- Transmission matrix
 - analysis, 25–31
 - elements, 29–30
 - equation, 17, 30
 - input, 30–31
 - square, 29
 - total, 30
 - two-port network, 30
- Troposphere refraction, 88
 - absence of, 104
 - accounting for, 101–4
 - index, 103
 - influence on link clearance, 117–18
 - interference interpretation, 104
 - interference ray scheme and, 102
- Tropospheric ray, 102
- Unidirectional pattern, 86
- Uniform theory of diffraction (UTD), 251
- Universal approximate equation, 219–21
- Vector potential
 - electric field, 2
 - far-field, 3
 - wave equation for, 1–3
- Wave equations
 - far-field solution to, 3–5
 - for magnetic vector potential, 1–3
 - solution geometry, 3
 - for time-harmonic fields, 1–5
- Wave polarization, 5–6, 14
 - arbitrary, 17
 - circular, 6
 - defined, 5
 - elliptical, 6
 - linear, 6, 16, 34
- Wedge-shaped wide hill, 116–17
- Wood zone plates, 147–49, 157
 - aperture phase, 147–48
 - cross-section geometry, 190
 - depth of grooves geometry, 190
 - focusing gain, 182
 - half-wave, 147
 - illustrated, 148
 - near-field intensity distribution, 184
 - origination, 148
 - phase-reversal, 148
 - ray shadowing, 192
 - ray tracing, 191
 - ring types, 149
 - stepwise phase-front transformation, 180
 - Wood-Wiltse, 148–49
 - See also* Fresnel zone plates
- Young, Thomas, 21–22, 37

This page intentionally left blank